Shock Wave-Boundary-Layer Interactions in High-Speed Intakes

Kiril Boychev

Submitted in fulfilment of the requirements for the
Degree of Doctor of Philosophy

James Watt School of Engineering
College of Science and Engineering
University of Glasgow

March 2021

Abstract

Shock wave boundary layer interaction (SWBLI) occurs in many aerospace applications such as wings in high-speed flight, missiles, and supersonic intakes. Key to the design of the latter is compressing a large volume of air with SWBLIs while maintaining maximum total pressure recovery and minimum flow distortion over a wide operating range. Under specific conditions, the formation of multiple SWBLIs (shock trains) within the intake can occur. Over the years, many numerical methods and models have been employed to predict the flow physics of shock trains. This work aims to determine the suitability of non-linear RANS turbulence closures for modelling shock trains in ducted geometries by implementing several non-linear closures in the University of Glasgow HMB3 CFD solver. First, the best modelling techniques for matching the experimental conditions were identified by performing validations against several shock train experiments. As a next step, several non-linear RANS closures were implemented in the solver. All closures improved the predicted wall pressures by accounting for the secondary flows present near the duct corners. The closures accounted for the secondary flow by predicting a fair level of normal Reynolds stress anisotropy near the corner of the duct. It was found that even simple non-linear closures based on quadratic constitutive relations result in significant improvements compared to linear closures. Additional simulations were performed at different Mach numbers, Reynolds numbers, and back (exit) pressures to assess the robustness of the non-linear closures and the sensitivity of the solution to changes in modelling parameters. It was observed that the flow distortion decreases rapidly downstream of the first shock in the shock train and that it is greatly influenced by its structure. As a final step, simulations of a shock train in a geometry representative of a high-speed intake were performed to assess the suitability of the closures for practical (real-world) applications. Three different geometries resulted in considerably different shock train structures compared to the ones in ducts. The flow distortion downstream of the shock train was found to be sensitive to both the incidence and roll angles. The SWBLI exhibited upstream and downstream movements within the intake with increasing incidence and roll angles.

Declaration

I certify that the thesis presented here for examination for a PhD degree of the University of Glasgow is solely my own work other than where I have clearly indicated that it is the work of others (in which case the extent of any work carried out jointly by me and any other person is clearly identified in it) and that the thesis has not been edited by a third party beyond what is permitted by the University's PGR Code of Practice.

I declare that the thesis does not include work forming part of a thesis presented successfully for another degree.

I declare that this thesis has been produced in accordance with the University of Glasgow's Code of Good Practice in Research.

I acknowledge that if any issues are raised regarding good research practice based on review of the thesis, the examination may be postponed pending the outcome of any investigation of the issues.

March 2021

.....

Kiril Boychev

Acknowledgements

First and foremost, I would like to express my gratitude to my supervisor Prof George Barakos for his invaluable support and encouragement throughout the project. He has been a role model for me throughout my academic years, and I strongly appreciate the advice and knowledge he gave and shared with me. The project would also not have been possible without the guidance and support from Dr Scott Shaw and MBDA Missile Systems Ltd. Specifically, I would like to thank Dr Scott Shaw for his constructive feedback and the opportunity to present my work. I would also like to thank Dr Rene Steijl for advising me on different matters and Dr Mark Woodgate for assisting me with various programming-related problems. Lastly, I would like to thank my colleagues, close friends, and family who made the project experience pleasant. I would not have been where I am now without their never-ending support.

Publications

Journal Papers

K. Boychev, G.N. Barakos, and R. Steijl, "Flow physics and sensitivity to RANS modelling assumptions of a multiple shock wave/turbulent boundary layer interaction", *Aerospace Science and Technology*, Vol. 97, Issue 1, 2019, DOI: https://doi.org/10.1016/j.ast.2019.105640

K. Boychev, G.N. Barakos, R. Steijl, and S. Shaw, "Parametric study of multiple shock-wave/turbulent-boundary-layer interactions with a Reynolds stress model", *Shock Waves*, Vol. 36, Issue 1, 2021, DOI: https://doi.org/10.1007/s00193-021-01011-z

Papers in Conference Proceedings

K. Boychev, G.N. Barakos, R. Steijl, and S. Shaw, "High fidelity simulations of supersonic intakes", *Proceedings of the AIAA Scitech 2020 Forum and Exposition, 6-10 January 2020, Orlando, Florida*.

K. Boychev, G.N. Barakos, R. Steijl, "Numerical Simulations of Multiple Shock Wave Boundary Layer Interactions", *Proceedings of the AIAA Scitech 2021 Forum and Exposition, 11-15 & 19-21 January 2021, Virtual Event*.

K.Boychev, G.N. Barakos, R. Steijl, "Parametric Study of Multiple Shock Wave/Turbulent Boundary Layer Interactions with a Reynolds Stress Model", *8th European Congress on Computational Methods in Applied Science and Engineering (ECCOMAS 2020), 14th World Congress on Computational Mechanics (WCCM XIV), 11-15 January 2021, Virtual Congress*.

Papers in Conferences without Proceedings

N. Tylor et al., "The Prediction of Vortex Interactions on a Generic Missile Configuration Using CFD: Current Status of Activity in NATO AVT-316", *Proceedings of the AVT-307 Research Symposium on Separated Flow: Prediction, Measurement and Assessment for Air and Sea Vehicles, 7-9 October 2019, Trondheim, Norway*.

Presentations without Proceedings

K. Boychev, G.N. Barakos, and R. Steijl, "Multiple shock wave/turbulent boundary layer interactions", *32nd Scottish Fluid Mechanics Meeting*, 30 May 2019.

K. Boychev, G.N. Barakos, and R. Steijl, "Flow physics and sensitivity to RANS modelling assumptions of multiple shock wave/turbulent boundary layer interactions", *UK Fluids Network*, 28 August 2019.

Contents

Abstract i

Declaration ii

Acknowledgements iii

Publications iv

1 Introduction 1

1.1 Background and motivation . . . 1

1.1.1 Shock wave boundary layer interactions in high-speed intakes . . . 2

1.1.2 Normal shock interactions . . . 5

Attached (weak) normal shock interaction . . . 5

Separated (strong) normal shock interaction . . . 6

1.1.3 Onset of separation end effect of confinement . . . 7

1.1.4 Multiple normal shock interactions . . . 11

Summary of experiments . . . 16

Recent numerical simulations . . . 20

1.1.5 Control of shock wave boundary layer interactions . . . 28

1.2 Chapter summary . . . 30

1.3 Thesis Objectives . . . 31

1.4 Thesis Outline . . . 31

2 Numerical models and CFD methods 33

2.1 Formulation . . . 33

2.2 Numerical Method . . . 35

2.3 Turbulence Modelling . . . 37

2.3.1 Similarities between temporal averaging and spatial filtering . . . 37

2.3.2 Linear Two-Equation Eddy-viscosity models . . . 39

Wilcox's $k-\omega$ model . . . 40
Meter's $k-\omega$ BSL Baseline (BSL) model . . . 40
Menter's $k-\omega$ SST model . . . 42
2.3.3 Non-linear Two-Equation Eddy-viscosity models . . . 42
$k-\omega$ EARSM model . . . 43
Quadratic constitutive relations . . . 43
2.3.4 Hybrid RANS/LES methods . . . 45
Very Large Eddy Simulation (VLES) . . . 45
Limited Numerical Scales (LNS) . . . 46
Detached Eddy Simulation (DES) . . . 46
Scale Adaptive Simulation (SAS) . . . 48
2.4 Grid generation techniques . . . 50
2.4.1 Fully matched grids . . . 50
2.4.2 Overset grids . . . 50
2.5 Summary of HMB development . . . 52

3 Validation of CFD methods for SWBLIs 53
3.1 Normal shock interactions . . . 53
3.1.1 Grids and numerical setup . . . 53
3.1.2 Comparison with experimental data . . . 56
Scale-resolving simulations . . . 58
3.2 Multiple normal shock interactions . . . 63
3.2.1 Grids and numerical setup . . . 63
3.2.2 Comparison with experimental data . . . 68
Two-dimensional calculations . . . 68
Three-dimensional calculations . . . 78
Effect of turbulence models . . . 81
3.2.3 Further insight into the quadratic constitutive relations . . . 100
Effect of the C_{cr1} constant . . . 100
Comparing QCR V1 $C_{cr1} = 0.4$ and EARSM . . . 106
3.2.4 Turbulent kinetic energy limiters . . . 109
Application of the P_k limiter . . . 109
Shock spacings . . . 111
Limiting the source terms in the k and ω equations away from walls . 112
3.2.5 Scale-resolving simulations . . . 114
Numerical Setup . . . 115

Results and Discussion . . . 119
3.3 Chapter summary . . . 123

4 Sensitivity of MSWBLIs to inflow conditions and geometry 125
4.1 Grids and numerical setup . . . 125
4.2 Effect of Reynolds and Mach number . . . 129
4.3 Effect of confinement . . . 130
4.4 Effect of aspect ratio . . . 134
4.5 Matching pre-shock Mach number . . . 137
4.6 Effect of cross-section . . . 139
4.7 Efficiency metrics . . . 143
4.8 Chapter summary . . . 147

5 MSWBLIs in high-speed intakes 149
5.1 Fore-body intake geometry . . . 149
5.2 Grids and numerical setup . . . 153
5.3 Cases . . . 155
5.4 Investigating turbulence modelling . . . 156
5.5 Effect of total angle, σ . . . 160
5.5.1 Configuration A . . . 160
5.5.2 Configuration B . . . 161
5.5.3 Configuration C . . . 162
5.5.4 Efficiency metrics . . . 162
5.6 Effect of roll angle, λ . . . 168
5.6.1 Configuration A . . . 168
5.6.2 Configuration B . . . 168
5.6.3 Configuration C . . . 169
5.6.4 Efficiency metrics . . . 169
5.7 Chapter summary . . . 176

6 Conclusions and future work 178
6.1 Conclusions . . . 178
6.2 Future work . . . 181

A Jarrin's synthetic turbulence method implementation 182

B Generation of mean inflow profiles 196

C Simulations of a store body **224**

D Fore-body intake geometry drawings **249**

List of Tables

1.1 Normal shock interactions. 17
1.2 Shock trains with a λ-foot structure. 18
1.3 Shock trains with a χ structure. 19
1.4 Corner separation sizes predicted by RANS and Hybrid RANS/LES simulations (adapted from Bruce *et al.* [19] and Arvidson *et al.* [6]) of the $M_r = 1.40$ interaction studied experimentally by Bruce *et al.* [19] (^{a} corner size estimated from time averaged skin friction pattern). 21
1.5 Numerical simulations of normal shock wave boundary layer interactions. . . 23
1.6 Numerical simulations of multiple normal shock wave boundary layer interactions. 27

2.1 Turbulence models and methods used in this work, implemented in HMB3; $^+$ - different variants of the model are available; * - any k-ω model can be used with this method 39

3.1 Grid parameters; dash indicates hyperbolic stretching; values in brackets indicate spacing in wall units obtained using an average y^+ of 0.732. 54
3.2 Simulation parameters. 55
3.3 Two-dimensional grid parameters; values in brackets indicate spacing in wall units. 66
3.4 Three-dimensional grid parameters; values in brackets indicate spacing in wall units. 66
3.5 Two-dimensional simulations parameters. 67
3.6 Three-dimensional simulations parameters. 67
3.7 Grid sizes and refinement ratios for the coarse, medium, and fine grids. 76
3.8 Order of convergence, asymptotic solution and grid convergence index calculated from the coarse, medium, and fine grids. 76
3.9 Simulation parameters. 93

3.10 Distances between the shocks; $d_1 = \Delta$. 112

4.1 Shock train parametric cases; cases in bold have adjusted M_u to match the reference M_r. 128
4.2 Grid parameters; colon symbol stretching. 128

5.1 Total pressure recovery for mixed compression intake designed with one-dimensional isentropic relations. 151
5.2 Grid parameters for the fore-body intake. 154
5.3 Fore-body intake cases. 156
5.4 Confinement levels for configuration C at $\sigma = 0$ deg predicted by the $k-\omega$ SST and $k-\omega$ EARSM turbulence models. 159
5.5 Stagnation pressures at $x/h = 30$ (engine face). 167
5.6 Stagnation pressures at $x/h = 30$ (engine face). 175

C.1 Grid parameters (all dimensional quantities are given in millimetres). 226
C.2 Simulation parameters. 227
C.3 GCI for the C_Z aerodynamic coefficient. 232
C.4 Unsteady simulations parameters. 243

List of Figures

1.1 Missile high-speed intake. 1
1.2 Intake types based on their compression method; (a) external, (b) mixed, and (c) internal. 2
1.3 Terminal shock structures (adapted from Sajben *et al.* [114]); (a) normal shock wave, (b) normal shock wave with λ-foot, (c) multiple normal shock waves, and (d) multiple oblique shock waves. 3
1.4 Basic shock wave boundary layer interactions in two dimensional flow according to Dèlery *et al.* [34] (adapted from Dèlery *et al.* [34]). 4
1.5 Shock interference types (adapted from Sanderson [116]). 5
1.6 Weak normal shock interaction; (adapted from Dèlery [33]). 5
1.7 Strong normal shock interaction (adapted from Dèlery [33]). 6
1.8 Schlieren visualisations of a normal shock interaction at $M_r = 1.23$ (a), $M_r = 1.33$ (b), and $M_r = 1.45$ (c) (adapted from Doerffer *et al.* [39].) 7
1.9 Pre-shock Mach number and incompressible shape factor for attached and separated normal shock interactions; filled symbols correspond to separated interactions and empty symbols to attached interactions (adapted from Dèlery [37]). 8
1.10 Oil flow visualisations of a normal shock interaction at $M_r = 1.30$ (a), $M_r = 1.40$ (b), and $M_r = 1.50$ (c) (adapted from Bruce *et al.* [19]). 9
1.11 Schematic of the normal shock wave structure near a corner and of the corner flow. 9
1.12 Pre-shock Mach number and flow confinement for attached and separated normal shock interactions from table 1.1; filled symbols correspond to separated interactions and empty symbols to attached interactions [7, 19, 28, 41, 65, 66, 115]; * - boundary layer thickness estimated from corner flow sizes and LDA measurements 10

1.13 Pre-shock Mach number and flow confinement for single and multiple normal shock interactions from tables 1.1 and 1.2 [7, 19, 22, 23, 51, 65, 66, 98, 99, 115, 129, 131, 149]. 11
1.14 Schematic of two strong normal shock waves interacting with a boundary layer (adapted from Carroll [23]). 11
1.15 Schlieren from the multiple normal shock interaction experiment by Carroll *et al.* [23, 25–27] (top), schematic of a multiple normal shock interaction in rectangular duct (middle), and schematic of a multiple normal shock interaction in an intake (bottom). 13
1.16 Pre-shock Mach number and flow confinement for single, multiple normal shock interactions, and multiple oblique shock interactions from tables 1.1 and 1.2 [5,7,18,19,22,23,35,39,51–53,70,77,78,98,99,115,129–131,148,149]. 15
1.17 Qualitative sketch of a typical experimental setup used in control of normal SWBLI studies. 28

2.1 Fully matched grid topology of a fore-body intake geometry 50
2.2 Fully matched grid topology of a duct with a bump 51
2.3 Overset grid topology of a store geometry (left); detailed view of the store grid topology (right); grid slices (bottom) 51

3.1 Sketch of the experimental setup of the SWBLI experiment by Dèlery [36]. . 54
3.2 Numerical domain and boundary conditions (top); grid blocking topology (bottom). 55
3.3 Lower wall pressure on the coarse and fine grids with the $k-\omega$ SST model. . 56
3.4 Lower wall pressure on the coarse and fine grids with the $k-\omega$ EARSM model. 56
3.5 Mach number contours on the fine grid with the $k-\omega$ EARSM model. 57
3.6 Streamwise velocity profiles from the coarse grid at $x/h = 2.81$, $x/h = 3.02$, and $x/h = 3.44$. 57
3.7 Streamwise velocity profiles from the fine grid at $x/h = 2.81$, $x/h = 3.02$, and $x/h = 3.44$. 58
3.8 Reynolds stress profiles at $x/h = 2.81$, $x/h = 3.02$, and $x/h = 3.44$. 58
3.9 Synthetic eddy method at the inlet. 59
3.10 Lower wall pressure for the DES simulation performed on the coarse and fine grids (a) and effect of averaging on the coarse grid (b). 60
3.11 Instantaneous Q criterion iso-surfaces $Q = 10$ colored by Mach number for the $k-\omega$ SST DES simulation on the coarse grid (top) and fine grid (bottom). 61

3.12 Lower wall pressure for the SAS and LNS simulations performed on the fine grid. 61
3.13 Instantaneous Q criterion iso-surfaces $Q = 10$ colored by Mach number for the $k-\omega$ SST SAS (top), the $k-\omega$ SST LNS (middle), and the $k-\omega$ EARSM LNS (bottom) simulations. 62
3.14 Sketch of the experimental setup of the MSWBLI experiment by Carroll [24]. 64
3.15 Numerical domain and boundary conditions (top); grid blocking topology (bottom). 64
3.16 Iteration history of the residuals. 68
3.17 Wall pressure (a) and Mach number contours for the coarse (b), medium (c), and fine (d) grids. 69
3.18 Centreline Mach number for the coarse, medium, and fine grids. 69
3.19 Skin friction coefficient for the coarse, medium, and fine grids. 70
3.20 Streamwise velocity contours u/V_u for the fine grid (a) and profiles (b-k) for the coarse, medium, and fine grids. 71
3.21 Turbulent kinetic energy k/V_u^2 for the fine grid (a) and profiles (b-k) for the coarse, medium, and fine grids. 72
3.22 Reynolds stress contours $\overline{u'u'}/V_u^2$ for the fine grid (a) and profiles (b-k) for the coarse, medium, and fine grids. 73
3.23 Reynolds stress contours $-\overline{u'v'}/V_u^2$ for the fine grid (a) and profiles (b-k) for the coarse, medium, and fine grids. 74
3.24 Reynolds stress contours $\overline{v'v'}/V_u^2$ for the fine grid (a) and profiles (b-k) for the coarse, medium, and fine grids. 75
3.25 Wall pressure (a) and Mach number contours for the k-ω (b), baseline k-ω (c), $k-\omega$ SST (d), and $k-\omega$ EARSM (e) turbulence models on the two-dimensional fine grid. 77
3.26 Wall pressure (a) and Mach number contours for the three-dimensional coarse (b), medium (c), fine (d), and veryfine (e) grids obtained with the $k-\omega$ SST turbulence model. 78
3.27 Centreline Mach number for the three-dimensional coarse, medium, fine, and veryfine grids obtained with the $k-\omega$ SST turbulence model. 79
3.28 Wall pressure for the three-dimensional medium and fine grids obtained with the $k-\omega$ EARSM turbulence model. 79
3.29 Centreline Mach number for the three-dimensional medium and fine grids obtained with the $k-\omega$ EARSM turbulence model. 79

3.30 Numerical schlieren obtained from the very fine grid (top) and experimental schlieren (bottom). 80
3.31 Experimental, very fine grid wall pressure, and wall pressure computed with the Waltrup and Billig empirical equations [14, 145]. 81
3.32 Wall pressure (a) and Mach number contours the standard k-ω (b), baseline k-ω (c), $k-\omega$ SST (d), and $k-\omega$ EARSM (e) turbulence models. 82
3.33 $M = 1$ (shaded green) and $u/V_u = -1 \times 10^{-3}$ (shaded blue) isosurfaces for the standard k-ω (a), baseline k-ω (b), $k-\omega$ SST (c), and $k-\omega$ EARSM (d) turbulence models. 84
3.34 Visualisation of the wall shear stress using friction lines just above the wall for the k-ω (a), baseline k-ω (b), $k-\omega$ SST (c), and $k-\omega$ EARSM (d) turbulence models. 84
3.35 Comparison of the visualisation of the $k-\omega$ EARSM wall shear stress using friction lines just above the wall (top) with the oil flow visualisation from the experiment (bottom). 84
3.36 Centreline Mach number for the standard k-ω, baseline k-ω, $k-\omega$ SST , and $k-\omega$ EARSM turbulence models. 85
3.37 Skin friction for the $k-\omega$ SST and the $k-\omega$ EARSM turbulence models. . . 85
3.38 Streamwise velocity u/V_u contours (a) for the $k-\omega$ EARSM and profiles (b-k) for the standard k-ω, baseline k-ω, $k-\omega$ SST , and the $k-\omega$ EARSM turbulence models on the medium grid. 86
3.39 Wall normal velocity v/V_u contours (a) for the $k-\omega$ EARSM and profiles (b-k) for the standard k-ω, baseline k-ω, $k-\omega$ SST , and the $k-\omega$ EARSM turbulence models on the medium grid. 87
3.40 Turbulent kinetic energy k/V_u^2 contours (a) for the $k-\omega$ EARSM and profiles (b-k) for the standard k-ω, baseline k-ω, $k-\omega$ SST , and the $k-\omega$ EARSM turbulence models on the medium grid. 88
3.41 Reynolds stress $\overline{u'u'}/V_u^2$ contours (a) for the $k-\omega$ EARSM and profiles (b-k) for the standard k-ω, baseline k-ω, $k-\omega$ SST , and the $k-\omega$ EARSM turbulence models on the medium grid. 89
3.42 Reynolds stress $-\overline{u'v'}/V_u^2$ contours (a) for the $k-\omega$ EARSM and profiles (b-k) for the standard k-ω, baseline k-ω, $k-\omega$ SST , and the $k-\omega$ EARSM turbulence models on the medium grid. 90
3.43 Reynolds stress $\overline{v'v'}/V_u^2$ contours (a) and profiles (b-k) for the standard k-ω, baseline k-ω, $k-\omega$ SST , and the $k-\omega$ EARSM 91

3.44 Wall pressure and Mach number contours for the $k-\omega$ SST , $k-\omega$ SST QCR V1, and the $k-\omega$ SST QCR V2 models. 92
3.45 Separation $u/V_u = 1\times10^{-3}$ and sonic $M=1$ iso-surfaces for the $k-\omega$ SST , $k-\omega$ SST QCR V1, and the $k-\omega$ SST QCR V2 models. 94
3.46 Wall shear stress visualisation using friction lines just above the surface for the $k-\omega$ SST , $k-\omega$ SST QCR V1, and the $k-\omega$ SST QCR V2 models. . . 95
3.47 Comparison of the visualisation of the $k-\omega$ SST QCR V1 wall shear stress using friction lines just above the surface (top) to the experiment (bottom). . . 95
3.48 Reynolds stress $\overline{u'u'}/V_u^2$ contours for the $k-\omega$ SST model and profiles. . . . 96
3.49 Reynolds stress $-\overline{u'v'}/V_u^2$ contours for the $k-\omega$ SST model and profiles. . . 97
3.50 Reynolds stress $-\overline{v'v'}/V_u^2$ contours for the $k-\omega$ SST model and profiles. . . 98
3.51 Turbulent kinetic energy k/V_u^2 contours for the $k-\omega$ SST model and profiles. 99
3.52 Wall pressure and Mach number contours for the $k-\omega$ SST QCR V1 (b), $k-\omega$ SST QCR V1 $C_{cr1}=0.2$, and the $k-\omega$ SST QCR V1 $C_{cr1}=0.3$ models. 100
3.53 Streamwise vorticity contours for the $k-\omega$ SST $C_{cr1}=0.0$, $k-\omega$ SST QCR V1 , $k-\omega$ SST QCR V1 $C_{cr1}=0.2$, and the $k-\omega$ SST QCR V1 $C_{cr1}=0.3$ models. 101
3.54 Reynolds stress $\overline{v'w'}/V_u^2$ contours for the $k-\omega$ SST $C_{cr1}=0.0$, $k-\omega$ SST QCR V1 , $k-\omega$ SST QCR V1 $C_{cr1}=0.2$, and the $k-\omega$ SST QCR V1 $C_{cr1}=0.3$ models. 103
3.55 Reynolds stress $(\overline{v'v'}-\overline{w'w'})/V_u^2$ contours for the $k-\omega$ SST $C_{cr1}=0.0$, $k-\omega$ SST QCR V1 , $k-\omega$ SST QCR V1 $C_{cr1}=0.2$, and the $k-\omega$ SST QCR V1 $C_{cr1}=0.3$ models. 104
3.56 Comparison of the $k-\omega$ SST and $k-\omega$ SST QCR V2 $\frac{\partial}{\partial y\partial z}(\overline{v'v'}-\overline{w'w'})/V_u^2$ and $-(\frac{\partial^2}{\partial y^2}-\frac{\partial^2}{\partial z^2})\overline{v'w'}/V_u^2$ contours. 105
3.57 Wall pressure and Mach number contours for the $k-\omega$ SST , $k-\omega$ SST QCR V1 $C_{cr1}=0.4$, and the $k-\omega$ EARSM models. 106
3.58 Streamwise vorticity contours for the $k-\omega$ SST , $k-\omega$ SST QCR V1, $k-\omega$ SST QCR V2, and the $k-\omega$ EARSM models. 107
3.59 Separation $u/V_u = 1\times10^{-3}$ and sonic $M=1$ iso-surfaces for the $k-\omega$ SST , $k-\omega$ SST QCR V1 $C_{cr1}=0.4$, and the $k-\omega$ EARSM models. 108
3.60 Wall pressure and Mach number contours for the $k-\omega$ SST QCR V1 $C_{cr1}=$ 0.4 model with and without the P_k limiter. 109
3.61 Turbulent kinetic energy k/V_u^2 contours for the $k-\omega$ SST QCR V1 $C_{cr1}=$ 0.4 model with and without the P_k limiter. 110

3.62 Definition of the distance Δ used to nondimensionalise the distances between the shocks; red-line indicates the approximate boundary layer edge. 111
3.63 Comparison of shock spacings. 112
3.64 F_{clip} contours for the $k-\omega$ SST QCR V1 $C_{cr1} = 0.4$ model. 113
3.65 Wall pressure and Mach number contours for the P_k limiter and $F_{clip} = 0.6$ simulations. 114
3.66 Reconstructed stresses for a non-dimensional timestep of $\Delta t = 0.03$ (top) and $\Delta t = 0.05$ (bottom). 117
3.67 Inlet profiles featuring velocity fluctuations superimposed on the mean velocities. 118
3.68 Q-criterion ($Q = 0.03$) colored by the Mach number at two flow-through times and wall pressure averaged over one flow-trough time. 119
3.69 Mean velocity profile from $k-\omega$ SST and blending functions. 120
3.70 Comparison of the mean streamwise velocity to the law of the wall. 121
3.71 Q-criterion ($Q = 0.03$) colored by the Mach number at two flow-through times and wall pressure averaged over one flow-trough time. 122

4.1 Grid A (a), cross-section of grid A (b), cross-section of grid B (c). The quarter of the numerical domain is outlined by the red-line. 126
4.2 Cross-section of grid A (a), grid C (b), and grid D (c). The red lines indicate block boundaries. 126
4.3 Wall pressure (top) and Mach number contours (bottom) for the reference and reduced M_u and Re_h cases of table 4.1. 129
4.4 Visualisation of the wall shear stress using friction lines at the wall for cases 1, 3, and 4 of table 4.1. 130
4.5 Wall pressure (top) and Mach number contours (bottom) for the reference and reduced δ_r/h cases of table 4.1. 131
4.6 Shock train length L/h and onset x_r/h with respect to confinement level; L/h is obtained from the mid-plane slices at the location where the supersonic contours end. 132
4.7 Visualisation of the wall shear stress using friction lines at the wall for cases 1, 6, and 5 of table 4.1. 132
4.8 Iso-surfaces of $M = 1.0$ (green) and $u/V_u = 1 \times 10^{-3}$ (blue) for the reference, lower M_u, lower Re_h and lower δ_r/h cases of table 4.1. 133
4.9 Wall pressure (a) and Mach number contours (b-c) for the reference and reduced w/h case of table 4.1. 134

4.10 Visualisation of the wall shear stress using friction lines at the wall for cases 1 and 7 of table 4.1. 135
4.11 Centreline Mach number distributions for the cases of table 4.1. 136
4.12 Skin friction coefficient distributions for the cases of table 4.1. 136
4.13 Wall pressure (top) and Mach number contours (bottom) for the reference and lower δ_r/h and Re_h cases of table 4.1. 138
4.14 Visualisation of the wall shear stress using friction lines on the wall for cases 1, 8, and 9 of table 4.1. 138
4.15 Iso-surfaces of $M = 1.0$ (shaded green) and $u/V_u = 1 \times 10^{-3}$ (shaded blue) for the reference and lower δ_r/h and Re_h cases of table 4.1. 139
4.16 Wall pressure (top) and Mach number contours (bottom) for the reference, circular, and rounded geometry cases of table 4.1. 140
4.17 Iso-surfaces of $M = 1.0$ (green) and $u/V_u = 1 \times 10^{-3}$ (blue) for the reference, circular, and rounded geometry cases of table 4.1. 141
4.18 Streamwise vorticity contours for the reference, circular, and rounded geometry cases of table 4.1 142
4.19 Mach number contours for cases 12 to 16 of table 4.1. 143
4.20 Quadratic surface fit for FD; $R^2 = 0.982$. 145
4.21 Quadratic surface fit for TPR; $R^2 = 0.994$. 146
4.22 Flow distortion for the reference, lower M_u and lower Re_h cases. 147

5.1 Fore-body intake geometry, configurations,A, B, and C. Schematic of the intake geometries is shown on the right. 150
5.2 Intake start/unstart limits based on the Kantrowitz and isentropic contraction limits. 152
5.3 Fore-body intake numerical domain and boundary conditions. 153
5.4 Configuration C grid (left) and blocking (right). 154
5.5 Fore-body intake axis definitions. 155
5.6 Wall pressure (b) and Mach number contours (a,c) for configuration C $k-\omega$ SST (top) and $k-\omega$ EARSM (bottom). 158
5.7 Total pressure recovery (left) and flow distortion (right) efficiency metrics at $\sigma = 0$ deg and $\sigma = 5$ deg. 163
5.8 Wall pressure (b) and Mach number contours (a,c) for configuration A at $\sigma = 0$ deg (top) and $\sigma = 5$ deg (bottom). 164
5.9 Wall pressure (b) and Mach number contours (a,c) for configuration B at $\sigma = 0$ deg (top) and $\sigma = 5$ deg (bottom). 165

5.10 Wall pressure (b) and Mach number contours (a,c) for configuration C at $\sigma = 0$ deg (top) and $\sigma = 5$ deg (bottom). 166
5.11 Total pressure recovery (left) and flow distortion (right) efficiency metrics at $\sigma = -3, 0, 5,$ and 10 deg. 167
5.12 Configuration A Mach number contours (top) and wall pressures (bottom) at $\lambda = 3$ deg and $\lambda = 0$ deg. 171
5.13 Configuration B Mach number contours (top) and wall pressures (bottom) at $\lambda = 3$ deg and $\lambda = 0$ deg. 172
5.14 Configuration C Mach number contours (top) and wall pressures (bottom) at $\lambda = 3$ deg and $\lambda = 0$ deg. 173
5.15 Total pressure recovery (left) and flow distortion (right) efficiency metrics at $\sigma = 5$ deg and $\lambda = 3$ deg. 174

A.1 Reference frame and definition of the eddy sizes 183
A.2 Eddies, inlet plane grid, and resulting velocity components 184
A.3 Instantaneous velocity time history (top) and turbulent kinetic energy spectrum (bottom) 185

B.1 Generated van Driest transformed mean velocity u_c^+ of Musker's [96] law-of-the wall and law-of-the wake 197
B.2 Definition of the wall-normal distances 198
B.3 Mean streamwise velocity profile for a rectangular inlet with two walls 199

C.1 Missile geometry. 225
C.2 Body-fixed coordinate system; the flow coordinate system is coloured in blue. 225
C.3 Blocking topology of the store body grid. 226
C.4 Cell volume at $x/L_{ref} = 0.5$ for the very fine (left), extra-fine (middle), and super-fine (right) grids. 227
C.5 Aerodynamic loads for the store body resulting from pressure and viscous contributions. 228
C.6 Aerodynamic loads for the store body resulting from pressure contributions. . 229
C.7 Aerodynamic loads for the store body resulting from viscous contributions. . 230
C.8 Stagnation pressure for the $k-\omega$ SST model on the very fine (top), extra-fine (middle), and super-fine (bottom) grids at $x/d_{ref} = 21.5$. 234
C.9 Turbulent kinetic energy contours for the $k-\omega$ SST model on the very fine (top), extra-fine (middle), and super-fine (bottom) grids at $x/d_{ref} = 21.5$. . . . 235

C.10 Surface pressure contours for the $k-\omega$ SST model on the fine (green) very fine (blue), extra-fine (grey), and super-fine (red) grids. 236
C.11 Difference in the pressure coefficient ΔC_p between grids. 237
C.12 Difference in the pressure coefficient ΔC_p between grids. 238
C.13 Vortex trajectories obtained on the fine (green), very fine (blue), extra-fine (red), and super-fine (grey) grids. 238
C.14 Stagnation pressure for the $k-\omega$ SST model on the very fine (top), extra-fine (middle), and super-fine (bottom) grids at $x/d_{ref} = 21.5$. 239
C.15 Turbulent kinetic energy contours for the $k-\omega$ SST model on the very fine (top), extra-fine (middle), and super-fine (bottom) grids at $x/d_{ref} = 21.5$. . . . 240
C.16 Surface pressure contours for the $k-\omega$ SST model on the fine (green) very fine (blue), extra-fine (grey), and super-fine (red) grids. 241
C.17 Vortex trajectories obtained on the fine (green), very fine (blue), extra-fine (red), and super-fine (grey) grids. 242
C.18 Stagnation pressure contours for the $k-\omega$ SST model (left) and the $k-\omega$ EARSM model (right) at $x/d_{ref} = 7.5$, $x/d_{ref} = 12.5$, and $x/d_{ref} = 19$. 244
C.19 Turbulent kinetic energy contours for the $k-\omega$ SST model (left) and the $k-\omega$ EARSM model (right) at $x/d_{ref} = 7.5$, $x/d_{ref} = 12.5$, and $x/d_{ref} = 19$. 245

Nomenclature

Subscripts, superscripts and operators

$(.)_{i,j,k}$	Cell index
$(.)_i$	Inviscid or incompressible quantity (context specific)
$(.)_v$	Viscous quantity
$(.)_0$	Stagnation (total) quantity
$(.)_u$	Upstream quantity
$(.)_{ref}$	Reference quantity
$(.)_{max}$	Minimum of a quantity
$(.)_{min}$	Maximum of a quantity
$(.)_r$	Quantity at the start of the wall pressure rise
$\overline{(.)}, <(.)>$	Reynolds averaged quantity
$\|(.)\|$	Norm of a quantity
$(.)'$	Fluctuation component of a quantity

Latin symbols

a_{ij}	Reynolds stress anisotropy tensor (N/m^2)
b_{ij}	QCR stress tensor (N/m^2)
C	Constant (-)
d	Diameter, wall-distance (m)
e	Specific internal energy (J/kg)
E	Total energy (J)
f	Frequency (Hz)
f_i	Body forces (m/s^2)
$\mathbf{F}, \mathbf{G}, \mathbf{H}$	Flux vectors in the x,y, and z directions
H	Boundary layer shape parameter (-), height (m)
$h = H/2$	Half height (m)
I	Turbulence intensity (-)
J	Jacobian matrix
k	Specific turbulent kinetic energy
L	Length (m)
L_s	Separation length (m)
l	Length scale (m)
$l_{v\kappa}$	von Kármán's length scale (m)
M	Mach number (-)
p	Static pressure (Pa)
$P_k = \tau_{ij}\frac{\partial u_i}{\partial x_j}$	Turbulent kinetic energy production term (Nm^{-2}s^{-1})
q_i	Heat flux vector (W/m^2)
Q	Destruction term in the equation for specific dissipation rate
R	Specific gas constant (287.058 Jkg^{-1}K^{-1})
$\mathbf{R}$	Vector of conserved residuals
Re	Reynolds number (-)
S	Area (m^2)
$S_{ij} = \frac{1}{2}\left(\frac{\partial u_i}{\partial x_j} + \frac{\partial u_i}{\partial x_j}\right)$	Strain rate tensor (1/s)
S_t	Strouhal number (-)
S_μ	Sutherland's constant (-)
$\mathbf{S}$	Source term

t	Time (s)
T	Temperature (K)
$\mathbf{V} = (u, v, w)^T$	Velocity vector (m/s)
$V = \lvert\mathbf{V}\rvert$	Velocity vector magnitude (m/s)
u_i	Velocity vector components (m/s)
$\forall_{i,j,k}$	Cell volume (m^3)
W	Width (m)
$w = W/2$	Half width (m)
$\mathbf{W}$	Vector of conserved variables
$\mathbf{x} = (x, y, z)^T$	Position vector (m)
x_i	Position vector components (m)

Greek symbols

γ	Ratio of specific heats of air (1.4)
δ	Boundary layer thickness (m)
δ^*	Boundary layer displacement thickness (m)
δ_{ij}	Kronecker delta
Δ	Grid spacing (m), distance (m) (context specific)
η	Pressure ratio (-)
θ	Boundary layer momentum thickness (m)
κ	von Kármán's constant (-)
λ	Roll angle (deg)
μ	Dynamic viscosity (Pa.s)
μ_t	Turbulent (Eddy) viscosity (Pa.s)
μ_t/μ	Turbulent to molecular viscosity ratio
$\nu = \mu/\rho$	Kinematic viscosity (m^2/s)
ρ	Density (kg/m^3)
σ	Incidence angle (deg)
τ_{ij}	Viscous stress tensor (Pa)
ω	Specific dissipation rate (1/s)
$\Omega_{ij} = \frac{1}{2}\left(\frac{\partial u_i}{\partial x_j} - \frac{\partial u_i}{\partial x_j}\right)$	Vorticity tensor (1/s)

Acronyms

CFD	Computational Fluid Dynamics
DDES	Delayed Detached Eddy Simulation
DES	Detached Eddy Simulation
EARSM	Explicit Algebraic Reynolds Stress
EVM	Eddy Viscosity Model
HMB	Helicopter Multi-block
IDDES	Improved Delayed Detached Eddy Simulation
LES	Large Eddy Simulation
LEVM	Linear Eddy Viscosity Model
LNS	Limited Numerical Scales
MSWBLI	Multiple Shock Wave Boundary Layer Interaction
NLEVM	Non-Linear Eddy Viscosity Model
QCR	Quadratic Constitutive Relation
RANS	Reynolds Averaged Navier Stokes
RSM	Reynolds Stress Model
SA	Spalart Allmaras
SP	Spanwise periodic
SST	Shear Stress Transport
SWBLI	Shock Wave Boundary Layer Interaction
URANS	Unsteady Reynolds Averaged Navier Stokes
VLES	Very Large Eddy Simulation
*V*1	Version 1
*V*2	Version 2
WMLES	Wall-modelled LES
WRLES	Wall-resolved LES

Chapter 1

Introduction

1.1 Background and motivation

When the flow past an object travelling at high-speed becomes supersonic, shock waves form, caused either by a change of the object's geometry, downstream obstacle, or back pressure forcing the flow to become subsonic (Anderson [4]). The interaction of shock waves with turbulent boundary layers results in complex phenomena due to the rapid retardation of the boundary layer caused by the adverse-pressure gradient imparted by the shock wave. Shock wave boundary layer interactions or SWBLIs occur in a variety of flow devices such as supersonic (high-speed intakes), wind tunnel diffusers or supersonic gas ejectors. SWBLIs are often used to decelerate (compress) the oncoming flow in high-speed intakes. Such intakes are used by air-breathing engines to compress a large volume of air with minimal total pressure and flow distortion losses while avoiding the possibility of an unstart over a wide operating range. Figure 1.1 shows a schematic of an air-breathing engine of a missile.

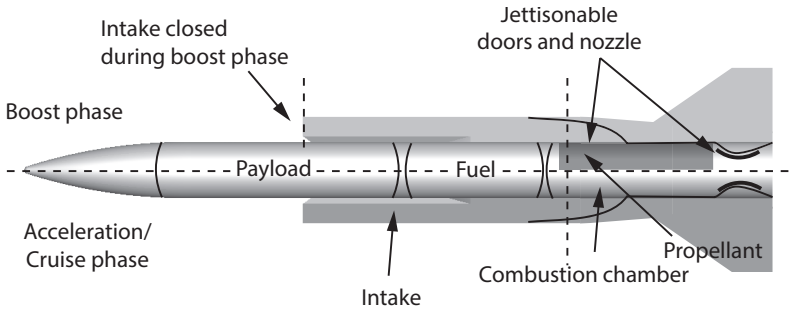

Figure 1.1: Missile high-speed intake.

Accurately predicting SWBLIs with existing turbulence models is still a challenge. Methods such as (U)RANS have been successfully used to predict SWBLIs, however, the most com-

mon Boussinesq turbulence models used by the (U)RANS methods may fail to predict more challenging SWBLI flows. Another drawback is the inability of (U)RANS to capture the inherent unsteadiness of the SWBLI. On the other hand, scale resolving methods such as LES still require the Reynolds number to be reduced by an order of magnitude or the use of wall functions to lower the computational cost. Hybrid RANS/LES methods such as the detached eddy simulation (DES) and its variants or the scale resolving simulation (SAS) rely on linear eddy-viscosity models which are known for their inability to model secondary (corner) flows, which are very important in confined shock wave boundary layer interactions. In addition, the formation of multiple shock waves (or shock trains) within intakes or ducts increases the complexity of the problem and thus there is a demand for a robust numerical method capable of predicting such interactions with a reasonable degree of accuracy at a tractable computational cost. Starting from the multiple shock wave boundary layer experiments of Carroll *et al.* [23, 25–27] the work assesses the effect of non-linear turbulence model closures on the predicted boundary layer profiles and wall pressures and performs a sensitivity analysis and a quantification of the compression efficiency of shock trains under different upstream and downstream conditions. The compression efficiency and stability of shock trains in high-peed intakes are then assessed by considering several fore-body intake geometries.

1.1.1 Shock wave boundary layer interactions in high-speed intakes

High-speed intakes are used by aircraft and missiles to decelerate (compress) the oncoming flow with minimal total pressure losses (Mahoney [81]). Keeping the flow distortion minimal is also important during the deceleration process. Figure 1.2 shows are three types of high-speed intakes based on the compression method they use.

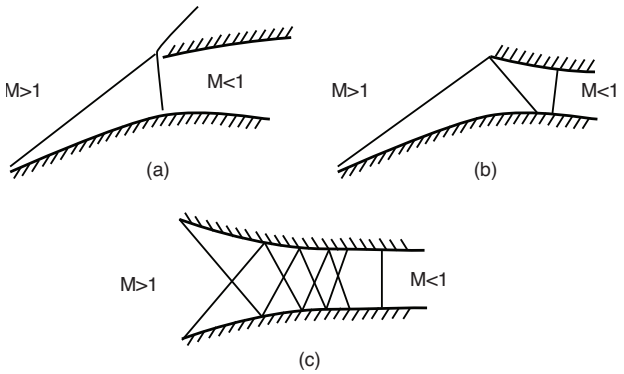

Figure 1.2: Intake types based on their compression method; (a) external, (b) mixed, and (c) internal.

External and mixed compression intakes both use supersonic compression which is achieved

through a series of oblique shock waves. For intakes of the external compression type, the terminal shock (the shock after which the flow becomes subsonic $M < 1$) is located at the lip of the intake. For the latter, the terminal shock is located inside the intake at the location of minimal cross-sectional area (the intake throat). The third type of intake uses only internal compression, and as the name suggests, compression is performed only inside the intake. In comparison to the oblique shock waves, the terminal shock wave is strong, therefore minimising the Mach number before it M_r is important for keeping the total pressure losses low. The boundary layers developing inside the intake interact with the oblique shock waves and the terminal shock. Depending on the strength of the terminal shock (governed by the pre-shock Mach number M_r) and the state of the boundary layer (θ_r, δ_r^*), different terminal shock structures can form. Figure 1.3 shows a schematic of four different terminal shock structures.

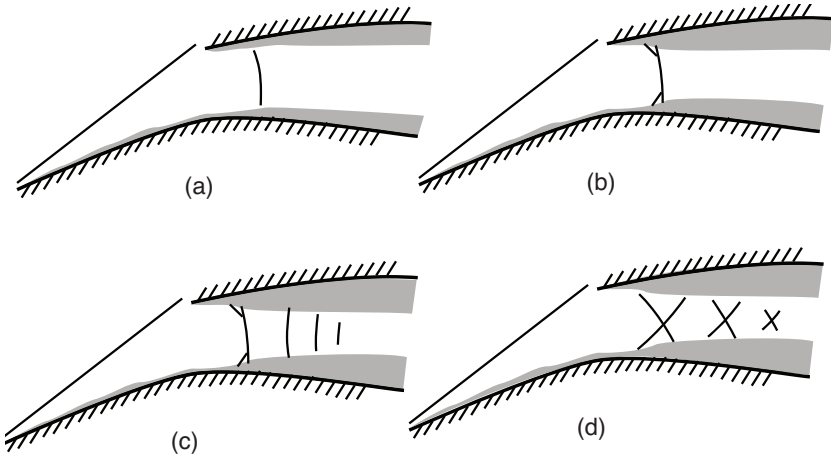

Figure 1.3: Terminal shock structures (adapted from Sajben *et al.* [114]); (a) normal shock wave, (b) normal shock wave with λ-foot, (c) multiple normal shock waves, and (d) multiple oblique shock waves.

According to Sajben [114] for pre-shock Mach numbers in the range of $M_r = 1.0 - 1.3$ a weak normal shock, Figure 1.3 (a), is observed. At higher pre-shock Mach numbers $M_r = 1.3 - 1.6$ a normal shock wave with a λ-foot, Figure 1.3 (b), is observed. For pre-shock Mach numbers $M_r = 1.6 - 2.0$ multiple normal shock waves, Figure 1.3 (c) are observed. Further increase of the pre-shock Mach number leads to multiple oblique shock waves, Figure 1.3 (d). The classification of the terminal shock structures proposed by Sajben [114] is similar to the classification of shock waves in constant area ducts proposed by Matsuo [83]. The formation of multiple shock waves inside the intake can have a strong impact on the performance, therefore it is important to understand the mechanisms responsible for the formation of multiple shock waves. If one considers a two-dimensional supersonic flow, according to Dèlery *et al.* [34], there are four basic interactions between a shock wave and a boundary layer. Figure 1.4

shows these interactions - the impinging reflecting shock wave (a), the ramp induced shock wave (b), the normal shock wave (c), and the shock wave created by a pressure jump (d).

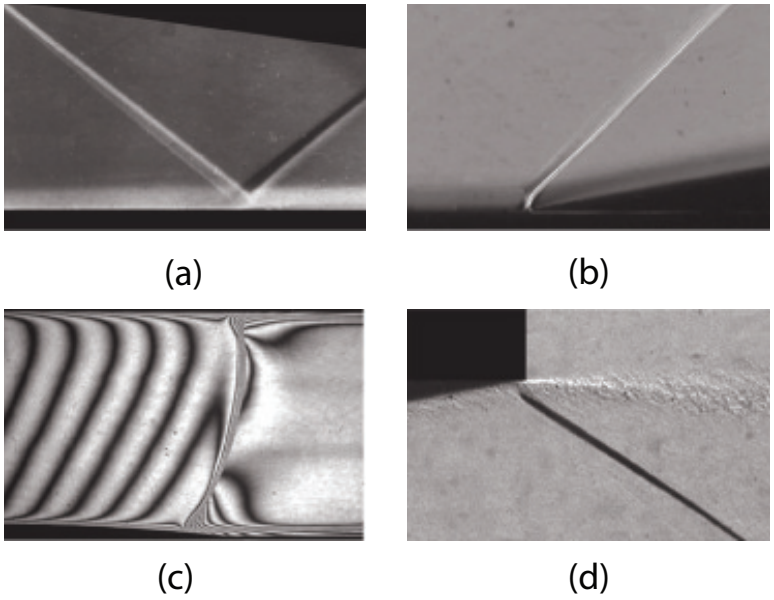

Figure 1.4: Basic shock wave boundary layer interactions in two dimensional flow according to Dèlery *et al.* [34] (adapted from Dèlery *et al.* [34]).

In the first interaction, the incoming flow undergoes a deflection through the incident shock wave, generated by a wedge. For the flow to be parallel to the wall the formation of a reflecting shock wave is needed. The deflection of the flow through the reflected shock wave is equal and opposite to the deflection through the incident (impinging) shock wave. In the second interaction, the flow undergoes a deflection by a shock wave generated by a ramp. The deflection of the flow is equal to the inclination of the ramp. In the third interaction, the flow is forced to become subsonic through back pressure forcing. In internal (confined) flows a normal shock wave is also formed when downstream choking requires a stagnation pressure loss to satisfy mass conservation. Interactions, where the flow downstream of the shock wave is fully or partially subsonic, are of particular interest as downstream disturbances (pressure fluctuations) can influence the shock wave. An example of such interaction is the terminal shock inside a high-speed intake. The fourth interaction is commonly observed in over-expanded nozzles. Figure 1.5 below shows a qualitative schematic of different interactions. The impinging reflecting shock interaction and the ramp induced shock interaction are clearly identifiable in 1.5f and d. According to Edney's [45] classification, the interactions in figures 1.5a and b can be referred to as type I and type II interactions.

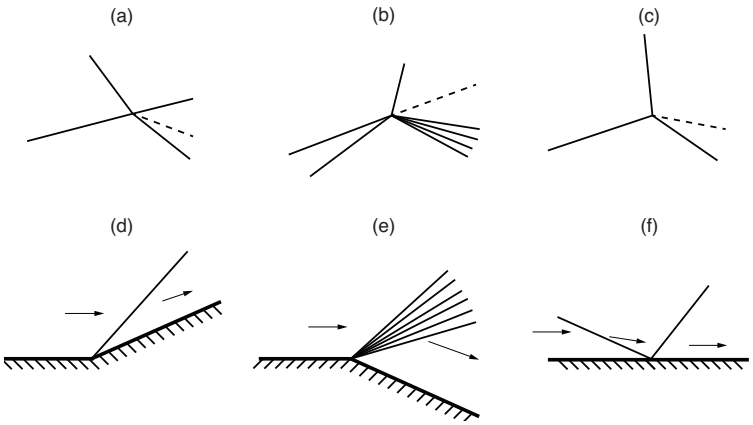

Figure 1.5: Shock interference types (adapted from Sanderson [116]).

The following subsections focus on confined normal shock interactions which typically represent the terminal shock in a high-speed intake. Such interactions are often type I and II.

1.1.2 Normal shock interactions

Attached (weak) normal shock interaction

For low adverse pressure gradients corresponding to a pre-shock Mach number $M_r < 1.3$, the boundary layer remains attached. Figure 1.6 shows a qualitative sketch of an attached normal shock interaction.

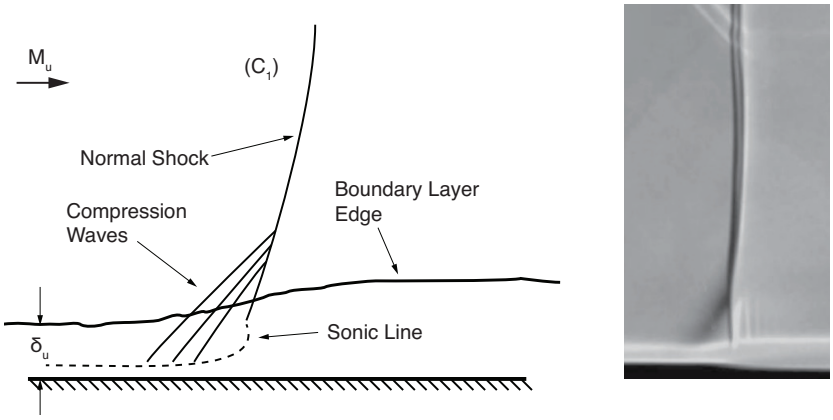

Figure 1.6: Weak normal shock interaction; (adapted from Dèlery [33]).

The pressure rise transmitted through the subsonic channel causes the boundary layer upstream of the shock to thicken. The thickening of the subsonic part of the boundary layer creates compression waves in the adjacent supersonic part. The compression waves reduce the Mach number and to adjust to the decreasing Mach number the shock C_1 progressively

bends and weakens until it becomes vanishingly weak at the sonic line ($M = 1$). The stagnation pressure loss increases significantly near the wall. Away from the wall, the stagnation pressure loss corresponds to the one in inviscid flow. Between these two limits, the stagnation pressure recovery increases above the value of the one in inviscid flow. In this region, the flow encounters the weak compression waves followed by a weaker shock. The sharp pressure rise at the wall that would be observed in an inviscid flow is replaced by a gradual pressure rise. The spreading of the pressure rise is characterised by the interaction length, L, which is defined as the distance between the location of the initial pressure rise x_r and the location at which the shock would meet the wall in an inviscid flow. The above interaction is termed "weak" as the boundary layer remains attached.

Separated (strong) normal shock interaction

As the shock strength is increased a critical point will be reached at which the boundary layer will separate. This usually corresponds to an incompressible shape factor, H_i, at separation, between 2.2 and 2.7 as shown by Dèlery [37]. Figure 1.7 shows a qualitative schematic of a separated normal shock interaction.

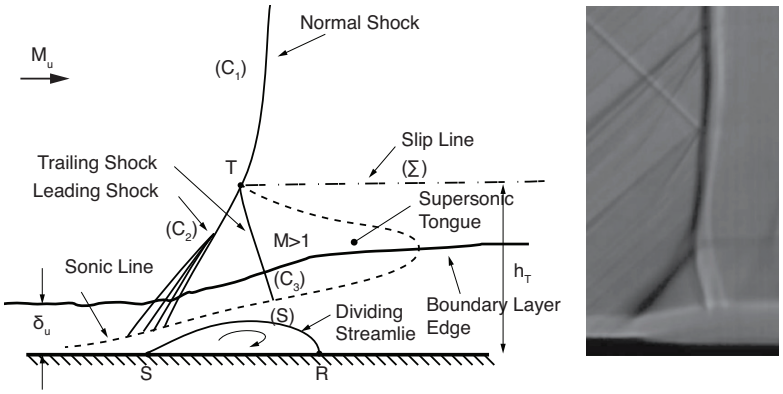

Figure 1.7: Strong normal shock interaction (adapted from Dèlery [33]).

A region of recirculating fluid bound by the dividing streamline (S) is present in figure 1.7. Although the recirculating region itself may be very thin, it has a profound effect on the overall flow structure. The recirculating fluid amplifies the transmission of the pressure rise and results in a larger interaction length. In addition, the concave streamline curvature due to the presence of a recirculating region creates a series of compression waves which coalesce to form an oblique shock C_2. The oblique shock C_2 intersects the normal shock C_1. Since the pressure rise across C_2 is less than the one across C_1 an oblique shock C_3 is formed. The C_2 and C_3 shocks form the so-called λ-foot and intersect at the triple point T. The triple point is the origin of a slip surface which corresponds to a discontinuity in the stagnation pressure

and entropy. The static pressure and flow direction on either side of the slip surface are the same. A region of supersonic flow below the slip surface may exist. Seddon *et al.* [117] and Om *et al.* used the term supersonic tongue to describe this region. The stagnation pressure losses near the wall are greater than the case of figure 1.6. Away from the wall, downstream of the normal shock C_1, the stagnation pressure loss corresponds to the one in an inviscid flow. Similarly to the case of figure 1.6, increased stagnation pressure recovery is present in the region downstream of the λ-foot. A discontinuity in the stagnation pressure is identifiable across the slip surface. The streamwise spreading of the static pressure rise is characterised by a steep increase at the separation point S followed by a gradual increase over the separation region. At the reattachment point, R, the static pressure begins to rise asymptotically towards the one in an inviscid flow. Figure 1.8 compares Schlieren visualisations of an attached and separated normal shock interactions.

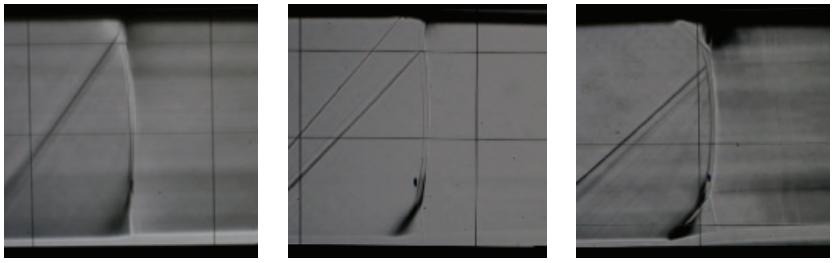

Figure 1.8: Schlieren visualisations of a normal shock interaction at $M_r = 1.23$ (a), $M_r = 1.33$ (b), and $M_r = 1.45$ (c) (adapted from Doerffer *et al.* [39].)

As the upstream Mach number M_r increases, the weak interaction transforms into a strong interaction. A λ-foot, caused by the separation at the foot of the shock, is clearly observed at $M_r = 1.45$ (figure 1.8c).

1.1.3 Onset of separation end effect of confinement

As the flowfields of the attached and separated interactions are different, it is important to accurately predict the onset of separation. Intuitively, two factors could affect the onset of separation - the upstream Mach number M_r, correlated to the adverse pressure gradient imparted by the shock and the properties of the upstream boundary layer. Experiments by Seddon [117], Dèlery [37], Kooi [79], and Sajben *et al.* [115] agree that the M_r is most important factor of the two. One might expect that a boundary layer with a lower momentum (higher shape factor) to separate more easily. However, in reality, the shape factor of the boundary layer has a minor effect on the onset of separation (Dèlery [37]). Figure 1.9

shows the incompressible boundary layer factor $H_{i,r}$ for attached and separated normal shock interactions.

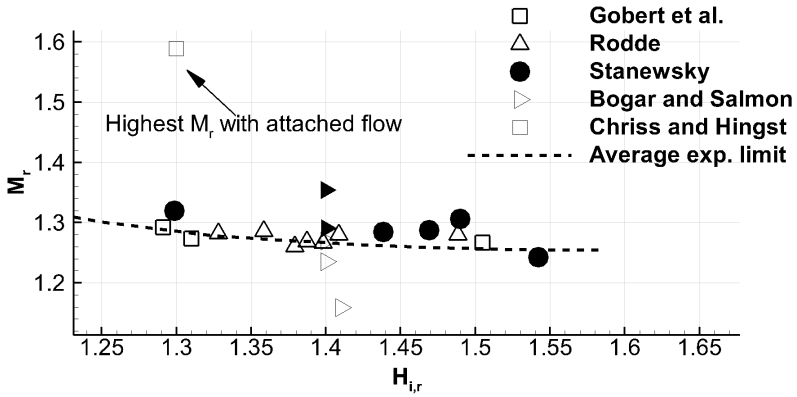

Figure 1.9: Pre-shock Mach number and incompressible shape factor for attached and separated normal shock interactions; filled symbols correspond to separated interactions and empty symbols to attached interactions (adapted from Dèlery [37]).

This insensitivity of separation to the shape factor is rather counter-intuitive. A low shape factor boundary layer is more resistant to separation, however, it has a smaller subsonic channel through which the pressure rise can be transmitted upstream. This results in a shorter interaction length and a steeper pressure rise which subjects the boundary layer to a stronger adverse pressure gradient making it more susceptible to separation. These two effects tend to approximately compensate one another and result in the onset being insensitive to the shape factor. Multiple studies [37,79,115,117] showed that the onset of separation is weakly dependant on the shape factor and occurs at upstream Mach numbers in the rage of $M_r = 1.3 - 1.35$. Figure 1.9, however, shows an attached normal shock interaction studied by Chriss and Hingst [28] at an upstream Mach number of $M_r = 1.59$. This raises the question of whether there is another parameter apart from the upstream Mach number affecting the onset of separation. The shock interactions shown in Figure 1.9 are performed in wind tunnel test sections and are often referred to as interactions in ducts. The flow within a duct is confined and the confinement imposes stream surfaces on the symmetry planes which increase any wall-normal variations. As stated by Babinsky [9], confinement can significantly affect the flow. The flow confinement is characterised by the ratio of the upstream boundary layer thickness to the duct half-height δ_r/h. To further understand how the flow confinement affects the onset of separation figure 1.10 compares oil flow (OLF) visualisations of attached and separated normal interactions.

Separation is clearly identifiable at $M_r = 1.50$, but not at $M_r = 1.40$ in the experiment by Bruce *et al.* [19]. Similar observations were made in the experiments by Sajben *et al.* [115],

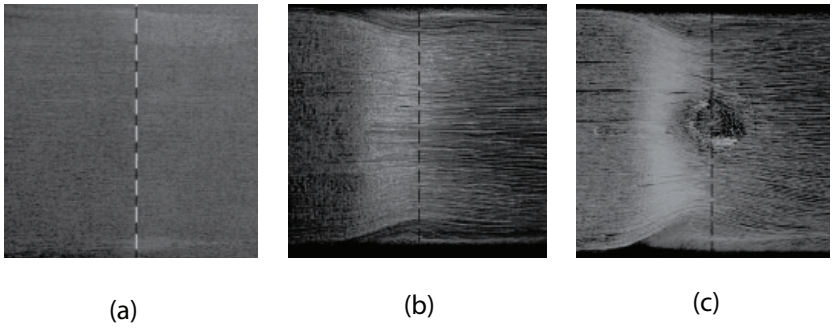

Figure 1.10: Oil flow visualisations of a normal shock interaction at $M_r = 1.30$ (a), $M_r = 1.40$ (b), and $M_r = 1.50$ (c) (adapted from Bruce *et al.* [19]).

Atkin *et al.* [7], and Doerffer *et al.* [41] - no centreline separation was observed for upstream Mach numbers as high as $M_r = 1.4$. The flow in the corner of the duct has a low momentum due to the intersection of the floor and sidewall boundary layers. The low momentum causes the flow at the corner to separate giving a displacement effect, requiring the external flow to deflect. In the corner region, a pair of two counter-rotating streamwise vortices are present. The dynamics of these vortices and their effect on the corner separation have been studied by Gessner [55], Morajkar *et al.* [91,92], Peltier *et al.* [120], and more recently by Sabnis [113]. The streamline curvature, identifiable in Figure 1.10 (b) and (c) is associated with a series of compression waves which propagate into the flowfield. A qualitative sketch of the corner interaction is shown in Figure 1.11. The compression waves are represented by a single weak conical shock.

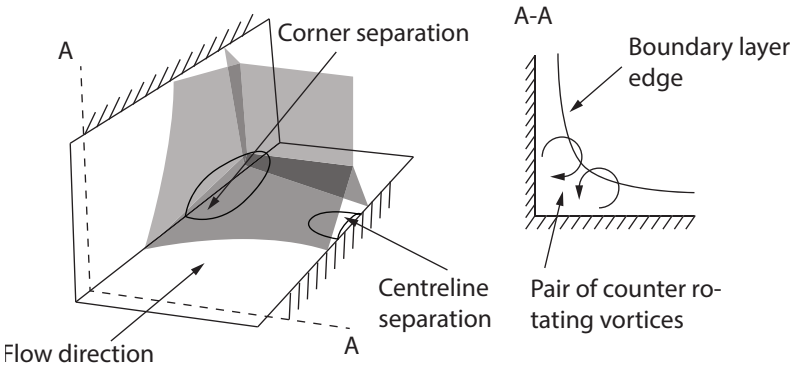

Figure 1.11: Schematic of the normal shock wave structure near a corner and of the corner flow.

The λ-foot of the normal shock merges with the conical shock. As a result, the size of the λ-foot increases close to the corner. Experiments by Burton *et al.* [38], Bruce *et al.* [19], Burton *et al.* [22], and Handa *et al.* [62] agree on the increase of the λ-foot near the corner. Burton *et al.* [38] and Bruce *et al.* [19] observed increased pressure smearing in the corner

which is indicative of an increased λ-foot. Burton *et al.* [22] attributed the increase of the λ-foot to the series of compression waves caused by the corner separation. Handa *et al.* [62] also observed the λ-foot structures to increase towards the corner. The downstream Mach number was consistently higher in the corner regions, suggesting the presence of a larger λ-foot structure. The increased streamwise interaction length near the corner reduces the adverse pressure gradient and delays or decreases the shock-induced separation. Shock induced separation is more likely at the centreline where the effects of the corners are the weakest. The smearing of the pressure rise is affected by the relative size of the corner separations to the width of the duct. Larger corner separations result in more smearing and delay the shock-induced separation at the centreline. The smearing is responsible for the absence of separation at $M_r = 1.4$ in the experiments of Sajben *et al.* [115], Atkin *et al.* [7], Doerffer *et al.* [41], and Bruce *et al.* [19]. These experiments have a flow confinement of approximately $\delta_r/h \approx 0.1$. Figure 1.12 shows separated and attached interactions at different pre-shock Mach numbers and levels of confinement.

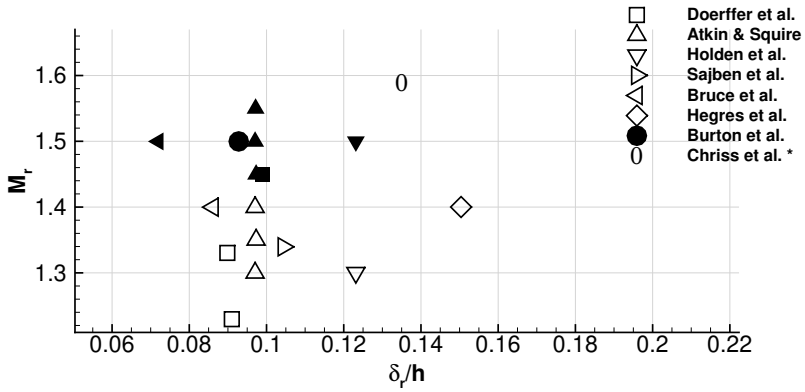

Figure 1.12: Pre-shock Mach number and flow confinement for attached and separated normal shock interactions from table 1.1; filled symbols correspond to separated interactions and empty symbols to attached interactions [7, 19, 28, 41, 65, 66, 115]; * - boundary layer thickness estimated from corner flow sizes and LDA measurements

In Figure 1.12, the highest Mach number with no separation ($M_r \approx 1.6$) was observed by Chriss *et al.* [28]. The sizes of the corner separations were considerably larger compared to other experiments. Large corner separations are typically associated with higher levels of flow confinement, as stated by Bruce [16]. In addition to delaying the onset of centre-line separation, the increase of δ_r/h can lead to multiple normal shock interactions or shock trains. Figure 1.13 shows the effect of the upstream Mach number M_r and the level of flow confinement δ_r/h on the formation of shock trains.

Atkin *et al.* [7] observed a single normal shock wave at $M_r = 1.55$ and $\delta_r/h \approx 0.1$. For a similar pre-shock Mach number $M_r \approx 1.55$ and higher level of flow confinement $\delta_r/h \approx$

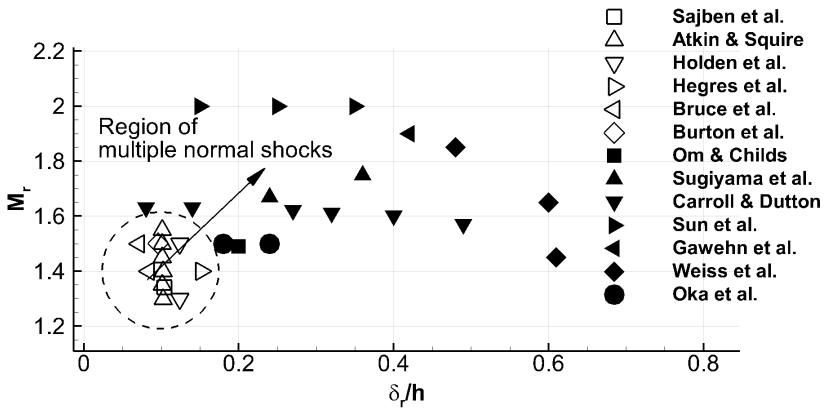

Figure 1.13: Pre-shock Mach number and flow confinement for single and multiple normal shock interactions from tables 1.1 and 1.2 [7, 19, 22, 23, 51, 65, 66, 98, 99, 115, 129, 131, 149].

0.42 Carroll *et al.* [23, 25–27] observed multiple normal shocks. This is in agreement with Babinsky and Harvey [9] who reported that multiple normal shocks are more likely to form when the ratio of boundary layer displacement thickness to duct height is greater than a few percent.

1.1.4 Multiple normal shock interactions

The previous sections showed that two parameters affect a confined normal shock interaction - the upstream Mach number M_r and the flow confinement δ_r/h. For higher levels of flow confinement, the centreline separation is delayed or decreased. If, however, the flow confinement is significant, multiple normal shocks can form. The fundamental characteristics of the multiple shock interaction were first described by Crocco [30]. Figure 1.14 shows a qualitative schematic of a multiple normal shock interaction (only the first two shocks are shown).

The main difference between the single normal shock interaction shown in Figure 1.7 and the multiple normal shock interaction is that the flow downstream of shock C_1 is re-accelerated to supersonic speeds due to the convex streamline curvature in this region. The re-acceleration to supersonic speed promotes the formation of a second shock C_2. The process is repeated until the shocks become vanishingly weak. Downstream of the vanishingly weak shock the flow remains mixed supersonic-subsonic below the slip surface, emanating from the triple point of shock C_1. Figure 1.15 shows a schematic and a Schlieren of a multiple normal shock interaction. The presence of the multiple normal shocks cannot be identified from the wall pressure distribution, however, it can be identified from centreline flow measurements or boundary layer momentum and displacement thickness measurements. Om and Childs [99] observed that the displacement thickness increased rapidly upstream of the first

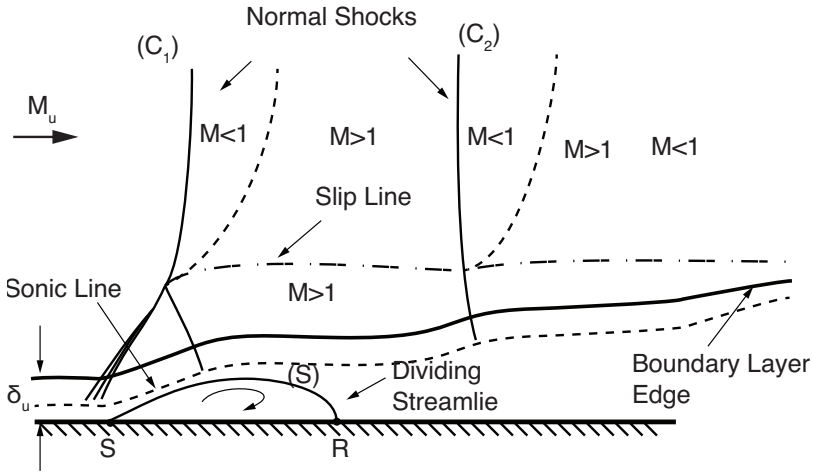

Figure 1.14: Schematic of two strong normal shock waves interacting with a boundary layer (adapted from Carroll [23]).

normal shock then decreased slightly before increasing again upstream of the second normal shock. The process was repeated until the normal shocks became vanishingly weak. Atkin and Squire [7] observed similar displacement thickness distribution across a single normal shock wave. However, the re-acceleration of the flow was not sufficient to promote the formation of multiple normal shocks.

The multiple normal shock interaction is commonly referred to as a shock train or pseudo-shock. Although these terms are used interchangeably in the literature, they describe different regions of the wall pressure rise across a multiple normal shock interaction. The pseudo-shock refers to the entire region of pressure rise which contains the shock train region and the mixing region. Pressure continues to rise in the latter region which is free of shocks but may feature regions of supersonic and subsonic flow.

Ikui [72], Sugiyama *et al.* [129, 130], Carroll *et al.* [23, 25–27], Arai *et al.* [5] and Sun *et al.* [131–133] amongst others performed experiments of shock trains. Carroll *et al.* [23] investigated the effect of confinement on a pseudo-shock at an upstream Mach number of $M_r = 1.61$ and a unit Reynolds number of $Re = 3 \times 10^7$. In the experiment, the flow confinement was varied from $\delta_r/h = 0.08$ to $\delta_r/h = 0.49$. The variation of confinement was achieved by adjusting the exit (back) pressure. An increase of the exit pressure displaces the shock train upstream where the boundary layer is thinner. To minimise the reduction of the upstream Mach number due to boundary layer growth, the test section had a divergence angle of 0.13 degrees. Regardless, a slight adverse pressure gradient was observed. As a

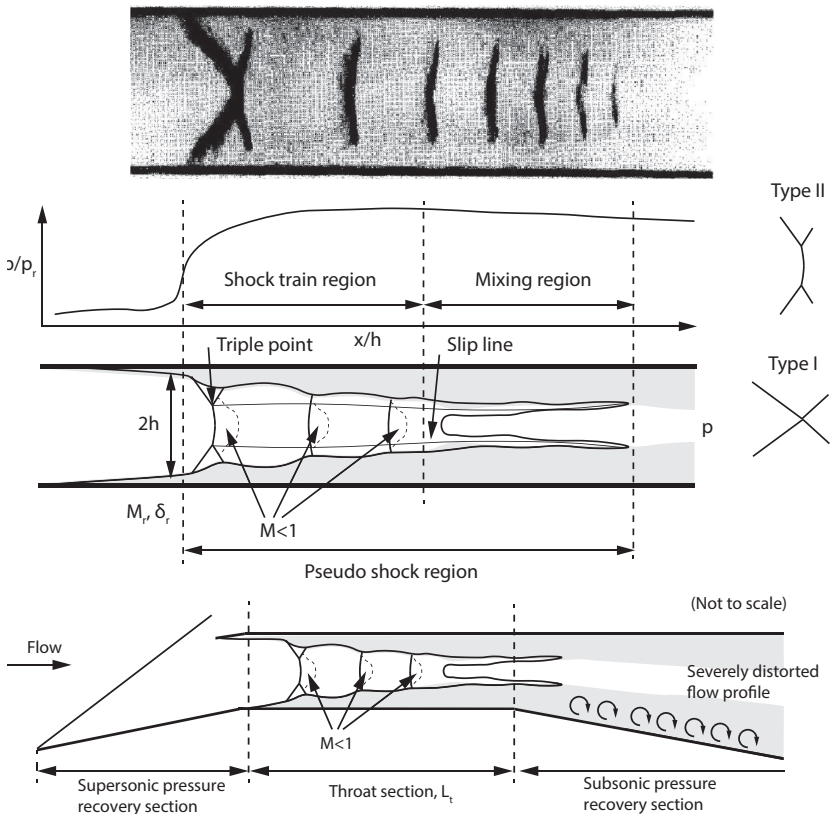

Figure 1.15: Schlieren from the multiple normal shock interaction experiment by Carroll *et al.* [23, 25–27] (top), schematic of a multiple normal shock interaction in rectangular duct (middle), and schematic of a multiple normal shock interaction in an intake (bottom).

result, the pre-shock Mach number varied slightly at the different levels of flow confinement. The largest variation of M_r amounted to 2.5%. Symmetry of the shock train with respect to the test section centreline was observed for all confinement levels except at $\delta_r/h = 0.08$. The asymmetry of the shock train at a confinement level $\delta_r/h = 0.08$ was slight. The first shock of the train always featured a λ-foot structure whereas subsequent shocks did not. The spacing between the subsequent shocks was found to increase with increasing flow confinement. The re-acceleration of the flow downstream of the first normal shock was similar to the one downstream of a single normal shock, with the difference that a larger level of flow confinement causes the flow above the slip surface to re-accelerate faster. Depending on the re-acceleration, choking downstream of the first shock wave may occur which will promote the formation of subsequent shocks. Both Carroll *et al.* [23, 25–27] and Arai *et al.* [5] observed that the length of the pseudo-shock region increased and the pressure recovery across the pseudo-shock region decreased with increasing δ_r/h. The pressure after a single normal shock wave at a pre-shock Mach number of $M_r = 1.61$ is $p/(p_{ref}\gamma M_{ref}^2) = 0.6634$ whereas the pressure after the shock train, at similar pre-shock Mach number and confinement ratios

of $\delta_r/h = 0.08$ and $\delta_r/h = 0.49$, is 91.9% and 73.4% of $p/(p_{ref}\gamma M_{ref}^2)$. The gradient of the wall pressure at the beginning of the interaction was observed to decrease with increasing δ_r/h. This was attributed to the growth of the λ-foot of the first shock. Several models describing the pressure rise across a pseudo-shock region have been proposed - the shockless model by Crocco [30], later improved by the diffusion model of Ikui *et al.* [73]. Waltrup & Billig [145] proposed a quadratic correlation based on experimental results of shock trains in cylindrical ducts. Corrections for rectangular ducts were later added by Billig [14]. Experiments by Weiss *et al.* [147] concluded that the correction by Billig [14] accurately reproduces the pressure gradient for the shock train in a rectangular duct for Mach numbers up to $M_r = 2$. An improved agreement was obtained by Wang *et al.* [146] who introduced an additional correction taking into account the boundary layer momentum thickness on two opposing walls. A detailed review of the various models was performed by Matsuo *et al.* [83] and more recently by Gnani *et al.* [57]. Recent experiments by Hunt *et al.* [71] showed that the pressure rise is a constant fraction of the pressure rise across a normal shock at the same upstream Mach number M_r. Furthermore, the mixing region pressure rise is a linear function when normalised by the corresponding pressure rise across a normal shock and the shock train length is constant when normalised by the Waltrup and Billig [145] correction factor C given by:

$$C = \left(M_r^2 - 1\right) Re_{\theta_r}^{1/4} \left(H_r \theta_r\right)^{-1/2} \tag{1.1}$$

In the experiments by Carroll *et al.* [23,25–27] the stagnation pressure, p_0, was kept constant while the back (exit) pressure was varied. The effect of the stagnation pressure and the preshock Mach number on a shock train was investigated by Gawehn *et al.* [51] and Weiss *et al.* [147]. For a decreasing stagnation pressure, equivalent to a decreasing Reynolds number, Weiss *et al.* [147] observed the shock train to relocate upstream to a slightly lower preshock Mach number. Similar observations were made by Gawehn *et al.* [51]. The Reynolds number was found to have a much smaller effect on the shock train length and position than the upstream boundary layer thickness (confinement). Both Gawehn *et al.* [51] and Weiss *et al.* [147] investigated the effect of the upstream Mach number M_r on the shock train. In the experiments, p_0 was kept constant and the back pressure was used to vary the preshock Mach number. Both observed the gradient of the wall pressure at the beginning of the interaction to increase, and the shock train length to decrease with decreasing M_r. The shock train length was also observed to be dependant on the ratio of the wall temperature to the free-stream flow by Fischer *et al.* [50] since adiabatic or hot-wall boundary layers are

less resistant to separation than cold-wall boundary layers which are thinner and have higher skin friction. Shock trains with a first shock featuring a λ-foot structure were observed by Ikui [72], Sun *et al.* [131–133], Sugiyama *et al.* [129, 130] and Edelman *et al.* [44] for upstream Mach numbers as high as $M_r \approx 2$. At higher upstream Mach numbers and levels of flow confinement, the λ-foot structures on opposite walls grow and eventually combine to form a χ structure. Figure 1.15 shows a schematic of the λ-foot and the χ structures.
Shock trains with a λ-foot structures can be classified as having a type II shock structure, and χ-shaped shock trains as having a type I shock structure (refer to figure 1.5). Carroll [23] observed that the χ structure extended to the subsequent shocks in the shock train. Ikui [72] observed an χ structured shock train at $M_r = 2.42$, Carroll [23] at $M_r = 2.45$, Geerts *et al.* [52–54] at $M_r = 2.38 - 2.44$ and Klomparens *et al.* [77, 78] at $M_r = 2.75$. Shock train with a χ structure at higher Mach numbers $M_r = 4.0$ were studied by Sun *et al.* [131–133] and Sugiyama *et al.* [129]. The observations show that there is a Mach number range in which the shock train transitions to χ structure. Heiser *et al.* [63] stated that this transition occurs at upstream Mach numbers of $M_r = 2 - 3$. An exception is the case by Sugiyama *et al.* [130], where a shock train with a χ structure was observed at $M_r = 1.9$. The appearance of a shock train with a χ structure at this Mach number was attributed to the high level of flow confinement $\delta_r/h = 0.560$. Figure 1.16 shows the pre-shock Mach number and the confinement level for the single normal, the normal shock train, and the χ structured shock train interactions from tables 1.1-1.3.

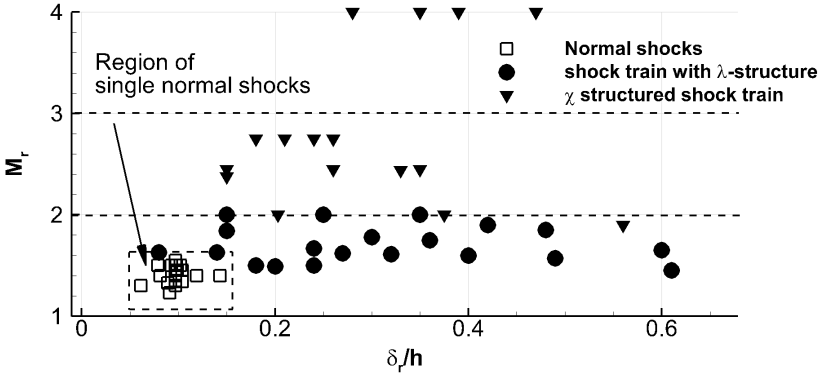

Figure 1.16: Pre-shock Mach number and flow confinement for single, multiple normal shock interactions, and multiple oblique shock interactions from tables 1.1 and 1.2 [5, 7, 18, 19, 22, 23, 35, 39, 51–53, 70, 77, 78, 98, 99, 115, 129–131, 148, 149].

Shock trains with a λ-foot structure are present for Mach numbers lower than $M_r = 2$ for confinements δ_r/h higher than 0.2 and shock trains with a χ structure are present for Mach numbers above $M_r = 2$. This shows that the flow confinement is important at lower up-

stream Mach numbers and less important at higher upstream Mach numbers in determining the structure of the shock train.

Summary of experiments

The relevant single and multiple shock wave boundary layer experiments, discussed in this chapter, are listed in tables 1.1, 1.2, and 1.3.

Experiment	δ_r (mm)	δ_r/h (-)	M_r (-)	Re (m^{-1})	**Measurements**
1981 Dèlery [35]	3.05	0.061	1.30	1.00×10^7	$\frac{p}{p_0}$, LDV, Interferometer
	5.20	0.104	1.45	1.00×10^7	
1991 Sajben *et al.* [115]	6.60	0.104	1.34	2.05×10^7	$\frac{p}{p_0}$, LDV, Schlieren, Shadowgraph
1992 Atkin *et al.* [7]	5.50	0.097	1.30	1.63×10^7	$\frac{p}{p_0}$, Shadowgraph, Interferometer, OLF
			1.35	1.67×10^7	
			1.40	1.68×10^7	
			1.45	1.70×10^7	
			1.50	1.70×10^7	
			1.55	1.73×10^7	
2008 Doerffer *et al.* [39]	4.55	0.091	1.23	1.41×10^7	$\frac{p}{p_0}$, Schlieren, PSP, OLF, CTA
	4.49	0.089	1.33	1.41×10^7	
	4.94	0.099	1.45	1.41×10^7	
2007-2011 Bruce *et al.* [16–20]	4.60	0.081	1.30	2.33×10^7	$\frac{p}{p_0}(x)$, LDA, Schlieren, PSP, OLF
	4.60	0.081	1.30	2.33×10^7	
	4.60	0.081	1.40	2.31×10^7	
	5.50	0.097	1.40	1.39×10^7	
	6.80	0.119	1.40	2.89×10^7	
	8.14	0.143	1.40	2.45×10^7	
	4.50	0.079	1.50	2.24×10^7	
	5.60	0.098	1.50	1.23×10^7	
	5.80	0.102	1.50	2.50×10^7	
2012 Burton *et al.* [22]	5.30	0.093	1.50	2.40×10^7	$\frac{p}{p_0}$, Schlieren, LDA, OLF, PSP

Table 1.1: Normal shock interactions.

Experiment	δ_r (mm)	δ_r/h (-)	M_r (-)	Re (m^{-1})	**Measurements**
1983 Om *et al.* [99]	5.15	0.198	1.49	4.90×10^6	$\frac{p}{p_0}$, Pitot tube
1988 Sugiyama *et al.* [130]	6.00	0.240	1.67	1.47×10^7	$\frac{p}{p_0}$, Schlieren
	9.00	0.360	1.75	1.49×10^7	
1988-1993 Carroll *et al.* [23, 25–27]	1.30	0.080	1.63	3.00×10^7	$\frac{p}{p_0}$, LDV, Schlieren, OLF
	2.20	0.140	1.63	3.00×10^7	
	4.40	0.270	1.62	3.00×10^7	
	5.40	0.320	1.61	3.00×10^7	
	6.70	0.400	1.60	3.00×10^7	
	8.30	0.490	1.57	3.00×10^7	
1996 Arai *et al.* [5]	7.50	0.300	1.78	1.30×10^7	$\frac{p}{p_0}$, LDV, Schlieren
	3.75	0.150	1.84	1.40×10^7	
2003 Sun *et al.* [131]	6.00	0.150	2.00	2.50×10^7	$\frac{p}{p_0}$, Schlieren
	10.00	0.250	2.00	2.50×10^7	
2006 Sugiyama *et al.* [129]	6.00	0.150	2.00	2.53×10^7	$\frac{p}{p_0}$, Schlieren
	10.00	0.250	2.00	2.53×10^7	
	14.00	0.350	2.00	2.53×10^7	
2010 Gawehn *et al.* [51]	2.30	0.420	1.90	1.91×10^6	$\frac{p}{p_0}$,Schlieren
2012 Weiss *et al.* [148]	2.11	0.600	1.65	4.70×10^7	$\frac{p}{p_0}$, Schlieren, Pitot tube
2014 Weiss *et al.* [149]	2.52	0.610	1.45	5.40×10^7	$\frac{p}{p_0}$, Schlieren, Pitot tube
	2.78	0.600	1.65	5.40×10^7	
	2.51	0.480	1.85	5.40×10^7	
2014 Oka *et al.* [98]	1.35	0.180	1.50	1.60×10^7	$\frac{p}{p_0}$
	1.80	0.240	1.50	1.60×10^7	

Table 1.2: Shock trains with a λ-foot structure.

Experiment	δ_r (mm)	δ_r/h (-)	M_r (-)	Re (m^{-1})	**Measurements**
1988 Sugiyama *et al.* [130]	14.00	0.560	1.90	1.47×10^7	$\frac{p}{p_0}$, Schlieren
1988-1993 Carroll *et al.* [23, 25]	3.00	0.150	2.45	2.99×10^7	$\frac{p}{p_0}$, Schlieren, OLF
	5.40	0.260			
	7.30	0.350			
2004 Sun *et al.* [132]	14.00	0.350	4.00	2.36×10^7	$\frac{p}{p_0}$, Schlieren
2006 Sugiyama *et al.* [129]	11.20	0.280	4.00	2.36×10^7	$\frac{p}{p_0}$, LDV, Schlieren
	15.60	0.390			
	18.80	0.470			
2015-2016 Geerts *et al.* [52–54]	3.89	0.153	2.38	?	$\frac{p}{p_0}$, Shadowgraph, Schlieren
	4.17	0.328	2.44		
2015-2016 Klomparens *et al.* [77, 78]	6.35	0.180	2.75	8.90×10^6	$\frac{p}{p_0}$, Schlieren
	7.35	0.210			
	8.50	0.240			
	9.25	0.260			
2017 Hunt *et al.* [70]	13.09	0.375	2.00	1.40×10^7	$\frac{p}{p_0}$, Schlieren, PIV
	7.10	0.203			

Table 1.3: Shock trains with a χ structure.

Recent numerical simulations

The previous sections showed that the flow separation at the centreline of the duct floor is affected by the flow confinement, δ_r/h. The flow confinement is affected by the size of the corner separations and an increased flow confinement can delay the onset of separation at the centreline leading to the formation of shock trains. To accurately predict a confined shock interaction one must accurately predict the size of the corner separations. Single normal shock interactions were studied numerically by many researchers, however, insightful studies were made by Blosch *et al.* [15], Bur *et al.* [21], Doerffer *et al.* [41], Bruce *et al.* [19, 20], and Arvidson *et al.* [6]. Bruce *et al.* [19, 20] numerically studied a $M_r = 1.40$ normal shock interaction considering a variety of turbulence models - the $k-\varepsilon$ by Yang-Shih [119], the Spallart-Allmaras [124], the $k-\omega$ SST by Menter [86], the Baldwin-Lomax [10], the $k-\omega$ by Wilcox [151], and the v2-f by Durbin [43]. All models produced solutions with attached flow (away from the corners) on the duct floor and sidewall, except the v2-f model which showed attached flow on the duct floor and a small separation bubble on the sidewall. The solutions with the $k-\varepsilon$, v2-f, and the $k-\omega$ turbulence models showed good qualitative agreement with the experiment. The solutions were symmetrical and had reasonably sized corner separations. The solutions with the remaining models were in significant disagreement with the experiment predicting asymmetric flow. Even with an enforced symmetry, the Spallart-Allmaras model was found to significantly overpredict the corner separations. A detached eddy simulation (DES) of the full duct also predicted an asymmetric flow-field. The asymmetry was in the form of a very large corner separation in one of the duct corners and a very small one in the diagonally opposite corner. As stated by Bruce *et al.* [19], the non-physical asymmetry is caused by the overprediction of the corner separations when the corner separations exceed approximately 35-40% of the duct width or height (whichever is the smaller). Arvidson *et al.* [6] performed DES and delayed DES simulations with the Spalart-Allmaras turbulence model, hybrid RANS/LES simulations with the zero-equation HYB0 turbulence model ([101, 102]) and RANS simulations with the Spalart-Allmaras, $k-\omega$ SST , $k-\omega$ EARSM by Hellsten *et al.* [64, 144], and the low-Re-number $k-\omega$ by Peng *et al.* [103] turbulence models of the same interaction studied by Bruce *et al.* [19, 20]. The Spalart-Allmaras and the $k-\omega$ SST predicted an asymmetric flowfield in agreement with the findings by Bruce *et al.* [19, 20]. Symmetric flowfield was predicted by the $k-\omega$ EARSM and the low-Re-number $k-\omega$ models. The size of the corner separation was slightly overpredicted by the latter. The absence of separation at the centreline of the duct floor was in agreement with the experiment. Due to the smaller size of the corner separations predicted by the $k-\omega$ EARSM model, separation was present at the centreline. This once again shows that accurate prediction of the corner separations is es-

	Model	Corner size (mm)	Corner size/tunnel width	Symmetric
Experiment		15	0.13	Yes
RANS [19]	SA	52	0.46	No
RANS [19]	$k-\varepsilon$	17	0.15	Yes
RANS [19]	V2F	24	0.21	Yes
RANS [19]	BL	44	0.39	Yes
RANS [19]	$k-\omega$ SST	46	0.40	No
RANS [19]	$k-\omega$	15	0.13	Yes
DES [19]	SA	-	-	No
RANS [6]	SA	46	0.40	No
RANS [6]	$k-\omega$ SST	43	0.37	No
RANS [6]	PHD LRN $k-\omega$	15	0.13	Yes
RANS [6]	$k-\omega$ EARSM	-	-	Yes
DES [6]	SA	43^a	0.37	Yes
DDES [6]	SA	-	-	No
Hybrid RANS/LES [6]	HYB0	29^a	0.25	Yes

Table 1.4: Corner separation sizes predicted by RANS and Hybrid RANS/LES simulations (adapted from Bruce *et al.* [19] and Arvidson *et al.* [6]) of the $M_r = 1.40$ interaction studied experimentally by Bruce *et al.* [19] (^{a} corner size estimated from time averaged skin friction pattern).

sential for predicting the interaction. Surprisingly, the Spalart Allmaras DES and the HYB0 hybrid RANS/LES simulations predicted asymmetric averaged flowfields. However, both simulations predicted a secondary shock downstream of the first shock. Further investigation showed that the cause of the secondary shock is the overpredicted corner separations which resulted in a greater re-acceleration of the flow. The overprediction of the corner separations was attributed to the poor prediction of the boundary layer upstream of the interaction by the Spalart-Allmaras DES, the Spalart-Allmaras DDES and the HYB0 hybrid RANS/LES simulations. Table 1.4 shows the predicted corner separation sizes for the $M_r = 1.40$ interaction by Bruce *et al.* [19, 20] and Arvidson *et al.* [6].

The effect of different turbulence models on a normal shock interaction was also investigated in the UFAST project [39]. DES, RANS, and URANS simulations with the $k-\omega$, $k-\omega$ SST , and the $k-\tau$ turbulence model by Speziale *et al.* [125] of the normal $M_r = 1.45$ interaction by Doerffer [40, 41] were performed. Upstream of the interaction, the turbulence models predicted a stagnation pressure profile in good agreement with the experiment. The centreline separation size, however, was underpredicted by all models. The underprediction of the centreline separation led to the overprediction of the centreline wall pressure downstream of the interaction. As shown earlier by Bruce *et al.* [19] turbulence models

overpredicting the corner separations and underpredict the centreline separation. The issue of asymmetry was again present. Asymmetrical flowfields were predicted by the $k-\omega$ and $k-\omega$ SST models. A Spallart-Allmaras DES simulation and a simulation with a Reynolds Stress Model also predicted asymmetric flowfields. The flow asymmetry was in the form of very large corner separation in one of the duct corners and a very small one in the diagonally opposite corner. Symmetric results were only obtained with the $k-\tau$ turbulence model. A 5 mm chamfer equivalent to the boundary layer thickness was introduced to the lower duct edges (the edges formed by the floor and sidewalls), nevertheless, the asymmetry observed with some turbulence models shifted to the upper edges of the duct. Chamfering all edges eliminated the asymmetry. Ono *et al.* [31] also studied normal shock interactions numerically. No asymmetry was observed in the predicted flow field by the $k-\omega$ turbulence model. The upstream Mach number was $M_r = 1.60$ and the cross-section dimensions of the duct were 20 mm $\times$19.5 mm giving an aspect ratio of 0.975. For the $M_r = 1.40$ interaction studied numerically by Bruce *et al.* [19, 20], symmetry was also present with the $k-\omega$ model. The cross-section dimensions of the duct were 178 mm $\times$114 mm giving an aspect ratio of 0.6404. Although the duct used by Ono *et al.* [31] has a higher aspect ratio, the size of the corner separations are below 35-40% of the duct width. As stated earlier by Bruce *et al.* [19, 20], flow asymmetry was observed when the corner-interaction size exceeds 35-40% of the duct width or height. The effects of downstream forcing of a normal interaction were studied by Bur *et al.* [21], Doerffer *et al.* [39], and Bruce *et al.* [20]. Bruce *et al.* [20] performed URANS simulations with the Yang-Shih $k-\varepsilon$ model of a $M_r = 1.40$ interaction. Apart from some discrepancies at higher perturbation frequencies ($f = 90$ Hz), the simulations and experiment showed good agreement in the shock position, velocity and acceleration. Discrepancies, however, were observed in the interaction size. The height of the triple point h_T above the wall during the normal shock motion was overpredicted on average by around 40%. Additionally, the simulations predicted a larger h_T during the upstream shock motion than the downstream shock motion. This was inconsistent with the experiments. Similar findings were observed in earlier two-dimensional URANS simulations by Bur *et al.* [21]. Unsteady URANS simulations of the normal $M_r = 1.45$ interaction by Doerffer [40, 41] in the UFAST project [39] had a shock position amplitude and period comparable to the high-frequency oscillations of the shock position measured in the experiment. Table 1.5 lists the numerical simulations of normal shock wave boundary layer interactions discussed in this section.

Study	**Simulation**	Re (m^{-1})	M_r	**Inflow**	**Experimental study**
2003-04 Doerffer *et al.* [40,41]	2D (U)RANS ($k-\tau$ CLS)	1.41×10^7	1.20	STG	2003-04 Doerffer *et al.* [40,41]
	-	-	-	-	
	2D (U)RANS ($k-\tau$ CLS)	1.41×10^7	1.40	STG	
2010 UFAST [39]	$k-\omega$	1.41×10^7	1.45	STG	2010 Doerffer *et al.* [39]
	$k-\omega$ URANS, SA-DES	1.41×10^7	1.45	STG	
2006 Bur *et al.* [21]	$k-\varepsilon$ URANS (2D)	1.18×10^7	1.33	STG	2006 Bur *et al.* [21]
2011 Bruce *et al.* [19,20]	SA, YS $k-\varepsilon$, $k-\omega$ SST	2.33×10^7	1.30	STG	2011 Bruce *et al.* [19]
	SA, YS $k-\varepsilon$, $k-\omega$ SST	2.31×10^7	1.40	STG	
	SA, YS $k-\varepsilon$, $k-\omega$ SST	2.24×10^7	1.50	STG	
	YS $k-\varepsilon$ URANS	2.31×10^7	1.40	STG	
2012 Arvidson *et al.* [6]	PDH LRN $k-\omega$, $k-\omega$ EARSM	2.31×10^7	1.40	STG	2008 Bruce *et al.* [17,18]
	HYB0, SA-DES, SA-DDES	2.31×10^7	1.40	STG	
2013 Ono *et al.* [31]	3D RANS ($k-\omega$)	-	1.60	STG	2013 Ono *et al.* [31]
2016-17 Pizzella *et al.* [104,105]	SA	5.31×10^7	1.60	STG	2006 Ogawa & Babinsky [97]
	SA	3.12×10^7	1.60	STG	
2017 Roy *et al.* [112]	$k-\omega$ SST (2D)	-	1.30	STG	2006 Ogawa & Babinsky [97]

Table 1.5: Numerical simulations of normal shock wave boundary layer interactions.

Similarly to single normal interactions, numerical methods have been used to simulate multiple normal shock wave boundary layer interactions. Here only the most recent numerical simulations are outlined, omitting earlier simulations, as at that time, newer two-equation and one-equation turbulence models were not yet developed. The shock train experiment by Carroll *et al.* [23,27] was considered by Morgan *et al.* [93,94] who performed two-dimensional RANS and wall-resolved LES (WRLES) simulations. The RANS results show that the choice of turbulence model greatly affects the results. All turbulence models showed mean separation at the foot of the first shock wave, inconsistent with the experiment. The k-ω and k-ω SST failed to predict the slip lines emanating from the triple point and the subsonic core flow. The only model that was able to predict these flow features was the SA. The onset of the interaction varied as much as 15% of the length of the domain. Significant differences in the structure of the first shock wave were also reported. The SA model predicted the first shock with a λ-foot structure. The k-ω SST model predicted two oblique shock waves crossing at the centreline and the k-ω model two oblique shock waves meeting at a point just below the centreline. The subsequent failure of both models to predict the subsonic core flow can be attributed to the difference in the structure of the first shock. The flow decelerates less through an oblique shock wave compared to a normal one. The spanwise periodic (SP) wall-resolved LES simulations showed better agreement with the experiments, however, the shock train was shorter and the onset of the interaction was at a higher level of flow confinement. No mean separation was predicted, which was consistent with the experiment. The LES simulations were performed at a Reynolds number an order of magnitude lower than the experimental one, due to the forbidding computational resource requirements of LES near solid surfaces at high Reynolds numbers. Although spanwise periodic simulations cannot account for three-dimensional effects, Morgan *et al.* used them to perfect his numerical setup before attempting three-dimensional simulations. In his three-dimensional simulations he had to reduce the back pressure in order to obtain a stable solution. The omission of the divergence angle of the duct may have contributed to the instability. Despite the reduced back pressure, the three-dimensional simulation showed better agreement in the boundary layer growth compared to the spanwise periodic simulation. Improved agreements with the experiment were observed in the boundary layer displacement thickness δ^*, momentum thickness θ. Roussel *et al.* [111] also performed three-dimensional wall-resolved LES simulations of the experimental study by Carroll *et al.* [23,27] considering the effect of inlet boundary conditions - loosely coupled boundary layers on adjacent walls and accounting for the near corner effects by the Lund *et al.* [80] recycling rescaling method. Similarly to the simulations of Morgan *et al.* [93, 94], Roussel *et al.* [111] performed three-dimensional wall-resolved LES simulations at a lower Reynolds number and neglected the divergence angle of the duct.

Favourable agreement in the shock wave shape and structure with the experiment and the three-dimensional wall-resolved LES simulation of Morgan *et al.* [93, 94] was observed. This showed that downstream of the inlet the flow is weakly affected by the inlet boundary condition. Wall-modelled LES simulations of the same experiment by Carroll *et al.* [23, 27] were performed by Vane *et al.* [142]. The researchers concluded that the resolution of the grid is more significant than the matching location for the wall model in determining the location of the first shock. Vane *et al.* [142] also pointed that although the shock train structure from the spanwise periodic simulations was qualitatively similar, three-dimensional effects due to the presence of side walls must be included. This confirms the results of Morgan *et al.* [93, 94] where the inclusion of side walls improved the boundary layer parameters. A note was made by Vane *et al.* [142] that the assumption of an equilibrium boundary layer does not hold in the presence of shock waves, however, since the wall model is applied only in the inner part of the boundary layer (10-20% of δ), the wall-modelled LES still accounts for the non-equilibrium effects in the outer part of the boundary layer (80-90% of δ). Grids consisting of 2.5 to 14.6 million cells were used for the simulations. Giglmaier *et al.* [56] performed simulations of a shock train with a variety of linear turbulence models and ω-based Reynolds stress models. The SA and $k-\omega$ SST models resulted in unphysically long pseudo-shock regions and neither the onset of the interaction nor the pressure distribution matched the experiment. The $k-\omega$ and the ω-based RSMs predicted similar shock trains and the pre-shock Mach number for all was approximately $M_r = 1.7$. The $k-\varepsilon$ model and the ε-based RSMs underpredicted the separation at the centreline, which resulted in small wiggles in the wall pressure distribution. From the RSMs considered the k-ω EARSM resulted in the best agreement with the experiment. Grids consisting of 4.6 to 6.7 million cells were used for the simulations. Similar observations for the effect of the turbulence models were made by Quaatz *et al.* [107] who preformed RANS and wall-resolved LES simulations of the shock train experiment by Gawehn *et al.* [51]. The $k-\varepsilon$ and the $k-\omega$ SST models showed wiggles in the pressure distribution. Both the $k-\omega$ EARSM and the wall-resolved LES showed good agreement with the experiment, although the wall pressure downstream of the onset was slightly underpredicted by the latter. A grid consisting of 387 million cells was used for the wall-resolved LES simulation. Fiévet *et al.* [48, 49] investigated the effect of the inflow boundary layer on a shock train using wall resolved LES. The simulation approximated the experiment by Klomparens *et al.* [77, 78]. The molecular viscosity was multiplied by a factor of 4 to obtain a lower Reynolds number. It was found that the position of the shock train has a nonlinear dependence on the boundary layer thickness (100% change in streamwise position for a 25% change in δ/h). Two-and three-dimensional RANS simulations of the experiment by Sun *et al.* [131–133] were performed by Gnani *et al.* [58]. Significant

dependence of the solution on the grid density was observed for the two-dimensional simulations. Different first shock wave structures were predicted by the $k-\varepsilon$, $k-\omega$, and the $k-\omega$ SST models. Similarly to the findings of Morgan, the $k-\omega$ SST predicted a shock train with a χ structure rather than one with a λ-foot structure. The best agreement in the wall pressure with the experiment was observed with the $k-\omega$ model. The sensitivity of the solution might also be attributed to the absence of a divergence angle which would act to stabilise the shock train. The effect of different duct geometries, such as increased duct divergence angles, was investigated by Huang *et al.* [69] and Sethuraman *et al.* [118]. Satisfactory agreement with the shock train results from the experiment by Sun *et al.* [131] was achieved with the $k-\varepsilon$ and $k-\omega$ SST models. Increase of the divergence angle led to the shock train relocating upstream at lower levels of flow confinement. The relocation was accompanied by a transition of the shock train from a χ structure to a one with a λ-foot structure. Wall-modelled LES simulations of the shock train experiment by Weiss [147] were performed by Mousavi *et al.* [95] who considered Smagorinsky-Lilly, Wall-Adapting Local Eddy-Viscosity, and Algebraic Wall-Model subgrid models. Grids consisting of 32 to 54 million cells were used and it was concluded that the WMLES solution was more accurate than the WALE solution. Table 1.6 summarises the numerical simulations of the shock trains considered in this section.

Study	**Type**	Re_{δ_r}	M_r	δ_r/h	**Experimental study**
2012-14 Morgan *et al.* [93,94]	SA, $k-\omega$, $k-\omega$ SST (2D)	1.62×10^5	1.61	0.270	1988-93 Carroll *et al.* [23,27]
	WRLES (SP)	1.62×10^4	1.61	0.320	
	WRLES (SP)	1.62×10^4	1.61	0.270	
	WRLES (SP)	1.62×10^4	1.61	0.250	
	WRLES	1.62×10^4	1.61	0.270	
2013 Vane *et al.* [142]	WMLES	1.62×10^5	1.61	0.270	1988-93 Carroll *et al.* [23,27]
2014 Giglmaier *et al.* [56]	SA, $k-\varepsilon$, $k-\omega$, $k-\omega$ SST $k-\omega$ EARSM (and other RSMs)	$\times10^5$	1.60	0.350	2014 Giglmaier *et al.* [56]
2014 Quaatz *et al.* [107]	WMLES	1.91×10^6	1.90	0.420	2010 Gawehn *et al.* [51]
2015 Roussel *et al.* [111]	WRLES	1.00×10^4	1.61	0.219	1988-93 Carroll *et al.* [23,27]
	WRLES	1.00×10^4	1.61	0.219	
2016-17 Fiévet *et al.* [48,49]	WRLES	3.07×10^4	1.97	0.250	2015-16 Klomparens *et al.* [77,78]
	WRLES	3.47×10^4	1.97	0.280	
	WRLES	4.27×10^4	1.96	0.340	
2018 Gnani *et al.* [58]	$k-\varepsilon$, $k-\omega$, $k-\omega$ SST	2.50×10^4	1.97	0.250	2003-05 Sun *et al.* [131–133]
2019 Mousavi *et al.* [95]	WMLES	4.70×10^6	1.65	0.600	2010 Weiss *et al.* [147]

Table 1.6: Numerical simulations of multiple normal shock wave boundary layer interactions.

1.1.5 Control of shock wave boundary layer interactions

The control of normal SWBLIs through flow control devices was studied extensively experimentally (Doerffer *et al.* [40]; Holden & Babinsky [66, 67]; Herges *et al.* [65]; Bruce *et al.* [16,19]; Burton *et al.* [22]; Titchener *et al.* [136–138]). These experimental studies consider both passive flow control devices (vortex generators;grooves;slots;porous plates;bumps) and active flow control devices (blowing;suction). Figure 1.17 shows the different types of flow control devices and their placement.

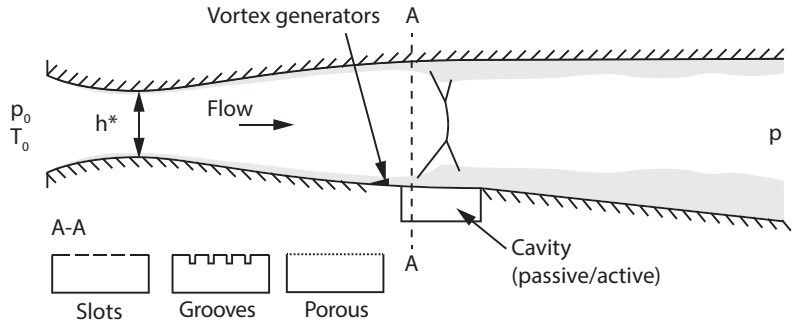

Figure 1.17: Qualitative sketch of a typical experimental setup used in control of normal SWBLI studies.

Holden & Babinsky [66, 67] investigated the effect of streamwise slots, grooves, and bumps on a $M_r = 1.30$ and $M_r = 1.50$ normal SWBLI. For the baseline (no-control devices) $M_r = 1.30$ interaction, no boundary layer separation was observed. Additionally, there was no clearly defined λ-shock structure. The introduction of streamwise slots promoted flow to recirculate from the high-pressure region downstream of the shock wave to the low-pressure region upstream of the shock wave. The recirculation of the flow creates a viscous "bubble". The bubble turns the outer (inviscid) flow causing a bifurcated λ-shock structure to develop. Behind the λ-shock structure, the stagnation pressure p_0 losses were reduced. In addition to the reduced p_0 losses, the slots introduced streamwise vortices which are thought to be beneficial in delaying downstream separations. The streamwise grooves also resulted in the development of a bifurcated λ-shock structure. Compared to the streamwise slots, they were found less effective as they caused a re-expansion after the compression by the leading leg of the λ-shock structure. The cause of re-expansion was attributed to the non-uniform streamwise recirculation resulting from the grooves. The grooves geometry was modified in an attempt to eliminate the detrimental re-expansion. Tapering of the grooves "nose" led to greater re-expansion, however, the introduction of "baffles" in the grooves resulted in an interaction very similar to the one with the streamwise slots. The modified grooves featuring baffles were as effective as the streamwise slots. The effect of streamwise bumps was also investigated. The height of the bumps in the experiment was less than the height of the up-

stream boundary layer $\delta_u = 7$ mm. It was found out that the boundary layer does not "rise" over the bump crests. Rather it gets thinner as it moves along the bumps, suggesting that the boundary layer "spills off" the top of the bump to the sides. This "spillage" limits the effective displacement of the flow outside the boundary layer and reduces the strength of the leading shock. The weaker leading shock suggests that the turning effect of three-dimensional bumps is not as great as that of a viscous bubble generated by the streamwise slots. Thus, only the effect of streamwise slots on the $M_r = 1.50$ normal SWBLI was investigated. For the base-line (no-slot control), separation was present at the centreline, however, no distinct "plateau" was observed in the wall pressure measurements as would be expected for a separated SWBLI. The wall pressure measurements were very similar to the ones by Atkin & Squire [7] for a $M_r = 1.50$ interaction. Similarly to the $M_r = 1.30$ interaction, the introduction of streamwise slots resulted in a bifurcated λ-shock structure. The SWBLI was fairly two dimensional in the spanwise direction. For the no-control interaction, the separation region was uniform in the spanwise direction, whereas for the controlled interaction attached and separated regions were observed in the spanwise direction. Holden *et al.* [67] studied the effect of wedge and vane-type vortex generators (sub-boundary layer) on a $M_r = 1.50$ interaction. For the no-control interaction, a small λ-shock structure, indicative of flow separation, was observed. As in the $M_r = 1.50$ interaction studied by Holden & Babinsky [66, 67] no "plateau" in the wall pressure distribution was observed due to the short separated region. The effectiveness of the vortex generators was found dependent on the location of the shock wave. When the shock wave was located downstream of the vortex generators, an unfavourable re-expansion region was observed. From the two types of vortex generators, the vane-type were more effective as they were observed to eliminate the shock wave induced separation. Their effectiveness was attributed to the generation of more energetic streamwise vortices that energise the boundary layer. Herges *et al.* [65] performed further experimental studies on the effect of ramp and vane-type vortex generators (sub-boundary layer) and porous plate over a cavity on a $M_r = 1.40$ SWBLI. In their experiments, a constant area section followed by a 5-degree diverging section was used. The vortex generators and the porous plate were located in the constant area section. Vortex generators were found to reduce fluctuations of the normal shock wave when the shock wave was located in the diverging section. Vane type vortex generators were more effective in reducing the fluctuations than the ramped type ones. Both types of vortex generators were found to increase slightly the fluctuations when the shock wave was located upstream of the diverging section. Opposite tendencies were observed with the porous plate. It reduced the fluctuations when the shock wave was located upstream of the diverging section. Additionally, the sensitivity of the location of the shock wave to stagnation pressure p_0 changes was improved by the porous plate. Further experimental studies

on vortex generators (sub-boundary layer) were performed by Bruce *et al.* [19] and Burton *et al.* [22]. They investigated the effect of vortex generators (sub-boundary layer) placed near the corners of a rectangular duct upstream of a $M_r = 1.50$ SWBLI. For the no-control interaction, separation was present. The introduction of vane-type vortex generators increased the sizes of the corner separation. The increase of the corner separations resulted in the disappearance of the centreline separation. As discussed previously, the corner separations result in the formation of compression waves which can affect the centreline separation, provided the corner separations are of appropriate size. The effects of corner suction through suction slots was investigated by Bruce *et al.* [16, 19] for an unseparated $M_r = 1.40$ SWBLI. Suction resulted in the appearance of a centreline separation. The appearance of the centreline separation is due to the decrease of the corner separations. Burton *et al.* [22] observed similar increase of the centreline separation for a $M_r = 1.50$ SWBLI with corner suction. Titchener *et al.* [135] also investigated the effect of suction on a $M_r = 1.40$ normal SWBLI. The experimental setup was similar to the one used by Bruce *et al.* [19]. The only difference was that the constant area section was followed by a 6 deg diverging section. Separation was observed at the centreline. For a $M_r = 1.40$ SWBLI without a diverging section, Bruce *et al.* [16, 19] did not observe any centreline separation. This shows that the introduction of a diverging section affects the SWBLI. Suction reduced the corner separations and resulted in a more two-dimensional SWBLI. Nevertheless, the reduction of the corner separation increased the separation at the centreline. This was in agreement with the experiments by Bruce *et al.* [19] where suction was shown to increase centreline separation. Additional experimental studies by Titchener *et al.* [136–138] on the effects of vortex generators revealed that the introduction of vortex generators to the centreline delays separation locally, but results in larger corner flow separations. Combination of corner suction and centreline vortex generators resulted in 6% improvement in wall pressure p recovery and 15% reduction in stagnation pressure losses.

1.2 Chapter summary

Currently, linear turbulence models are still extensively used to simulate multiple shock wave boundary layer interactions. Although these models are well established and robust, they sometimes fail to provide reasonable predictions for MSWBLIs. Works presenting reasonable predictions often disregard spanwise effects. However, spanwise effects play a key role in defining the structure of MSWBLIs. As discussed in the above chapter, spanwise effects also control the formation of MSWBLIs. Overpredicting the corner flows might result in an interaction that is not representative of the flow under investigation. Scale resolving methods such as hybrid RANS-LES and DES alleviate some of the shortcomings of the linear

turbulence models by accounting for more of the flow physics. The improvements that the methods offer are mainly in the separation sizes. However, similarly to linear models, the use of hybrid RANS-LES models may result in asymmetric solutions. Large Eddy Simulations show promise as they model even more of the flow physics. However, their use necessitates the reduction of the Reynolds number. Most practical cases involving MSWBLIs have Reynolds numbers that are too high for wall-resolved LES. In addition, the use of scale resolving methods can result in an isolator unstart at the experimental conditions which makes comparison with experiments difficult. Non-linear turbulence models (RSM-based) show improved results, but are not yet extensively used for MSWBLI interactions. Based on the above observations, there is a need for a systematic study of a MSWBLI that assesses the predictive capability of non-linear models using constitutive relations. To address the above requirement, models including quadratic and higher constitutive relations are to be implemented in the existing flow solver. After investigating their effect on confined MSWBLI interactions (in ducts) it must be determined if they are robust enough for simulations of geometries representative of high-speed intakes.

1.3 Thesis Objectives

This thesis has the following objectives:

- To establish best practices and best numerical methods in simulating multiple shock wave boundary layer interactions.
- To investigate the flow physics and the sensitivity of a multiple shock wave boundary layer interaction to changes in upstream and downstream parameters such as Mach number, Reynolds number, and exit (back) pressure.
- To investigate the effect of quadratic constitutive stress relations on multiple shock wave boundary layer interactions.
- To investigate the sensitivity of a multiple shock wave boundary layer interaction to different corner geometries.
- To investigate the sensitivity of the shock wave boundary layer interaction to the freestream parameters and intake geometry.

1.4 Thesis Outline

The thesis is organised as follows:

Chapter 1 presents the motivation behind the current work, a literature review, and the objectives of the thesis.

Chapter 2 presents the numerical method including the governing equations and the available turbulence models. The different grid generation techniques used for the numerical simulations are also outlined.

Chapter 3 presents validation of single and multiple normal shock wave boundary layer interactions against experiments. Different numerical methodologies are considered including non-linear constitutive models and scale-resolving methods. Recommendations are given regarding the best numerical methodology for simulating multiple shock wave boundary layer interactions.

Chapter 4 presents a sensitivity study of a multiple shock wave boundary layer interaction to several flow parameters and different geometries. Performance metrics in terms of flow distortion and total pressure recovery are defined and used to quantify the "efficiency" of the interaction.

Chapter 5 couples the internal shock wave boundary layer interaction with an external flow around a fore-body representing a missile. The sensitivity of the intake performance metrics to free-stream parameters and different geometries is investigated.

Chapter 6 summarises the findings and gives direction for future work.

Appendix A presents the implementation and application of a synthetic turbulence generation method.

Appendix B presents the procedure for generation of mean inflow profiles.

Appendix C presents simulations of a missile at a high incidence angle.

Appendix D presents drawings of a fore-body intake geometry used to couple the external and internal flows.

Chapter 2

CFD flow solver

All numerical simulations in this work were performed with the Helicopter Multi Block (HMB3) CFD solver [12, 127] of the University of Glasgow. The flow solver is parallel and was initially developed to analyse rotorcraft flows with structured multi-block grids. Over a number of years, HMB3 has been revised and updated to work with moving, sliding, overlapping and unstructured grids. In addition, the solver offers a variety of turbulence models and hybrid RANS/LES methods. It has been successfully used for a variety of flows including rotors and wind turbines, transonic cavity flows, shock wave boundary layer interactions, and supersonic flows around missiles.

2.1 Formulation

The HMB3 flow solver considers the equation of motion of an ideal Newtonian fluid, governed by the conservation of mass, momentum, energy and an equation of state. Although these equations are given in a variety of books (White [150]; Versteeg *et al.* [143]) they are reproduced here for completeness and to introduce the notation and non-dimensionalisation used throughout the remainder of the work. The conservation of mass; the conservation of momentum; the conservation of energy; and the equation of state are given by:

$$\begin{aligned} \frac{\partial \rho}{\partial t} + \frac{\partial}{\partial x_i}(\rho u_i) &= 0, \\ \frac{\partial}{\partial t}(\rho u_i) + \frac{\partial}{\partial x_j}\left(\rho u_i u_j\right) &= \rho f_i - \frac{\partial p}{\partial x_i} + \frac{\partial \tau_{ij}}{\partial x_j}, \\ \frac{\partial}{\partial t}(\rho E) + \frac{\partial}{\partial x_j}\left[u_j(\rho E + p)\right] - \frac{\partial}{\partial x_j}\left(u_i \tau_{ij}\right) + \frac{\partial q_j}{\partial x_j} &= 0, \end{aligned} \tag{2.1}$$

The above equations are obtained from the application of the conservation of mass, the conservation of linear momentum (Newton's 2^{nd} Law), and the conservation of total energy (the 1^{st} Law of Thermodynamics). The viscous stress tensor is given by τ_{ij}, q_j is the heat flux vector, f_i represents any acting body force, E is the total energy per unit mass, ρ is the density, $u_i = (u,v,w)^T$ are the velocity components and $x_i = (x,y,z)^T$ is the position in three-dimensional Cartesian coordinates. The total energy is E is defined as:

$$E = e + \frac{1}{2}u_i u_i = e + k, \tag{2.2}$$

where $k = \frac{1}{2}u_i u_i$ is the kinetic energy per unit mass and e is the specific internal energy. The heat flux vector q_i is obtained from Fourier's Law:

$$q_i = -k\frac{\partial T}{\partial x_i} = -\frac{\gamma R}{Pr(\gamma-1)}\frac{\partial T}{\partial x_i}, \tag{2.3}$$

where k is the heat conductivity, γ is the specific ratio of heats, Pr is the Prandtl number, and μ is the molecular viscosity. Assuming a Newtonian fluid, and applying Stoke's hypothesis that the bulk viscosity is zero, the viscous stress tensor τ_{ij} is defined as:

$$\tau_{ij} = 2\mu\left(S_{ij} - \frac{1}{3}\frac{\partial u_k}{\partial x_k}\delta_{ij}\right), S_{ij} = \frac{1}{2}\left(\frac{\partial u_i}{\partial x_j} + \frac{\partial u_j}{\partial x_i}\right). \tag{2.4}$$

Sutherland's Law is used to relate the molecular viscosity to the temperature:

$$\frac{\mu}{\mu_{ref}} = \left(\frac{T}{T_{ref}}\right)^{3/2}\frac{1+\tilde{S_\mu}}{T/T_{ref}+\tilde{S_\mu}}, \qquad \tilde{S_\mu} = S_\mu/T_{ref}, \tag{2.5}$$

where the constant $\tilde{S_\mu}$ is taken to be 0.368, $T_{ref} = 300$ K, and $S_\mu = 110.5$ K according to White [150]. Equations 2.1 through 2.5 represent a closed system of equations that is assumed to govern the dynamics of fluid flow in this work. The equations are non-dimensionalised using the fundamental dimensions of mass, time, and temperature. The non-dimensionalisation leads to the following non-dimensional form of the variables:

$$\begin{aligned} \tilde{x_i} = \frac{x_i}{L_{ref}}, \tilde{\rho} = \frac{\rho}{\rho_{ref}}, \tilde{u_i} = \frac{u_i}{V_{ref}}, \tilde{T} = \frac{T}{T_{ref}}, \tilde{t} = \frac{V_{ref}}{L_{ref}} t \\ \tilde{p} = \frac{p}{p_{ref} \gamma M_{ref}^2}, \tilde{\mu} = \frac{\mu}{\mu_{ref}}, \tilde{e} = \frac{e}{V_{ref}^2}, \tilde{k} = \frac{k}{V_{ref}^2}, \end{aligned} \tag{2.6}$$

where γ is the ratio of specific heats.
The non-dimensional system of equations can be written in vector form:

$$\frac{\partial \mathbf{W}}{\partial t} + \frac{\partial \left(\mathbf{F}^i + \mathbf{F}^v\right)}{\partial x} + \frac{\partial \left(\mathbf{G}^i + \mathbf{G}^v\right)}{\partial y} + \frac{\partial \left(\mathbf{H}^i + \mathbf{H}^v\right)}{\partial z} = \mathbf{S}, \tag{2.7}$$

where $\mathbf{W}$ is the vector of conserved variables and $\mathbf{S}$ is a source term:

$$\mathbf{W} = (\rho, \rho u, \rho v, \rho w, \rho E)^T. \tag{2.8}$$

The flux components in the x-, y-, and z-direction are denoted by $\mathbf{F}$, $\mathbf{G}$ and $\mathbf{H}$, respectively, with superscripts i and v used to denote the inviscid and viscous terms. The flux terms for the inviscid and viscous components are:

$$\begin{aligned} \mathbf{F}^i &= \left(\rho u, \rho u^2 + p, \rho uv, \rho uw, u(\rho E + p)\right)^T & \mathbf{F}^v &= \tfrac{1}{Re}\left(0, \tau_{xx}, \tau_{xy}, \tau_{xz}, u\tau_{xx} + v\tau_{xy} + w\tau_{xz} + q_x\right)^T \\ \mathbf{G}^i &= \left(\rho v, \rho uv, \rho v^2 + p, \rho vw, v(\rho E + p)\right)^T & \mathbf{G}^v &= \tfrac{1}{Re}\left(0, \tau_{xy}, \tau_{yy}, \tau_{yz}, u\tau_{xy} + v\tau_{yy} + w\tau_{yz} + q_y\right)^T \\ \mathbf{H}^i &= \left(\rho w, \rho uw, \rho vw, \rho w^2 + p, w(\rho E + p)\right)^T & \mathbf{H}^v &= \tfrac{1}{Re}\left(0, \tau_{xz}, \tau_{yz}, \tau_{zz}, u\tau_{xz} + v\tau_{yz} + w\tau_{zz} + q_z\right)^T \end{aligned}$$

2.2 Numerical Method

The HMB3 flow solver solves the governing equations defined in the previous section using a cell-centred finite volume method combined with an implicit dual time-stepping method. The computational domain is discretised in a finite number of non-overlapping control volumes and the governing equations are solved in integral conservation form for each of the control volumes. The governing equations in integral conservation form, using the Arbitrary Lagrangian-Eulerian (ALE) formulation for time-dependent domains with moving boundaries, are:

$$\frac{d}{dt}\left(\int_{V(t)} \mathbf{W} dV\right) + \int_{\partial V(t)} \left(\mathbf{F}^i(\mathbf{W}) - \mathbf{F}^v(\mathbf{W})\right) \cdot \mathbf{n} dS = \mathbf{S}, \tag{2.9}$$

where $V(t)$ is the time-dependent volume of the control volume and the $\partial V(t)$ is its boundary.

The spatial discretisation of these equations leads to a set of Ordinary Differential Equations (ODEs) in time, for each control volume (or cell). The semi-discrete form of equation 2.9 is:

$$\frac{d}{dt}\left(\mathbf{W}_{i,j,k}\forall_{i,j,k}\right) = -\mathbf{R}_{i,j,k}(\mathbf{W}), \tag{2.10}$$

where i,j,k represent the spatial components, $\mathbf{W}_{i,j,k}$ and $\mathbf{R}_{i,j,k}(\mathbf{W})$ represent the vectors of conservative flow variables and the flux residual. The volume of the cell i,j,k is $\forall_{i,j,k}$. A curvilinear coordinate system i,j,k is used to aid the formulation of the discretised terms since body-conforming grids are used. Osher's [100] upwind scheme is used for the convective fluxes, however, the flux-splitting scheme of Roe [110] is also available. The Monotone Upwind Scheme for Conservation Laws (MUSCL) developed by van Leer [141] is used to provide high-order accuracy in space and spurious oscillations due to large changes in the flow quantities (e.g. across shock waves) are removed with the van Albada [139] limiter. The differentiable nature of the limiter improves the convergence. The viscous terms are discretised using a second-order central scheme. The boundary conditions are set by using ghost cells on the exterior of the computational domain. For solid bodies the ghost cell values are extrapolated from the interior ensuring the normal component of velocity on the solid wall is zero (when solving the Euler equations) and the no-slip wall condition is set (when solving the Navier-Stokes equations). Approximating the time derivative of Equation 2.10 by a second-order backward difference leads to the following temporal discretisation of Equation 2.10:

$$\frac{3\mathbf{W}^{n+1}_{i,j,k}\forall^{n+1}_{i,j,k} - 4\mathbf{W}^{n}_{i,j,k}\forall^{n}_{i,j,k} + \mathbf{W}^{n-1}_{i,j,k}\forall^{n-1}_{i,j,k}}{2\Delta t} + R_{i,j,k}(\mathbf{W}^{n+1}) = 0. \tag{2.11}$$

Equation 2.11 is non-linear in $\mathbf{W}^{n+1}_{i,j,k}$ and does not have an explicit, closed-form solution. Therefore an iterative method (Jameson's original implicit dual-time stepping approach) is used to solve the equation in pseudo-time τ, i.e. for each real time step Δt the solution is marched in pseudo time steps $\Delta\tau$. The system of equations solved in pseudo-time is given by:

$$\begin{aligned} \frac{\mathbf{W}^{m+1}_{i,j,k} - \mathbf{W}^{m}_{i,j,k}}{\Delta\tau} + \mathbf{R}^{*}_{i,j,k}(\mathbf{W}^{m+1}) = 0, \\ \mathbf{R}^{*}_{i,j,k}(\mathbf{W}^{m}) = R_{i,j,k}(\mathbf{W}^{m}) + \frac{3\mathbf{W}^{m}_{i,j,k}\forall_{i,j,k}}{2\Delta t} - \frac{4\mathbf{W}^{n}_{i,j,k}\forall^{n}_{i,j,k}}{2\Delta t} + \frac{\mathbf{W}^{n-1}_{i,j,k}\forall^{n-1}_{i,j,k}}{2\Delta t}, \end{aligned} \tag{2.12}$$

where $\mathbf{R}^{*}_{i,j,k}$ is the modified flux residual. To evaluate the modified flux residual $\mathbf{R}^{*}_{i,j,k}$ at pseudo time step $m+1$ the modified flux residual is approximated via a linear expansion in

pseudo-time truncated to first order:

$$\mathbf{R}^*_{i,j,k}(\mathbf{W}^{m+1}) \approx \mathbf{R}^*_{i,j,k}(\mathbf{W}^m) + \frac{\partial \mathbf{R}^*_{i,j,k}}{\partial \mathbf{W}_{i,j,k}} \left(\mathbf{W}^{m+1}_{i,j,k} - \mathbf{W}^m_{i,j,k} \right), \tag{2.13}$$

where $\frac{\partial \mathbf{R}^*_{i,j,k}}{\partial \mathbf{W}_{i,j,k}} = \frac{\partial \mathbf{R}_{i,j,k}}{\partial \mathbf{W}_{i,j,k}} + \frac{3\forall_{i,j,k}}{2\Delta t}\mathbf{I}$. Substituting equation 2.13 in equation 2.12 and changing from conservative variables $\mathbf{W}$ to primitive variables $\mathbf{P} = (\rho, u, v, w, p)^T$ results in the following system of equations:

$$\left[\left(\frac{\forall_{i,j,k}}{\Delta\tau} + \frac{3\forall_{i,j,k}}{2\Delta t} \right) \frac{\partial \mathbf{W}_{i,j,k}}{\partial \mathbf{P}_{i,j,k}} + \frac{\partial \mathbf{R}_{i,j,k}}{\partial \mathbf{P}_{i,j,k}} \right] \Delta \mathbf{P}_{i,j,k} = -\mathbf{R}^*_{i,j,k}(\mathbf{W}^m), \tag{2.14}$$

where $\Delta \mathbf{P}_{i,j,k} = \mathbf{P}^{m+1}_{i,j,k} - \mathbf{P}^m_{i,j,k}$. The implicit system of equations is solved in a coupled manner. For a block-structured mesh, Equation 2.14, results in a large sparse matrix and thus is solved via a Krylov subspace algorithm, the generalised conjugate gradient method. The Block Incomplete Lower-Upper BILU [8] factorisation is used as a pre-conditioner in a decoupled manner between grid blocks to reduce the communication between preprocessors when the flow solver is used in parallel mode. The Jacobian matrix $\frac{\partial \mathbf{R}_{i,j,k}}{\partial \mathbf{P}_{i,j,k}}$ is first-order approximate. During the Jacobian calculation, the variables at the cell faces are not reconstructed using the MUSCL approach. Furthermore, a thin shear layer type approximation is adopted for the computation of the viscous fluxes. In this way, the ill-conditioning of the problem is avoided and the overall size of the linear system is reduced. Only the destruction terms are accounted for in the approximate Jacobian.

2.3 Turbulence Modelling

2.3.1 Similarities between temporal averaging and spatial filtering

A structural similarity exists between the spatially filtered and Reynolds-averaged Navier Stokes equations. After Reynolds-averaging the Navier Stokes equations, the transport equation for the Reynolds-averaged velocity $\overline{u_i}$ reads:

$$\rho \frac{\partial \overline{u_i}}{\partial t} + \rho \frac{\partial}{\partial x_j} \left(\overline{u}_j \overline{u}_i \right) = -\frac{\partial \overline{p}}{\partial x_i} + \frac{\partial}{\partial x_j} \left(2\mu \overline{S_{ij}} \right) - \frac{\partial \tau^{RANS}_{ij}}{\partial x_j}. \tag{2.15}$$

$$\tag{2.16}$$

The analogous equation for the filtered velocity $\overline{u_i}$ reads:

$$\rho \frac{\partial \overline{u_i}}{\partial t} + \rho \frac{\partial}{\partial x_j} \left(\overline{u}_j \overline{u}_i \right) = -\frac{\partial \overline{p}}{\partial x_i} + \frac{\partial}{\partial x_j} \left(2\mu \overline{S_{ij}} \right) - \frac{\partial \tau_{ij}^{LES}}{\partial x_j}. \tag{2.17}$$

$$\tag{2.18}$$

The above equations require modelling of the τ_{ij}^{RANS} and τ_{ij}^{LES} terms. A RANS model depends on physical quantities describing the entirety of the turbulent fluctuations e.g.:

$$\tau_{ij}^{RANS} = f\left(\frac{\partial \overline{u}_i}{\partial x_j}, k, \omega, C \right), \tag{2.19}$$

$$\tag{2.20}$$

where C is a model coefficient, k is the specific turbulent kinetic energy, and ω is the specific dissipation rate of k. The latter two are determined from respective transport equations which will be discussed in subsequent subsections. LES based on the Smagorinsky model [121] uses a relation like

$$\tau_{ij}^{LES} = f\left(\frac{\partial \overline{u}_i}{\partial x_j}, \Delta, C \right), \tag{2.21}$$

$$\tag{2.22}$$

where Δ is a length scale (subgrid scale) related to the numerical grid, e.g. $\Delta = \left(\Delta_x \Delta_y \Delta_z\right)^{1/3}$. A model qualifies as a LES model if it explicitly contains in one or the other way the length scale of the computational grid. RANS models on the other hand depend on physical quantities (k,ω) and geometric features like the wall distance. Several turbulence models are implemented in the HMB3 solver including the $k-\omega$ by Wilcox [152], the BSL $k-\omega$ by Menter [86], the $k-\omega$ SST by Menter [86], and the $k-\omega$ EARSM by Hellsten *et al.* [64, 144]. In addition, the QCR extensions by Spalart [122] and Sabnis [113] were added to the $k-\omega$ SST model by Menter [86] in this work. Various hybrid RANS/LES methods such as the Detached Eddy simulation (DES) by Spalart [122] and its variants, the Scale-Adaptive-Simulation (SAS) by Egorov and Menter *et al.* [47, 87, 88], and the Limited Numerical Scales (LNS) by Batten *et al.* [13] are available. Table 2.1 summarises the models and methods in a chronological order.

Table 2.1: Turbulence models and methods used in this work, implemented in HMB3; $^{+}$ - different variants of the model are available; * - any k-ω model can be used with this method

Model / Method	Year	References
k-ω^{+}	1988-2006	Wilcox [151, 152]
k-ω BSL	1994	Menter [86]
k-ω SST	1994	Menter [86]
k-ω SST + QCR V1	2000	QCR by Spalart [122]
k-ω EARSM	2005	Hellsten, Wallin, and Johansson [64]
k-ω SST + QCR V2	2020	QCR by Sabnis [113]
k-ω SST / DES	2001	Strelets [128]
k-ω^{*} / LNS	2002	Batten *et al.* [13]
k-ω SST / SAS	2008	Egorov and Menter [47, 87, 88]
k-ω SST / DDES	2012	Gritskevich *et al.* [60]
k-ω SST / IDDES	2012	Gritskevich *et al.* [60]

2.3.2 Linear Two-Equation Eddy-viscosity models

The linear two-equation Eddy-viscosity models (EVMs) model the Reynolds stress tensor τ_{ij}^{RANS} as:

$$\tau_{ij}^{RANS} = -\rho\overline{u_i'u_j'} = -\rho \begin{bmatrix} \overline{u'u'} & \overline{u'v'} & \overline{u'w'} \\ & \overline{v'v'} & \overline{v'w'} \\ Symm. & & \overline{w'w'} \end{bmatrix} = 2\mu_t\overline{S}_{ij}^{*} - \frac{2}{3}\rho\delta_{ij}k,$$

$$\overline{S}_{ij}^{*} = \overline{S}_{ij} - \frac{1}{3}\frac{\partial\overline{u}_k}{\partial x_k}\delta_{ij}, \qquad (2.23)$$

$$\overline{S}_{ij} = \frac{1}{2}\left(\frac{\partial\overline{u}_i}{\partial x_j} + \frac{\partial\overline{u}_j}{\partial x_i}\right),$$

$$k = \frac{1}{2}\left(\overline{u'u'} + \overline{v'v'} + \overline{w'w'}\right),$$

where μ_t is the turbulent eddy viscosity and $\overline{S}_{ij}$ is the strain rate tensor. The term $-\frac{2}{3}\rho\delta_{ij}k$ is required so that the equality in equation 2.23 is valid upon contraction $\overline{u_i'u_i'} = 2k$. Equation 2.23 is the Boussinesq approximation [90]. Simply put, the Reynolds stress tensor represents momentum diffusion due to turbulence in the mean flow. Boussinesq assumed that the Reynolds stress tensor is aligned with and proportional to the mean strain rate tensor $\overline{S}_{ij}$. This reduces the six unknown Reynolds stresses to only one unknown μ_t - the turbulent eddy viscosity. The turbulent eddy viscosity has the dimension of [m^2/s] and the most suitable choice to model it is to use the turbulent kinetic energy k and a secondary turbulent quantity. For the $k-\omega$ family of turbulence models, the secondary turbulent quantity is ω, the reciprocal to the time scale of vorticity, or more commonly referred to as the specific dissipation rate of

turbulent kinetic energy. Since ω has the dimension of [s^{-1}], the eddy viscosity is:

$$\mu_t \sim \rho \frac{k}{\omega}. \tag{2.24}$$

For the family of $k-\omega$ turbulence models, the transport equations for the turbulent kinetic energy and the specific dissipation rate read:

$$\begin{aligned} \frac{\partial(\rho k)}{\partial t} + \frac{\partial(\rho \overline{u}_j k)}{\partial x_j} &= P_k - \beta^* \rho \omega k + \frac{\partial}{\partial x_j}\left[(\mu + \sigma_k \mu_t)\frac{\partial k}{\partial x_j}\right], \\ \frac{\partial(\rho \omega)}{\partial t} + \frac{\partial(\rho \overline{u}_j \omega)}{\partial x_j} &= \gamma \frac{\omega}{k} P_k - \beta \rho \omega^2 + \frac{\partial}{\partial x_j}\left[(\mu + \sigma_\omega \mu_t)\frac{\partial \omega}{\partial x_j}\right] + \rho Q_\omega, \end{aligned} \tag{2.25}$$

where $P_k = \tau_{ij}^{RANS} \frac{\partial \overline{u}_j}{\partial x_i}$ is the turbulent kinetic energy production term, and γ, σ_k, σ_ω,β,β^* are model coefficients. The term Q_ω is model dependant. Subsequent subsections discuss the formulations of the term and the values of the model coefficients.

Wilcox's $k-\omega$ model

The popular $k-\omega$ model was developed by Wilcox [152] in 1988. Since the introduction of the model other notable modifications to the model have been made which are discussed in subsequent subsections. The Q_ω term and the eddy viscosity definition for the $k-\omega$ model are given by:

$$\begin{aligned} Q_\omega &= \sigma_d \frac{1}{\omega}\frac{\partial k}{\partial x_k}\frac{\partial \omega}{\partial x_k}, \\ \mu_t &= \rho \frac{k}{\omega}. \end{aligned} \tag{2.26}$$

Meter's $k-\omega$ BSL Baseline (BSL) model

Menter's $k-\omega$ BSL model retains the robust and accurate formulation of the Wilcox $k-\omega$ model in the near-wall region and takes advantage of the freestream independence of the k-ε model in the outer part of the boundary layer. The difference between this model and the original $k-\omega$ model is that an additional cross-diffusion term appears in the ω equation and that the model coefficients are different. The original model is multiplied by a function F_1 and the transformed model by a function $(1-F_1)$ and both are added together. The function F_1 is designed to be one in the near-wall region (activating the original model) and zero away from

the surface. Blending takes place in the wake region of the boundary layer. The Q_ω term and the eddy viscosity definition for the $k-\omega$ BSL model are given by:

$$\begin{aligned} Q_\omega &= 2\left(1-F_1\right)\frac{\sigma_{\omega 2}}{\omega}\frac{\partial k}{\partial x_j}\frac{\partial \omega}{\partial x_j}, \\ \mu_t &= \rho\frac{k}{\omega}. \end{aligned} \tag{2.27}$$

Let ϕ_1 represent any constant from the original $k-\omega$ model, ϕ_2 any constant in the transformed k-ε model (σ_{k2},...) and ϕ the corresponding constant of the new model (σ_k,...), then the relationship between them is:

$$\begin{aligned} \phi &= F_1\phi_1 + (1-F_1)\phi_2, \\ F_1 &= tanh\left(arg_1^4\right), \\ arg_1 &= min\left[max\left(\frac{\sqrt{k}}{0.09\omega d_w}, \frac{500\nu}{d_w^2\omega}\right), \frac{4\rho\sigma_{\omega 2}k}{CD_{k\omega}d_w^2}\right], \\ CD_{k\omega} &= max\left(2\rho\sigma_{\omega 2}\frac{1}{\omega}\frac{\partial k}{\partial x_j}\frac{\partial \omega}{\partial x_j}, 10^{-20}\right), \end{aligned} \tag{2.28}$$

where d_w is the distance to the nearest wall. The constants of the original $k-\omega$ model (Wilcox) are:

$$\begin{aligned} \sigma_{k1} = 0.5,\ \sigma_{\omega 1} = 0.5,\ \beta_1 = 0.0750, \\ \beta^* = 0.09,\ \kappa = 0.41,\ \gamma_1 = \beta_1/\beta^* - \sigma_{\omega 1}\kappa^2/\sqrt{\beta^*}, \end{aligned} \tag{2.29}$$

and the constants of the standard k-ε are:

$$\begin{aligned} \sigma_{k2} = 1.0,\ \sigma_{\omega 2} = 0.856,\ \beta_2 = 0.0828, \\ \beta^* = 0.09,\ \kappa = 0.41,\ \gamma_2 = \beta_2/\beta^* - \sigma_{\omega 2}\kappa^2/\sqrt{\beta^*}. \end{aligned} \tag{2.30}$$

It is recommended to use a limiter for the production of turbulent kinetic energy k:

$$P_{k,limited} = min\left(P_k, 20\beta^*\rho\omega k\right).$$

Additional details about the model can be found on the Turbulence Modelling Resource of

NASA Langley Research Center [2] and the corresponding references.

Menter's $k-\omega$ SST model

Menter's $k-\omega$ SST model differs from the Menter $k-\omega$ BSL model only by a modification of the eddy viscosity and the value of the σ_{k1} constant ($\sigma_{k1} = 0.85$). The Q_ω term and the eddy viscosity definition for the $k-\omega$ model are given by:

$$\begin{aligned} Q_\omega &= 2\,(1-F_1)\,\frac{\sigma_{\omega 2}}{\omega}\frac{\partial k}{\partial x_j}\frac{\partial \omega}{\partial x_j}, \\ \mu_t &= \rho\frac{a_1 k}{max(a_1\omega, |\overline{\Omega}_{ij}|F_2)}, \\ F_2 &= tanh(arg_2^2), \\ arg_2 &= max\left(\frac{\sqrt{k}}{0.09\omega d_w}, \frac{500\nu}{d_w^2\omega}\right), \\ |\overline{\Omega}_{ij}| &= \sqrt{2\overline{\Omega}_{ij}\overline{\Omega}_{ij}}, \\ \overline{\Omega}_{ij} &= \frac{1}{2}\left(\frac{\partial \overline{u}_i}{\partial x_j} - \frac{\partial \overline{u}_j}{\partial x_i}\right), \end{aligned} \tag{2.31}$$

where the function F_2 is designed to be one for boundary layer flows and zero for free shear layers. Since in adverse pressure gradient boundary layers the production of k is larger than its dissipation ($\Omega > a_1\omega$) the modification of the Eddy-viscosity satisfies Bradshaw's assumption that shear stress in a boundary layer is proportional to the turbulent kinetic energy k ($\tau = \rho a_1 k$). Similarly to Menter's $k-\omega$ Baseline model, it is recommended to use a limiter for the production of turbulent kinetic energy k:

$$P_{k,limited} = min\,(P_k, 20\beta^*\rho\,\omega k)\,.$$

Additional details about the model can be found on the Turbulence Modelling Resource of NASA Langley Research Center [2] and the corresponding references.

2.3.3 Non-linear Two-Equation Eddy-viscosity models

The linear dependency between the turbulent stress and the mean strain-rate tensor (Boussinesq approximation) can be too restrictive for some flows. Improvements have been made by adding additional terms aimed at compressibility, streamline curvature or better anisotropy of

the Reynolds stress tensor (non-Boussinesq constitutive relations). This is especially true for flows in ducts with sharp corners giving rise to secondary flows. To improve the prediction of existing two-equation turbulence models, a non-linear constitutive model for the turbulent stress tensor is usually adopted. An example model is the Explicit Algebraic Reynolds Stress $k-\omega$ ($k-\omega$ EARSM) model by Hellsten *et al.* [64, 144].

$k-\omega$ EARSM model

The Explicit Algebraic Reynolds Stress $k-\omega$ model proposed by Hellsten [64] is derived from Menter's BSL $k-\omega$ model [86] but uses the explicit algebraic Reynolds-stress model of Wallin and Johansson [144] as a constitutive model for the turbulent stress tensor (the constant coefficients are also re-calibrated). The non-linear contribution is thus introduced in the production of k. The k production term P_k is not limited.

$$
\begin{aligned}
Q_\omega &= \sigma_d \frac{1}{\omega} max\left(\frac{\partial k}{\partial x_k}\frac{\partial \omega}{\partial x_k}, 0\right), \\
\mu_t &= \rho \frac{C_\mu k}{\beta^* \omega}, \\
\tau_{ij}^{RANS} &= \tau_{ij}^{RANS} - a_{ij}^{ex}\rho k, \\
a_{ij}^{ex} &= \beta_3\left(\overline{\Omega}_{ik}^{'}\overline{\Omega}_{kj}^{'} - \frac{1}{3}II_\Omega\delta_{ij}\right) + \beta_4\left(\overline{S}_{ik}^{'}\overline{\Omega}_{kj}^{'} - \overline{\Omega}_{ik}^{'}\overline{S}_{kj}^{'}\right) \\
&+\beta_6\left(\overline{S}_{ik}^{'}\overline{\Omega}_{kl}^{'}\overline{\Omega}_{lj}^{'} + \overline{\Omega}_{ik}^{'}\overline{\Omega}_{kl}^{'}\overline{S}_{lj}^{'} - II_\Omega\overline{S}_{ij}^{'} - \frac{2}{3}IV\delta_{ij}\right) \\
&+\beta_9\left(\overline{\Omega}_{ik}^{'}\overline{S}_{kl}^{'}\overline{\Omega}_{lm}^{'}\overline{\Omega}_{mj}^{'} - \overline{\Omega}_{ik}^{'}\overline{\Omega}_{kl}^{'}\overline{S}_{lm}^{'}\overline{\Omega}_{mj}^{'}\right), \\
\overline{\Omega}_{ij}^{'} &= \frac{\tau}{2}\overline{\Omega}_{ij}, \quad \overline{S}_{ij}^{'} = \frac{\tau}{2}\overline{S}_{ij}, \quad II_\Omega = \overline{\Omega}_{kl}^{'}\overline{\Omega}_{lk}^{'}, \quad IV = \overline{S}_{kl}^{'}\overline{\Omega}_{lm}^{'}\overline{\Omega}_{mk}^{'}.
\end{aligned}
\tag{2.32}
$$

Additional details about the model can be found on the Turbulence Modelling Resource of NASA Langley Research Center [2] and the corresponding references.

Quadratic constitutive relations

The quadratic constitutive relation (QCR) was developed by Spalart [122] as an extension to the one-equation Spalart-Allmaras [123, 124] linear eddy viscosity model which better predicts the anisotropy of the Reynolds stresses. The relation considers terms that are quadratic in the mean vorticity and strain tensors. There have been two versions of the quadratic constitutive relation developed by Spalart. The original version - QCR-2000 [122] and a more recent QCR-2013 [82] version. The latter version features an additional term which accounts

for the $\frac{2}{3}\rho k\delta_{ij}$ term in the Boussinesq equation 2.23, since the Spalart-Allmaras model does not provide k. The QCR can also be applied to two-equation eddy viscosity models. In this case, the additional term in the QCR is redundant, since the two-equation eddy viscosity model provides k. An additional QCR stress tensor b_{ij}^{QCR} is added to the existing stress tensor τ_{ij} as follows:

$$\tau_{ij}^{RANS} = 2\mu_t \overline{S}_{ij}^{*} - \frac{2}{3}\rho k\delta_{ij} - b_{ij}^{QCR}, \tag{2.33}$$

where the definition of b_{ij}^{QCR} depends on the QCR version. In the original QCR-2000 [122] version b_{ij}^{QCR} is given by:

$$b_{ij}^{QCR} = C_{cr1}\left(O_{ik}\tau_{jk} + O_{jk}\tau_{ik}\right), \tag{2.34}$$

where $\tau_{ij} = 2\mu_t \overline{S}_{ij}^{*} - \frac{2}{3}\rho k\delta_{ij}$ is the stress tensor given by the Boussinesq approximation, $O_{ij} = 2\Omega_{ij}/\sqrt{\frac{\partial u_m}{\partial x_n}\frac{\partial u_m}{\partial x_n}}$ is the antisymmetric normalised rotation tensor, and $C_{cr1} = 0.3$ is a model coefficient, calibrated in the outer part of an equilibrium boundary layer by requiring a fair level of anisotropy $\overline{u'^2} > \overline{w'^2} > \overline{v'^2}$. Another QCR version, developed by Sabnis [113], was also considered. This QCR version differs from the QCR-2000 [122] version by the addition of one additional term, quadratic in the strain tensor, and is given by:

$$\begin{aligned} b_{ij}^{QCR} = {} & \frac{4C_{cr1}\mu_t}{\sqrt{\overline{S}_{kl}\overline{S}_{kl} + \overline{\Omega}_{kl}\overline{\Omega}_{kl}}}\left(\overline{\Omega}_{ik}\overline{S}_{kj}^{*} - \overline{S}_{ik}^{*}\overline{\Omega}_{kj}\right) \\ & + \frac{4\tilde{C}_{cr3}\mu_t}{\sqrt{\overline{S}_{kl}\overline{S}_{kl} + \overline{\Omega}_{kl}\overline{\Omega}_{kl}}}\left(\overline{S}_{ik}^{*}\overline{S}_{kj}^{*} - \frac{1}{3}\overline{S}_{kl}^{*}\overline{S}_{kl}^{*}\delta_{ij}\right), \\ \overline{\Omega}_{ij} = {} & \frac{1}{2}\left(\frac{\partial \overline{u}_i}{\partial x_j} - \frac{\partial \overline{u}_j}{\partial x_i}\right), \end{aligned} \tag{2.35}$$

where $C_{cr1} = 0.7$ and $\tilde{C}_{cr3} = 0.8$ are model coefficients. Channel, boundary layer, and pipe flows at moderate Reynolds numbers were used to calibrate the model coefficients. The QCR-2000 version by Spalart [122] and the QCR by Sabnis [113] are referred to as QCR V1 and QCR V2 in this section. Additional details about the QCR by Spalart [122] can be found on the Turbulence Modelling Resource of NASA Langley Research Center [2] and the corresponding references.

2.3.4 Hybrid RANS/LES methods

The structural similarity between the LES and RANS equations suggest the concept of unified modelling. This approach is based on using the same transport equations for some resolved quantity. The transition from RANS to LES is controlled by a specific criterion. Several types of RANS/LES methods have been developed over the years including:

- Unsteady statistical methods - URANS, SAS methods.
- Global hybrid RANS/LES methods - based on a single set of governing equations. RANS mode is used near the wall and LES mode away from the wall (where the grid is sufficiently fine for LES), VLES, LNS, Explicit blending of RANS and LES, DES methods.
- Zonal hybrid RANS/LES methods - pure LES mode is used in some pre-defined regions of the domain and pure RANS mode in the remaining regions, segregated and interfacing methods.

Very Large Eddy Simulation (VLES)

The Very Large Eddy Simulation (VLES) method was presented by Speziale [126]. The subgrid-scale stresses are obtained by reducing (damping) the Reynolds stresses in regions where the grid spacing Δ approaches the Kolmogorov length scale $\eta = (\nu^3/\varepsilon)^{1/4}$:

$$\tau_{ij}^{LES} = \alpha \tau_{ij}^{RANS}, \tag{2.36}$$

where

$$\alpha = \left[1 - exp\left(-\frac{\beta\Delta}{\eta}\right)\right]^n, \tag{2.37}$$

where α is the damping parameter, β and n are some modelling (unspecified) parameters and Δ some representative grid spacing. As the limit $\frac{\Delta}{\eta} \to 0$ are relevant scales are resolved i.e. the subgrid scales vanish completely (e.g. $\tau_{ij}^{LES} = 0$) leading to DNS. The regular RANS behaviour is recovered (e.g. $\tau_{ij}^{LES} = \tau_{ij}^{RANS}$ at the other limit as $\frac{\Delta}{\eta} \to \infty$ as the mesh becomes coarse or the Reynolds number becomes extremely large. Properly reaching both the DNS and RANS limits does not guarantee that the corresponding approach provides correct LES mode. Since the original function proposed by Speziale compares the grid spacing with the

Kolmogorov scale, it reduces the RANS stresses significantly only in regions where the grid resolution approaches the one required for DNS.

Limited Numerical Scales (LNS)

A variant of VLES, LNS (Limited Numerical Scales) has been introduced by Batten [13] as a means of closure for Speziale's approach [126]. The LNS achieves this goal by redefining Speziale's damping parameter α with the following ratio of effective viscosity norms:

$$\alpha = \frac{min\left[(\mathscr{L}\mathscr{U})_{LES}, (\mathscr{L}\mathscr{U})_{RANS}\right]}{(\mathscr{L}\mathscr{U})_{RANS}}, \tag{2.38}$$

where $(\mathscr{L}\mathscr{U})_{LES}$ is the length scale/velocity scale product of an LES subgrid-scale model, and $(\mathscr{L}\mathscr{U})_{RANS}$ is the corresponding product for the given RANS model. No additional closure coefficients are required. In the case where consistent models are assumed for both LES and RANS stress tensors, the damping parameter selects the shear stress of minimum magnitude. When fine grids regions are encountered by the LNS method, due to the scaling of the predicted Reynolds stress tensor by α, the eddy viscosity is instantaneously decreased to the levels implied by the underlying subgrid model. Any RANS turbulence model can be combined with any pre-existing SGS model. As an example, assuming a linear Boussinesq closure, the definition above implies that the eddy viscosity simply gets multiplied by α:

$$\mu_t = \alpha \mu_t^{RANS} \quad 0 \leq \alpha \leq 1, \tag{2.39}$$

$$\alpha = min\left\{\frac{\mu_t^{LES}}{\mu_t^{RANS} + \varepsilon}, 1\right\}, \tag{2.40}$$

where $\varepsilon = 10^{-20}$ to allow $\alpha \to 0$ without singularities in low Reynolds number regions. Note that the LNS formulation contains no additional (empirical) constants beyond those appearing in the baseline RANS and LES models.

Detached Eddy Simulation (DES)

The Detached Eddy Simulation (DES) method in its original formulation (DES97) was developed by Spalart *et al.* [124]. DES97 is based on the Spalart-Allmaras (SA) one-equation turbulence model by Spalart *et al.* [124] and switches from RANS mode in the near-wall

region to LES mode away from the surface depending on the subgrid length scale Δ and the distance to the wall d_w. To achieve the switch, the destruction term in the transport equation for the turbulent viscosity is modified by introducing a modified distance $\tilde{d}$:

$$\tilde{d} = min\left(d_w, C_{DES}\Delta\right),\ \Delta = max\left(\Delta x, \Delta y, \Delta z\right), \tag{2.41}$$

where d_w is the distance to the nearest wall, Δx, Δy, and Δz is the grid spacing in the x-y- and z-directions and C_{DES} is a coefficient set to 0.65 (calibrated from decaying homogeneous turbulence). Close to the wall where $\Delta_x \approx \Delta_y >> \Delta_z$ and $\tilde{d} = d_w$ the model reduces to the SA RANS model. Away from the wall where $d_w >> \Delta$ and $\tilde{d} = C_{DES}\Delta$ the model acts as a subgrid-scale model. A similar approach can be used to create DES formulations of existing two-equation turbulence models. However, unlike the one-equation SA model which contains the length-scale d_w only in the destruction term of the k equation, two-equation models contain the length-scale ($l^{RANS} = f(k, \omega, C)$) implicitly or explicitly in a number of terms in both transport equations. A common approach is to modify only the length scale in the k equation destruction term (as in the SA model). This modification is not chosen arbitrarily as it meets the requirement of a derivable Smagorinsky-like form for the eddy viscosity ($\mu_t \sim \rho C|S_{ij}|\Delta^2$). The DES formulation of Menter's $k-\omega$ SST turbulence model reads:

$$\begin{aligned} D_k &= \beta^* \rho\, \omega k F_{DES}, \\ F_{DES} &= max\left(\frac{l_{RANS}}{l_{LES}}, 1\right), \\ l_{LES} &= C_{DES}\Delta, \\ l_{RANS} &= \frac{\sqrt{k}}{\beta^* \omega}, \\ \Delta &= max(\Delta x, \Delta y, \Delta z), \end{aligned} \tag{2.42}$$

where F_{DES} is a function of the RANS and LES length-scales. If $l_{RANS} > l_{LES}$ then F_{DES} will increase the destruction of k and allow the solution to go unsteady. There is however a problem with the original DES formulation when it comes to near-wall regions. Since the grid is generally fine close to walls, it could happen that the solution is triggered to go unsteady there. This is generally an unwanted result, since near-wall turbulent structures are very small and require a very fine grid to be resolved properly with LES. These requirements might not be satisfied by the mesh and hence a poorly resolved LES simulation close to the walls might

be the result. To mitigate this problem, a Delayed Detached Eddy Simulation (DDES) was proposed by Spalart [122]. A a modified F_{DES} function (called F_{DDES}) is introduced in the k equation destruction term:

$$\begin{aligned} D_k &= \beta^* \rho \omega k F_{DDES}, \\ F_{DDES} &= max(\frac{l_{RANS}}{l_{LES}}(1-F_S), 1), \end{aligned} \tag{2.43}$$

where F_S is a shielding function. For the DDES formulation of Menter's $k-\omega$ SST model the F_1 or F_2 function is selected as the shielding function. Since F_1 and F_2 become 1 in the boundary layer, the shielding function also becomes 1, setting the F_{DDES} term to 1. The model coefficient C_{DES} is obtained from:

$$\begin{aligned} C_{DES1} &= 0.78,\ C_{DES2} = 0.61, \\ C_{DES} &= F_1 C_{DES1} + (1-F_1) C_{DES2}. \end{aligned} \tag{2.44}$$

Scale Adaptive Simulation (SAS)

The DES method relies on the comparison of the turbulent length scale computed from the turbulence model and the local grid spacing. The decrease of the eddy viscosity, which allows the switch to LES mode, is controlled entirely by the destruction term D_k. Menter [85] showed that a destruction term can be formulated without the explicit grid dependency in his KE1E model. The destruction term was based on the von Kármán length scale which acts as an integral length scale in boundary layer regions. For a simple boundary layer, the von Kármán length scale l_{vK} reads:

$$\begin{aligned} D &= c_2 \left(\frac{\nu_t}{l_{vK}} \right)^2, \\ l_{vk} &= \kappa \left| \frac{\frac{\partial \bar{u}}{\partial y}}{\frac{\partial^2 \bar{u}}{\partial y^2}} \right|, \end{aligned} \tag{2.45}$$

where u is the velocity parallel to the wall and y is the wall-normal coordinate. For general multi-dimensional calculations, the model includes modifications to avoid the singularity for the vanishing mean strain-rate Menter *et al.* [89] used the following invariant formulation of the von Kármán length scale

$$l_{vK} = \kappa \sqrt{\frac{\frac{\partial \bar{u}_i}{\partial y_j}\frac{\partial \bar{u}_i}{\partial y_j}}{\frac{\partial^2 \bar{u}_l}{\partial y_m^2}\frac{\partial^2 \bar{u}_l}{\partial y_m^2}}}, \kappa = 0.41, \tag{2.46}$$

and proposed the following modification to the KE1E model:

$$\begin{aligned} \tilde{l_{vK}} &= max(l_{vK}, C_{SAS}\tilde{\Delta}), \\ \tilde{\Delta} &= max(\Delta x, \Delta y, \Delta z), C_{SAS} = 0.6. \end{aligned} \tag{2.47}$$

It was found that l_{vK} introduced a dynamic behaviour into the KE1E model. Menter and Egorov [87,88] used the same approach to introduce a dynamic behaviour into the $k-\omega$ SST model. An additional destruction term ρQ_{SAS} is added to the equation for the specific dissipation rate of the $k-\omega$ SST model.

$$Q_{SAS} = max\left[\zeta_2 \kappa S^2 \left(\frac{l_{RANS}}{\tilde{l_{vK}}}\right)^2 - C\frac{2k}{\sigma_\Phi} max\left(\frac{|\frac{\partial \omega}{\partial x_i}|^2}{\omega^2}, \frac{|\frac{\partial k}{\partial x_i}|^2}{k^2}\right), 0\right], \tag{2.48}$$

where

$$\begin{aligned} \zeta_2 &= 3.51, \\ \sigma_\Phi &= 2/3, \\ C &= 2, \\ \kappa &= 0.41, \\ l_{RANS} &= C_\mu^{1/4}\frac{\sqrt{k}}{\omega}, \\ \tilde{l_{vK}} &= max\left(\frac{\kappa S}{|\nabla^2 u|}, 0.26\,(\Delta x \Delta y \Delta z)^{1/3}\right), \\ S &= \sqrt{2 S_{ij} S_{ij}}. \end{aligned} \tag{2.49}$$

When $Q_{SAS} = 0$ the resulting model mode is RANS (e.g. in attached boundary layers). When $Q_{SAS} > 0$ the model switches to scale-resolving mode.

2.4 Grid generation techniques

Multi-block structured grids were used in this work as they offer improved convergence (grid lines are aligned with the predominant flow direction) and require less memory. Unlike unstructured grids, multi-block structured grids, as the name suggests, consist of multiple blocks that divide the computational domain into simple sub-domains. For complex geometries, the division of the computational domain into sub-domains can be challenging. The orientation, size, and the ordering of the blocks is referred to as the grid topology. Depending on the computations considered in this work fully matched or overset grids were used. A brief outline of the two methods is given below. All block-structured grids were generated using the ANSYS ICEM-Hexa [1] grid generation software.

2.4.1 Fully matched grids

Fully matched grids, as the name suggests, are grids where the entire domain is represented by a single multi-block structured grid. If the geometry is complex, the generation of a fully-matched grid can be challenging. In such cases, the overset method can be used to simplify the grid topology. Figures 2.1 and 2.2 show fully matched grids of a fore-body with an intake and a duct with a bump.

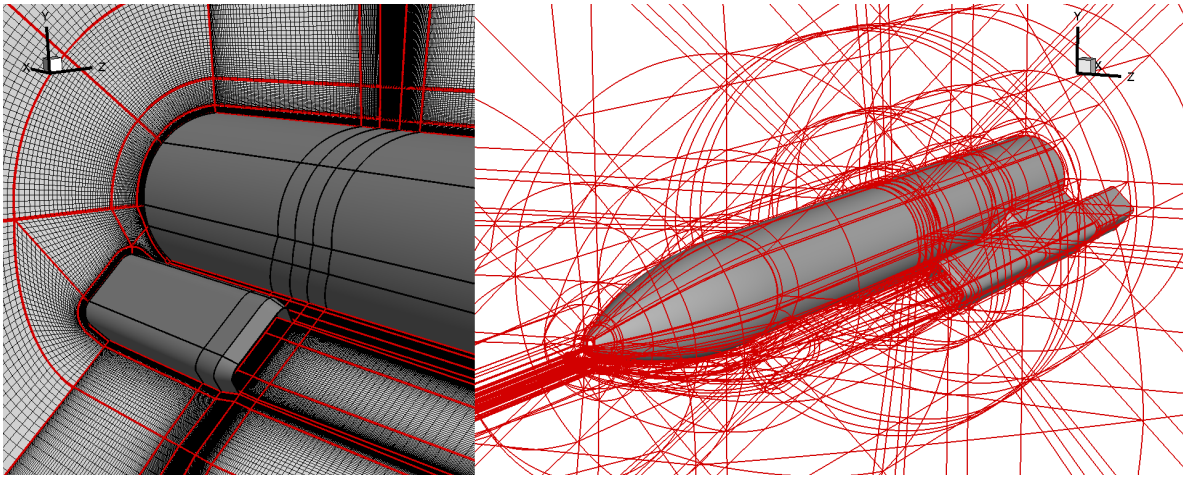

Figure 2.1: Fully matched grid topology of a fore-body intake geometry

The first grid employs O-topology whereas the latter grid uses an H-topology.

2.4.2 Overset grids

The overset method allows computation on grids which consist of independently generated, overlapping, non-matching grids. The grids are sorted hierarchically with higher grid levels

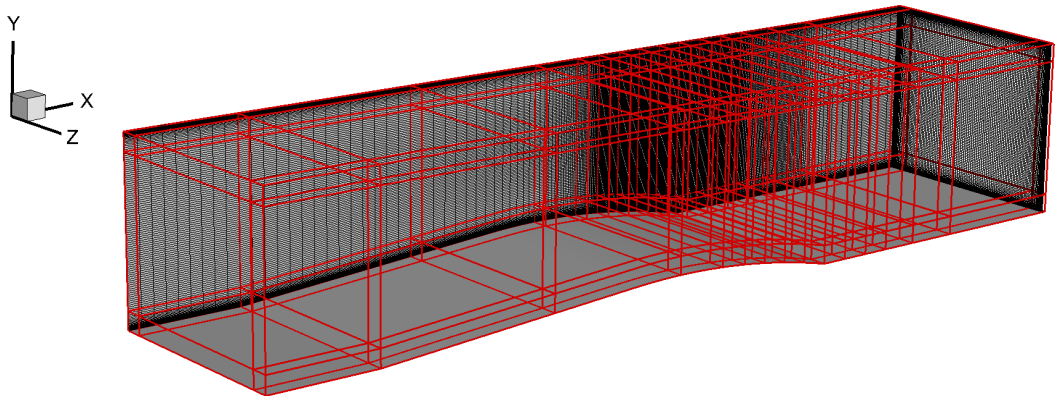

Figure 2.2: Fully matched grid topology of a duct with a bump

having higher priority. The exchange of information between the grids is performed by interpolation considering the level priority of the grids. Figure 2.3 shows an overset grid of a generic store.

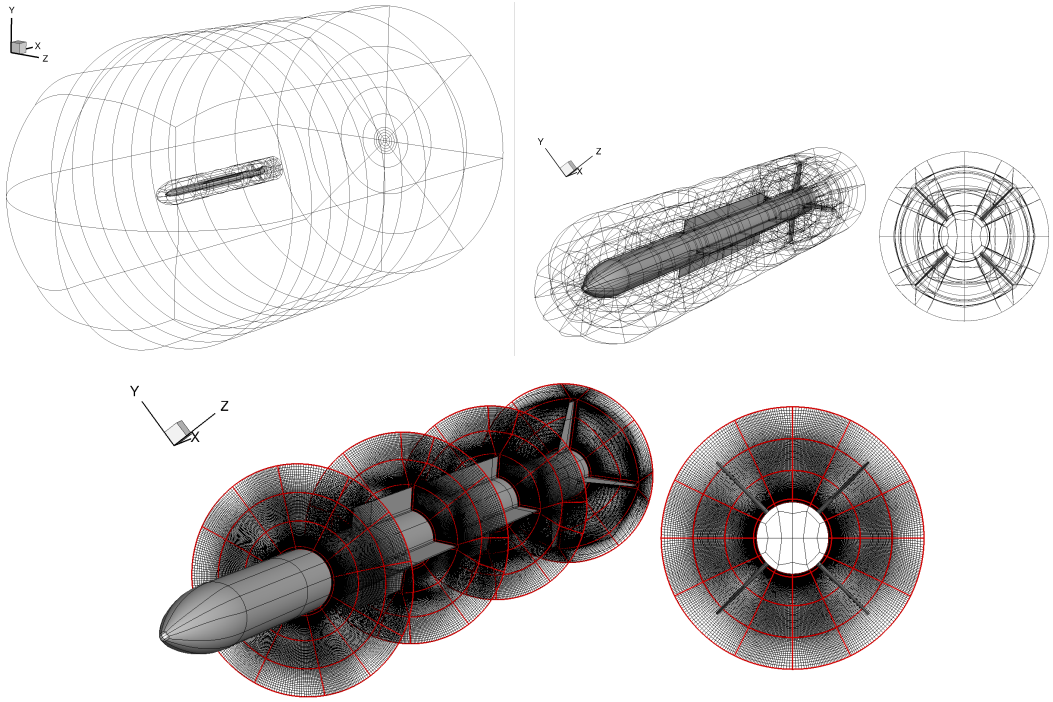

Figure 2.3: Overset grid topology of a store geometry (left); detailed view of the store grid topology (right); grid slices (bottom)

The overset grid consists of two independently generated grids (two levels). The background (or far-field) grid (level 0) represents the entire computational domain and the store grid (level 1) represents a portion of the computational domain around the store. When using an overset grid, a cell search is carried out to identify which cells do not need interpolation as they

overlap with cells belonging to a higher-level grid or with a solid and which cells do need interpolation. A range-tree algorithm is used for the search. The interpolation weights are also calculated during the search. Zero-order, least squares, and inverse distance weighting are the available interpolation methods. No additional treatment is implemented to ensure conservation during the interpolation. More information about the method and its implementation in the HMB3 flow solver can be found in Jarwowsky *et al.* [75]. The details of the grids used in the thesis are documented in the respective chapters.

2.5 Summary of HMB development

Modifications to the HMB flow solver were performed as part of the work presented in this thesis. The modifications include but are not limited to improving and validating existing turbulence models as well as the addition of new turbulence models. The list below outlines the modifications:

- Verification and validation of the implemented k-ω EARSM turbulence model
- Verification and validation of the implemented k-ω SST turbulence model
- Addition of different quadratic constitutive relations to the family of k-ω turbulence models in HMB3, including the $k-\omega$, k-ω, BSL, and k-ω SST turbulence models
- Implementation of a synthetic eddy method (SEM) for turbulence generation
- Implementation of a 3D profile generator, used by the synthetic eddy method

Chapter 3

Validation of the CFD methods for SWBLIs *

3.1 Normal shock interactions

Simulations were carried out of the single normal SWBLI experiment by Dèlery [36] to validate the CFD method. In the experiments of Dèlery [36], a rectangular test section with a bump mounted on the lower wall was used to accelerate the flow to a pre-shock Mach number of $M_r = 1.42$. The width of the test section was constant and equal to $W = 120$ mm. The height of the test section upstream of the bump was $H = 100$ mm, and the unit Reynolds number was $Re = 1.4 \times 10^7$ m^{-1}. Wall pressure and boundary layer measurements were performed at several streamwise locations. Figure 3.1 shows a schematic of the experimental setup used by Dèlery [36].

3.1.1 Grids and numerical setup

The numerical domain, shown in figure 3.2 below, was non-dimensionalised with the height of the test section upstream of the bump ($H = 100$ mm). In addition, the domain only considered the test section slightly upstream and downstream of the bump. Multiblock structured grids of the numerical domain were created using an H-topology. Figure 3.2 (bottom) shows the grid blocking topology. The grid was non-dimensionalised using H as the reference dimension. To ensure a y^+ value of 1, the minimum wall distance Δy_{min} was set to $10^{-5}H$. Grids stretching was employed away from the wall using a hyperbolic distribution. Table 3.1

*The shock train results in this chapter are published in K. Boychev *et al.* "Flow physics and sensitivity to RANS modelling assumptions of a multiple shock wave/turbulent boundary layer interaction", Aerospace Science and Technology, Vol. 97, Issue 1, 2019, DOI: https://doi.org/10.1016/j.ast.2019.105640

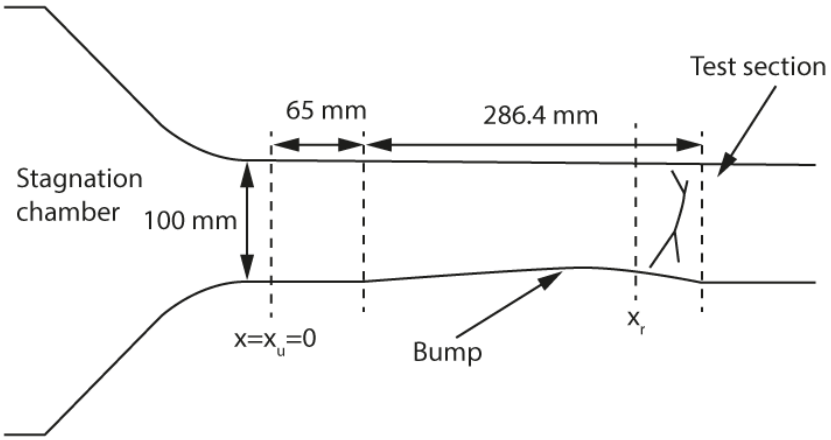

Figure 3.1: Sketch of the experimental setup of the SWBLI experiment by Dèlery [36].

lists the grid parameters. Values in brackets indicate spacing in wall units. The spacings in wall units were calculated using an average y^+ obtained by averaging the y^+ values of all cells adjacent to the wall.

Table 3.1: Grid parameters; dash indicates hyperbolic stretching; values in brackets indicate spacing in wall units obtained using an average y^+ of 0.732.

Grid	min $\Delta x/H$	$\Delta y/H$	$\Delta z/H$	Points	Cells
Coarse	0.005 (370)	10^{-5}-0.02-10^{-5}	10^{-5}-0.02-10^{-5}	4.55×10^6	4.13×10^6
Fine	0.005 (370)	10^{-5}-0.01-10^{-5}	10^{-5}-0.01-10^{-5}	13.57×10^6	12.62×10^6

Numerical simulations were performed investigating the effect of turbulence modelling and method (statistical or scale-resolving) on the upper and lower wall pressure. The outlet pressure ratio was set to $\eta = 0.8153$ and the inlet Mach number to $M_u = 0.6$. The inlet Mach number was obtained from the experimental pressure ratio at that location ($p/p_0 \approx 0.7793$) and the stagnation pressure ($p_0 \approx 95000$ Pa) using isentropic relations. The Reynolds number was set to $Re_H = 1.4 \times 10^6$ and was based on the height of the test section, upstream of the bump ($H = 100$ mm). The steady simulations were performed at a CFL of 2 until the flux residuals were reduced to 10^{-5}. The unsteady simulations used a non-dimensional time step of $\frac{\Delta t}{H/V_u} = 10^{-3}$ which based on the height of the test section translates to a dimensional time step of $\Delta t \approx 5 \times 10^{-7}$ s. A total of 400 unsteady steps were performed. The wall pressure was averaged over the last 100 unsteady steps. The implementation of the synthetic eddy method (SEM), detailed in Appendix A, was tested during the simulations. It was of interest to determine if HMB3 can run the SEM algorithm without any errors. The streamwise grid spacing at the inlet was intentionally made larger to prevent the propagation of the fluctuations from the synthetic eddy method downstream. As expected, the fluctuations did not affect the solution, and the test showed that the HMB3 can run the SEM algorithm without any errors. The

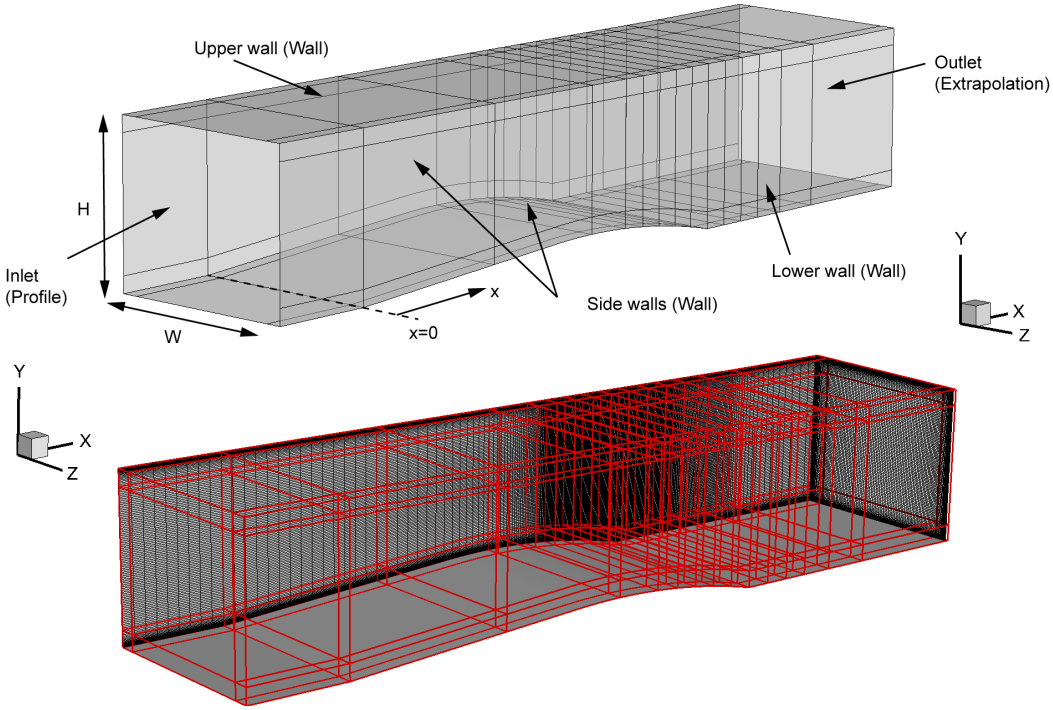

Figure 3.2: Numerical domain and boundary conditions (top); grid blocking topology (bottom).

solution is driven by the unsteadiness at the end of the test section bump. Table 3.2 lists the simulation parameters. As the flow at the inlet is subsonic ($M_u = 0.6$) the RANS simulations were initialised with the flow conditions at the inlet. At the inlet a turbulence intensity of $I_u = 1\%$ and a Mach number of $M_u = 0.6$ were prescribed. This Mach number was selected to match the experimental pressure ratio at the inlet location.

Table 3.2: Simulation parameters.

Grid	η	$\frac{\Delta t}{H/V_u}$	Forcing	Turb. model	Method
Coarse	0.8153	-	No	$k-\omega$ SST	RANS
Coarse	0.8153	-	No	$k-\omega$ SST QCR V1	RANS
Coarse	0.7908	-	No	$k-\omega$ EARSM	RANS
Fine	0.8153	-	No	$k-\omega$ SST	RANS
Fine	0.8153	-	No	$k-\omega$ SST QCR V1	RANS
Fine	0.7908	-	No	$k-\omega$ EARSM	RANS
Fine	0.8153	1×10^{-3}	Yes	$k-\omega$ SST	SAS
Fine	0.8153	1×10^{-3}	Yes	$k-\omega$ SST	LNS
Fine	0.8153	1×10^{-3}	Yes	$k-\omega$ SST	DES
Fine	0.8153	1×10^{-3}	Yes	$k-\omega$ EARSM	LNS

3.1.2 Comparison with experimental data

The effect of grid refinement was investigated first. Figures 3.3 to 3.4 compare the wall pressure on the lower wall between the coarse and fine grids for the different turbulence models considered. For the experimental pressure ratio of $\eta = 0.8153$ the $k-\omega$ SST and $k-\omega$ SST QCR models agreed with the experiment on the location of the shock. However, both models were unable to capture the pressure drop immediately downstream of the shock caused by the separation. The inability to capture the downstream pressure drop is related to the underprediction of the separation at that location.

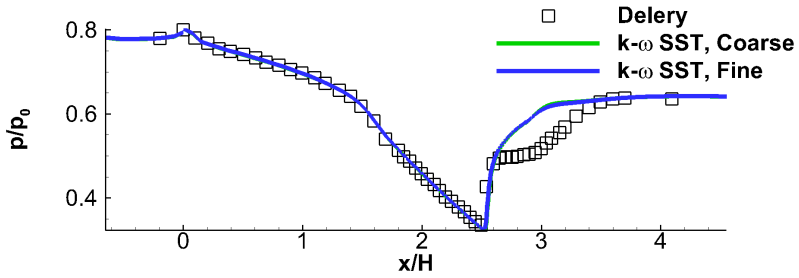

Figure 3.3: Lower wall pressure on the coarse and fine grids with the $k-\omega$ SST model.

For the $k-\omega$ EARSM model, the pressure ratio had to be decreased to $\eta = 0.7908$ in order to match the experimental shock location. Nevertheless, the non-linear model predicted the separation better than the linear models and resulted in a closer agreement with the experiment up to $x/H \approx 3$. Further downstream the wall pressure was underpredicted by the model. Figure 3.5 shows the Mach number contours for the fine grid.

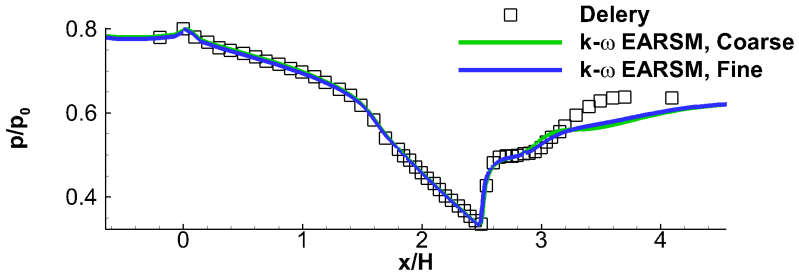

Figure 3.4: Lower wall pressure on the coarse and fine grids with the $k-\omega$ EARSM model.

In addition to the lower wall pressure, boundary layer profiles were extracted at three streamwise locations and compared to the experimental measurements. Experimental boundary layer measurements were performed at the centreline of the lower wall at $x/h = 2.81$, $x/h = 3.02$, and $x/h = 3.44$. The start of the bump on the lower wall marked the $x/H = 0$ location. The streamwise velocity and Reynolds stresses were non-dimensionalised with the speed of

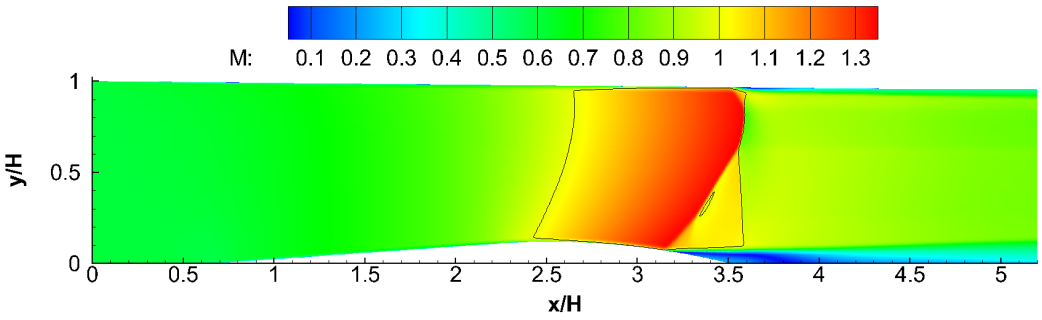

Figure 3.5: Mach number contours on the fine grid with the $k-\omega$ EARSM model.

sound at stagnation conditions $u/a_0 \approx 347.12$ m/s. Figure 3.6 shows the u/a_0 profiles obtained from the coarse grid at the three streamwise locations and compares them with the experimental measurements. The linear models were observed to significantly underpredict the separation at the centreline. Even the addition of QCR terms to the linear $k-\omega$ SST model did not improve the separation predictions. The underprediction of the separation was also reflected by the overprediction of the lower wall pressure.

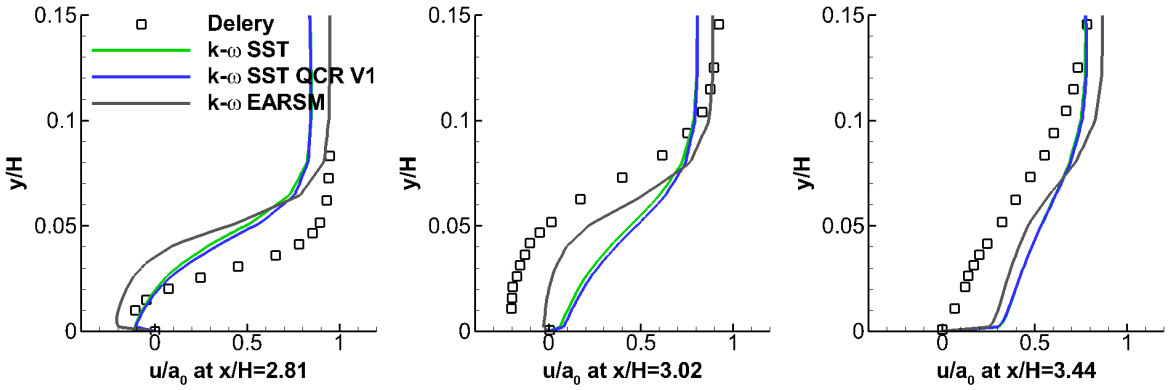

Figure 3.6: Streamwise velocity profiles from the coarse grid at $x/h = 2.81$, $x/h = 3.02$, and $x/h = 3.44$.

The $k-\omega$ EARSM non-linear model improved the wall pressure predictions by capturing the separation sizes at locations $x/h = 3.02$ and $x/h = 3.44$ better. The model overpredicted the separation at location $x/h = 2.81$ but improved the shear stress predictions. Barakos et al. [11] showed that non-linear models result in improved shear stress predictions for the case. Figure 3.7 shows the u/a_0 profiles obtained from the fine grid.

No significant differences between the profiles from the fine grid and coarse grid were observed. As expected, the $k-\omega$ EARSM exhibited greater sensitivity to the grid refinement

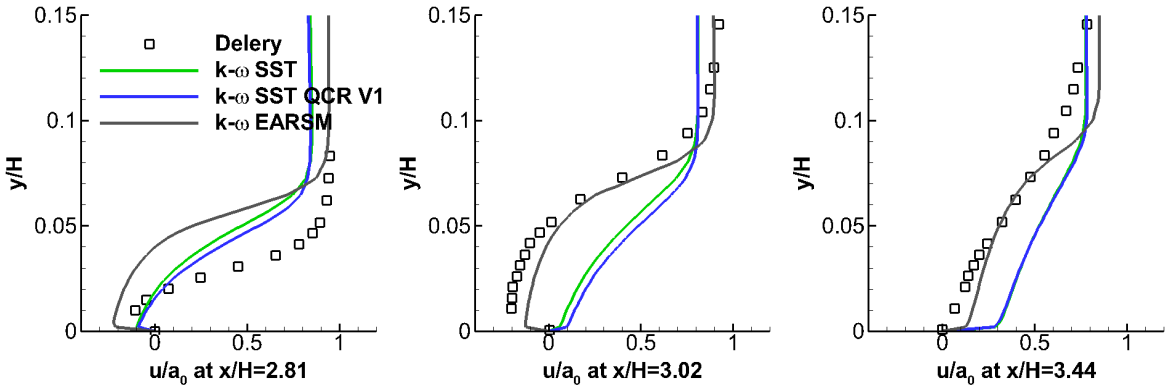

Figure 3.7: Streamwise velocity profiles from the fine grid at $x/h = 2.81$, $x/h = 3.02$, and $x/h = 3.44$.

due to its use of higher-order derivatives. Figure 3.8 shows the shear Reynolds stress $-\overline{u'v'}/a_0^2$. Both the $k-\omega$ SST and $k-\omega$ EARSM models underpredicted the $-\overline{u'v'}/a_0^2$ Reynolds stress, however, the $k-\omega$ EARSM model predicted a distribution which is in a closer agreement with the experiment, downstream of $x/H = 2.81$.

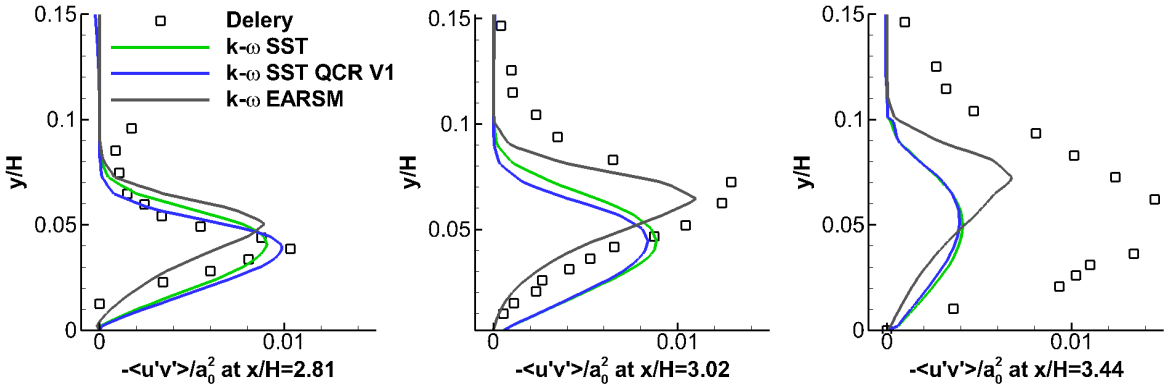

Figure 3.8: Reynolds stress profiles at $x/h = 2.81$, $x/h = 3.02$, and $x/h = 3.44$.

Scale-resolving simulations

Since no significant differences in the wall pressure or the streamwise velocity profiles were observed, the fine grid was selected for further scale-resolving simulations of the experiment. The implemented synthetic eddy method (SEM), outlined in Appendix A, was used to generate turbulence at the inlet. The use of the SEM method for this case was not necessary as the separation at the end of the test-section bump acts as a source of unsteadiness and is sufficient to trigger the scale resolving mode of the methods. Nevertheless, the SEM method was used to be tested. The velocity fluctuations generated by SEM were superimposed onto

the mean profile specified at the inlet. A turbulence intensity of 1% was assumed along with isotropy of the normal Reynolds stresses $\overline{u'u'} : \overline{v'v'} : \overline{w'w'} = 1 : 1 : 1$ resulting in the following non-dimensional Reynolds stress tensor

$$\overline{u_i'u_j'} = \begin{bmatrix} \overline{u'u'} & \overline{u'v'} & \overline{u'w'} \\ & \overline{v'v'} & \overline{v'w'} \\ \text{Symm.} & & \overline{w'w'} \end{bmatrix} = \begin{bmatrix} 1\times10^{-4} & 0 & 0 \\ & 1\times10^{-4} & 0 \\ \text{Symm.} & & 1\times10^{-4} \end{bmatrix} \tag{3.1}$$

Figure 3.9 shows the turbulent kinetic energy scaled by the Reynolds number, kRe_H, at the inlet. The turbulent spots, indicated by the higher values kRe_H, are generated by a collection of isotropic eddies, convected through the inlet plane. At every timestep, each eddy is convected using the streamwise velocity at the inlet. When an eddy reaches a specific downstream distance, usually equal to twice the size of the eddy, it is regenerated at the same distance upstream of the inlet. The decision to use the fine grid for the scale-resolving simulations instead of the coarse grid is further supported by Figures 3.10 and 3.11. Figure 3.10 compares the wall pressure between the two grids which was obtained by averaging 100 unsteady steps. The effect of averaging is also shown in the figure. The fine grid resolves the separation at the end of the bump and the subsequent increase in wall pressure. The agreement with the experiment is satisfactory, however, further adjustment of the back pressure can lead to additional improvements. The coarse grid fails to capture the pressure drop due to the separation. Iso-surfaces of the instantaneous Q-criterion, shown in Figure 3.11, indicate the capability of the fine grid to resolve more turbulent structures. Such structures are absent at the centreline of the coarse grid.

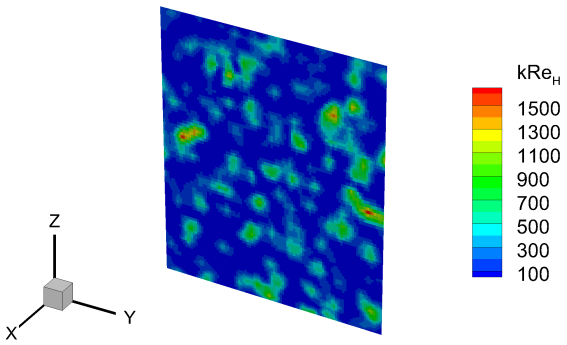

Figure 3.9: Synthetic eddy method at the inlet.

Additional scale-resolving simulations were performed using the scale-adaptive-simulation (SAS) and the limited numerical scales (LNS) approach. Figure 3.12 shows the wall pres-

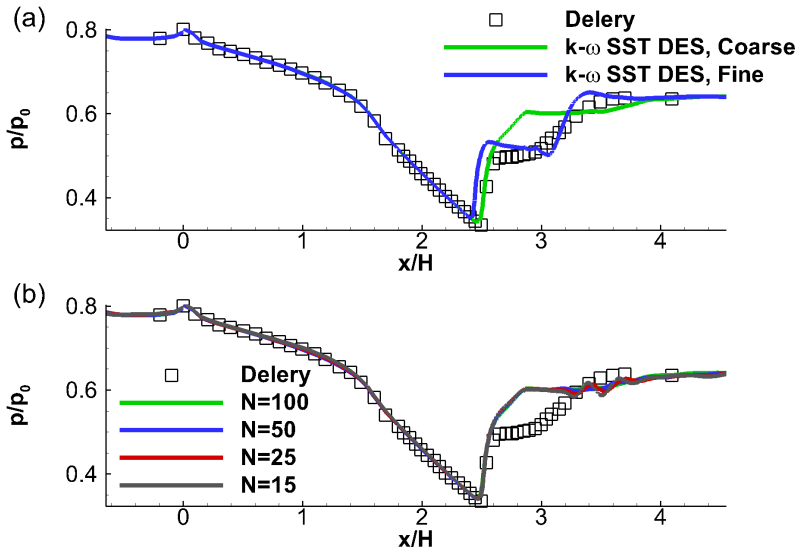

Figure 3.10: Lower wall pressure for the DES simulation performed on the coarse and fine grids (a) and effect of averaging on the coarse grid (b).

sure obtained from the $k-\omega$ SST SAS, and the $k-\omega$ SST LNS, and the $k-\omega$ EARSM LNS models. The SAS method, like the DES, captures the drop in the wall pressure due to the separation and its increase downstream of $x/H \approx 3$. The onset of the interaction is slightly upstream, which suggests that further modifications of the back pressure can lead to additional improvements. Unlike DES, the SAS resolves fewer turbulent structures. However, it resolves turbulent structures in the separated centreline region which leads to improved wall pressure predictions. Due to the relative ease of the implementation of the LNS method, it was of particular interest to see whether it can resolve as many turbulent structures as the DES and the SAS. The LNS method was applied to two turbulence models - the $k-\omega$ SST and the $k-\omega$ EARSM . Unfortunately, neither of the methods resulted in improvements as significant as the ones observed with the DES and SAS methods. Very few turbulent structures were resolved by the $k-\omega$ SST LNS method and turbulent structures were absent at the centreline. As a result, the pressure was significantly overpredicted at the location of the centreline separation.

The $k-\omega$ EARSM LNS method offered slight improvements over the $k-\omega$ SST LNS method, however, the wall pressure was still overpredicted. The non-linear nature of the model resulted in more turbulent structures in the corner regions, downstream of the start of the interaction. Like the $k-\omega$ SST LNS method, no turbulent structures at the centreline were observed.

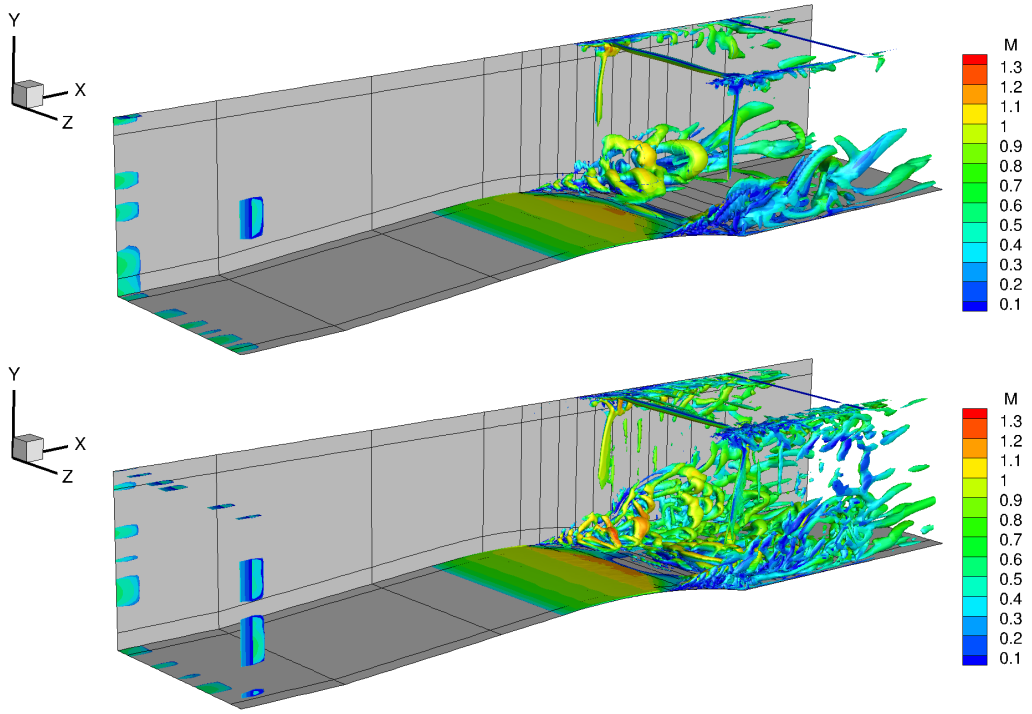

Figure 3.11: Instantaneous Q criterion iso-surfaces $Q = 10$ colored by Mach number for the $k-\omega$ SST DES simulation on the coarse grid (top) and fine grid (bottom).

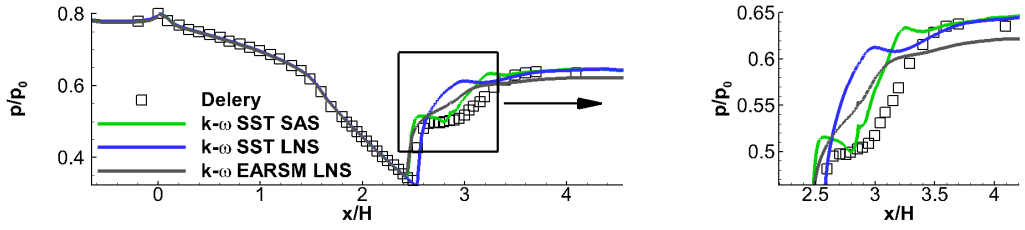

Figure 3.12: Lower wall pressure for the SAS and LNS simulations performed on the fine grid.

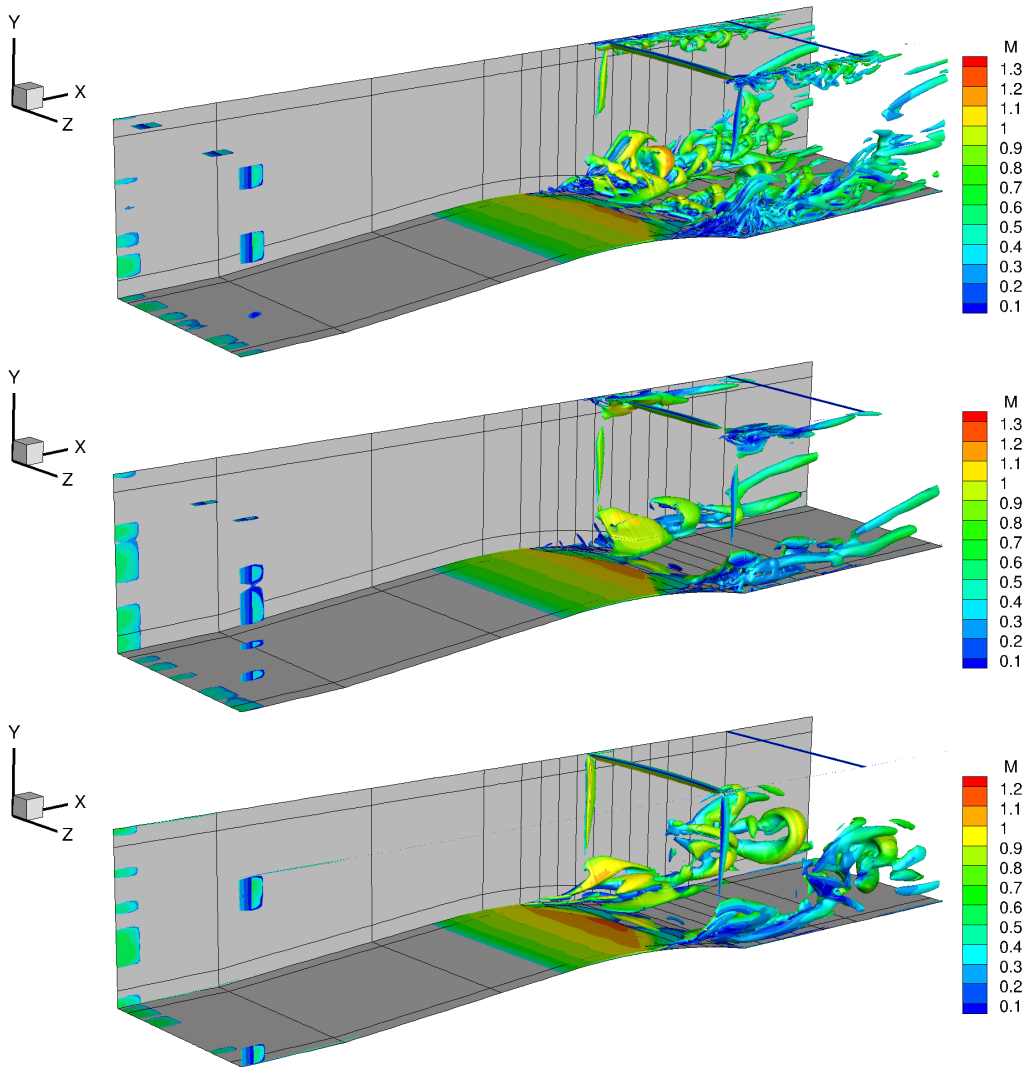

Figure 3.13: Instantaneous Q criterion iso-surfaces $Q = 10$ colored by Mach number for the $k-\omega$ SST SAS (top), the $k-\omega$ SST LNS (middle), and the $k-\omega$ EARSM LNS (bottom) simulations.

To summarise, the $k-\omega$ SST DES and SAS resulted in an improved prediction of the averaged lower pressure as shown in Figures 3.10 and 3.12. The former did not improve the wall pressure predictions on the coarse grid. The $k-\omega$ SST LNS did not result in significant improvement of the averaged wall pressure compared to the $k-\omega$ EARSM simulations. From Figure 3.13 it was observed that the LNS capability to resolve the flow is considerably less than the DES and the SAS. The developed LNS formulation of the $k-\omega$ EARSM model did not result in significant improvements in the averaged wall pressure compared to the $k-\omega$ EARSM simulations. Although the LNS method was relatively simple to implement, it was shown that on similar sized grids it performs worse than the DES and SAS methods.

3.2 Multiple normal shock interactions

After the single normal shock cases, simulations of the multiple normal SWBLI experiment by Carroll *et al.* [24] were performed to validate the CFD method. The MSWBLI experiment by Carroll *et al.* [24] is of the few MSWBLI experiments that contains extensive flowfield measurements apart from wall pressure measurements, making it suitable for validation. In the experiment a 750 mm long rectangular test section was used. The upper and lower walls of the test section had a divergence angle of 0.13 deg. Taking into account the divergence angle, the width, and the height of the test section at $x_r = 264.8$ (the onset of the wall pressure rise) mm are $H = 33.75$ mm and $W = 76.2$ mm. The width of the test section is constant. Laser Doppler Velocimetry (LDV) measurements were performed from $x = 264.8$ mm to $x = 664.8$ mm at variable intervals. Over the length of the LDV measurements the upper and lower walls diverge by 0.91 mm. The unit Reynolds number was $Re = 3 \times 10^7$ m^{-1}. At $x_r = 264.8$, the boundary layer thickness and confinement were $\delta_r = 5.4$ mm and $\delta_r/h = 0.32$ where h is the half-height of the test section at this location ($h = H/2$). Figure 3.14 shows a schematic of the experimental setup used by Carroll [24].

3.2.1 Grids and numerical setup

The numerical domain, shown in figure 3.14, was non-dimensionalised with the half-height of the test section at the inlet ($h = 16.275 = H/2$ mm).

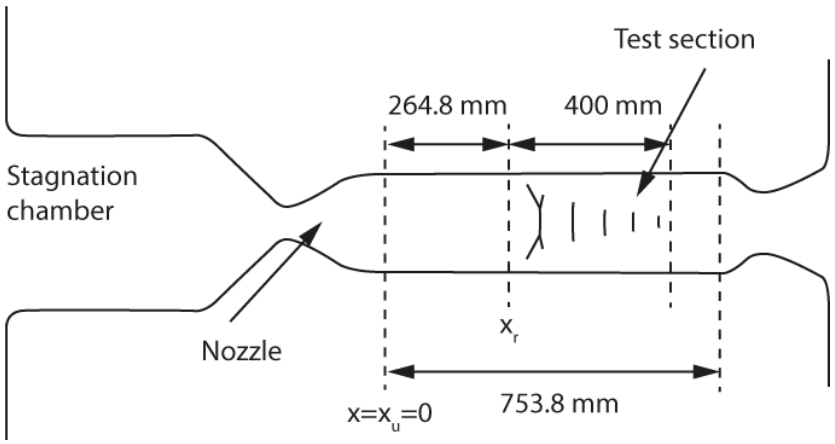

Figure 3.14: Sketch of the experimental setup of the MSWBLI experiment by Carroll [24].

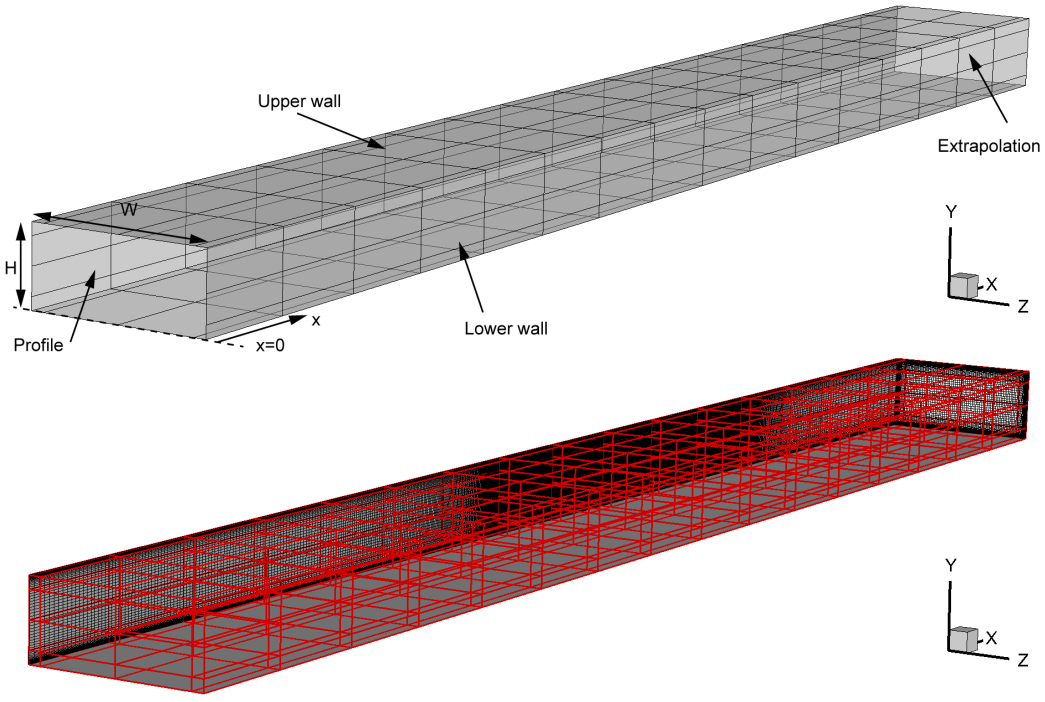

Figure 3.15: Numerical domain and boundary conditions (top); grid blocking topology (bottom).

Two-and-three dimensional multiblock structured grids of the numerical domain were created using an H-topology. Figure 3.15 (bottom) shows the grid blocking topology. The grid was non-dimensionalised using h as the reference dimension. To ensure a y^+ value of 1 the minimum wall distance Δy_{min} was set to $1 \times 10^{-5} h$. Grid stretching was employed away from the wall using a hyperbolic distribution. Tables 3.3 and 3.4 list the two-dimensional and three-dimensional grid parameters. For the two-dimensional simulations the Mach number at the inlet was set to $M_u = 1.64$. Due to the boundary layer developing on the side walls the inlet Mach number of the three-dimensional simulations was set to $M_u = 1.69$. The turbulence intensity and eddy viscosity ratio at the inlet were set to $I_u = 0.01$ (1%) and $\mu_t/\mu = 10$ for each simulation. All simulations used the third-order MUSCL scheme available in HMB3 for spatial reconstruction unless explicitly stated otherwise. Tables 3.5 and 3.6 show the two-and-three dimensional simulation parameters.

Table 3.3: Two-dimensional grid parameters; values in brackets indicate spacing in wall units.

Spacing	Coarse	Medium	Fine
Δx_{min}	0.038 (380)	0.018 (180)	0.008 (80)
Δx_{max}	0.3 (3×10^4)	0.3 (3×10^4)	0.3 (3×10^4)
Δy_{min}	10^{-5} (0.1)	10^{-5} (0.1)	10^{-5} (0.1)
Δy_{max}	0.05 (500)	0.05 (500)	0.05 (500)
Δz_{min}	10^{-5} (0.1)	10^{-5} (0.1)	10^{-5} (0.1)
Δz_{max}	0.05 (500)	0.05 (500)	0.05 (500)
Points	2.16×10^5	3.64×10^5	6.42×10^5

Table 3.4: Three-dimensional grid parameters; values in brackets indicate spacing in wall units.

Spacing	Extra coarse	Coarse	Medium	Fine	Very fine
Δx_{min}	0.048 (480)	0.038 (380)	0.018 (180)	0.018 (180)	0.018 (180)
Δx_{max}	0.3 (3×10^4)	0.3 (3×10^4)	0.3 (3×10^4)	0.3 (3×10^4)	0.3 (3×10^4)
Δy_{min}	10^{-5} (0.1)	10^{-5} (0.1)	10^{-5} (0.1)	10^{-5} (0.05)	10^{-5} (0.05)
Δy_{max}	0.05 (500)	0.05 (500)	0.05 (500)	0.05 (500)	0.03 (300)
Δz_{min}	10^{-5} (0.1)	10^{-5} (0.1)	10^{-5} (0.1)	10^{-5} (0.05)	10^{-5} (0.05)
Δz_{max}	0.05 (500)	0.05 (500)	0.05 (500)	0.05 (500)	0.03 (300)
Points	2.86×10^6	5.31×10^6	8.93×10^6	14.59×10^6	19.12×10^6

Table 3.5: Two-dimensional simulations parameters.

Grid	I_u %	M_u	M_r	δ_r mm	δ_r/h	x_r/h	p/p_u	p/p_r	Turb. model
Coarse	1.0	1.640	1.614	6.36	0.391	26.697	2.4841	2.3773	$k-\omega$ SST
Medium	1.0	1.640	1.614	6.61	0.406	27.523	2.4841	2.3756	$k-\omega$ SST
Fine	1.0	1.640	1.612	6.69	0.411	27.721	2.4841	2.3722	$k-\omega$ SST
Fine	1.0	1.640	1.606	7.83	0.481	32.200	2.4841	2.3460	k-ω
Fine	1.0	1.640	1.610	7.37	0.453	32.922	2.4841	2.3764	$k-\omega$ BSL
Fine	1.0	1.640	1.622	5.06	0.311	26.650	2.4841	2.4094	$k-\omega$ EARSM
Experiment [23]	-	-	1.610	5.40	0.320	0	-	2.2309	-

Table 3.6: Three-dimensional simulations parameters.

Grid	I_u %	M_u	M_r	δ_r mm	δ_r/h	x_r/h	p/p_u	p/p_r	Turb. model
Extra coarse (No symmetry)	1.0	1.69	1.617	5.25	0.323	21.353	2.4776	2.2239	$k-\omega$ SST
Extra coarse	1.0	1.69	1.617	5.25	0.323	21.353	2.4776	2.2239	$k-\omega$ SST
Coarse	1.0	1.69	1.623	5.45	0.335	22.396	2.4776	2.2425	$k-\omega$ SST
Medium	1.0	1.69	1.623	5.38	0.331	22.542	2.4776	2.2459	$k-\omega$ SST
Fine	1.0	1.69	1.624	5.41	0.332	22.729	2.4776	2.2475	$k-\omega$ SST
Medium	1.0	1.69	1.604	7.04	0.432	27.062	2.4776	2.1373	k-ω
Medium	1.0	1.69	1.612	6.46	0.397	27.393	2.4776	2.1634	$k-\omega$ BSL
Medium	1.0	1.69	1.622	5.06	0.311	26.391	2.4776	2.2485	$k-\omega$ EARSM
Experiment [23]	-	-	1.610	5.40	0.320	0	-	2.2309	

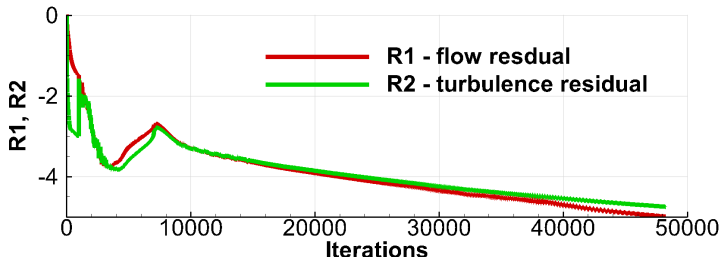

Figure 3.16: Iteration history of the residuals.

The initial solution was obtained from an inviscid normal shock solution with a pre-shock Mach number of M_u. Residuals were reduced to at least 5 orders of magnitude. Figure 3.16 shows an example iteration history of the residuals.

3.2.2 Comparison with experimental data

Two-dimensional calculations

Figure 3.17 shows the wall pressure and the Mach number contours obtained on the three two-dimensional grids. No error bars are shown for the wall pressure as the pressure ratio error was estimated to be $\Delta p/p_r = \pm 0.004$ (measurement uncertanties of ± 0.07 kPa were reported). As the number of grid points in the x-direction was increased the onset of the interaction moved downstream by $\Delta x/h = 1.0238$ (2 % of the length of the simulation domain). Since the three-grids had the same spacing in the y-direction an additional, extra fine, grid with a reduced spacing in the y-direction was considered. No difference in the wall pressure was observed between the fine and the extra fine grids. Slight differences in the Mach number contours were present in the form of shorter supersonic "tongues" and slightly larger Mach stem. These differences did not affect the wall pressure or the centreline Mach number, shown in figure 3.18, both of which suggested that the solution is grid converged. Figure 3.19 shows the skin friction coefficient comparison between the three two-dimensional grids and the experiment. The friction coefficient was identical between the three-grids showing boundary layer separation at $x/h \approx 0.4$ and reattachment at $x/h \approx 1.6$. To further support the solution is grid converged figures 3.20 to 3.24 compare profiles of streamwise velocity, turbulent kinetic energy, and Reynolds stresses between the simulations on the three-grids and the experiment. From figure 3.21 growth of turbulent kinetic energy, k, downstream of the Mach stem is observed. As the $k-\omega$ SST model was used in its simplest formulation, it did not include a limiter for k, therefore the growth of k downstream of the Mach stem was expected (triggered by the strong normal gradients). No significant differences in the Reynolds stress profiles between the medium and fine grids were observed. The $\overline{u'u'}/V_u^2$ Reynolds stress

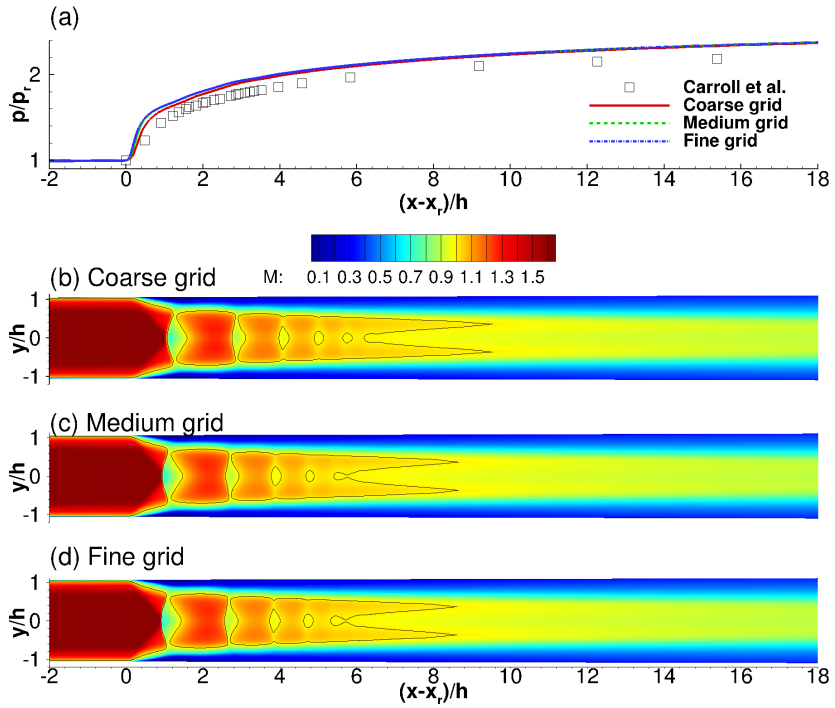

Figure 3.17: Wall pressure (a) and Mach number contours for the coarse (b), medium (c), and fine (d) grids.

was underpredicted throughout the beginning of the interaction whereas the $-\overline{u'v'}/V_u^2$ and $\overline{v'v'}/V_u^2$ components were overpredicted throughout the entire interaction. As a result, the turbulent kinetic energy was also overpredicted. However, the good agreement between the medium and fine grids in the Reynolds stress profiles also suggested that the solution is grid converged.

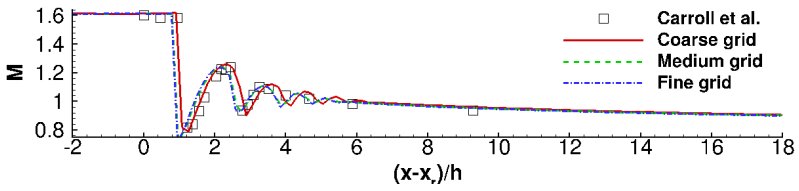

Figure 3.18: Centreline Mach number for the coarse, medium, and fine grids.

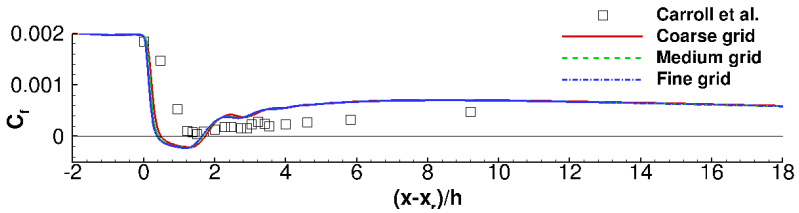

Figure 3.19: Skin friction coefficient for the coarse, medium, and fine grids.

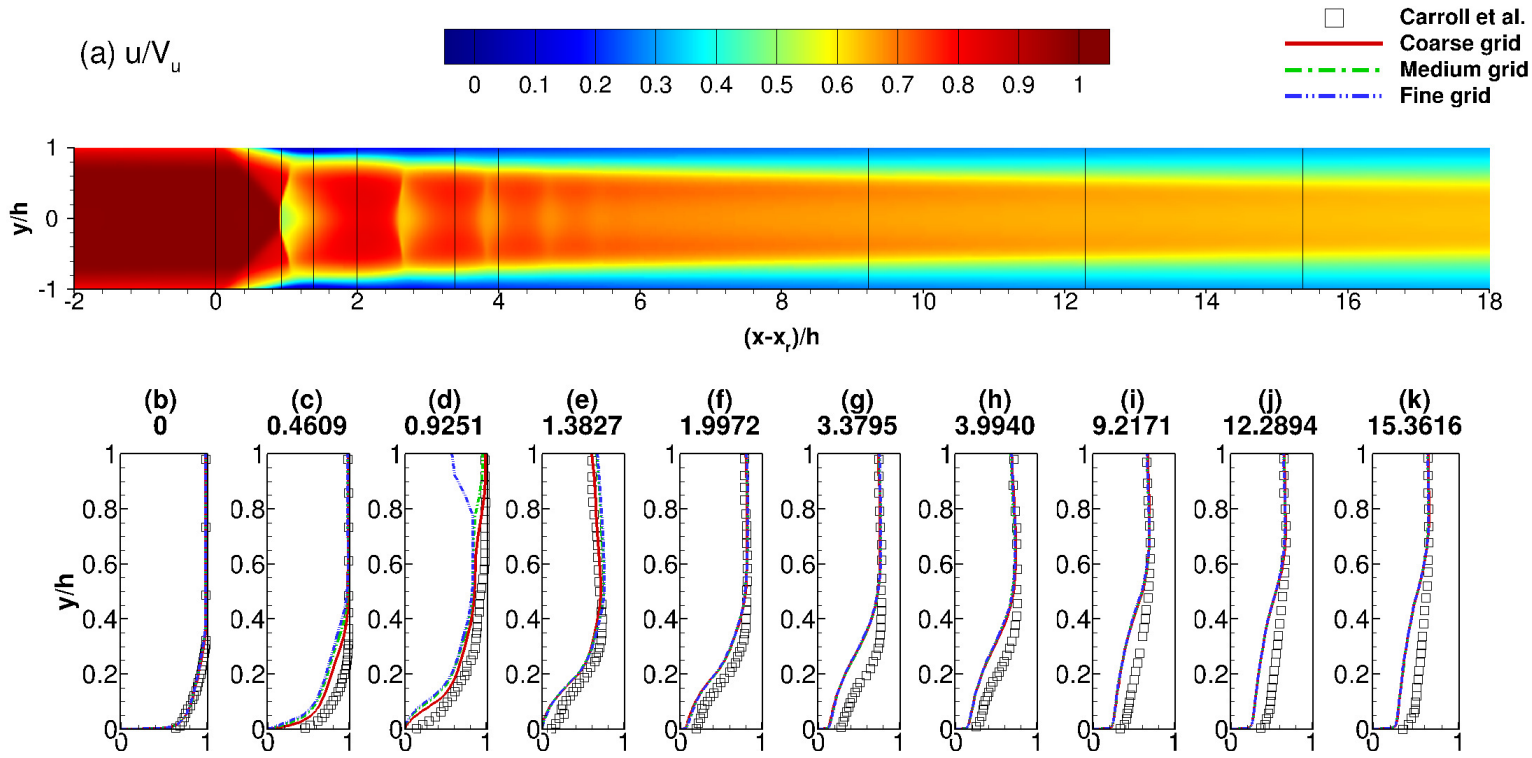

Figure 3.20: Streamwise velocity contours u/V_u for the fine grid (a) and profiles (b-k) for the coarse, medium, and fine grids.

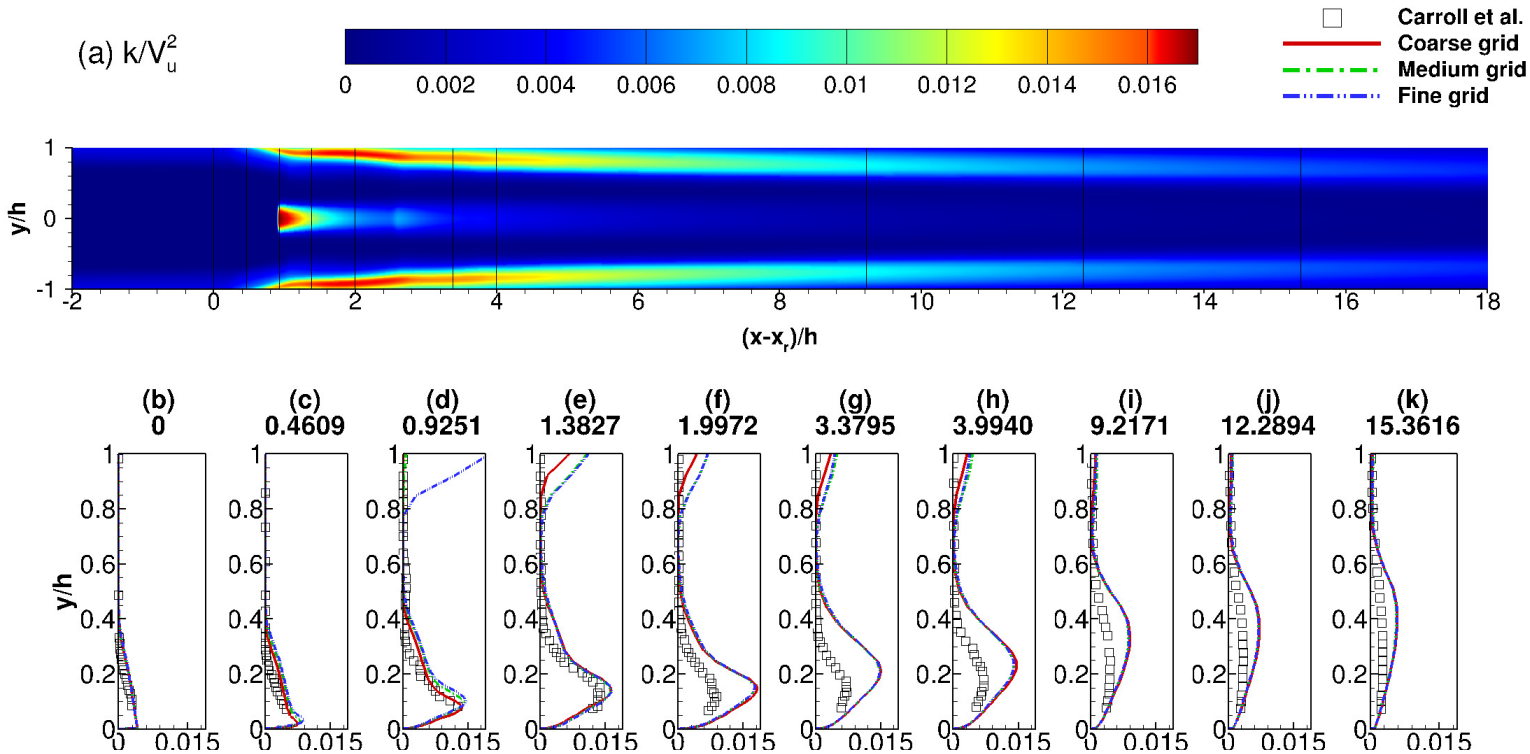

Figure 3.21: Turbulent kinetic energy k/V_u^2 for the fine grid (a) and profiles (b-k) for the coarse, medium, and fine grids.

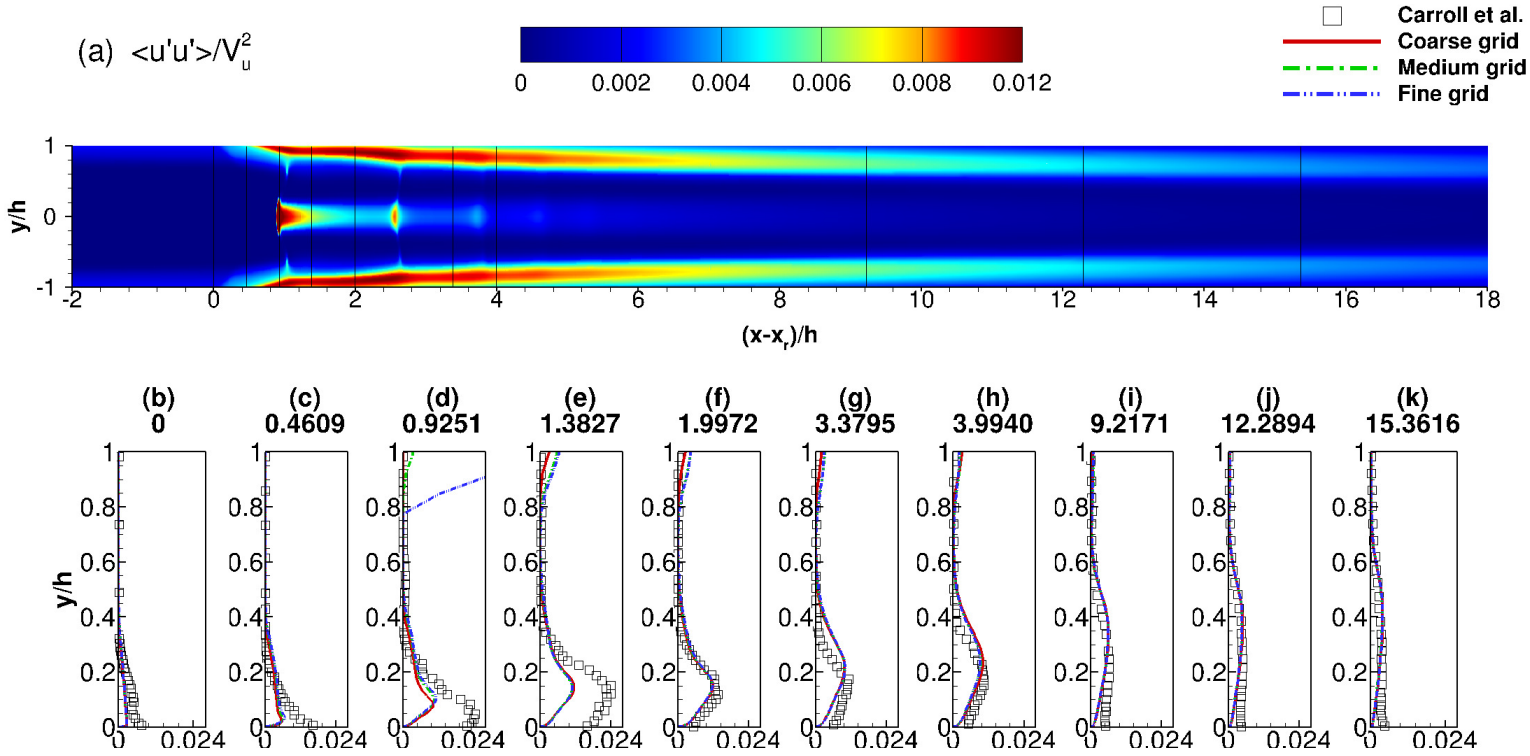

Figure 3.22: Reynolds stress contours $\overline{u'u'}/V_u^2$ for the fine grid (a) and profiles (b-k) for the coarse, medium, and fine grids.

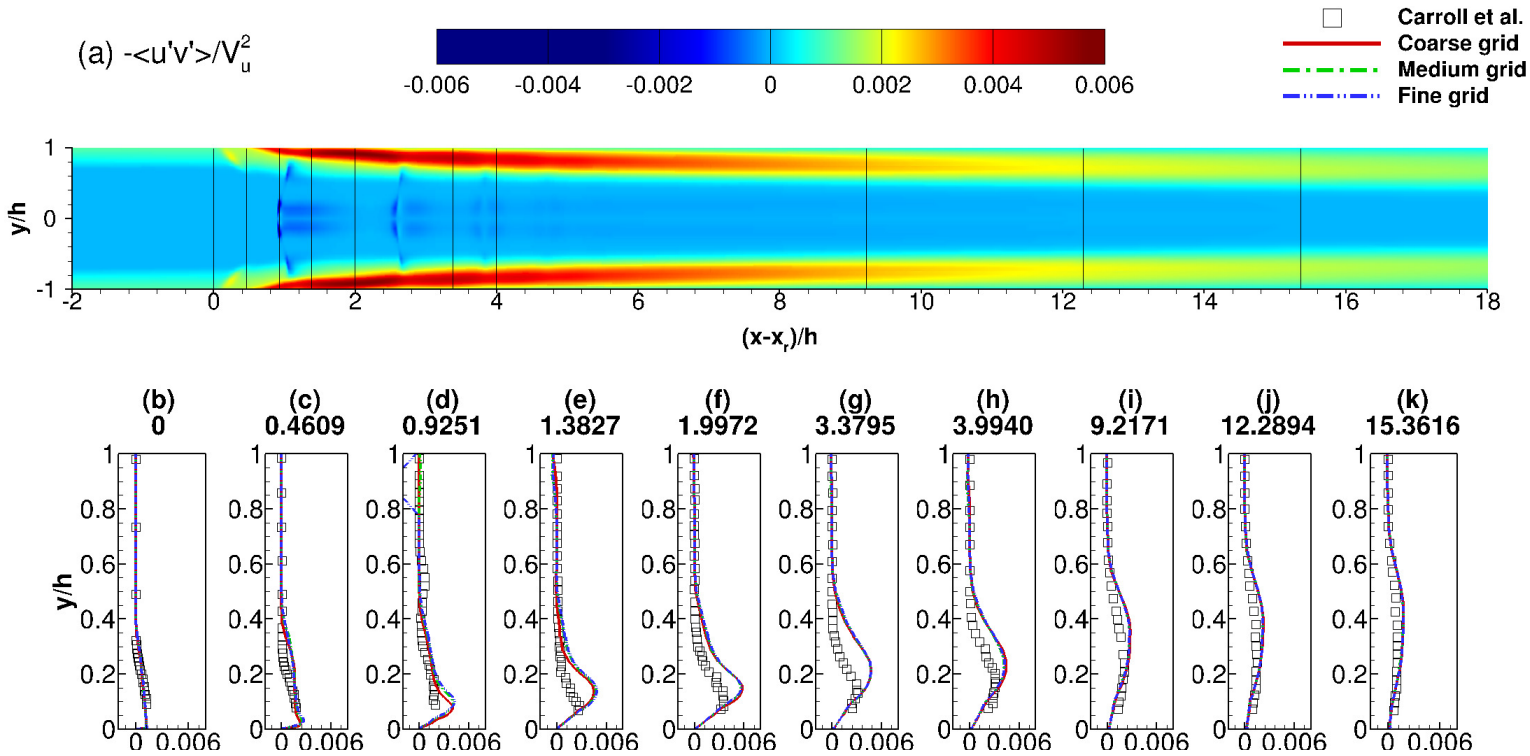

Figure 3.23: Reynolds stress contours $-\overline{u'v'}/V_u^2$ for the fine grid (a) and profiles (b-k) for the coarse, medium, and fine grids.

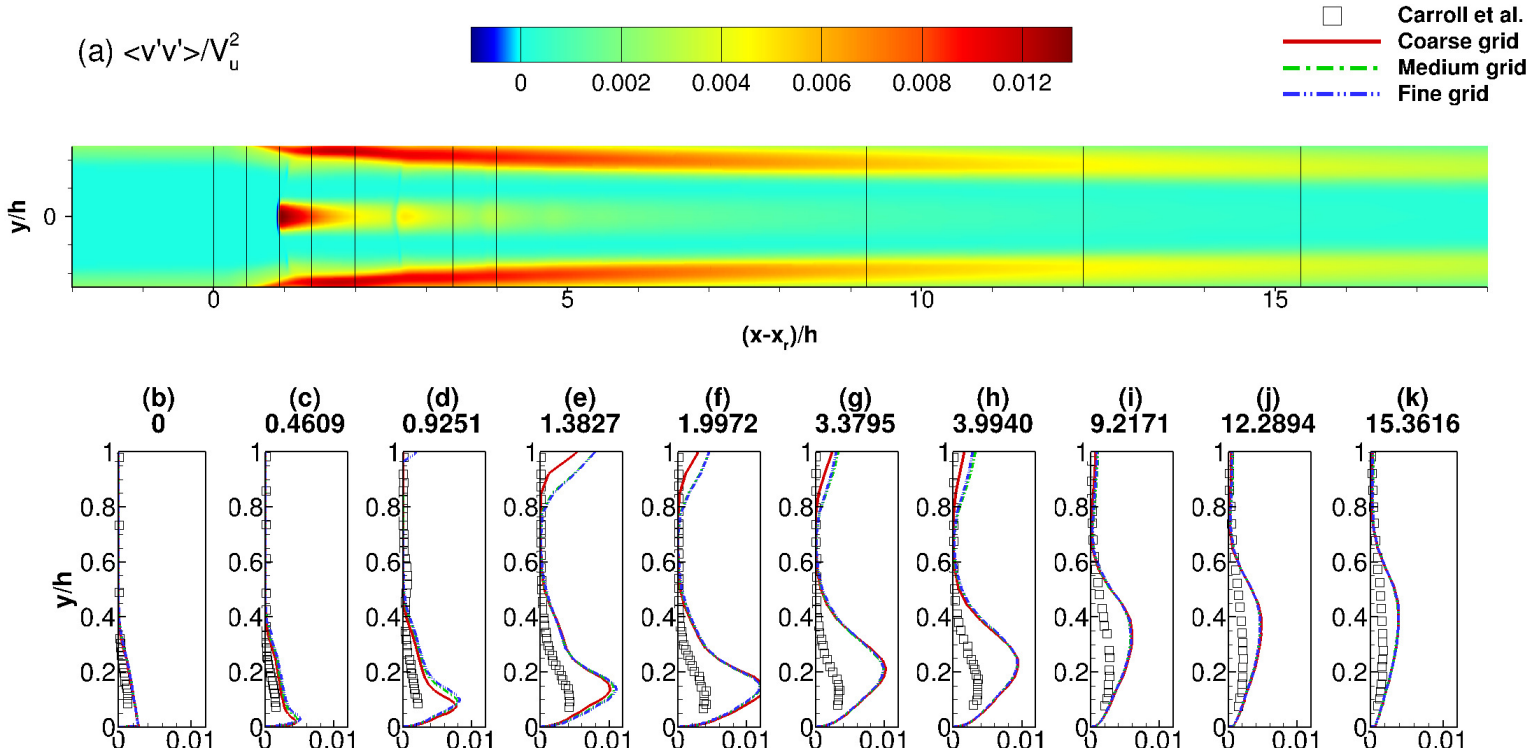

Figure 3.24: Reynolds stress contours $\overline{v'v'}/V_u^2$ for the fine grid (a) and profiles (b-k) for the coarse, medium, and fine grids.

The grid convergence index (GCI) method proposed by Roache [108, 109] was used to investigate the grid convergence. The details of the method are listed in Appendix C along with a Matlab script with an example. The grid convergence index (GCI) was calculated based on the number of grid points N and the onset of the interaction x_r and is listed in table 3.5. Table 3.7 shows the grid sizes and refinement ratios and table 3.8 the calculated order of convergence, the asymptotic solution for x_r, and the grid convergence index reported on the finer grids. The values of x_r are monotonic and the difference Δx_r decreases between the grid refinements. As a result the values of the grid convergence index, indicative of the solution error, also decrease. The values of the GCIs might increase if Δx_r increases between grid refinements. In this case the method is not applicable. When the ratio of the GCIs is close to one the results are in the asymptotic range of convergence, as is the case here. The ratio of GCIs, listed in the last column of table 3.8 is 0.9929. Despite the solution being grid converged the wall pressure at the beginning of the interaction is slightly overpredicted.

Table 3.7: Grid sizes and refinement ratios for the coarse, medium, and fine grids.

Grid	Grid size h	Refinement ratio r	x_r
Fine (1)	1.0000	1.7623	27.7206
Medium (2)	1.7623	1.6793	27.5227
Coarse (3)	2.9594	-	26.6968

Table 3.8: Order of convergence, asymptotic solution and grid convergence index calculated from the coarse, medium, and fine grids.

Order of convergence p	Asymptotic solution for x_r	GCI_{23} %	GCI_{12} %	$r^p GCI_{12}/GCI_{23}$
2.82869	27.7705	1.1254	0.2250	0.9929

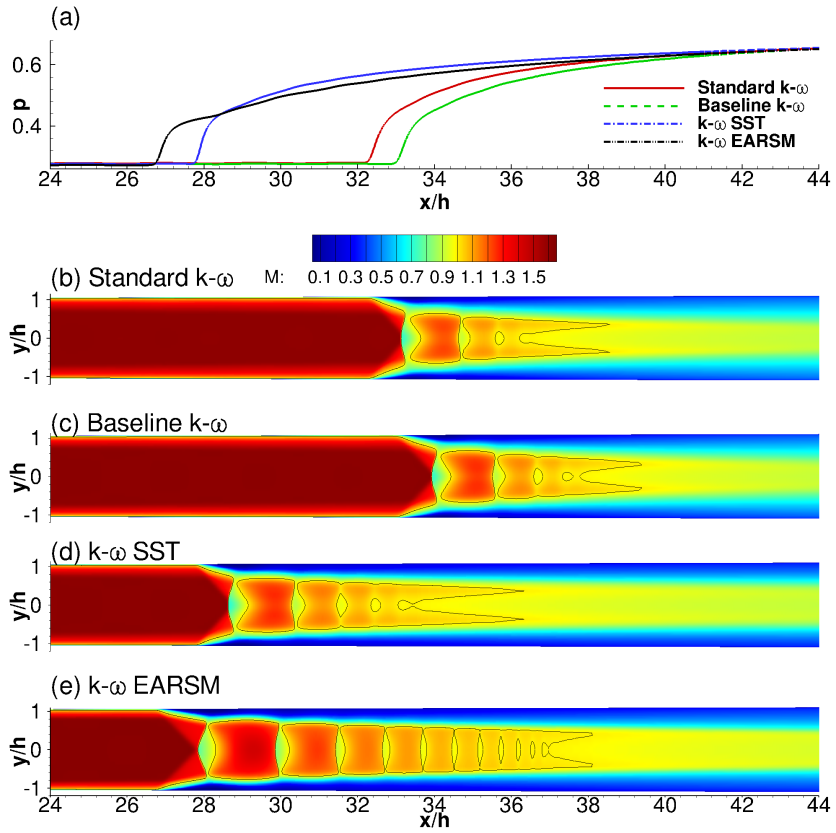

Figure 3.25: Wall pressure (a) and Mach number contours for the k-ω (b), baseline k-ω (c), $k-\omega$ SST (d), and $k-\omega$ EARSM (e) turbulence models on the two-dimensional fine grid.

Following the grid refinement study, a study on turbulence models was performed on the two-dimensional fine grid with the boundary conditions kept fixed. The standard k-ω [86], baseline k-ω [86], and $k-\omega$ EARSM [64,144] turbulence models were used. Figure 3.25 shows the wall pressure and Mach number contours. Substantial variation of the location of the first shock wave is observed depending on the turbulence model used. The $k-\omega$ EARSM model predicted the shock train at the most upstream location whereas the baseline k-ω at the most downstream location. The difference in the location was $\Delta x/h \approx 6.2882$ (13.67 % of the domain length). The shortest shock train was predicted by the k-ω model whereas the longest by the $k-\omega$ EARSM model. Since the length of the shock train is affected by the structure of the frist shock wave it is not unusual that the $k-\omega$ EARSM model predicts the longest shock train as the first shock wave does not have a distinct Mach stem. Differences in the Mach stem height (shock wave structure) are most likely due to overprediction/underprediction of the separation size. For the $k-\omega$ EARSM model the height of the separation (line where $u/V_u = -1\times10^{-3}$) is $y/h = 0.05437$ whereas for the baseline k-ω it is $y/h = 0.01883$.

Three-dimensional calculations

The above two-dimensional simulations do not model the sidewalls of the test section. Since boundary layers develop on the sidewalls as well, two dimensional simulations often fail to take into account the flow confinement resulting from the side walls. For test sections with small aspect ratio the effect of the sidewalls is expected to be substantial. The three-dimensional simulations consider only a quarter of the domain, employing symmetry boundary conditions at the x-y and x-z planes, as simulations of the full and quarter domain showed no differences in the wall pressure. Figure 3.26 shows the wall pressure and Mach number contours obtained with the $k-\omega$ SST turbulence model on the four three-dimensional grids listed in table 3.4.

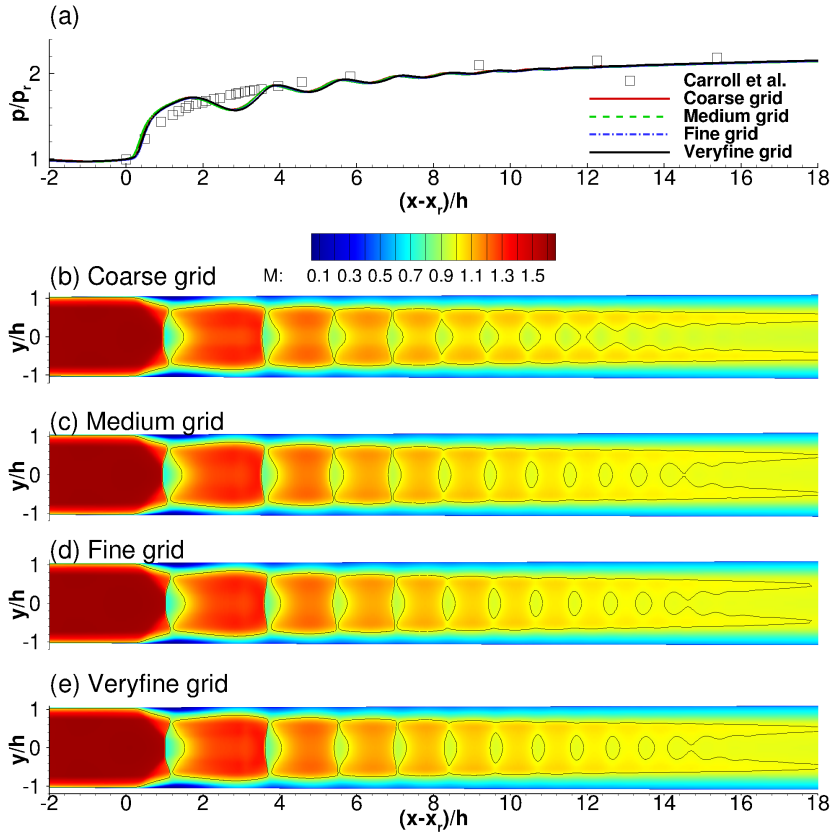

Figure 3.26: Wall pressure (a) and Mach number contours for the three-dimensional coarse (b), medium (c), fine (d), and veryfine (e) grids obtained with the $k-\omega$ SST turbulence model.

Similar wall pressure and centreline Mach number distributions on all grids were observed suggesting that the medium grid is adequate for capturing the three-dimensional flow features. Similar observations for the wall pressure and centreline Mach number (figures 3.28 and

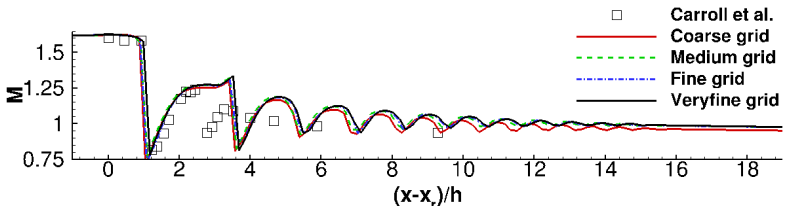

Figure 3.27: Centreline Mach number for the three-dimensional coarse, medium, fine, and veryfine grids obtained with the $k-\omega$ SST turbulence model.

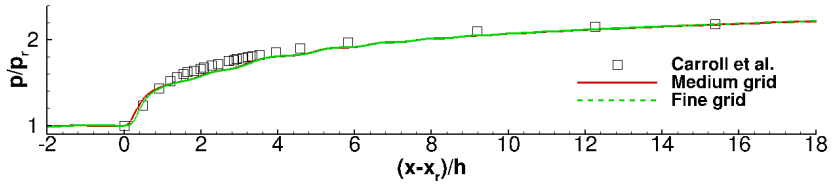

Figure 3.28: Wall pressure for the three-dimensional medium and fine grids obtained with the $k-\omega$ EARSM turbulence model.

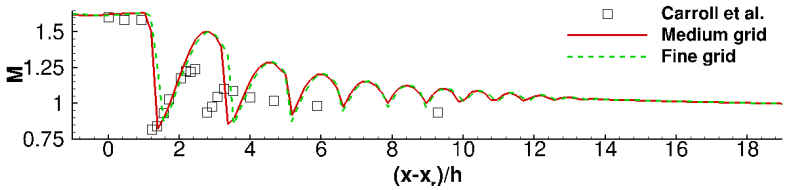

Figure 3.29: Centreline Mach number for the three-dimensional medium and fine grids obtained with the $k-\omega$ EARSM turbulence model.

3.29) on the medium and fine grids with the $k-\omega$ EARSM turbulence model were made. Figure 3.30 shows the comparison between the density gradient from the very fine grid and the experiment. The density gradient was obtained by taking the magnitude of the density gradient at the mid-plane of the duct. According to Edney's classification [45], the initial shock forms a type II shock pattern in the experiment. For detailed schematics of the six different shock patterns refer to the work by Dèlery [33]. The very fine grid results in a type I shock pattern, due to the larger separation at the foot of the shock predicted by the non-linear turbulence model. In contrast, the linear turbulence models predict a type II shock pattern with a Mach stem.

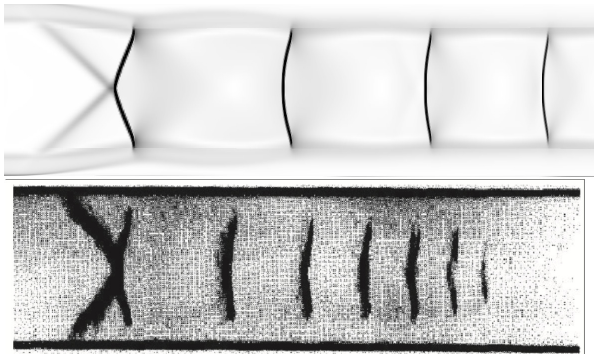

Figure 3.30: Numerical schlieren obtained from the very fine grid (top) and experimental schlieren (bottom).

As the predicted shock structure is type I, the flow decelerates less when compared to the experiment, which featured a type II structure. The reduced deceleration resulted in increased shock spacings.

Several shock train models have been developed over the years including the shockless model by Crocco [30] followed by the diffusion model and modified diffusion models by Ikui et al. [72], and the mass averaging pseudo-shock model by Matsuo et al. [83]. These models can only predict the pressure rise across the shock train. An empirical quadratic equation for cylindrical ducts was developed by Waltrup and Billig [145]. The equation gives the pressure distribution and the distance over which the pressure rise is spread. Further modifications to the equation were made by Billig [14] for square ducts. The equation for the pressure distribution is given by:

$$\frac{x\left(M_r^2-1\right)Re_{\theta_r}^{\alpha}}{H^{1/2}\theta_r^{1/2}} = 50\left(\frac{p}{p_r}-1\right)+170\left(\frac{p}{p_r}-1\right)^2, \tag{3.2}$$

where θ_r is the momentum thickness before the interaction, Re_{θ_r} is the momentum thickness

Reynolds number, $H = 2h$ is the duct height and α is either $1/4$ or $1/5$ for circular or square ducts respectively. The equation is used for predicting the monotonic pressure rise across the shock train region. It can not model the subsequent mixing region. Both circular and square duct equations have been applied and are presented in figure 3.31. The square duct equation shows better agreement with experiments, however, the equation underpredicts the pressure gradient at the beginning of the interaction.

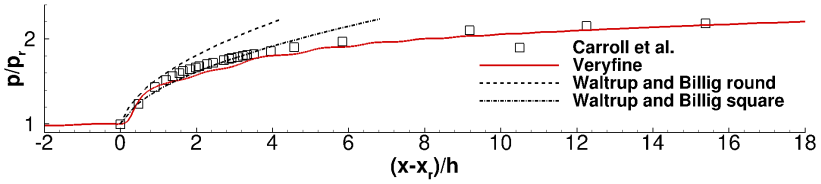

Figure 3.31: Experimental, very fine grid wall pressure, and wall pressure computed with the Waltrup and Billig empirical equations [14, 145].

Effect of turbulence models

Several turbulence models and their effect on the sensitivity of the solution to turbulence modelling was investigated. In particular, the turbulence models considered are the eddy-viscosity based - standard k-ω [86], baseline $k-\omega$ [86], and $k-\omega$ SST [86] models and the Reynolds stress based - the $k-\omega$ EARSM [64, 144] model. Figure 3.32 shows the wall pressure and the Mach number distribution for all models. The standard k-ω turbulence model predicted the shortest shock train with 4 shock waves downstream of the initial normal shock wave. The baseline k-ω and the $k-\omega$ SST turbulence models predict longer shock trains with the $k-\omega$ SST predicting the longest shock train of all models. This behaviour is similar, but not identical, to the two-dimensional simulations. All linear eddy-viscosity based models (EVMs) - the standard k-ω, baseline k-ω, and the $k-\omega$ SST predicted a wall pressure featuring small oscillations due to the strong shocks and large corner vortices. From the solid black line which indicates the sonic line, $M = 1$, it was observed that the EVMs predict the supersonic core flow to be much closer to the wall, due to the missing separation at the upper and lower walls. The Reynolds stress based $k-\omega$ EARSM model, on the other hand, predicted separation at the upper and lower walls and showed no pressure oscillations on the wall. From the Mach number contours, it was observed that the supersonic core flow is not as close to the wall as the one predicted by the EVMs. Figure 3.37 shows that the boundary layer predicted by the $k-\omega$ SST is less prone to separation resulting in stronger pressure oscillations where the shocks are formed. The $k-\omega$ EARSM model underpredicts the wall

pressure, due to the overprediction of the separation at the upper and lower walls as shown in figure 3.37. Nevertheless, the $k-\omega$ EARSM turbulence model gave the best agreement with the experiments. Figure 3.33 shows the three-dimensional structure of the pseudo-shock system. The $M = 1$ iso-surface visualises the structure of the shock train and the following mixing zone. The $u/V_u = -1 \times 10^{-3}$ iso-surface visualises the separation zones. For the EVMs the flow shows a large corner separation and no or little separation at the centreline. The shape of the shock train and the following mixing region is octagonal. In contrast, the RSM showed little corner separation due to its suppression by the secondary (corner) flows. The corner flows increase the fluid momentum near the corner by bringing higher momentum fluid from the core flow. The increased momentum suppresses the separation.

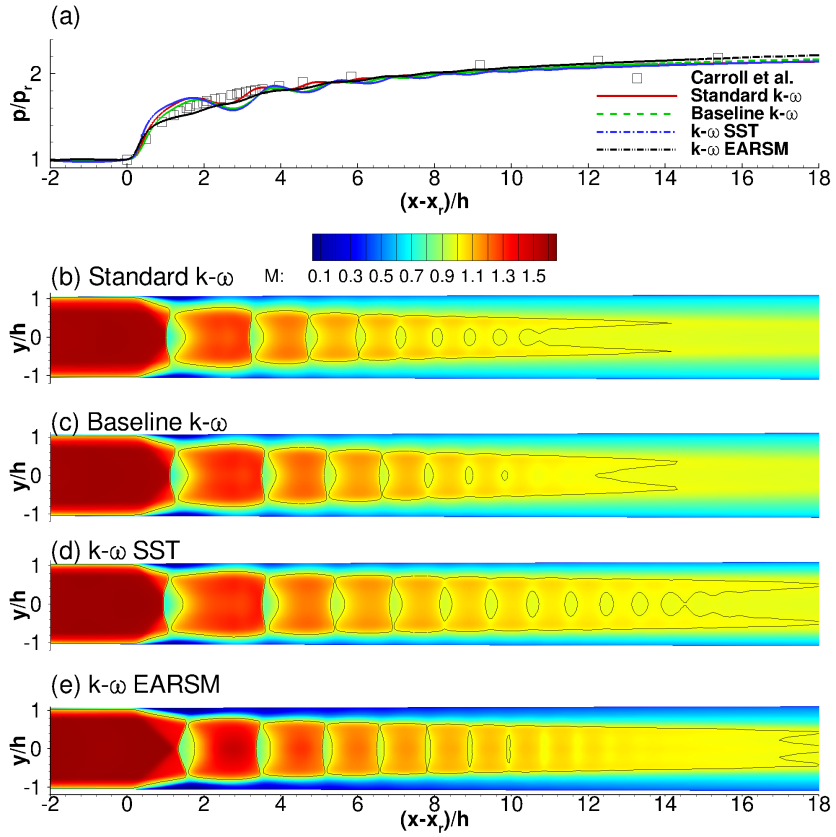

Figure 3.32: Wall pressure (a) and Mach number contours the standard k-ω (b), baseline k-ω (c), $k-\omega$ SST (d), and $k-\omega$ EARSM (e) turbulence models.

Larger separation was observed at the upper and lower walls and the shape of the pseudo-shock system was more rectangular than octagonal. Figure 3.34 shows the visualisation of the wall shear stress using friction lines just above the wall for each turbulence model and figure 3.35 compares the visualisation of the $k-\omega$ EARSM wall shear stress using friction lines just above the wall to the oil flow visualisation from the experiment. Red lines indicate

flow features such as the centreline separation and the corner flows. The friction lines were obtained by projecting the near wall velocity onto the wall using the following equations:

$$\begin{aligned} l_i &= \bar{u}_i^{wall} - \left(\bar{u}_j^{wall} n_j\right) n_i, \\ \hat{l}_i &= l_i / \sqrt{l_k l_k}, \\ \hat{m}_i &= \varepsilon_{ijk} n_j l_k, \end{aligned} \tag{3.3}$$

where $\bar{u}_i^{wall}$ is the velocity in the cell adjacent to the wall and $\hat{l}_i$ and $\hat{m}_i$ are the unit vectors along and normal to the flow direction. The skin friction coefficient can then be calculated using the following equations:

$$\begin{aligned} C_{fi} &= \sum_{j=1}^{3} \tau_{i,j}^{RANS} \hat{l}_j, + \sum_{j=1}^{3} \tau_{i,j}^{RANS} \hat{m}_j, \\ C_f &= 2\sqrt{C_{fk} C_{fk}} \end{aligned} \tag{3.4}$$

where C_f is the skin friction coefficient and $\tau_{i,j}^{RANS}$ is the Reynolds stress tensor. Apart from the large separation at the centreline predicted by the model, it appears to capture well the flow structure near the corners. In addition to the comparison of the three-dimensional structure of the pseudo-shock system, figures 3.38 to 3.43 compare the streamwise velocity, wall-normal velocity, turbulent kinetic energy, and Reynolds stress profiles at several stations with the experiment for the different eddy-viscosity and Reynolds stress turbulence models. These quantities, especially the Reynolds stresses are rarely compared as they are often not measured in MSWBLI experiments. Since in the MSWBLI experiment by Carroll et al. [24] the $\overline{u'u'}/V_u^2$, $-\overline{u'v'}/V_u^2$, and $\overline{v'v'}/V_u^2$ Reynolds stress components were measured they were compared to the simulations. From the profiles, it was observed that the EVMs and RSMs underpredict the $\overline{u'u'}/V_u^2$ Reynolds stress component throughout the beginning of the interaction. The $\overline{v'v'}/V_u$ component was overpredicted throughout the entire interaction by all models, with the $k-\omega$ EARSM model giving the largest overprediction. The agreement between the $-\overline{u'v'}/V_u^2$ component and the experiment was, nevertheless, satisfactory.

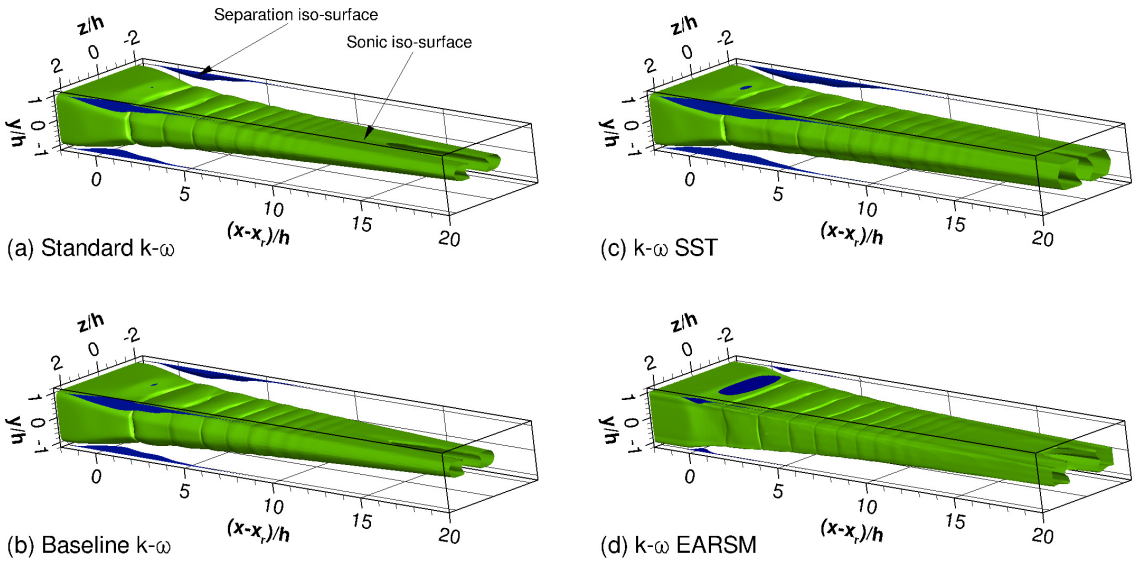

Figure 3.33: $M = 1$ (shaded green) and $u/V_u = -1 \times 10^{-3}$ (shaded blue) isosurfaces for the standard k-ω (a), baseline k-ω (b), $k-\omega$ SST (c), and $k-\omega$ EARSM (d) turbulence models.

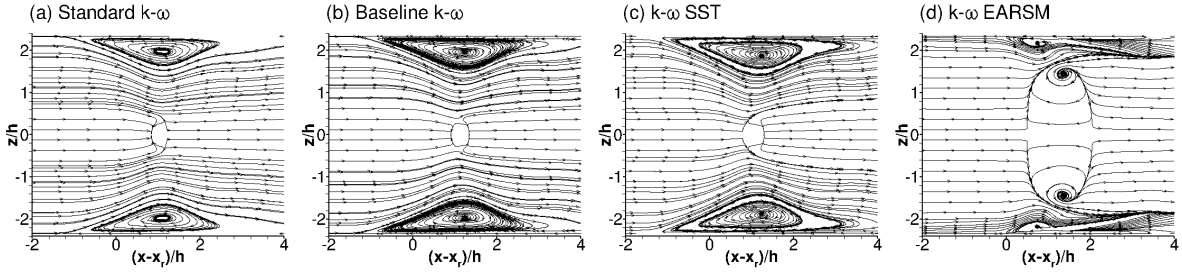

Figure 3.34: Visualisation of the wall shear stress using friction lines just above the wall for the k-ω (a), baseline k-ω (b), $k-\omega$ SST (c), and $k-\omega$ EARSM (d) turbulence models.

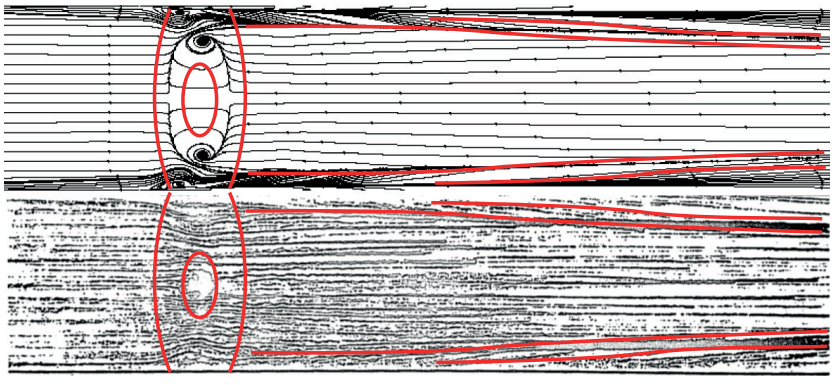

Figure 3.35: Comparison of the visualisation of the $k-\omega$ EARSM wall shear stress using friction lines just above the wall (top) with the oil flow visualisation from the experiment (bottom).

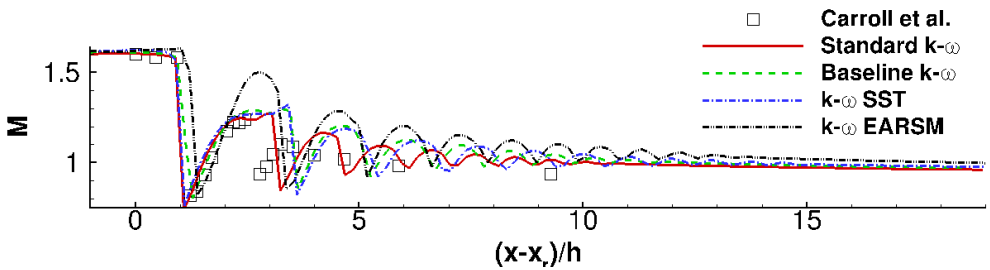

Figure 3.36: Centreline Mach number for the standard k-ω, baseline k-ω, $k-\omega$ SST , and $k-\omega$ EARSM turbulence models.

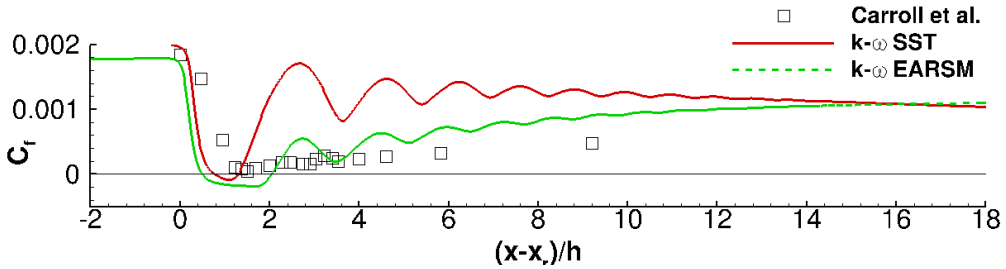

Figure 3.37: Skin friction for the $k-\omega$ SST and the $k-\omega$ EARSM turbulence models.

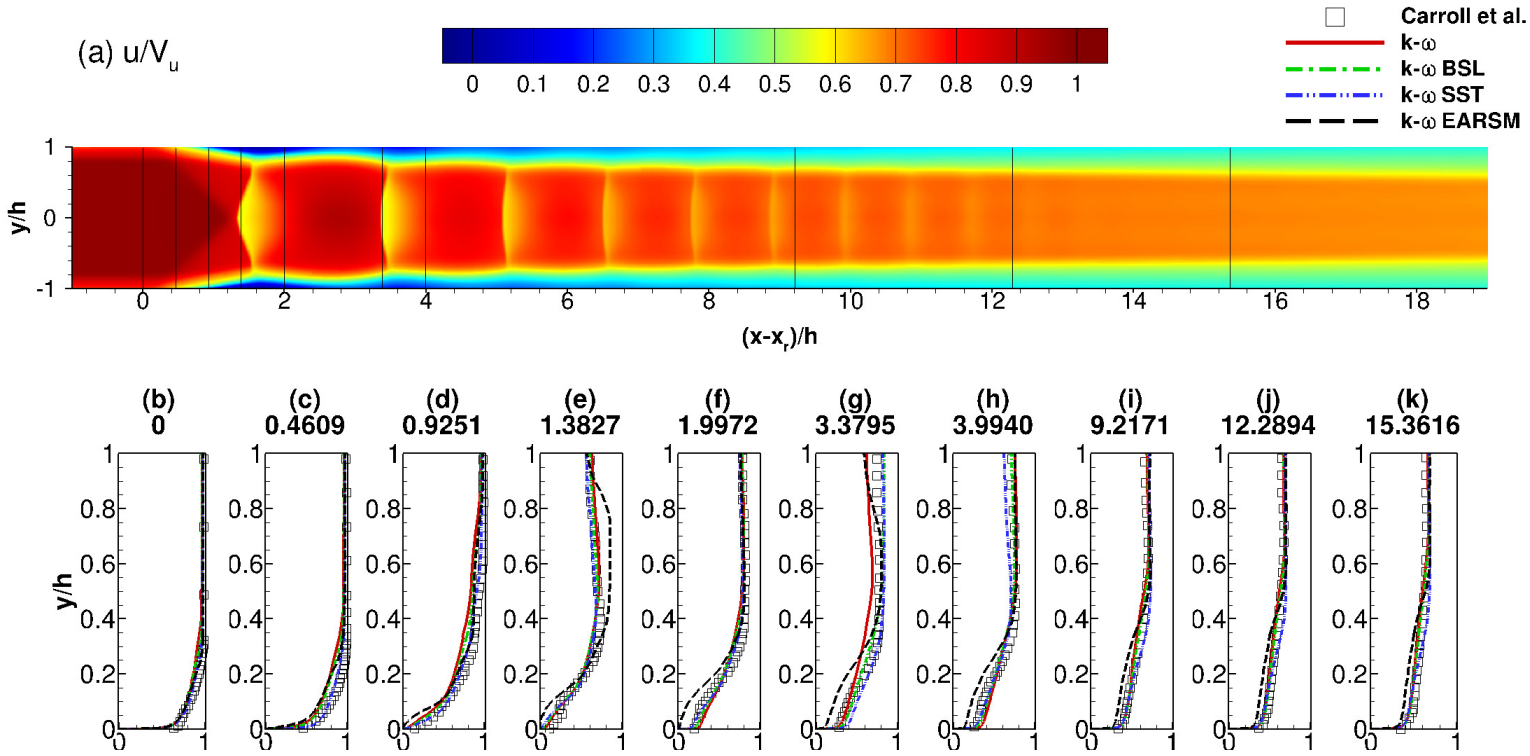

Figure 3.38: Streamwise velocity u/V_u contours (a) for the $k-\omega$ EARSM and profiles (b-k) for the standard k-ω, baseline k-ω, $k-\omega$ SST , and the $k-\omega$ EARSM turbulence models on the medium grid.

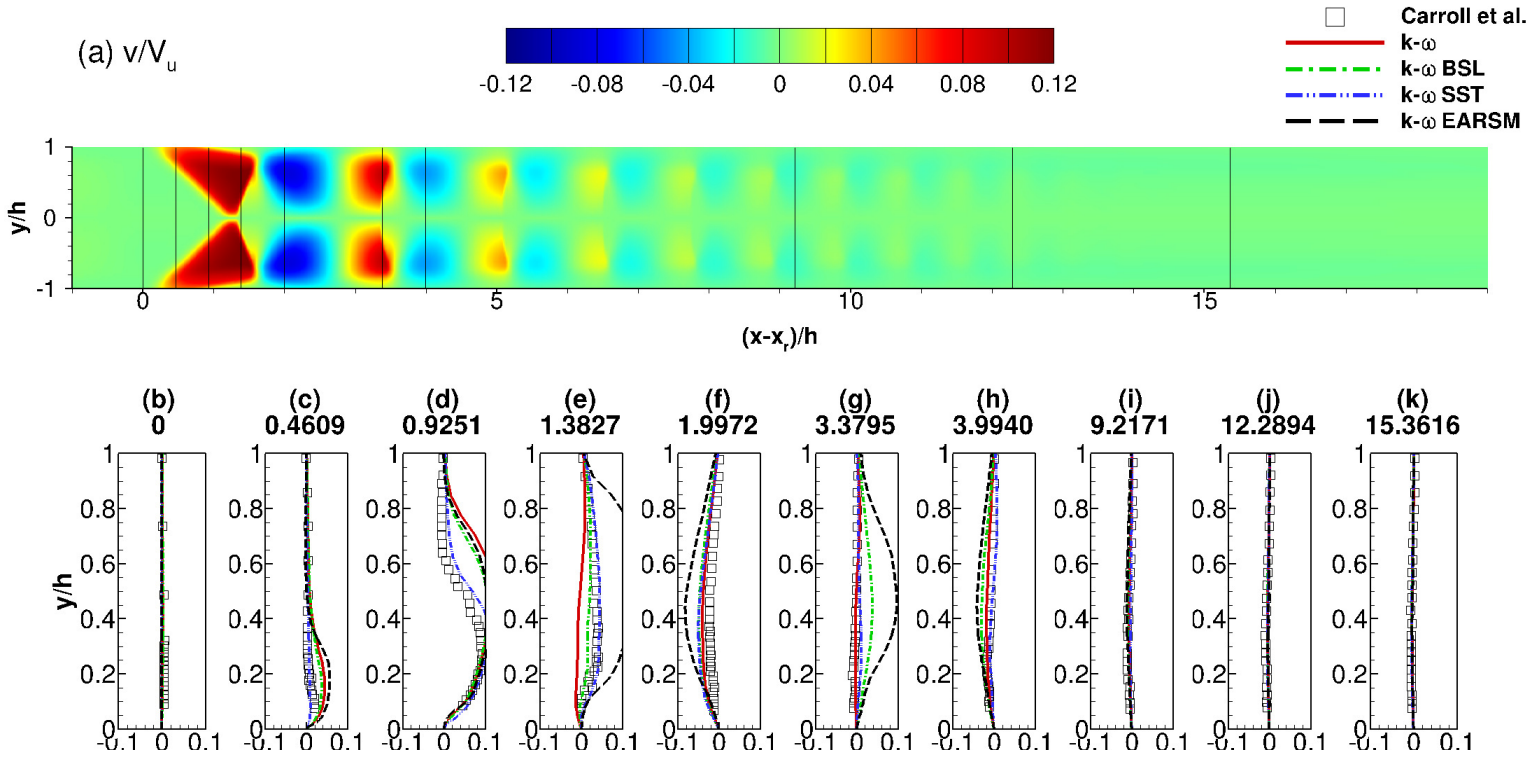

Figure 3.39: Wall normal velocity v/V_u contours (a) for the $k-\omega$ EARSM and profiles (b-k) for the standard k-ω, baseline k-ω, $k-\omega$ SST , and the $k-\omega$ EARSM turbulence models on the medium grid.

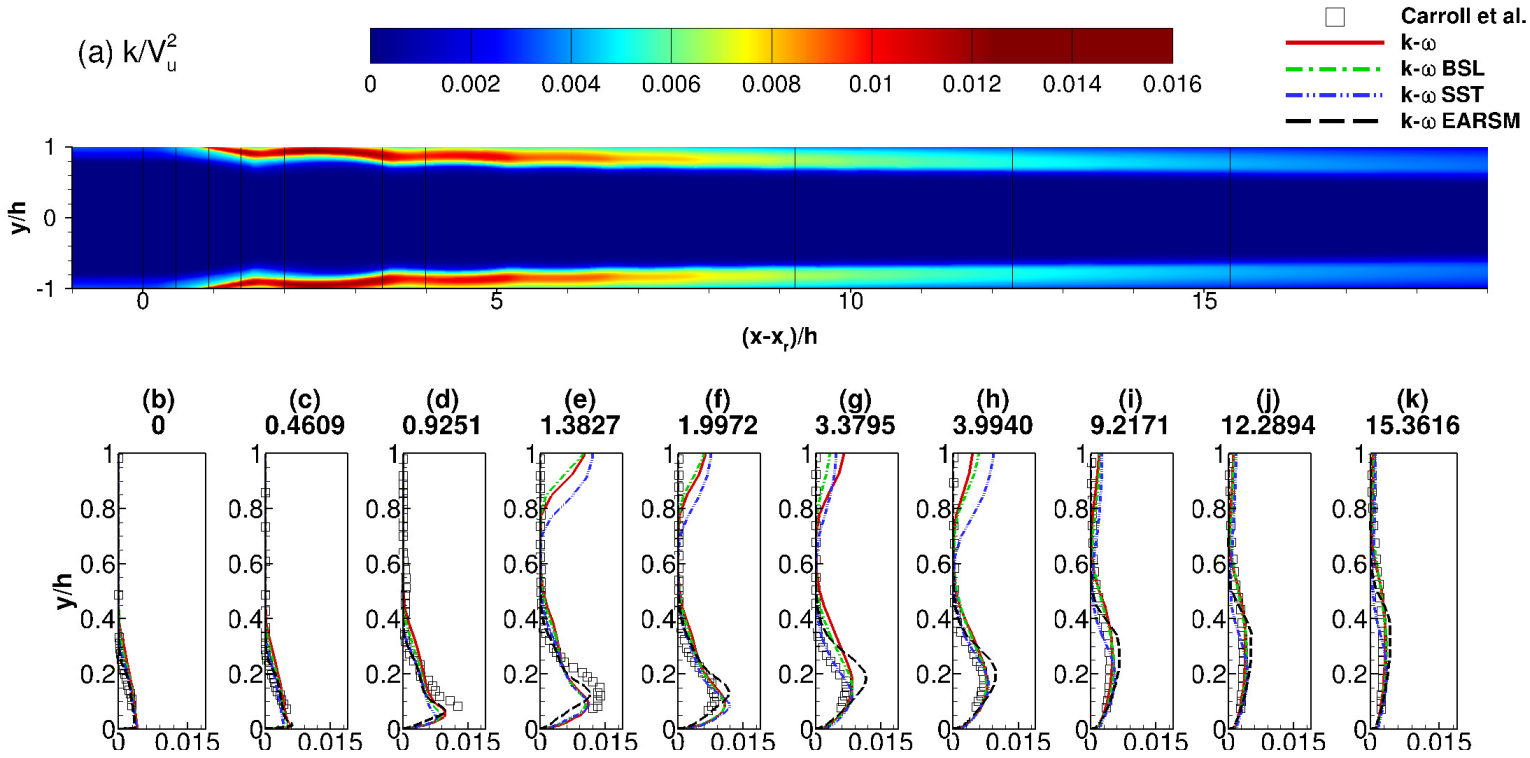

Figure 3.40: Turbulent kinetic energy k/V_u^2 contours (a) for the $k-\omega$ EARSM and profiles (b-k) for the standard k-ω, baseline k-ω, $k-\omega$ SST , and the $k-\omega$ EARSM turbulence models on the medium grid.

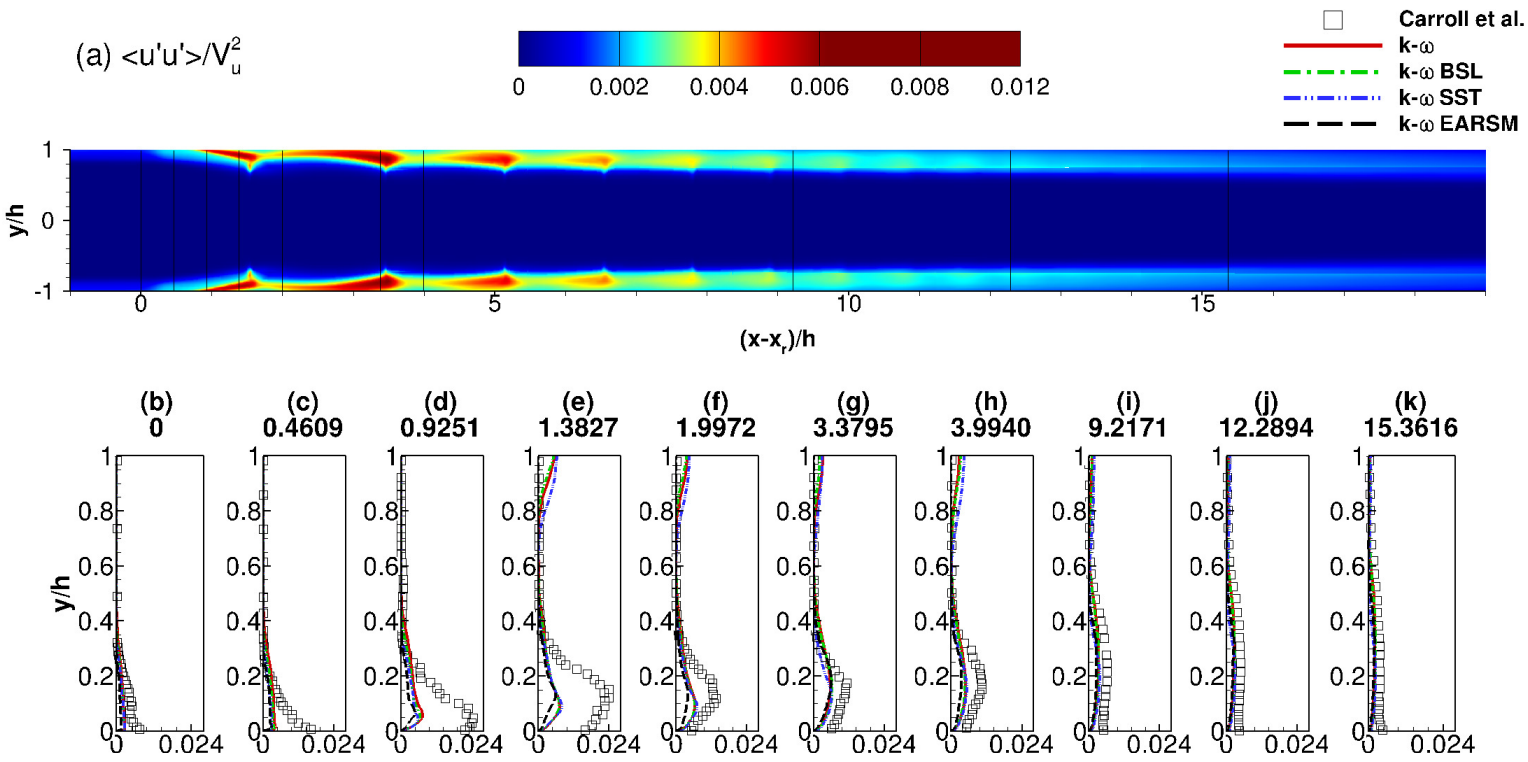

Figure 3.41: Reynolds stress $\overline{u'u'}/V_u^2$ contours (a) for the $k-\omega$ EARSM and profiles (b-k) for the standard k-ω, baseline k-ω, $k-\omega$ SST , and the $k-\omega$ EARSM turbulence models on the medium grid.

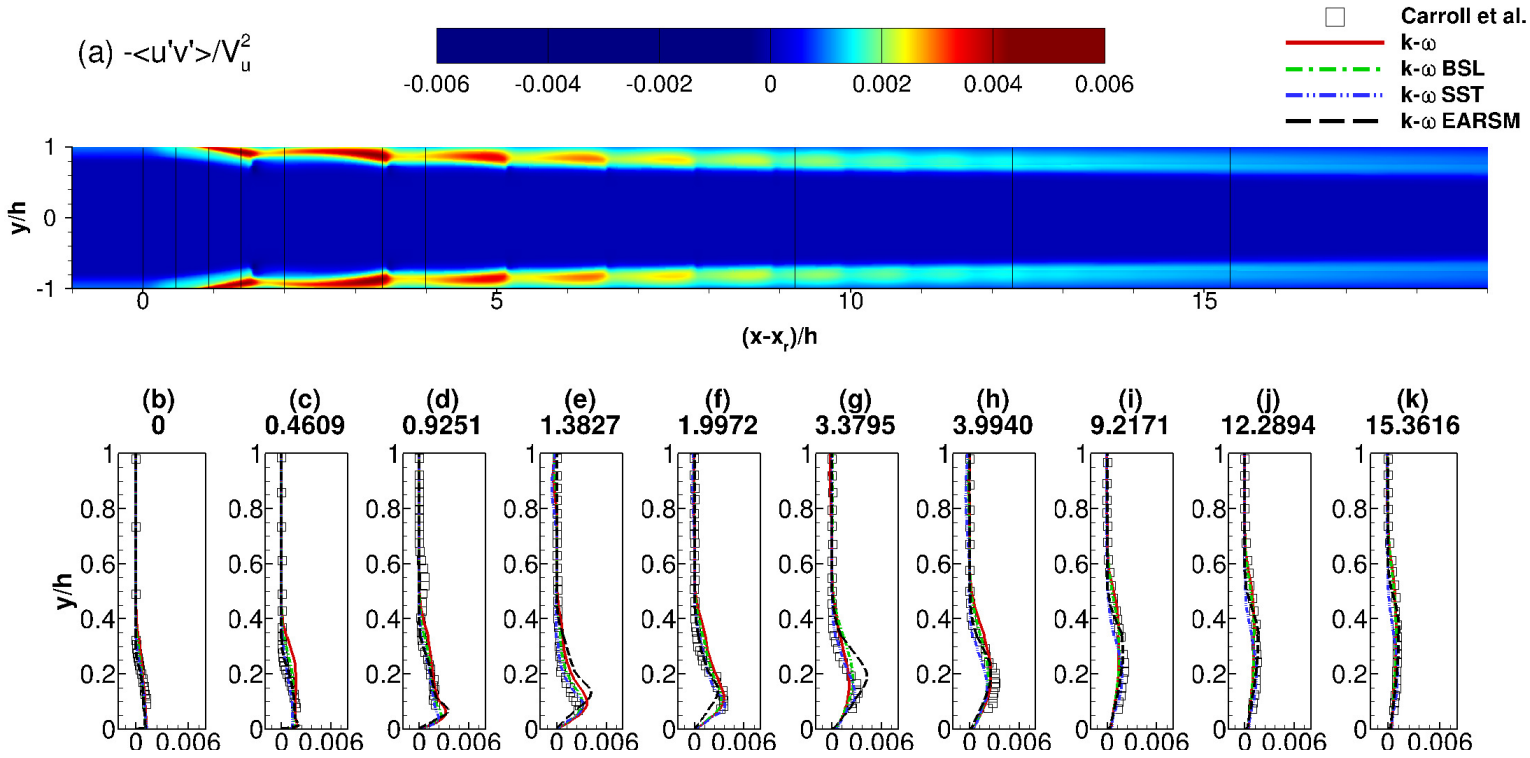

Figure 3.42: Reynolds stress $-\overline{u'v'}/V_u^2$ contours (a) for the $k-\omega$ EARSM and profiles (b-k) for the standard k-ω, baseline k-ω, $k-\omega$ SST , and the $k-\omega$ EARSM turbulence models on the medium grid.

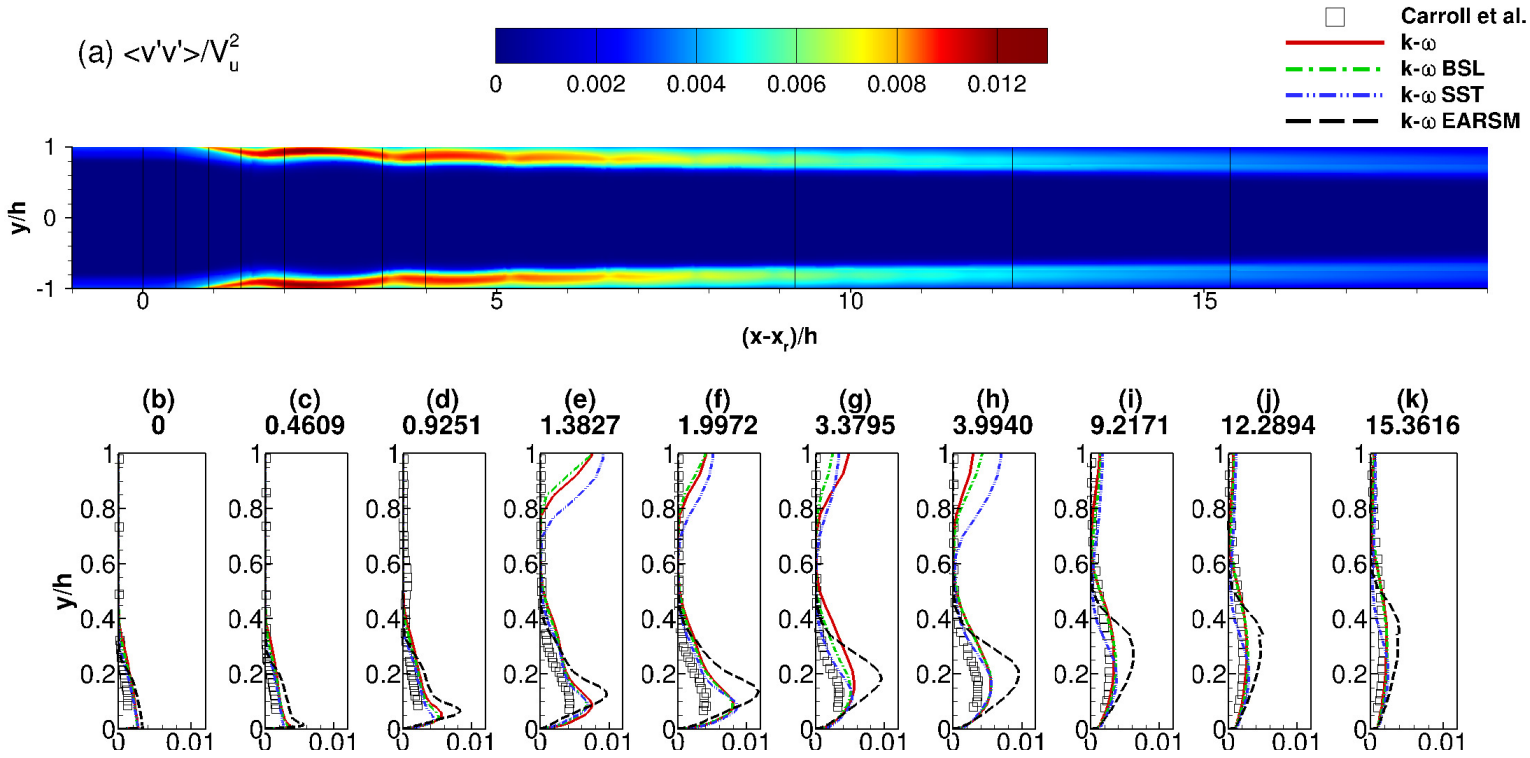

Figure 3.43: Reynolds stress $\overline{v'v'}/V_u^2$ contours (a) and profiles (b-k) for the standard k-ω, baseline k-ω, $k-\omega$ SST , and the $k-\omega$ EARSM .

The effect of the two QCRs - QCR V1 and QCR V2, presented in chapter 2, on the multiple shock wave boundary layer interaction by Carroll *et al.* [23] was investigated next. The QCRs do not have the complexity of the $k-\omega$ EARSM model and are relatively easy to implement. Simulations were performed on the medium grid and again, only a quarter of the domain was considered. The simulation parameters are listed in table 3.9 and the grid parameters in table 3.4.

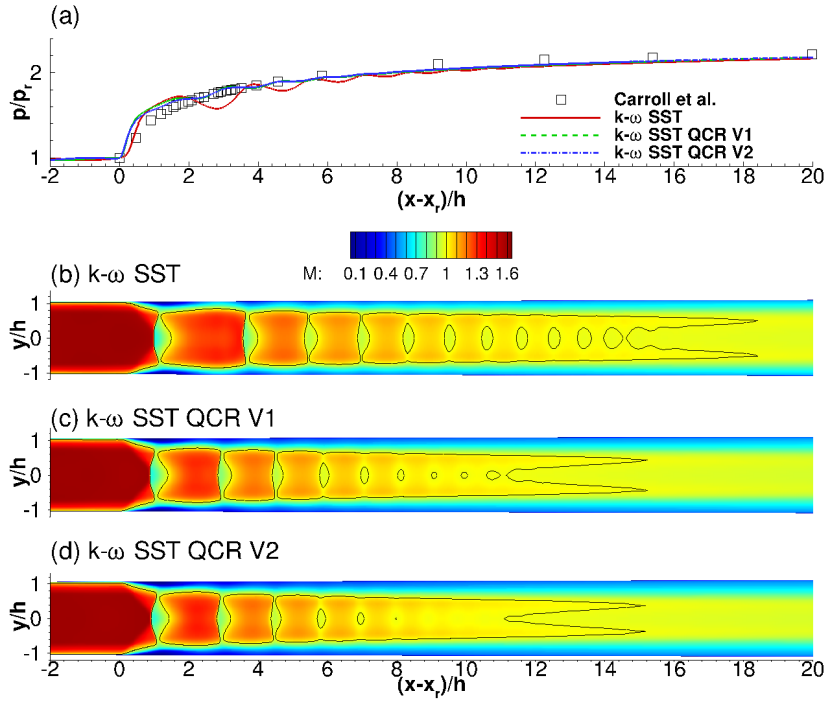

Figure 3.44: Wall pressure and Mach number contours for the $k-\omega$ SST , $k-\omega$ SST QCR V1, and the $k-\omega$ SST QCR V2 models.

Figure 3.44 shows the wall pressure and the Mach number contours at the mid-plane. The solid black line indicates $M=1$. The QCR extension reduces the pressure oscillations at the wall, however, the wall pressure is still slightly overpredicted. The overprediction appears at $(x-x_r)/h \approx 1$. The distance between the first and second shock in the shock train is smaller for the $k-\omega$ SST QCR V1 and V2 models and the supersonic flow is farther away from the wall (indicated by the sonic $M=1$ line). The size of the corner separations, shown by the iso-surfaces in figure 3.45, is considerably reduced by the introduction of the QCR extension. Both models reduced the streamwise and spanwise extent of the corner separations. As the size of the corner separations and the centreline separation are dependent in confined flows, the centreline separation increased.

Table 3.9: Simulation parameters.

Grid	I_u %	M_u	M_r	δ_r mm	δ_r/h	x_r/h	p/p_u	p/p_r	Turb. model
Medium	1.0	1.69	1.624	5.45	0.335	22.445	2.4776	2.1880	$k-\omega$ SST
Medium	1.0	1.69	1.604	6.13	0.377	25.399	2.4776	2.1787	$k-\omega$ SST QCR V1 $C_{cr1}=0.3$
Medium	1.0	1.69	1.604	6.23	0.383	25.896	2.4776	2.1803	$k-\omega$ SST QCR V2
Medium	1.0	1.69	1.623	5.01	0.308	26.426	2.4776	2.2357	$k-\omega$ EARSM
Medium	1.0	1.69	1.614	6.00	0.369	24.425	2.4776	2.1983	QCR V1 $C_{cr1}=0.2$
Medium	1.0	1.69	1.604	6.14	0.378	25.298	2.4776	2.1741	QCR V1 $C_{cr1}=0.4$
Medium	1.0	1.69	1.605	6.16	0.378	25.298	2.4776	2.1805	QCR V1 $C_{cr1}=0.4$ Pklim
Medium	1.0	1.69	1.619	5.18	0.318	20.932	2.6015	2.3183	QCR V1 $C_{cr1}=0.4$ p=1.05p
Medium	1.0	1.69	1.611	6.13	0.377	25.065	2.4776	2.1742	QCR V1 $C_{cr1}=0.4$ kwclip
Experiment [23]			1.6100	5.4000	0.3200			2.2309	

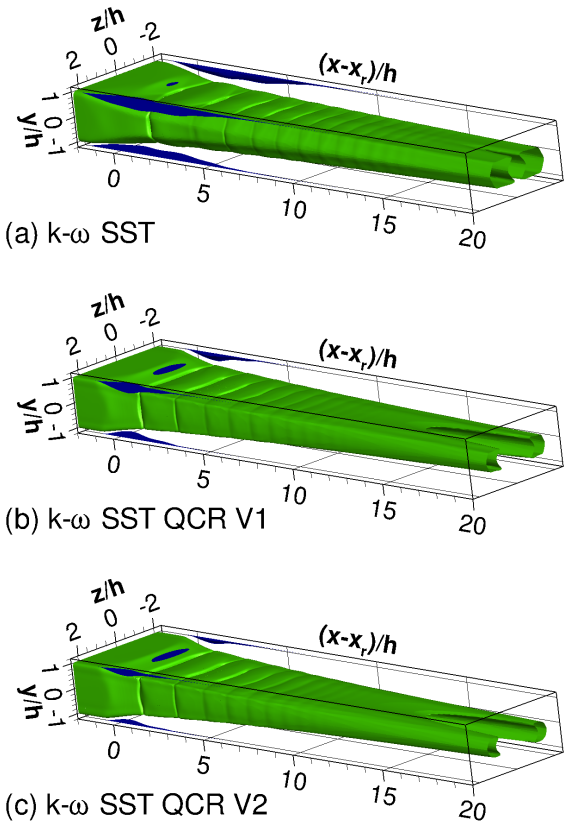

Figure 3.45: Separation $u/V_u = 1 \times 10^{-3}$ and sonic $M = 1$ iso-surfaces for the $k-\omega$ SST , $k-\omega$ SST QCR V1, and the $k-\omega$ SST QCR V2 models.

Figure 3.46 shows wall shear stress visualisation using friction lines just above the surface and figure 3.47 compares the wall shear stress visualisation of the $k-\omega$ SST QCR V1 to the experimental oil flow visualisation. The increase of the separated region at the centreline with respect to the reference is 3.15 and 3.5 times for the $k-\omega$ SST QCR V1 and V2 respectively. The onset of the corner separation begins at approximately $(x-x_r)/h \approx -1.2$ for the $k-\omega$ SST model. For the $k-\omega$ SST QCR V1 and V2 models the corner separation begins at approximately $(x-x_r)/h \approx -0.4$. The wall shear stress predicted by the QCR V1 model agrees better with the oil flow lines. Red lines in figure 3.47 indicate flow features such as the centreline separation and the corner flows. The turbulent kinetic energy profiles, shown in 3.51, agree well with the experiment, but closer inspection of the Reynolds stresses shows that the $\overline{u'u'}/V_u^2$ component is underpredicted and the $\overline{v'v'}/V_u^2$ component is overpredicted. The addition of the QCR extension does not affect the $\overline{u'u'}/V_u^2$ and $\overline{v'u'}/V_u^2$ components. The $\overline{v'v'}/V_u^2$ component is the most affected by the addition of the QCR extension. Both QCR V1 and V2 overpredict the $\overline{v'v'}/V_u^2$ component.

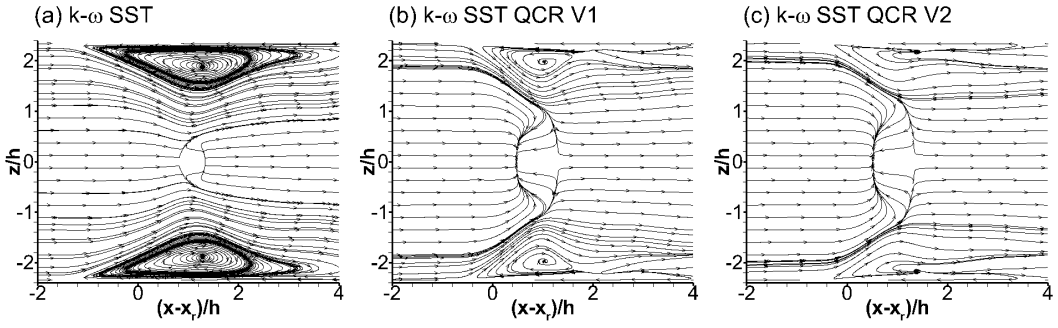

Figure 3.46: Wall shear stress visualisation using friction lines just above the surface for the $k-\omega$ SST , $k-\omega$ SST QCR V1, and the $k-\omega$ SST QCR V2 models.

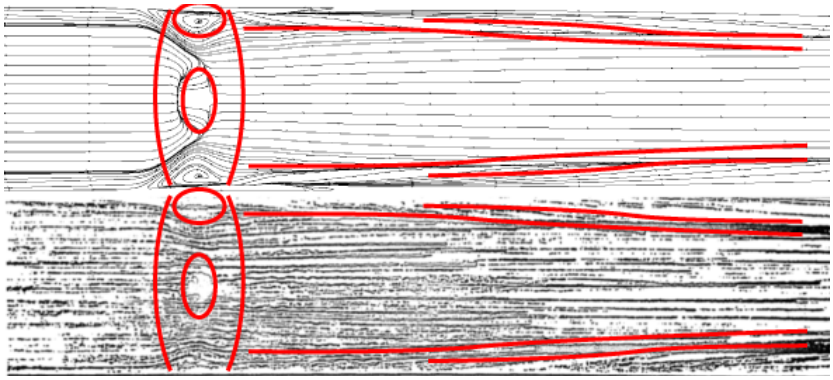

Figure 3.47: Comparison of the visualisation of the $k-\omega$ SST QCR V1 wall shear stress using friction lines just above the surface (top) to the experiment (bottom).

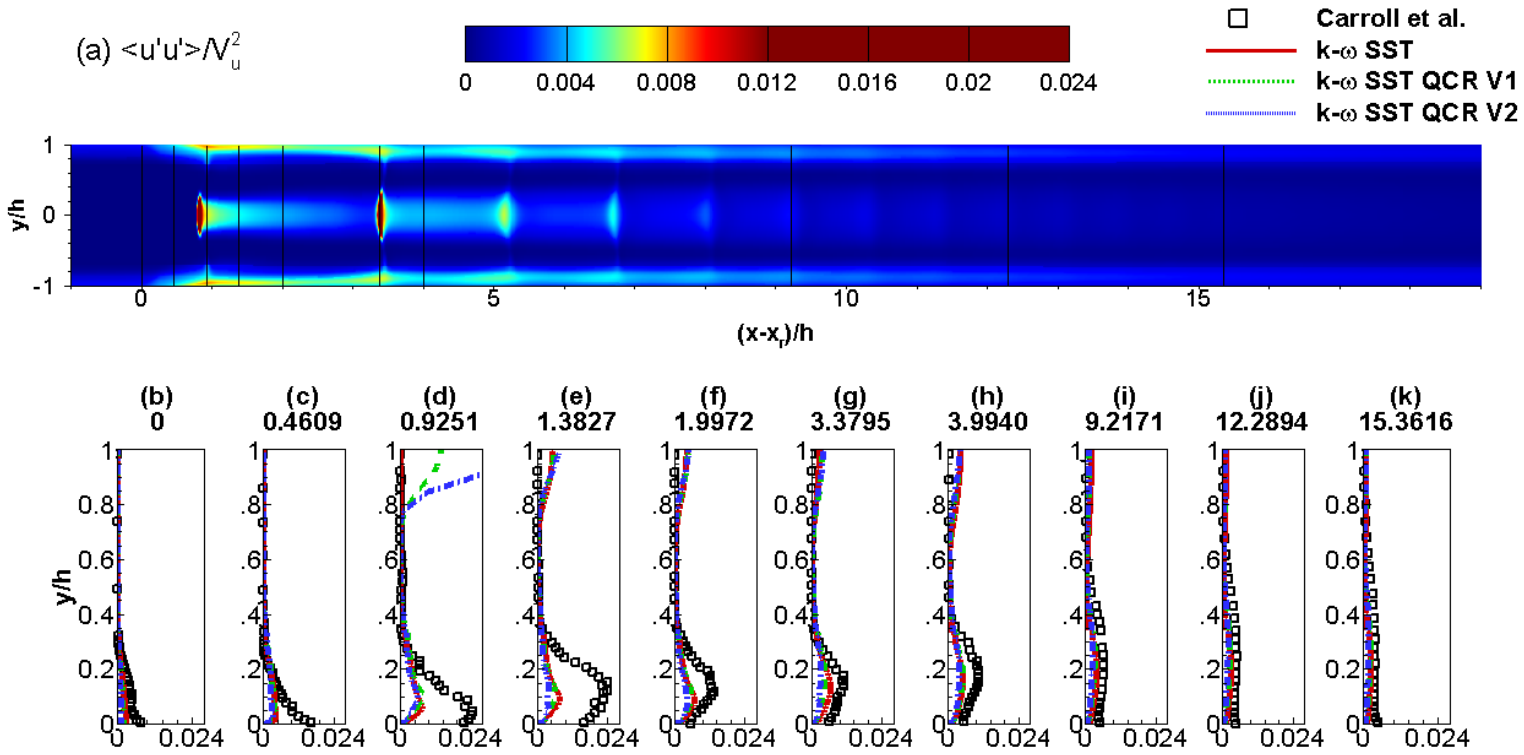

Figure 3.48: Reynolds stress $\overline{u'u'}/V_u^2$ contours for the $k-\omega$ SST model and profiles.

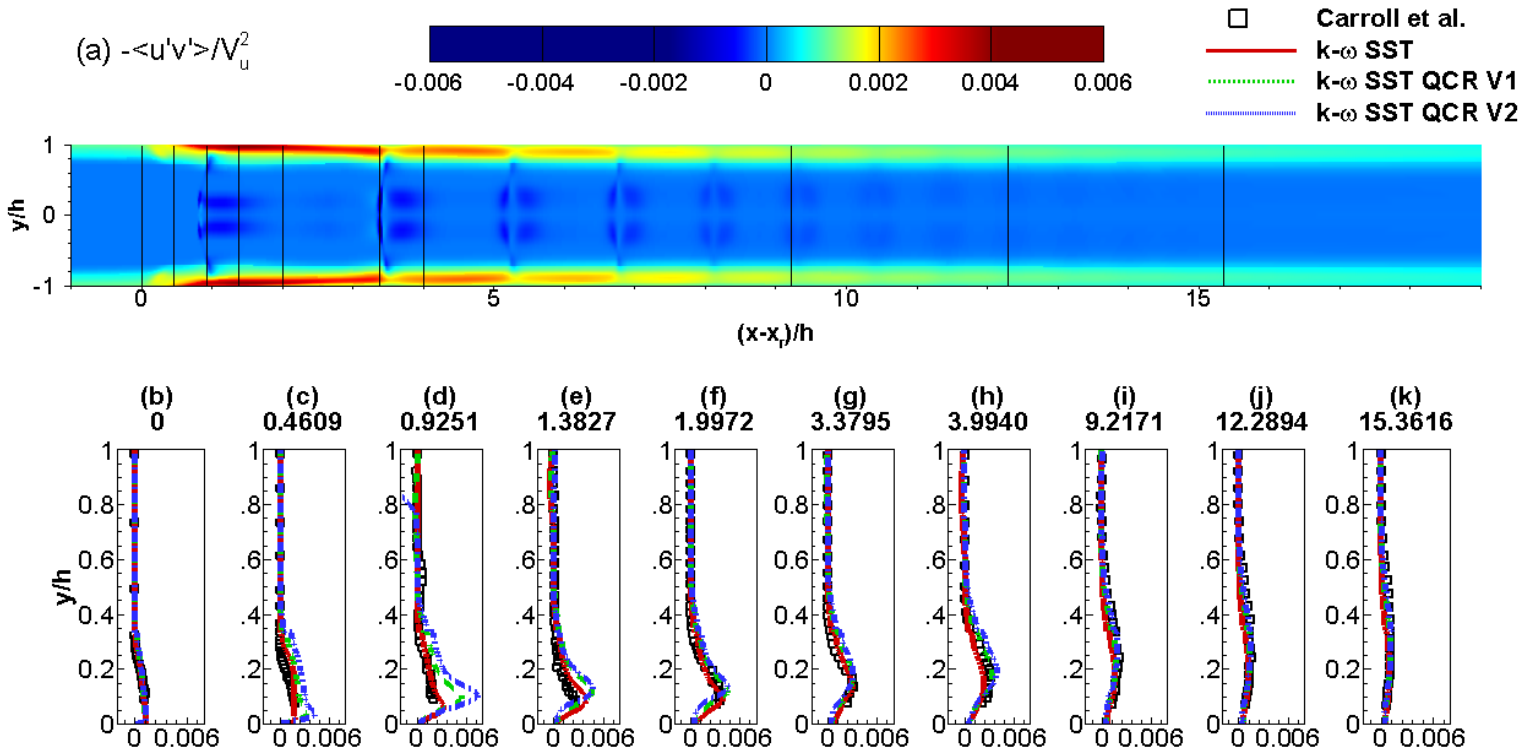

Figure 3.49: Reynolds stress $-\overline{u'v'}/V_u^2$ contours for the $k-\omega$ SST model and profiles.

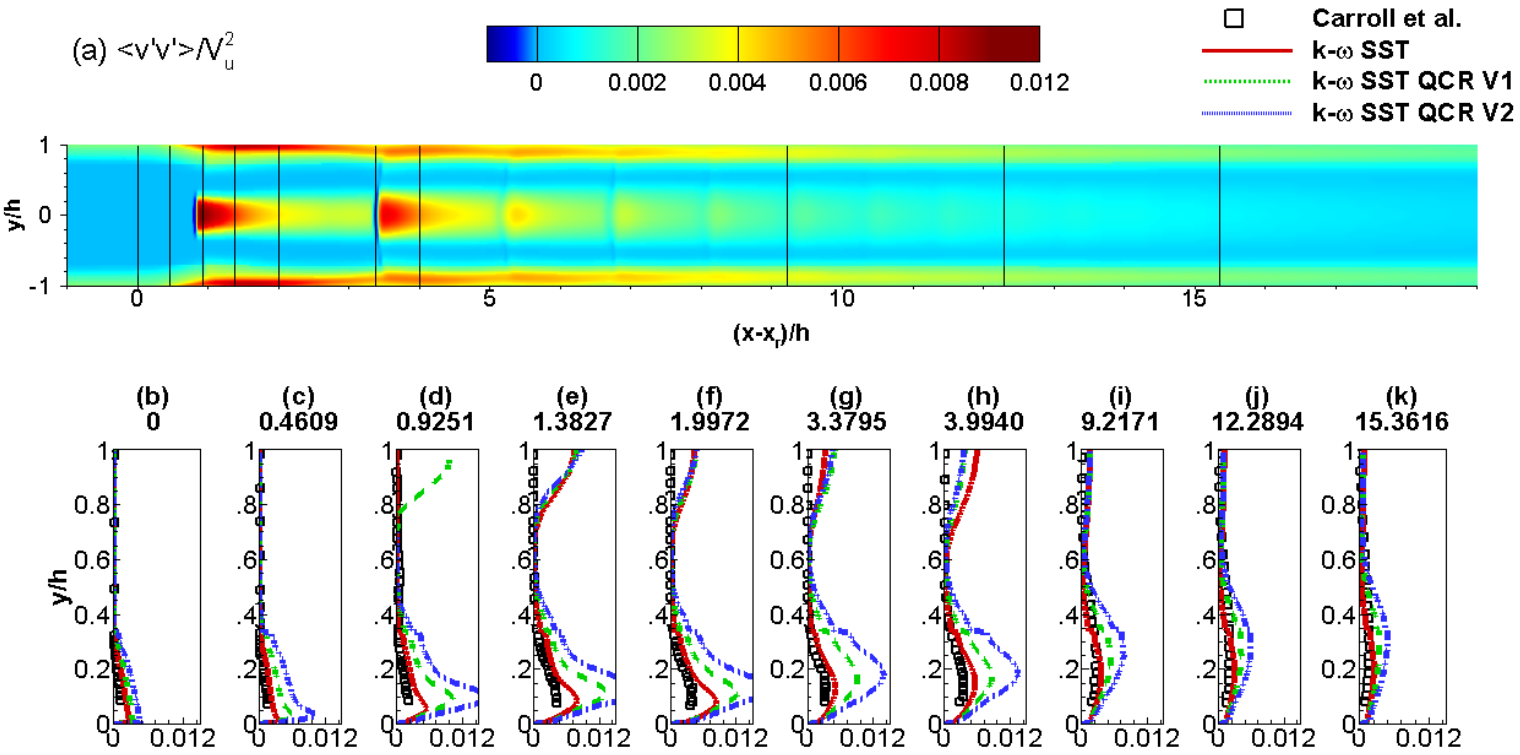

Figure 3.50: Reynolds stress $-\overline{v'v'}/V_u^2$ contours for the $k-\omega$ SST model and profiles.

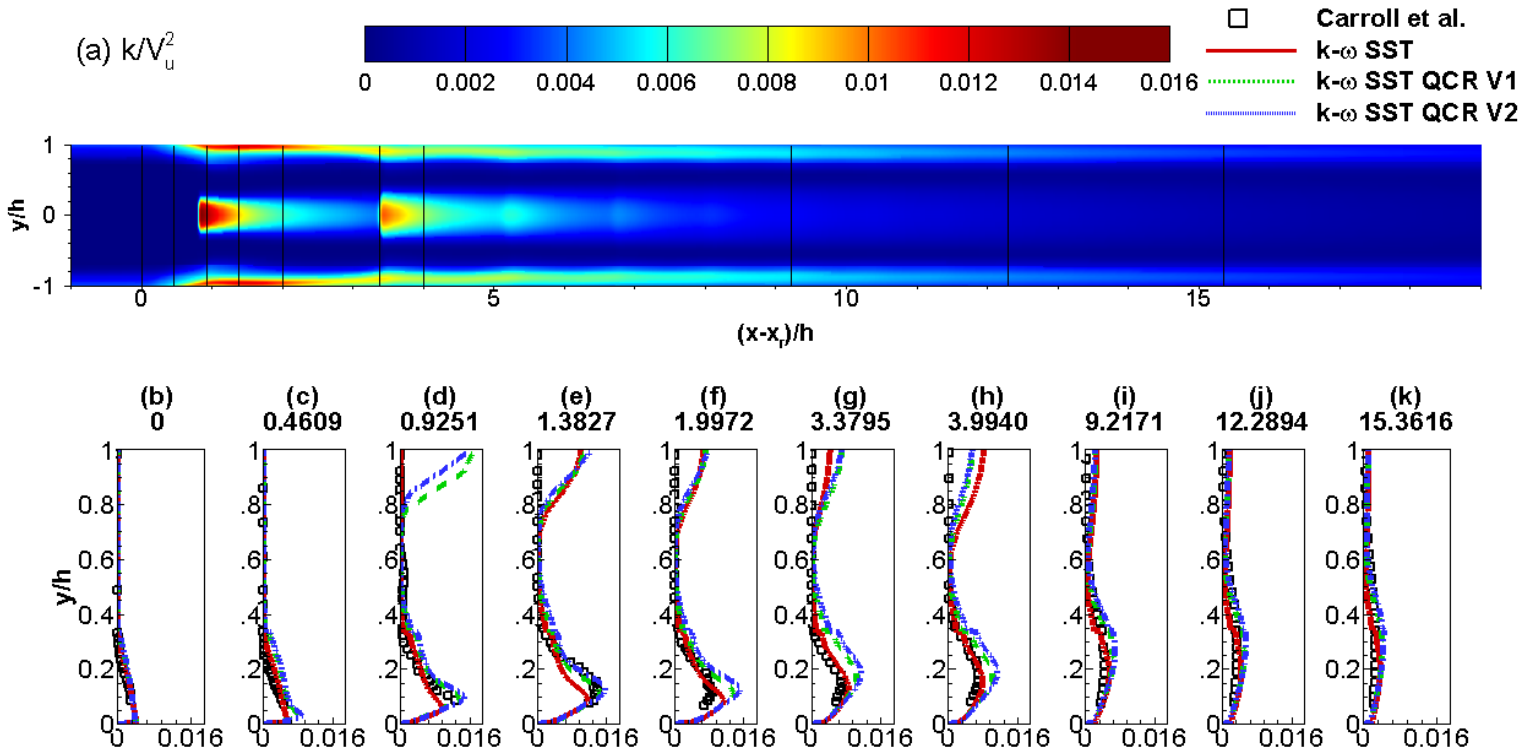

Figure 3.51: Turbulent kinetic energy k/V_u^2 contours for the $k-\omega$ SST model and profiles.

3.2.3 Further insight into the quadratic constitutive relations

Effect of the C_{cr1} constant

The $k-\omega$ SST QCR V1 model reduced the wall pressure oscillations. Similarly to the $k-\omega$ EARSM the corner separations reduced in size and the centreline separation increased in size. As stated previously the QCR V1 model, developed by Spalart [122], features a model constant C_{cr1} equal to 0.3. By considering the wall pressure predictions from the $k-\omega$ SST and the $k-\omega$ SST QCR V1 models one can see that reduction of the C_{cr1} constant will introduce pressure oscillations. Figure 3.52 shows the effect of the C_{cr1} constant on the wall pressure (a) and the Mach contours (b-d).

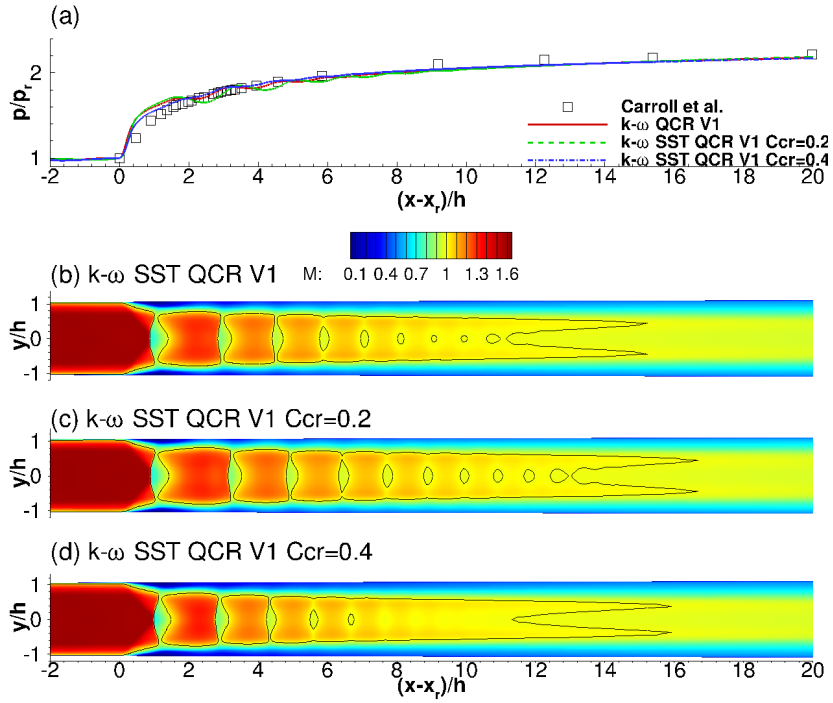

Figure 3.52: Wall pressure and Mach number contours for the $k-\omega$ SST QCR V1 (b), $k-\omega$ SST QCR V1 $C_{cr1}=0.2$, and the $k-\omega$ SST QCR V1 $C_{cr1}=0.3$ models.

Reduction of C_{cr1} by 0.1 introduced pressure oscillations. In the limit of $C_{cr1}\rightarrow 0$ the wall pressure will feature the same oscillations as predicted by the $k-\omega$ SST model. Increase of C_{cr1} by 0.1 further dampened the oscillations. The wall pressure was slightly overpredicted at the start of the interaction at $(x-x_r)/h\approx 1$, however, the agreement is improved when compared to the reference C_{cr1} value of 0.3. For all values of C_{cr1}, x_r moved downstream by approximately 4.3% to 6.2% of the domain length. The largest movement in x_r was observed when C_{cr1} was equal to 0.3 and 0.4 and was approximately 6.2% of the domain length. The

change in x_r between the simulations with $C_{cr1} = 0.3$ and $C_{cr1} = 0.4$ was approximately 0.2%. The movement downstream was accompanied by approximately 12% increase in the confinement levels. Table 3.9 lists the confinement levels and the boundary layer thickness at x_r. Figure 3.53 shows the streamwise vorticity contours for different values of C_{cr1} obtained three non-dimensional distances ($x/h = 3$) upstream of the onset of the interaction x_r.

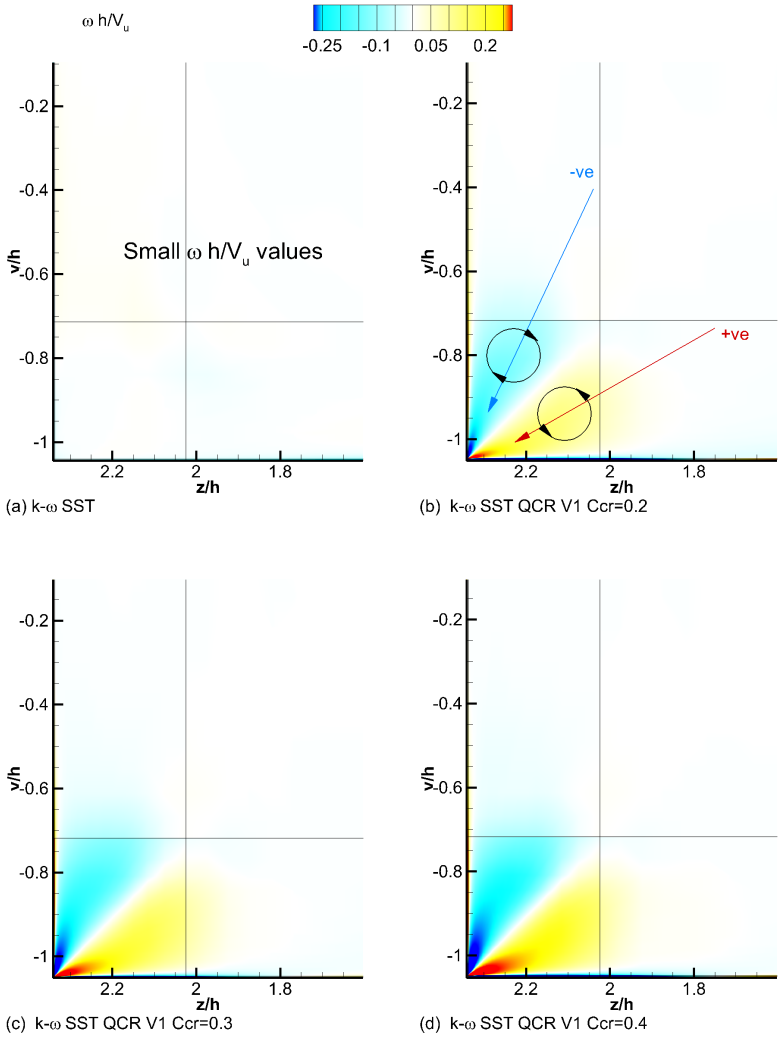

Figure 3.53: Streamwise vorticity contours for the $k-\omega$ SST $C_{cr1} = 0.0$, $k-\omega$ SST QCR V1 , $k-\omega$ SST QCR V1 $C_{cr1} = 0.2$, and the $k-\omega$ SST QCR V1 $C_{cr1} = 0.3$ models.

As the QCR V1 model C_{cr1} constant is increased from 0 to 0.4 (a-d) the regions of negative and positive vorticity increase in size and in strength. This is clearly observed when the $C_{cr1} = 0.2$ and $C_{cr1} = 0.4$ contours are compared. Higher values of streamwise vorticity result in stronger vortices near the duct corners. The vortices transport the higher momentum fluid above the wall towards the corner which reduces the corner separation, as the momentum near the corner is increased. The absence of negative or positive vorticity regions in the duct

corner when $C_{cr1} = 0$ shows the sensitivity of the corner vortices to the quadratic terms in the constitutive relation. The absence of vortices when $C_{cr1} = 0$ leads to the considerable overprediction of the corner separation. As shown in figure 3.59 (c) the QCR V1 model with the highest value of C_{cr1} predicts the smallest corner separations. No significant differences in the modelled Reynolds stresses was observed as the C_{cr1} constant was changed. The most sensitive Reynolds stress was $\overline{v'v'}/V_u$ where the change of C_{cr1} constant resulted in a slight increase of the peak values at $y/h \approx 0.18$. The absence of vorticity contours for the $k-\omega$ SST model ($C_{cr1} = 0$) can be explained from the streamwise vorticity equation (Pope [106]). Below is the vorticity equation and its Reynolds averaged form:

$$\begin{aligned} \frac{\partial \omega_i}{\partial t} + \frac{\partial}{\partial x_j}\left(u_j \omega_i\right) &= \omega_i \frac{\partial u_i}{\partial x_j} + \nu \frac{\partial^2 \omega_i}{\partial x_j^2} \\ ,\frac{\partial}{\partial x_j}\left(\overline{u_j}\,\overline{\omega_i}\right) &= \overline{\omega_i}\frac{\partial \overline{u_i}}{\partial x_j} + \nu \frac{\partial^2 \overline{\omega_i}}{\partial x_j^2} - \frac{\partial}{\partial x_j}\left(\overline{\omega_i' u_j'} - \overline{u_i' \omega_j'}\right). \end{aligned} \tag{3.5}$$

Further simplifications of the Reynolds averaged form of the equation, assuming fully developed flow give

$$\begin{aligned} \overline{v}\frac{\partial \overline{\omega_x}}{\partial y} + \overline{w}\frac{\partial \overline{\omega_x}}{\partial z} = \overline{\omega_y}\frac{\partial \overline{u}}{\partial y} + \overline{\omega_z}\frac{\partial \overline{u}}{\partial z} + \nu\left(\frac{\partial^2 \overline{\omega_x}}{\partial y^2} + \frac{\partial^2 \overline{\omega_x}}{\partial z^2}\right) \\ - \left(\frac{\partial^2}{\partial y^2} - \frac{\partial^2}{\partial z^2}\right)\overline{v'w'} \\ + \frac{\partial}{\partial y \partial z}\left(\overline{v'v'} - \overline{w'w'}\right). \end{aligned} \tag{3.6}$$

The first term on the right hand side of equation 3.6 is responsible for the generation of secondary flows in pipes with bends of any cross section, the second term is responsible for the viscous diffusion, and the third and fourth terms are responsible for the generation of secondary flows in ducts of non-circular cross section as the one used in the experiment of Carroll *et al.* [26]. The $\overline{v'w'}/V_u^2$ and the $(\overline{v'v'} - \overline{w'w'})/V_u^2$ Reynolds stress contours are shown in figures 3.54 and 3.55 below. Contours are saturated to ± 0.002.

Form the contours in figures 3.54 (a) and 3.55 (a) it is seen that the $\overline{v'w'}/V_u^2$ and the $(\overline{v'v'} - \overline{w'w'})/V_u^2$ Reynolds stresses are very small ≈ 0. As shown by figure 3.56 the resuting derivative terms are also very small. This explains the inability of the $k-\omega$ SST model to account for the secondary flows. Introduction of the QCR to the $k-\omega$ SST has a significant effect.

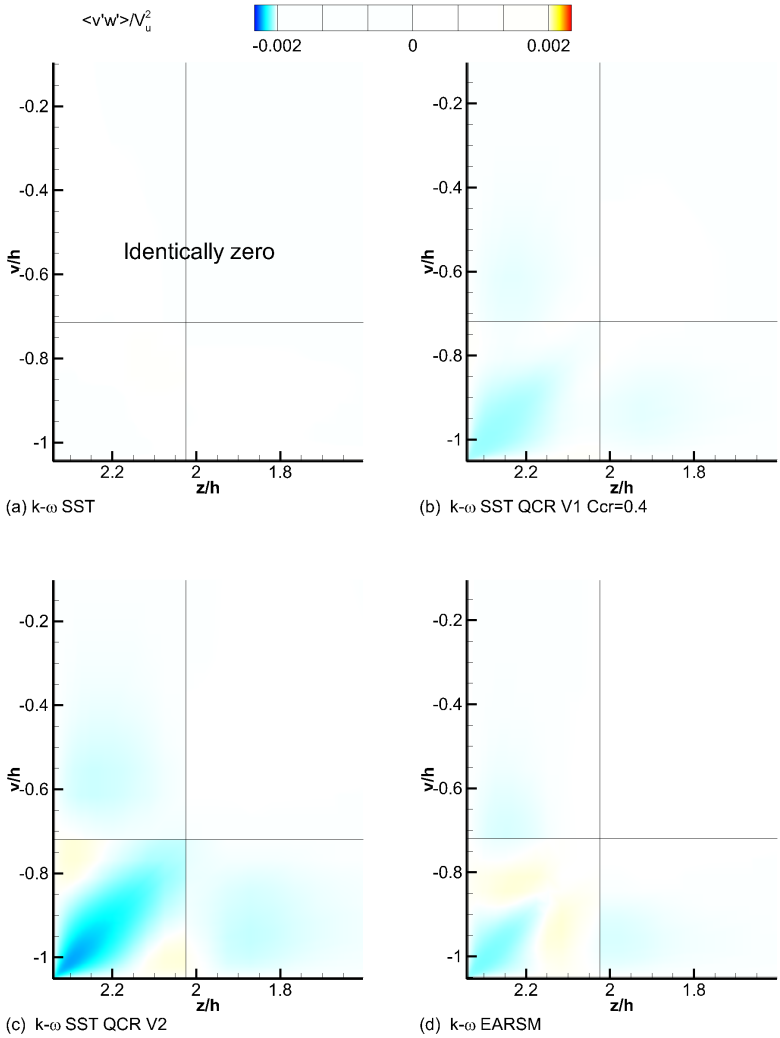

Figure 3.54: Reynolds stress $\overline{v'w'}/V_u^2$ contours for the $k-\omega$ SST $C_{cr1} = 0.0$, $k-\omega$ SST QCR V1 , $k-\omega$ SST QCR V1 $C_{cr1} = 0.2$, and the $k-\omega$ SST QCR V1 $C_{cr1} = 0.3$ models.

The EARSM and the QCR V1 model predict similar levels of anisotropy of the $\overline{v'v'}/V_u^2$ and $\overline{w'w'}/V_u^2$ stresses. The QCR V2 model increased the anisotropy levels significantly compared to the EARSM and the QCR V1 models. For both QCR models the regions of anisotropy extend further away from the wall than for the EARSM model. The latter features small regions of higher anisotropy near the corner bisector. Nevertheless the existence of anisotropy is responsible for the generation of the secondary flows and the reduction of the corner separations.

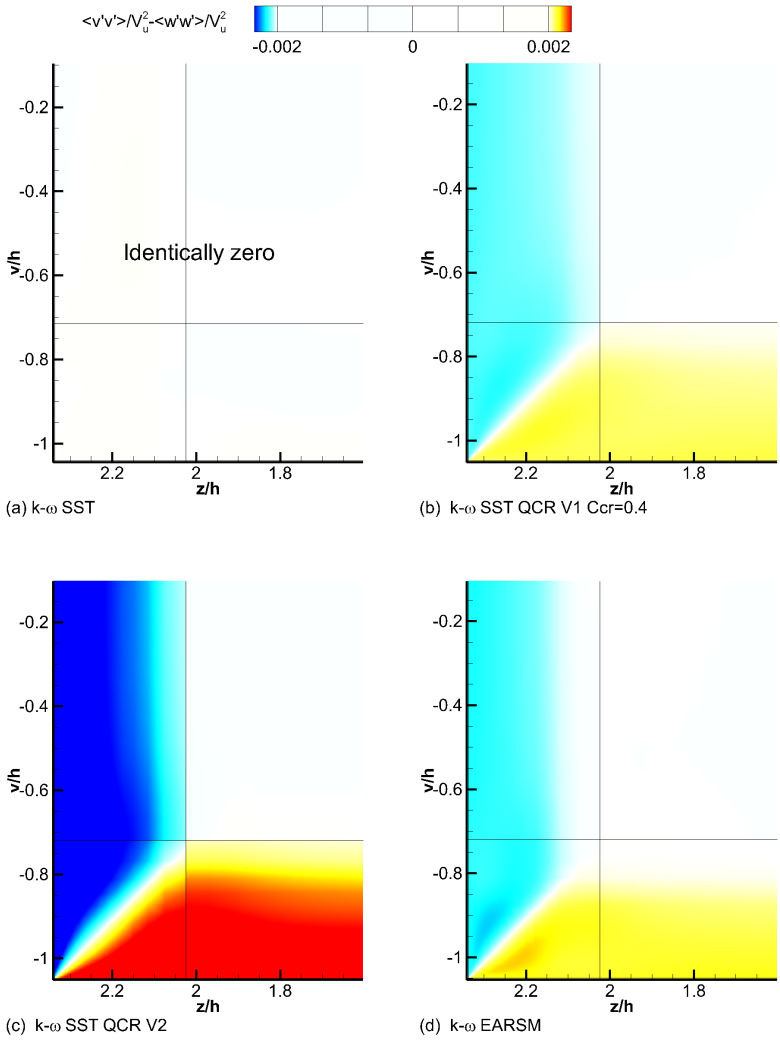

Figure 3.55: Reynolds stress $(\overline{v'v'} - \overline{w'w'})/V_u^2$ contours for the $k-\omega$ SST $C_{cr1} = 0.0$, $k-\omega$ SST QCR V1 , $k-\omega$ SST QCR V1 $C_{cr1} = 0.2$, and the $k-\omega$ SST QCR V1 $C_{cr1} = 0.3$ models.

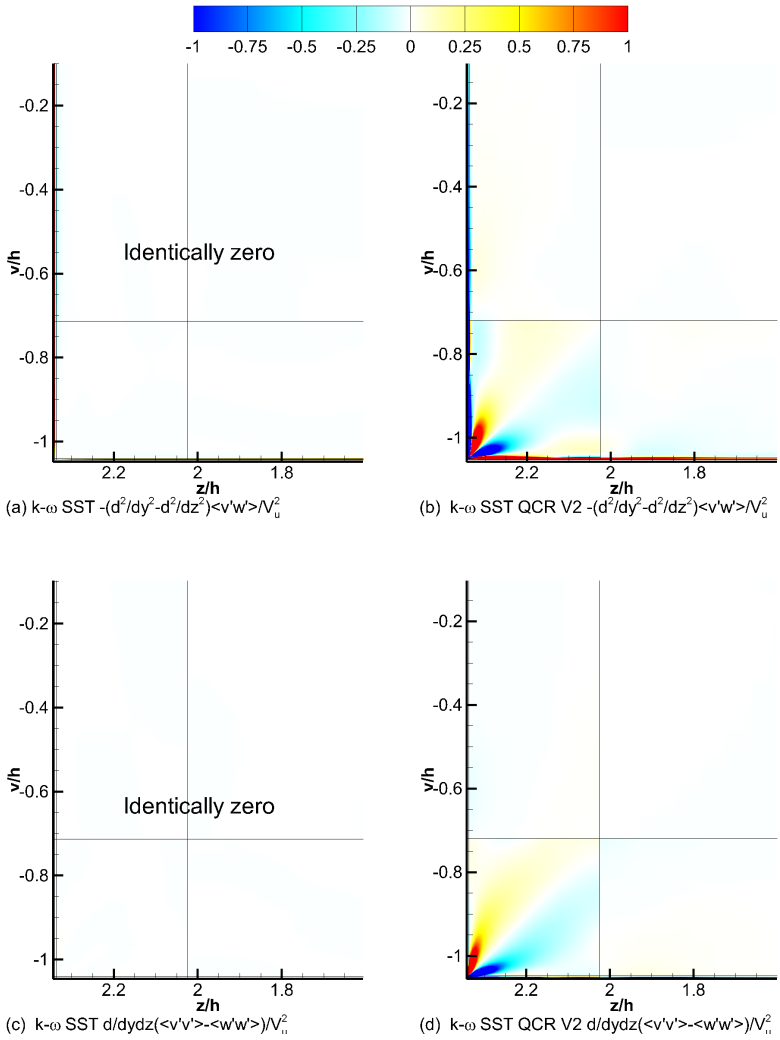

Figure 3.56: Comparison of the $k-\omega$ SST and $k-\omega$ SST QCR V2 $\frac{\partial}{\partial y \partial z}(\overline{v'v'} - \overline{w'w'})/V_u^2$ and $-(\frac{\partial^2}{\partial y^2} - \frac{\partial^2}{\partial z^2})\overline{v'w'}/V_u^2$ contours.

Comparing QCR V1 $C_{cr1} = 0.4$ and EARSM

Figure 3.57 compares the $k-\omega$ SST QCR V1 $C_{cr1} = 0.4$ model with the $k-\omega$ SST and the $k-\omega$ EARSM models. The effect of accounting for the secondary, corner, flows is clearly visible. If the flows are not accounted for by the turbulence model, wall pressure oscillations are present which are not in agreement with the experiment. This is further indicated by the centreline Mach number which shows stronger flow expansion downstream of the first shock and stronger subsequent shocks. The difference in x_r between the two models is approximately 2% of the domain length and the boundary layer is considerably thicker for the $k-\omega$ SST QCR V1 $C_{cr1} = 0.4$ model. The boundary layer is $\delta_r = 5.0$ mm thick, approximately 1.1 mm thicker. Comparison of the streamwise vorticity contours upstream of x_r in figure 3.58 shows that the $k-\omega$ EARSM has qualitatively similar vorticity strengths, however, the extent of the positive and negative vorticity regions is smaller. The smaller extent of the regions can be related to the larger corner separations compared to the $k-\omega$ SST QCR V1 $C_{cr1} = 0.4$ model. Both models, however, reduce the corner separations considerably as shown in figure 3.59.

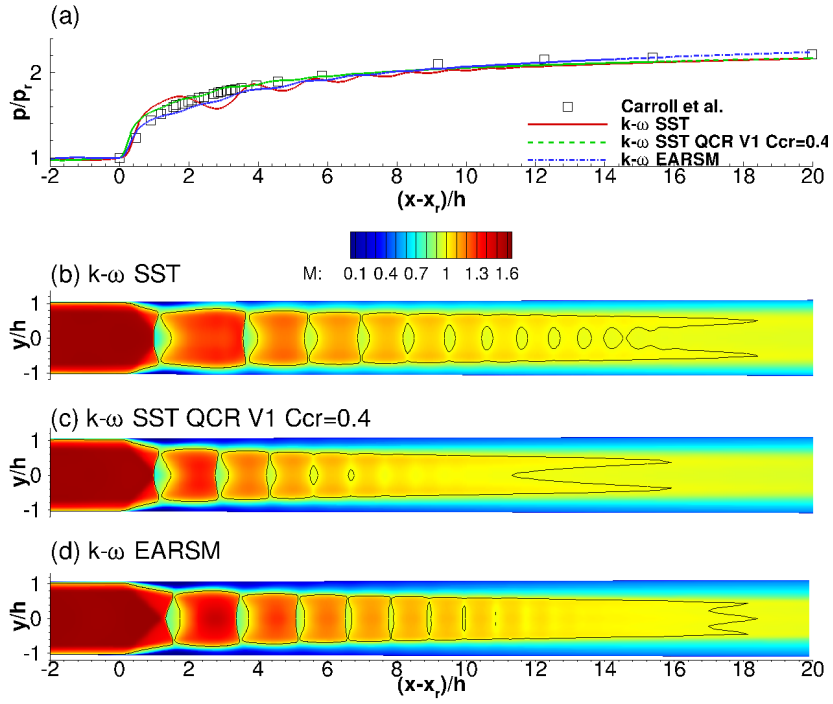

Figure 3.57: Wall pressure and Mach number contours for the $k-\omega$ SST , $k-\omega$ SST QCR V1 $C_{cr1} = 0.4$, and the $k-\omega$ EARSM models.

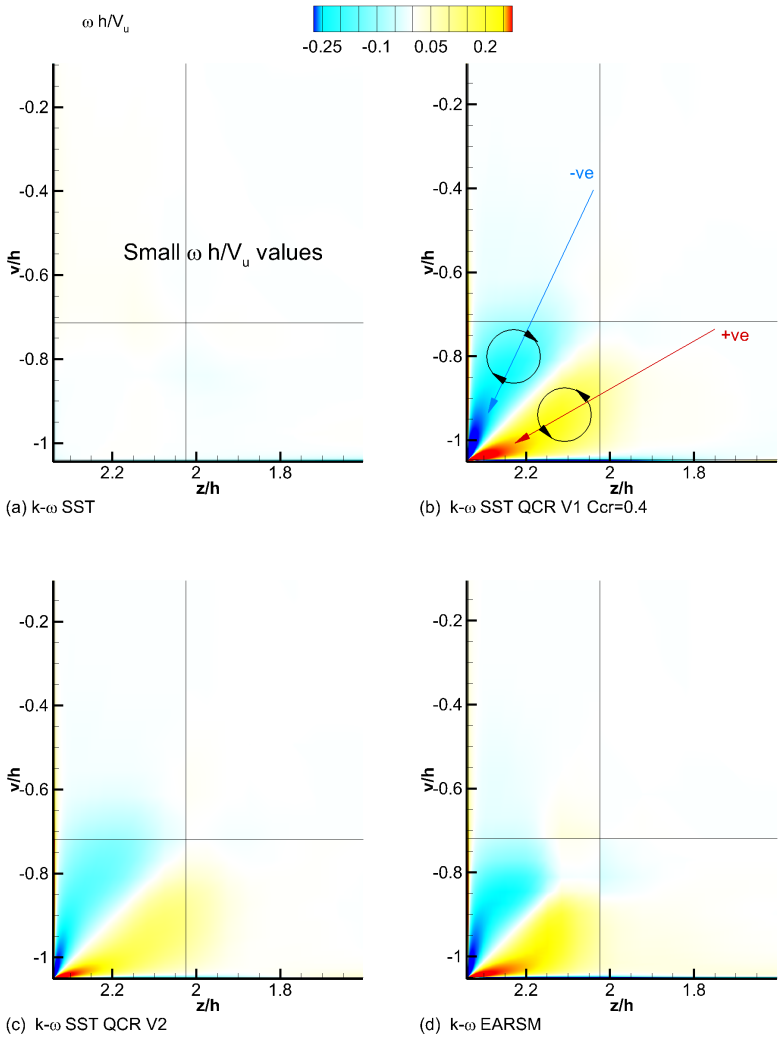

Figure 3.58: Streamwise vorticity contours for the $k-\omega$ SST , $k-\omega$ SST QCR V1, $k-\omega$ SST QCR V2, and the $k-\omega$ EARSM models.

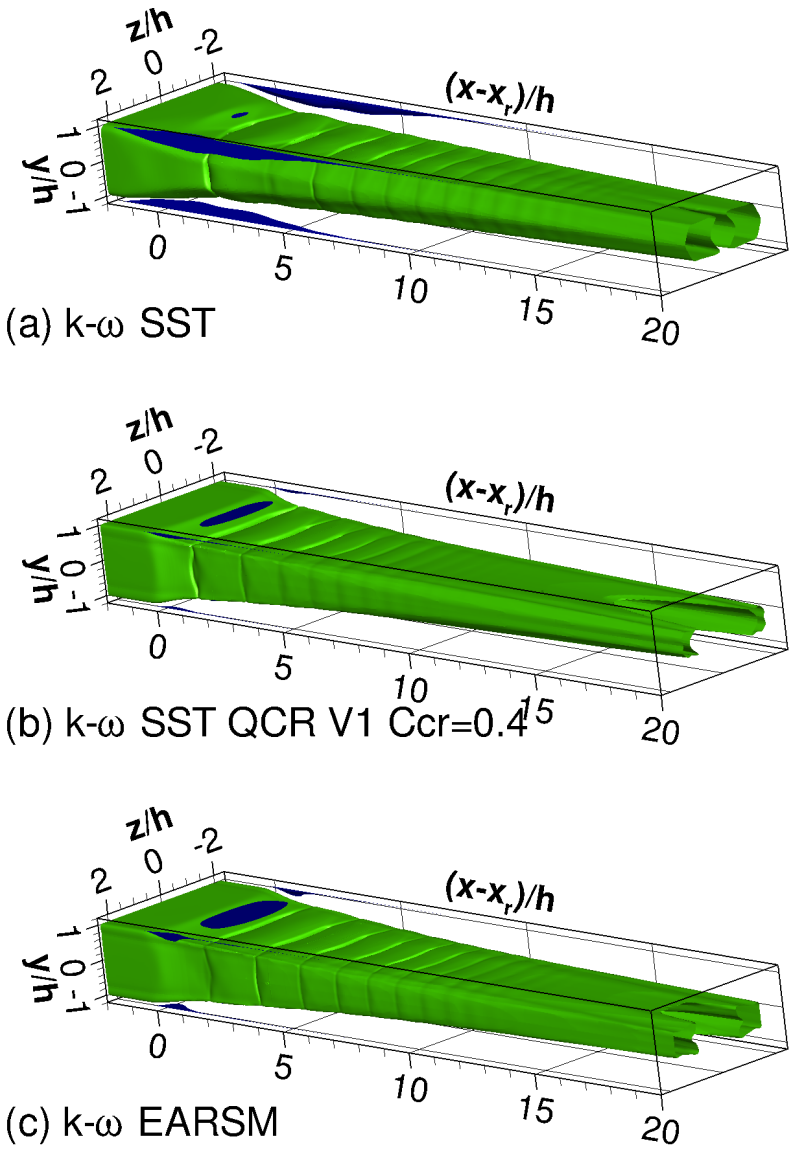

Figure 3.59: Separation $u/V_u = 1 \times 10^{-3}$ and sonic $M = 1$ iso-surfaces for the $k-\omega$ SST , $k-\omega$ SST QCR V1 $C_{cr1} = 0.4$, and the $k-\omega$ EARSM models.

3.2.4 Turbulent kinetic energy limiters

Application of the P_k limiter

LES simulations by Quaatz *et al.* [107] of the shock train experiment by Gawehn *et al.* [51] show higher values of k at the centreline. The higher values were due to the resolved shock motion which cannot be reproduced by steady-state RANS simulations. The RANS simulations of the experiment by Carroll *et al.* [26] presented so far do not use the turbulent kinetic energy production limiter - P_k. The P_k limiter of the k-ω family of equations is given by:

$$P_k = min\left(P, 20\beta^* \rho \omega k\right), \tag{3.7}$$

where P is given by $\tau_{ij}\frac{\partial u_i}{\partial x_j}$, β^* is a model constant, and ω and k are the specific dissipation rate an the turbulent kinetic energy. The function of the limiter is to limit the production of k in areas where the flow gradients are large. The effect on the limiter, particularly in the region downstream of the normal portion of the first shock, was investigated for the QCR V1 $C_{cr1} = 0.4$ model. The model was selected due to the region of high k values downstream of the normal portion of the first shock. The wall pressures for both models, shown in figure 3.60 (a) and the onset of the interactions, x_r, are identical.

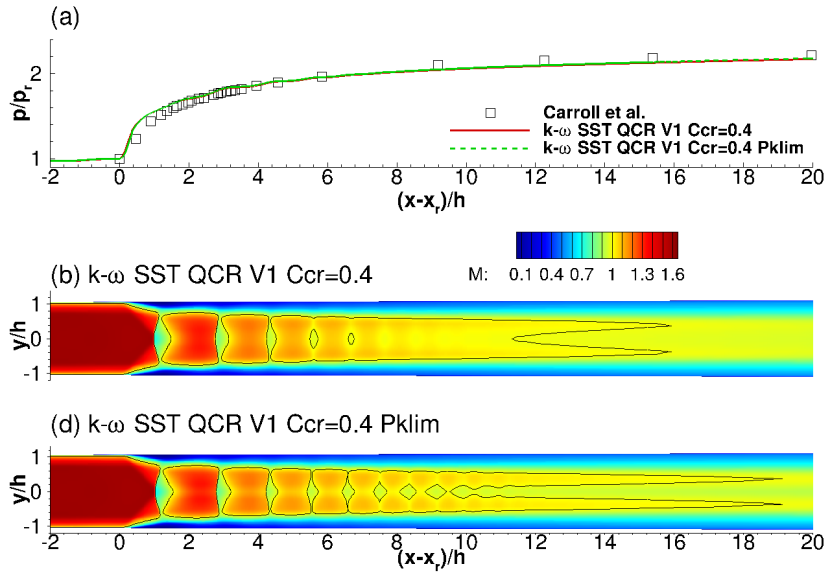

Figure 3.60: Wall pressure and Mach number contours for the $k-\omega$ SST QCR V1 $C_{cr1} = 0.4$ model with and without the P_k limiter.

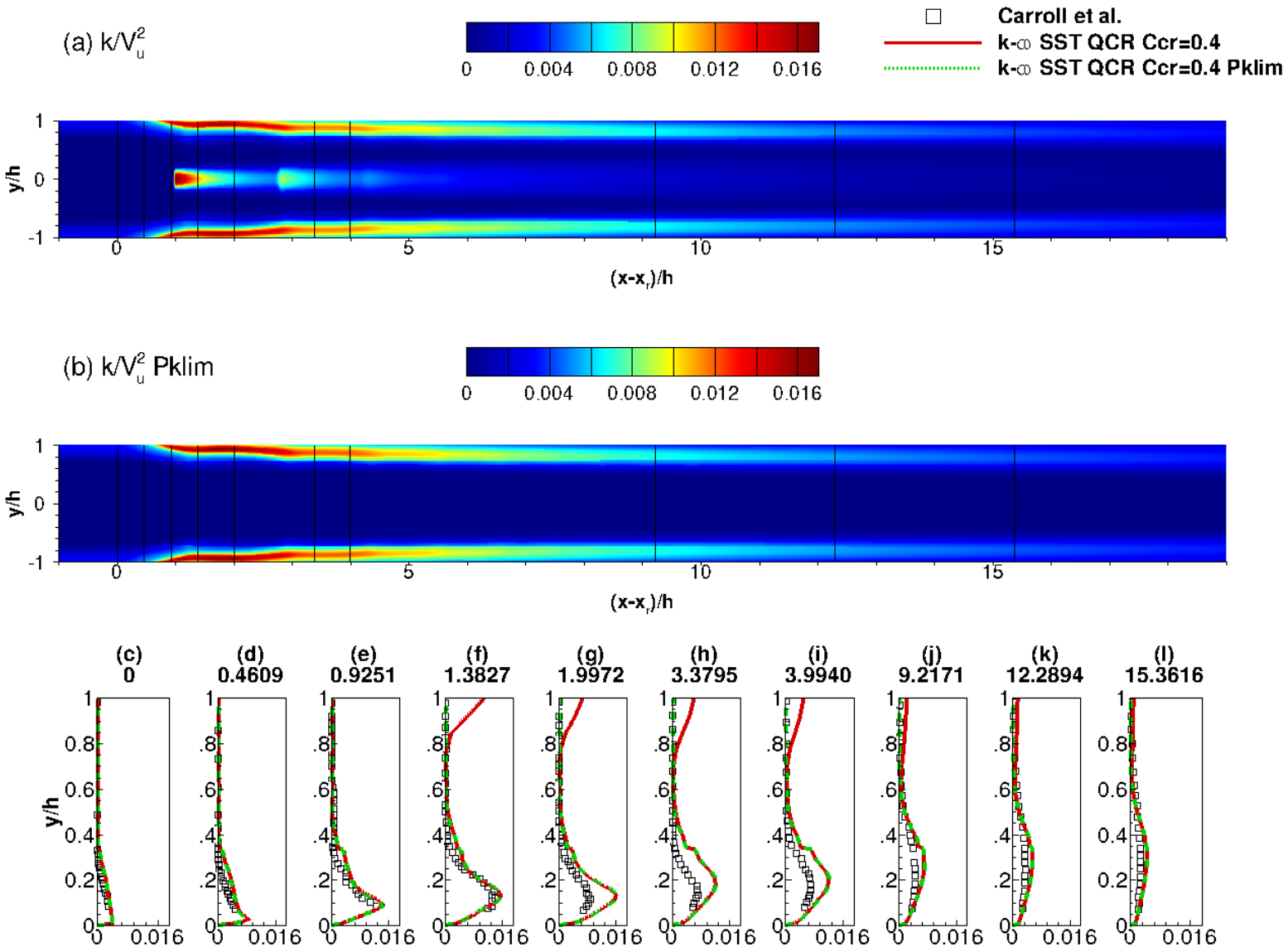

Figure 3.61: Turbulent kinetic energy k/V_u^2 contours for the $k-\omega$ SST QCR V1 $C_{cr1} = 0.4$ model with and without the P_k limiter.

The spacing between the first two shocks in the shock train is also identical and is approximately 1.77 non-dimensional distances. Figure 3.61 shows the k/V_u^2 contours with (a) and without (b) the P_k limiter. The main effect of activating the P_k limiter is to remove the high k values downstream of the normal portion of the first shock. No significant differences away from the centreline ($y/h < 0.8$) in the k/V_u^2, $\overline{u'u'}/V_u^2$, $-\overline{u'v'}/V_u^2$, and $\overline{v'v'}/V_u^2$ profiles were observed. This shows that the main effect of the P_k limiter is close to the centreline, where large gradients due to the shocks are present.

Shock spacings

The shock spacings of the QCR V1 $C_{cr1} = 0.4$, QCR V1 $C_{cr1} = 0.4$ Pklim and QCR V1 $C_{cr1} = 0.4$ p=1.05p simulations were compared against the experiment. The spacings were obtained either from the density gradient magnitude or from the experimental Schlieren and were nondimensionalised with respect to the spacing between the first and second shocks in the shock train, Δ, shown in figure 3.62. The nondimensionalisation was performed in order to reduce potential errors arising from the scaling of the experimental Schlieren image. Table 3.10 lists the spacings and figure 3.63 compares the spacings. Empty cells correspond to no measurement due to the difference in the number of downstream shocks between the experiment and the simulations. The effect of the P_k limiter on the d_1 is small. Without the limiter $d_1 = 1.7766h$ and with the limiter $d_1 = 1.7662$. The relative reduction of d_1 is approximately 0.5%. The $d_2\Delta$ distance is also weakly affected by the limiter. As the last shock for the case without the limiter is very weak, comparison of $d_3\Delta$ is difficult, nevertheless, $d_3\Delta$ and $d_3\Delta$ are overpredicted by approximately 11% and 25% when compared to the experiment.

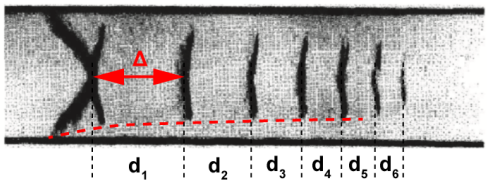

Figure 3.62: Definition of the distance Δ used to nondimensionalise the distances between the shocks; red-line indicates the approximate boundary layer edge.

The simulation with 5% increased back (exit) pressure relocates the shock train upstream where the flow confinement agrees more closely with the experimental one. Better agreement in the d_2/Δ distance between the simulation and the experiment is observed, however, d_2/Δ is still overpredicted by approximately 5%. The same observation holds for the d_3/Δ distance which is overpredicted by approximately 17%. The reduction of the over predictions by better matching the flow confinement prior to the interaction shows the importance of this

Table 3.10: Distances between the shocks; $d_1 = \Delta$.

Case	d_1/Δ	d_2/Δ	d_3/Δ	d_4/Δ	d_5/Δ	d_6/Δ
$k-\omega$ SST QCR V1 $C_{cr1} = 0.4$	1.00	0.81	0.70			
$k-\omega$ SST QCR V1 $C_{cr1} = 0.4$ Pklim	1.00	0.81	0.67	0.59		
$k-\omega$ SST QCR V1 $C_{cr1} = 0.4$ p=1.05p	1.00	0.77	0.64			
$k-\omega$ SST QCR V1 $C_{cr1} = 0.4$ kwclip	1.00	0.79	0.67	0.57		
Experiment	1.00	0.73	0.55	0.43	0.37	0.31

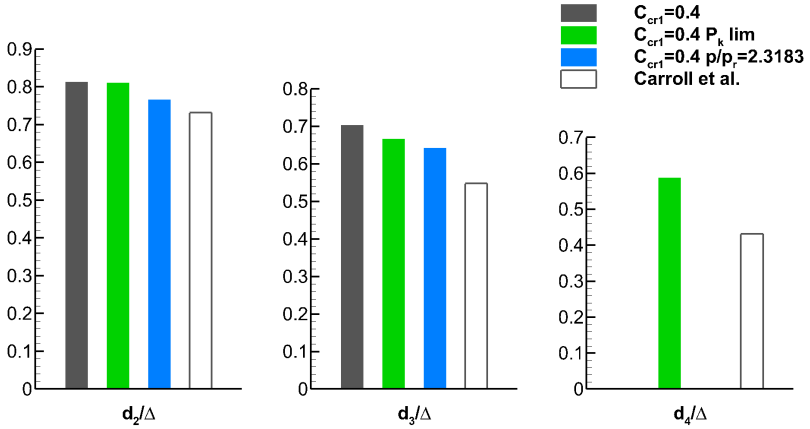

Figure 3.63: Comparison of shock spacings.

parameter. Sidewall boundary layers also affect the interaction, however, they were not characterised in the experiment which makes it impossible to compare the flow confinement in the $x-z$ plane.

Limiting the source terms in the k and ω equations away from walls

If one refers to the strong normal shock interaction schematic shown in figure 1.7 in chapter 1, the region between the triple point and the wall experiences increased stagnation pressure recovery later followed by a decrease due to the viscous losses associated with the boundary layer. Above the triple point, downstream of the normal portion of the shock, the stagnation pressure loss corresponds to a perfect fluid. As seen from previous simulations, the k/V_u^2 in the core flow is small and in the absence of a P_k limiter, the gradients imparted by the shocks are perceived as production. Nevertheless, no differences were observed in the wall pressure, the interaction onset, and the distance between the first and second shocks when the P_k limiter was used. Since k/V_u^2 in the core flow is small a method for removing the production and destruction terms from the k and ω equations in this region is presented. The modified k and ω transport equations for the family of $k-\omega$ turbulence models are

$$\begin{aligned}\frac{\partial(\rho k)}{\partial t}+\frac{\partial(\rho u_j k)}{\partial x_j}&=\frac{\partial}{\partial x_j}\left[(\mu+\sigma_k\mu_t)\frac{\partial k}{\partial x_j}\right]\\ \frac{\partial(\rho \omega)}{\partial t}+\frac{\partial(\rho u_j \omega)}{\partial x_j}&=\frac{\partial}{\partial x_j}\left[(\mu+\sigma_\omega\mu_t)\frac{\partial \omega}{\partial x_j}\right]\end{aligned} \tag{3.8}$$

The following function is used to retain or discard the production and destruction terms

$$F_{clip}=\frac{|\overline{\Omega}_{ij}|}{|\overline{S}_{ij}|} \tag{3.9}$$

where $|\overline{\Omega}_{ij}|$ and $|\overline{S}_{ij}|$ are the vorticity and shear stress norms. Near the wall F_{clip} is ≈ 1 and the production and destruction terms are retained. Away from the wall, near the centreline of the duct F_{clip} is ≈ 0 and the production and destruction terms are discarded. The approximate Jacobian, J, of the turbulence equations is

$$J\approx\begin{cases}\begin{bmatrix}-\beta^*\rho\omega & -\beta^*\rho k\\ 0 & -2\beta\rho\omega\end{bmatrix}, \text{for } F_{clip}\geq C\\ 0, \text{for } F_{clip}<C\end{cases} \tag{3.10}$$

A simulation with the QCR V1 $C_{cr1}=0.4$ model was performed where C was set to 0.6. Figure 3.64 shows the F_{clip} contours.

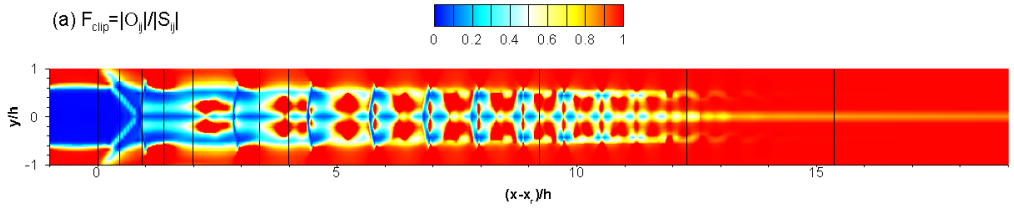

Figure 3.64: F_{clip} contours for the $k-\omega$ SST QCR V1 $C_{cr1}=0.4$ model.

Upstream of the interaction values of $F_{clip}\approx 1$ are observed in the near wall region. At the centreline the values of F_{clip} are negligible. Increased values of F_{clip} are observed as the flow passes through the leading leg of the λ-foot and downstream of the Mach stem. A pattern is observed where regions of high F_{clip} values are present upstream of the subsequent shocks in the shock train. These regions of higher F_{clip} values are associated with the slip line emanating from the triple point of the first shock which acts as a source of vorticity. As the boundary

layer thickens the high values of F_{clip} near the wall spread towards the centreline. After 13 non-dimensional distances the values of F_{clip} are approximately 1 throughout the entire duct height H. The onset of the interaction, x_r, moved upstream by approximately 1% compared to the QCR V1 $C_{cr1} = 0.4$ with the P_k limiter. Similarly to the simulation with the limiter, the distances between shocks, listed in table 3.10, were reduced. Nevertheless, d_2/Δ, d_2/Δ, and d_3/Δ were still overpredicted when compared to the experiment. The distance between the first and second shocks in the shock train was approximately $\Delta = 1.9462h$. Compared to the QCR V1 $C_{cr1} = 0.4$ with and without the P_k limiter, the distance increased by 10 %. Figure 3.65 compares the wall pressures and the Mach number contours of the simulations with the limiter and the $F_{clip} = 0.6$.

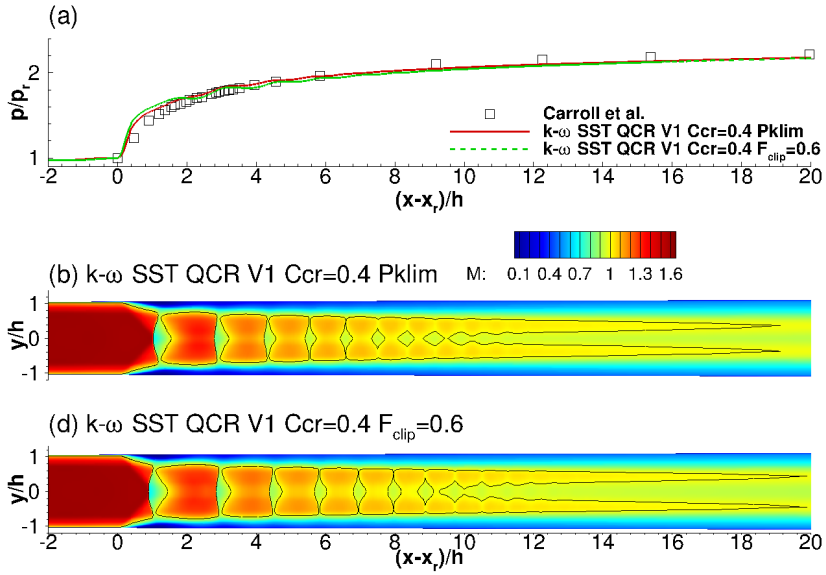

Figure 3.65: Wall pressure and Mach number contours for the P_k limiter and $F_{clip} = 0.6$ simulations.

The $F_{clip} = 0.6$ simulation predicts a steeper pressure rise at the beginning of the interaction a result of the larger Mach stem. The increase in Δ is clearly seen from the Mach contours. The number of downstream shocks predicted by the simulations differs, however, compared to the simulations without the P_k limiter both simulations predict more downstream shocks.

3.2.5 Scale-resolving simulations

From existing studies of multiple shock wave boundary layer interactions the following conclusions were drawn in chapter 1:

- Large eddy simulations (LES) still require significant resources due to the near-wall

resolution requirements. To reduce the requirements the Reynolds number of the problem is often lowered, however, its decrease affects the predicted flow.

- Wall-modelled LES has not been used as much as wall-resolved LES, however, some studies show that favourable results can be obtained at a fraction of the computational cost associated with LES.

Both the LES, WMLES, and hybrid RANS/LES methods require the generation of realistic turbulent inflow. Shallow separations often do not result in flow instabilities strong enough to trigger the scale resolving mode of the hybrid RANS/LES methods. The requirement of turbulent inflow further adds to the expense and complexity of such simulations. Nevertheless, the implemented synthetic turbulence method (SEM) detailed in appendix A was used to generate turbulent inflow for spanwise-periodic simulations of the multiple normal shock interaction by Carroll *et al.* [26] The known implicit detached delayed eddy simulation (IDDES) method by Gritskevich *et al.* [60] as well as a method using the blending function proposed by Edwards [46] were investigated.

Numerical Setup

A three-dimensional (spanwise-periodic) numerical domain of the same dimensions as the one detailed in chapter 3 was used. The domain consisted of 1188 blocks and featured $N_x = 2277$, $N_y = 168$, and $N_z = 26$ points in the x-, y-, and z-directions. The domain was non-dimensionalised with the duct half-height h and the minimum and maximum spacings were $(\Delta x/h)_{min} = 0.01h$, $(\Delta x/h)_{max} = 0.3$, $(\Delta y/h)_{max} = 1 \times 10^{-5}$, $(\Delta y/h)_{max} = 0.04$, and $(\Delta x/h) = 0.02$. Simulation of the full domain with the k-ω SST turbulence model was performed. The simulation was run until the flux residuals were reduced to at least 1×10^{-5}. From the obtained solution, mean profiles including the Reynolds stresses were extracted at $x/h = 20$. The profiles were then used to generate inflow turbulence using the synthetic eddy method detailed in Appendix A. The method scales the velocity fluctuations, caused by the synthetic Eddies, and adds them to the mean velocity profiles. The eddy sizes were constant and were set to $\sigma_x = 0.06$, $\sigma_y = \sigma_z = 0.03$. The eddy sizes depend on:

- The maximum cell size at $x/h = 20$ which was approximately ≈ 0.03. The size of the eddy must be atleast the size of the maximum cell.

- The maximum non-dimensional timestep Δt_{max}. The eddies can be isotropic $\sigma_x = \sigma_y = \sigma_z = 0.03$, however, this imposes a restriction on the maximum timestep Δt_{max}.

The maximum non-dimensional timestep was found to be $\Delta t = 0.03$ as it took the eddies approximately 4 unsteady steps to convect from the upstream SEM plane to the downstream SEM plane. Smaller timesteps did not have a significant effect on the reconstructed stresses. Larger timesteps reduced the quality of the reconstruction. Very large timesteps destroyed the reconstruction completely as it only required one unsteady step to convect the eddies through the SEM volume. Figure 3.66 shows the reconstructed stresses for a non-dimensional timestep of $\Delta t = 0.03$ and $\Delta t = 0.05$. From the figure, it is seen that the quality of the reconstructed stresses reduces with increasing timestep. A non-dimensional time step of $\Delta t = 0.03$ is equivalent to a dimensional time step of 1.0516×10^{-6} s. Based on the duct half-height at the inlet ($h = 16.275$ mm) one flow-throughout time (from $x/h = 0$ to $x/h = 46.3188$) would require at least 1544 unsteady steps. Due to computational restrictions, the slightly larger non-dimensional time step of $\Delta t = 0.05$ was selected. A total of 927 unsteady steps were required for one flow-through time at this time step. A profile file specifying ρ, u, v, w, p, k, ω was generated for every unsteady timestep by the SEM utility. Figure 3.67 shows the u, v, and w velocities from the profile file at the 100th unsteady timestep. To perform the scale resolving simulations of the multiple shock interaction the RANS domain was sliced at the $x/h = 20$ location. This location became the new domain inlet, where the profiles containing the fluctuations by the SEM method were specified. As a result, the domain considered by the hybrid RANS/LES simulations extended from $x/h = 20$ to $x/h = 46.3188$. Approximately 527 unsteady steps at $\Delta t = 0.05$ were required for one flow-through time.

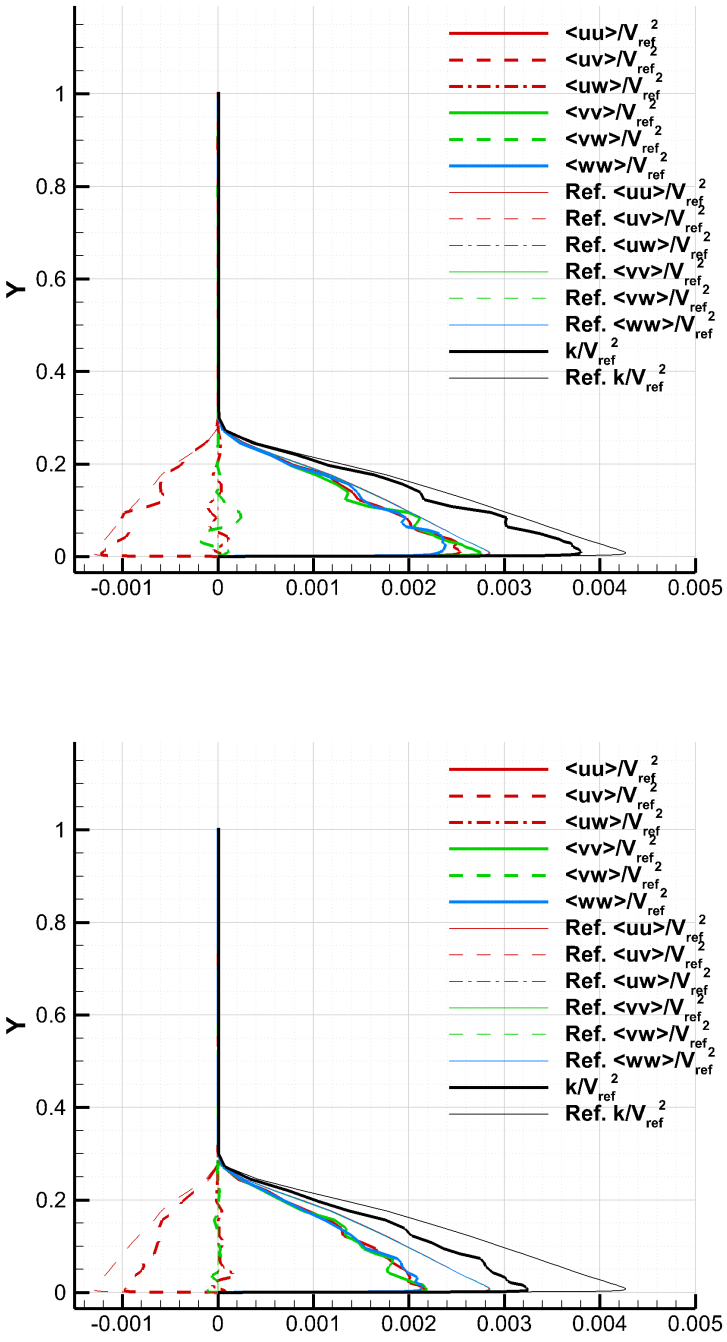

Figure 3.66: Reconstructed stresses for a non-dimensional timestep of $\Delta t = 0.03$ (top) and $\Delta t = 0.05$ (bottom).

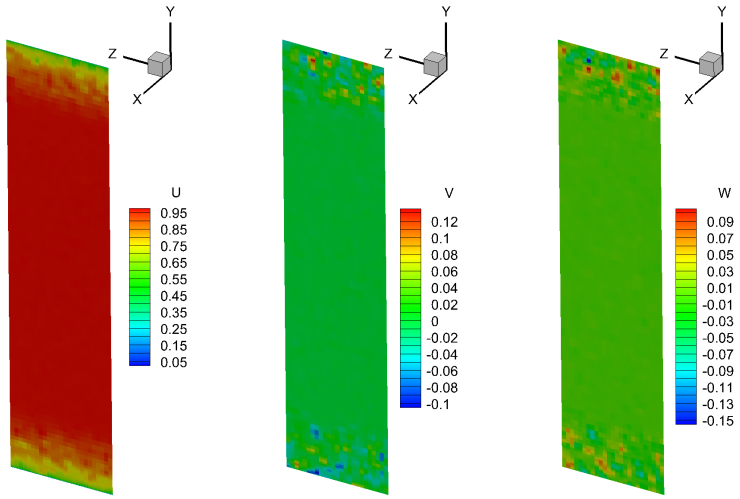

Figure 3.67: Inlet profiles featuring velocity fluctuations superimposed on the mean velocities.

Results and Discussion

First, an IDDES simulation of the multiple shock interaction was performed. The IDDES method was selected as it can act as a wall-modelled LES if inflow turbulence is provided and can reduce to DDES if not. The DES and DDES methods usually require the streamwise grid spacing to be of the order, or larger than, the boundary layer thickness. This allows the RANS mode to be maintained within the boundary layer and LES mode outside. For internal flows with thick boundary layers and shocks, where the streamwise spacing can be significantly smaller than the thickness of the boundary layer. Such a case renders the DES and DDES methods unsuitable. The ability of the IDDES to act as a wall modelled LES is preferred in such cases. Due to computational constraints, only surface pressure averaging was performed. Figure 3.68 shows the instantaneous Q-criterion coloured by the Mach number after two flow-through times and the wall pressure averaged over one flow-through-time.

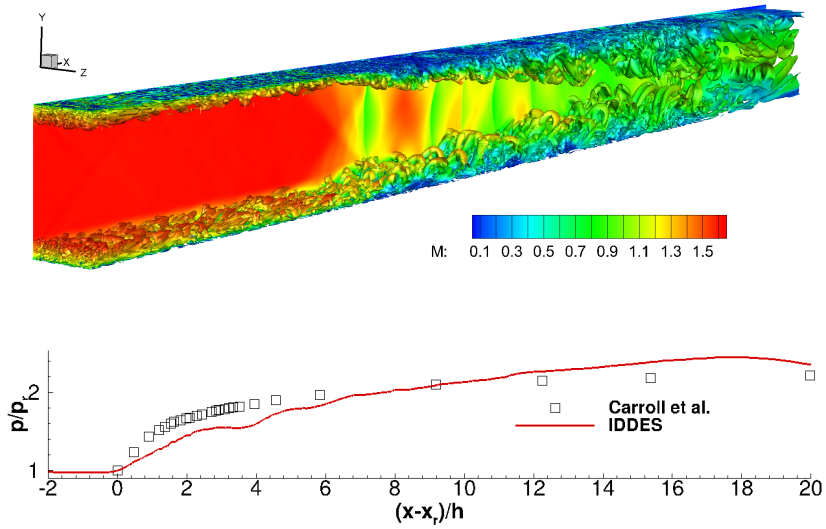

Figure 3.68: Q-criterion ($Q = 0.03$) colored by the Mach number at two flow-through times and wall pressure averaged over one flow-trough time.

The velocity fluctuations generated by the SEM are sensed by the IDDES method, however, the initial shock did not feature the distinct λ-foot structure and the pressure rise at the beginning of the interaction was smeared and underpredicted by the method. A possible explanation for the underprediction was the state of the boundary layer upstream of the interaction. The mean velocity profiles, as well as the gradients of the velocities and turbulence quantities, were obtained from the $k-\omega$ SST simulation at $x/h = 20$ to investigate where the switch between the RANS and LES method occurs. Figure 3.69 shows the mean velocity profiles at $x/h = 20$ and the blending function of the IDDES method - $\overline{f}_b$.

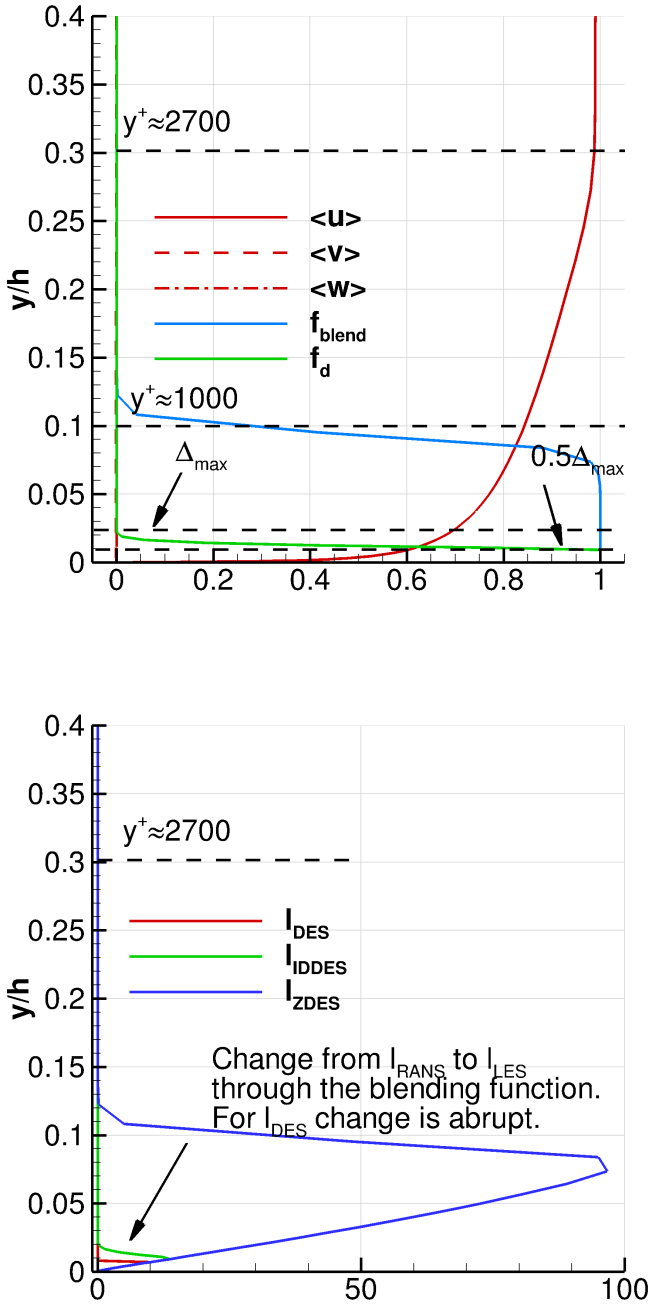

Figure 3.69: Mean velocity profile from $k-\omega$ SST and blending functions.

The $\overline{f}_b$ function (shown in figure 3.69) is responsible for the switch between the RANS length scale, l_{RANS}, and the LES length scale l_{LES}. The switch occurs smoothly in contrast to the DES method where the switch is abrupt. For the IDDES the switch was observed to occur between Δ_{max} and $0.5\Delta_{max}$. The maximum spacing, Δ_{max} is defined as the maximum of the local spacings - δ_x,δ_y,δ_z. Since the simulations were spanwise periodic, and the spacing in the z-direction was constant, the maximum spacing near the wall was $\Delta_{max} = 0.02$. This resulted in a switch between RANS and LES at approximately $y/h \approx 0.015$.

The boundary layer in a wall-bounded turbulent flows can be divided into two layers - an inner layer which consists of small scale structures and an outer layer which consists of large-scale structures. As detailed by Deck et al. [32] to resolve the large-scale structures of the outer layer and model the structures in the inner layer, the RANS to LES switch should occur at the outer edge of the inner layer. Figure 3.70 compares the mean streamwise velocity to the law of the wall.

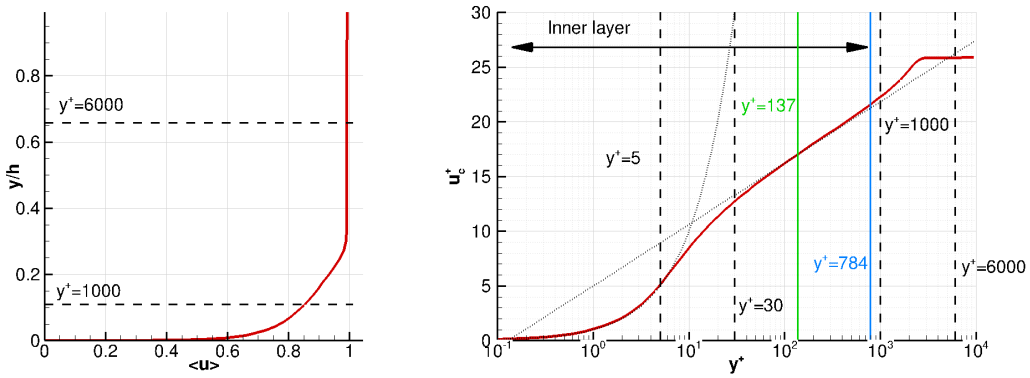

Figure 3.70: Comparison of the mean streamwise velocity to the law of the wall.

The switch between RANS and LES at $y/h \approx 0.015$ corresponds to $y^+ = 137$, approximately. The switch, therefore, is close to the inner edge of the log-law layer. Since the structures in the inner layer are small, the switch to LES at this location requires a finer grid capable of resolving the small structures. Han et al. [61] observed that a switch between RANS and LES near the inner edge of the log-law layer leads to skin friction underprediction. He considered a flat-plate boundary layer at a Reynolds number based on the boundary layer thickness of $Re_\delta = 2.5 \times 10^5$. From the methods that he employed, the IDDES resulted in the largest underprediction of C_f. Improved results were observed with a zonal DES and the hybrid RANS/LES method proposed by Edwards et al. [46]. Wall-modelled LES simulations of the experiment by Carroll et al. [26] were performed by Vane et al. [142] at the experimental Reynolds number of $Re_\delta = 1.62 \times 10^5$. The matching location between the LES and the

wall model was placed at approximately $y/h \approx 0.05$. The location corresponded to a y^+ of approximately 500. Figure 3.70 shows that the outer edge of the inner layer is located at approximately $y^+ = 1000$. The current switch location for the IDDES method occurs at approximately $y^+ = 137$, which is closer to the inner edge of the log-law layer. To shift the switch location towards the outer edge, a hybrid RANS/LES simulation with the blending function f_{blend} by Edwards et al. [46] was performed. The blending function f_{blend} is given by:

$$f_{blend} = \frac{1}{2}\left(1 - \tanh\left[5\left(\frac{\kappa}{\sqrt{C_\mu}}\eta^2 - 1\right) + \phi\right]\right), \tag{3.11}$$

where $\eta = d/\sqrt{(\alpha\chi)}$ and $\chi = \sqrt{\nu/(C_\mu\omega)}$ and ϕ is a constant set to 2.2976 so that $f_{blend} = 0.99$ occurs at $\kappa\eta^2 = \sqrt{C_\mu}$. The average location of the RANS to LES switch is defined by the constant α. In figure 3.69, $\alpha \approx 0.05$ which locates the switch around $y/h \approx 0.086$. This corresponds to an approximate y^+ value of 784. Similarly to the IDDES method the blending of the RANS and LES length scales is achieved by:

$$l_{blend} = f_{blend} l_{RANS} + (1 - f_{blend}) l_{LES} \tag{3.12}$$

The length scales resulting form the DES and IDDES blending functions and the blending function by Edwards et al. [46] are shown in figure 3.69.

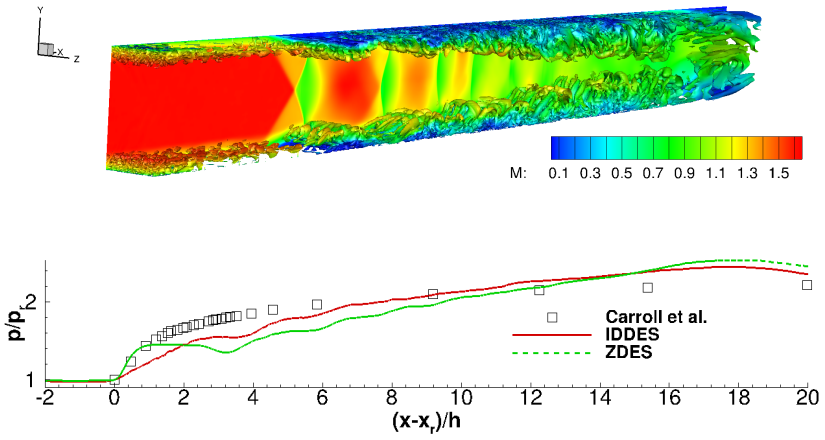

Figure 3.71: Q-criterion ($Q = 0.03$) colored by the Mach number at two flow-through times and wall pressure averaged over one flow-trough time.

The f_{blend} function retains the larger RANS length scale up to $y/h \approx 0.05$ non-dimensional distances away from the wall. Using the modified method, spanwise periodic simulations

of the multiple shock interaction experiment by Carroll et al. [26] were performed. The simulations were run for three flow-through times and averaging was performed over the last flow-through time. Figure 3.71 shows the instantaneous Q-criterion iso-surfaces ($Q = 0.03$) coloured by the Mach number and the averaged lower wall pressure. The wall pressure rise at the beginning of the interaction was captured better, however, downstream, similarly to the IDDES results, the wall pressure was underpredicted. From the iso-surfaces of the Q-criterion, it was observed that the resolved structures start to disappear downstream of the inlet, just before the onset of the interaction. The higher values of k near the wall, which extended up to $y/h \approx= 0.1$, were the cause for the disappearance of the structures introduced by the SEM. A re-thinking of the blending function is necessary to sustain the SEM turbulent structures.

3.3 Chapter summary

Improved agreements in the wall pressure between the simulations and the experiments of Dèlery *et al.* [33] and Carroll *et al.* [23] was observed when the $k-\omega$ EARSM turbulence model was used. The $k-\omega$ EARSM model which uses the constitutive relation by Wallin and Johansson [144] accounts for the secondary flows present in duct corners. The vortices in this region supply high momentum fluid from the core flow and reduce the size of the corner separations. Since the corner separations affect the separation at the centreline in confined flows, reduction of the corner separation resulted in an increase of the centreline separation. Two additional models - the $k-\omega$ SST QCR V1 and the $k-\omega$ SST QCR V2 based on the QCR by Spalart [122] and the QCR by Sabnis [113] were implemented in the HMB3 flow solver. Both models reduced the separations at the corner and showed improved agreements in the wall pressure compared to the $k-\omega$ SST model. The $k-\omega$ SST QCR V2 model was observed to predict higher levels of normal stress anisotropy compared to the QCR V1 and the EARSM models. Variation of the $k-\omega$ SST QCR V1 C_{cr1} model constant showed that a constant of $C_{cr1} = 0.4$ improves the prediction by reducing the corner separations even further. Inclusion of the P_k limiter did not have significant effect on the wall pressure and onset - the wall pressure and the onset of the interaction were almost identical. The higher values of k/V_u^2 at the centreline, downstream of the first and subsequent shocks were removed by the limiter. The spacing of the shocks did not vary significantly and it was overpredicted when compared to the experiment. Disregarding the production and destruction terms in the k and ω equations based on a function taking into account the ratio of rotation and strain had similar effect to the one of the limiter - no high values of k/V_u^2 were present at the centreline. The predicted wall pressure was favourable although a slight overprediction at the beginning of

the interaction was present. The spacing of the shocks, however, did not show improvement compared to the case with the limiter. Further simulations should be performed to investigate the effect of different F_{clip} values. The current limiter uses only the strain and rotation terms. More advanced limiters, based on other or additional flow quantities might lead to further improvements.

The IDDES and ZDES simulations showed that:

- Switching from RANS to LES near the inner edge of the log-law layer is not favourable as the grid in this region is not fine enough to resolve turbulent flow structures. The switching in IDDES occurs between $\Delta_{\max}$ and $0.5\Delta_{max}$ where $\Delta_{max} = max(\Delta x, \Delta y, \Delta z)$. The only way to control the switching location is to have one of the spacings fixed - a condition not feasible for three-dimensional simulations.

- Moving the RANS-LES interface to the outer edge of the log-law layer by a blending function can fix the switching problem, however, higher values of k can suppress the development of turbulent structures.

Both approaches - the IDDES and the zonal DES showed that performing a scale resolving simulation of a shock train interaction is not straightforward. In addition to providing a realistic turbulent inflow, either from a precursor simulation or from a synthetic turbulence generator, one must ensure a proper switching location between the RANS and LES methods. A switch too close to the inner edge of the log-law layer will result in LES mode where the grid is not fine enough to resolve the turbulent structures. On the other hand, a switch too close to the outer edge of the log-law layer can suppress the downstream development of the turbulent structures. Even when the RANS to LES interface was fixed, the results proved that scale resolving simulations of shock trains are difficult and the additional effort of tuning the RANS/LES model coefficients might offset the benefits of the scale resolving methods over the traditional RANS methods with non-linear turbulence models. Further studies must be performed to investigate the effects of the timestep size and the numerical scheme on the solution in order to obtain improved results.

Based on the findings in the chapter, shock trains should be simulated with turbulence models featuring constitutive relations. Such models are capable of accounting for the Reynolds stress anisotropy near the duct corners. The anisotropy gives rise to secondary flows. Not accounting for the secondary flows might result in unphysically large corner separations that will change the structure of the entire interaction.

Chapter 4

Sensitivity of MSWBLIs to inflow conditions and geometry *

This chapter presents a parametric study of a multiple shock wave boundary layer interaction in a duct. The effect of the duct geometry as well as the effect of upstream parameters such as the Mach number, boundary layer thickness (flow confinement), and the Reynolds number on the total pressure recovery and flow distortion are quantified. Simulations are carried out with the non-linear k-ω EARSM turbulence model due to its ability to account for the secondary flows. The test section geometry from the experiment of Carroll *et al.* [23] was selected as the baseline.

4.1 Grids and numerical setup

The numerical domain was non-dimensionalised with the half-height of the test section at the inlet ($h = 16.275$) mm. A total of four multiblock structured grids were used - A, B, C, D. The grids have similar spacing and stretching as the medium grid used in the validation studies of the MSWBLI experiment by Carroll *et al.* [26] presented in chapter 3. The only difference is the extended region of streamwise refinement. The refinement region was extended further upstream, compared to the validation grid, in order to accomodate any movement of the shock train due to changes in upstream or downstream conditions. Figure 4.1 (a) shows the streamwise extent of the refinement region and figures 4.1 (b) and 4.1 (c) the slices at $x/h = 0$ of grids A and B. Grid B has a width w/h of 1.76 which is (25% less) than grid A which has a width of $w/h = 2.43$. As no flow asymmetry was observed on the full grids, only a quarter of

*The results in this chapter are published in K. Boychev *et al.* "Parametric Study of Multiple Shock Wave/-Turbulent Boundary Layer Interactions With a Reynolds Stress Model", Shock Waves, Vol. 31, Issue 3, 2021, DOI: https://doi.org/10.1007/s00193-021-01011-z

each grid was used (indicated by the solid red line). Grids A and B have H-topologies whereas grids C and D have O-topologies. The change in topology was required by the change from sharp to rounded corners. H-topology is not used for rounded corners as it results in highly skewed cells near the corners.

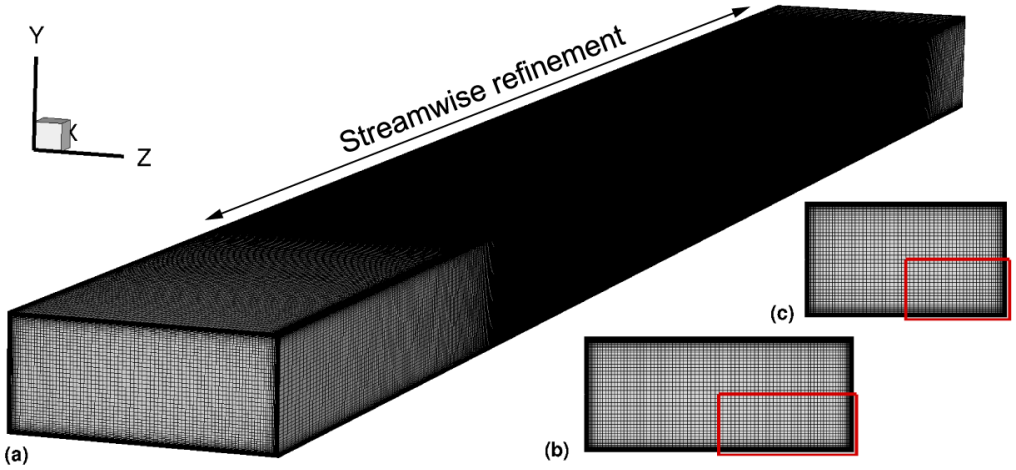

Figure 4.1: Grid A (a), cross-section of grid A (b), cross-section of grid B (c). The quarter of the numerical domain is outlined by the red-line.

Figure 4.2 shows the topologies of grids A, C, and D. Red lines indicate the block boundaries. The O-topologies of grids C and D are similar - four blocks at the centre, surrounded by blocks adjacent to the nearby walls. The inlet and outlet cross-sectional areas of grid A were matched by grids C and D. This resulted in a non-dimensional radius of $r_C/h = 1.7265$ for grid C and a non-dimensional half-height of $h_D/h = 1.0967$ for grid D at the inlet.

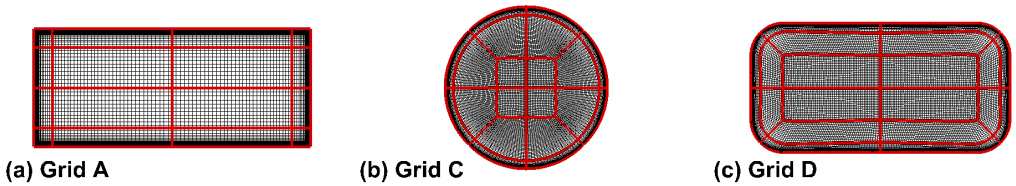

Figure 4.2: Cross-section of grid A (a), grid C (b), and grid D (c). The red lines indicate block boundaries.

The divergence angles of grids C and D were 0 $\alpha = 0.11$ and $\alpha = 0.07$ deg and were obtained by estimating the increase in r_C and h_D over the length of the domain. The divergence angle used in the experiment by Carroll *et al.* [26] was $\alpha = 0.13$ deg. Both A and B grids have a divergence angle of $\alpha = 0.13$ deg. For all grids a minimum wall normal distance of $\Delta y_{min} = 10^{-5}h$ was used to ensure $y^+ < 1$. Since the same reference half-height was used to non-dimensionalise all grids $h = 16.275$, the Reynolds number was not changed. To investigate

the effects of the Reynolds number, Re_h, and pre-shock Mach number, M_r, on the shock train, the shock train was first simulated at inlet-outlet conditions corresponding to the experiment by Carroll *et al.* [23]. Two additional simulations were then performed at the same inlet-outlet pressure ratio of $p/p_u = 2.4776$ and lower Mach (M_u) and Reynolds number (Re_h). For the lowest M_u case the pressure ratio had to be lowered, as the reference value resulted in an isolator unstart. The differences in the Mach and Reynolds numbers between the reference simulation and the simulations at lower M_u and Re_h were $\Delta M_u \approx 0.1$ and $\Delta Re_h \approx 4.4 \times 10^5$. A simulation at lower flow confinement (δ_r/h) was also performed. To decrease the flow confinement (δ_r/h) from the reference value ($\delta_r/h = 0.3084$) the outlet pressure was increased by $\approx 12\%$ and $\approx 16\%$. The increase of the outlet pressure relocated the shock-train upstream, where the boundary layer was thinner and hence the flow confinement was smaller. An additional case to investigate the effects of increased spanwise confinement (δ_r/w) was also performed. The aspect ratio of the duct was reduced from $w/h = 2.34$ to $w/h = 1.76$ (25% reduction). As changes of the inlet/outlet conditions or the geometry result in a different Mach number before the interaction, M_r, three additional cases were considered. The Mach number at the inlet, M_u, for each case was adjusted until a Mach number before the start of the interaction of $M_r \approx 1.61$ was obtained. This allowed investigation of the isolated effect of Re_h and δ_r/h on the interaction. The pressure ratio p/p_u was kept constant at $p/p_u = 2.4775$, $p/p_u = 2.7818$, and $p/p_u = 2.7818$ respectively. Tables 4.1 and 4.2 lists the parameters for the shock train parametric cases and the employed grids. The cases with matching pre-shock Mach number M_r are marked in bold. In addition to the above cases, a Latin Hypercube approach was used to generate combinations of inlet Mach number M_u, outlet pressure percentage η, and Reynolds number Re_h. The upper and lower limits for each parameter were set to $1.5 \leq M_u \leq 3.0$, $0.6 \leq \eta \leq 0.9$, and $1.0 \times 10^4 \leq Re_h \leq 1.0 \times 10^6$, where η was defined as the percentage of the pressure rise across an inviscid shock with a pre-shock Mach number of M_u. The use of p and M_u as parameters instead of δ_r/h and M_r was motivated by the fact that matching a specific δ_r/h and M_r requires iterative adjustments to M_u and p which is not practical. Table 4.1 also lists the parameters for the generated shock train parametric cases. All simulations were initialised with an inviscid shock with a pre-shock Mach number of M_u at the end of the domain. At the inlet the eddy viscosity rato for all cases was set to $\frac{\mu_t}{\mu} = 10$. Investigations showed that increasing the turbulence intensity at the inlet does not have a significant effect on the solution. Approximately $\times 10^5$ implicit steps at CFL of 4 were required for the steady-state solutions to converge to at least 5 orders of magnitude in the flux residuals.

Table 4.1: Shock train parametric cases; cases in bold have adjusted M_u to match the reference M_r.

Case (Grid)	Re_h	M_u	M_r	δ_r mm	δ_r/h	x_r/h	p/p_u	p/p_r	TPR	FD
Case 1, Reference (A)	4.9×10^5	1.690	**1.619**	5.02	0.31	26.1	2.4775	2.2296	0.758	0.644
Case 2, Lowest M_u (A)	4.9×10^5	1.490	1.446	2.80	0.17	14.0	2.1757	2.0208	0.862	0.474
Case 3, Lower M_u (A)	4.9×10^5	1.590	1.536	3.12	0.19	15.0	2.4772	2.2880	0.825	0.515
Case 4, Lower Re_h (A)	4.9×10^4	1.690	1.572	4.99	0.31	15.3	2.4775	2.0778	0.763	0.655
Case 5, Lowest δ_r/h (A)	4.9×10^5	1.690	1.643	2.46	0.15	11.6	2.8610	2.6939	0.798	0.524
Case 6, Lower δ_r/h (A)	4.9×10^5	1.690	1.644	3.23	0.20	15.6	2.7818	2.5540	0.783	0.573
Case 7, Reduced w/h (B)	4.9×10^5	1.690	**1.611**	4.79	0.29	25.1	2.4775	2.1979	0.756	0.649
Case 8, Lower δ_r/h (A)	4.9×10^5	1.665	**1.626**	2.69	0.17	12.3	2.7876	2.6176	0.805	0.529
Case 9, Lower Re_h (A)	4.9×10^4	1.740	**1.597**	6.07	0.37	20.1	2.4776	2.0048	0.729	0.734
Case 10, Circular (C)	4.9×10^5	1.690	1.651	5.29	0.32	30.0	2.4775	2.3209	0.763	0.629
Case 11, Rounded (D)	4.9×10^5	1.690	1.630	5.24	0.32	30.6	2.4775	2.2680	0.752	0.652
Case 12, $M_u = 1.620$ (A)	3.5×10^5	1.620	1.540	5.87	0.36	30.7	2.1393	1.8783	0.779	0.682
Case 13, $M_u = 1.736$ (A)	8.7×10^5	1.736	1.686	5.09	0.31	29.4	2.5642	2.3616	0.743	0.736
Case 14, $M_u = 1.890$ (A)	2.2×10^5	1.890	1.814	4.13	0.25	18.2	3.1774	2.8186	0.695	0.873
Case 15, $M_u = 2.036$ (A)	6.2×10^5	2.036	1.983	3.83	0.24	18.9	3.3509	3.0631	0.653	1.034
Case 16, $M_u = 2.157$ (A)	2.4×10^5	2.157	2.097	2.78	0.17	11.0	4.3285	3.8917	0.594	1.100
Experiment [23]			**1.610**	5.40	0.32	0		2.2309		

Table 4.2: Grid parameters; colon symbol stretching.

Grid	min $\Delta x/h$	$\Delta y/h$, $\Delta z/h$	Points
A	0.02	10^{-5}:0.05:0.07	14.61×10^6
B	0.02	10^{-5}:0.05:0.07	13.12×10^6
C	0.02	10^{-5}:0.05:0.07	9.41×10^6
D	0.02	10^{-5}:0.05:0.07	6.04×10^6

4.2 Effect of Reynolds and Mach number

The wall pressure and Mach number contours for the lower Mach and Reynolds results are shown in Figure 4.3. The inlet-outlet pressure ratio for both cases is constant and equal to the pressure ratio of the reference case. The shock train length increased considerably for the case at lower Re_h. The Mach number contours indicate that the supersonic core flow region now extends further downstream. There is no distinct termination of this region as observed in the other two cases. The onset of the interaction begins at $x_r/h = 15.3$. The difference with the reference case spans about 24% of the domain length. Although the location of the onset moves upstream for the lower Re_h case, both the reference, and the lower Re_h cases have similar levels of flow confinement - $\delta_r/h = 0.311$ and $\delta_r/h = 0.307$ and the pre-shock Mach number difference between the two cases was about 3%. This shows that for a constant pressure ratio p/p_u and a reduced Reynolds number Re_h, the confinement is the dominant parameter in determining the onset of the interaction. Figures 4.8 and 4.4 show the sonic and separation iso-surfaces, and the shear stress visualised with friction lines on the wall.

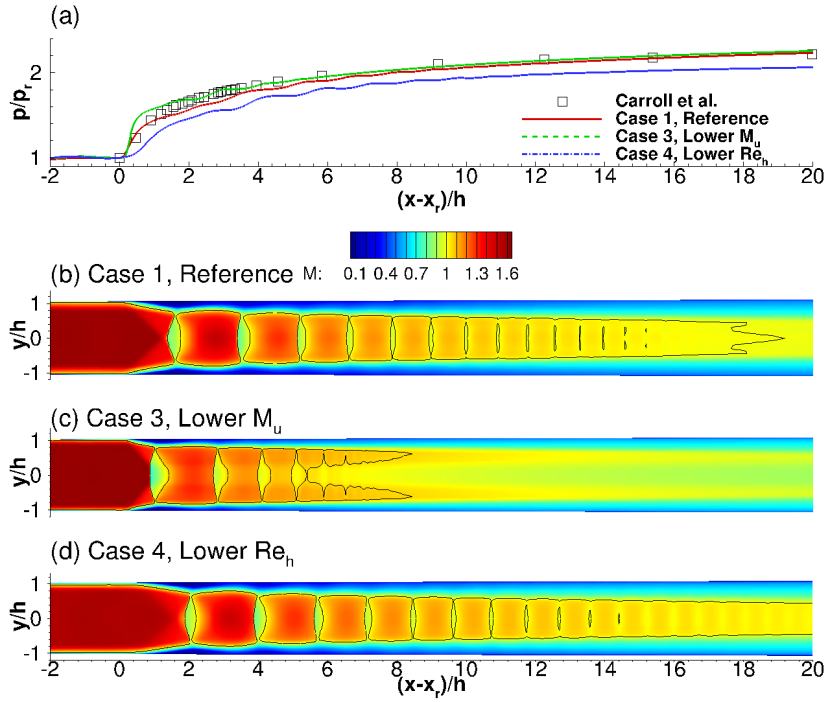

Figure 4.3: Wall pressure (top) and Mach number contours (bottom) for the reference and reduced M_u and Re_h cases of table 4.1.

Both the reference and lower Re_h cases feature large separation on the top and bottom walls with less pronounced corner separations for the latter. Experimental studies of oblique and normal SWBLIs performed by Dupont *et al.* [42], Doerffer *et al.* [39]. and Bruce *et al.* [19]

report that the extent of the shock-induced separations at the centreline of the duct is strongly affected by the state of the flow at the corners of the duct. In the experiment by Bruce *et al.* [19] reduction of the corner separation by upstream suction of the boundary layer resulted in a separated region at the centreline in a previously attached flow field. The case at lower Mach number M_u has larger corner separations and smaller separations on the upper and lower walls.

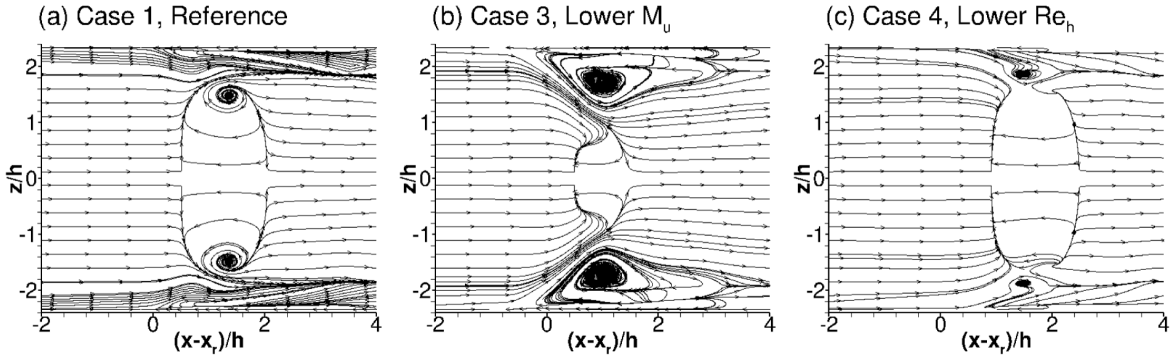

Figure 4.4: Visualisation of the wall shear stress using friction lines at the wall for cases 1, 3, and 4 of table 4.1.

The size of the centreline separation is reduced due to the increase of the corner separations which is in agreement with experiments. Both the reference and lower Re_h cases feature an oblique initial shock structure. The case at lower M_u shows an initial shock with a Mach stem. Such shock structure is usually observed at lower levels of confinement and lower pre-shock Mach numbers M_r. Considering the reference case and the cases at lower M_u and lower Re_h, the pressure recovery $p_0/p_{0,u}$ at $(x-x_r)/h$, 20 non-dimensional streamwise distances after the onset of the interaction, is highest for the case at lower M_u (0.825). The absolute difference in pressure recovery between the reference and lower Re_h case is $\Delta p_0/p_{0,u} = 0.0052$.

4.3 Effect of confinement

As the outlet pressure is increased by 12% for the reference case, the onset of the interaction moves upstream, to $x_r/h = 15.6$. The movement is equivalent to approximately 23% of the domain length. Figure 4.5 shows the wall pressure and Mach number contours for the reference and reduced δ_r/h cases. The upstream movement of the shock is accompanied by a reduction of the shock train length and by changes of the initial shock structure. The differences in pre-shock Mach number and confinement between the cases amount to approx-

imately 1.3% and 36.2%. As the confinement is reduced, the shock train becomes shorter and the spacing between subsequent shocks decreases (as observed by Carroll *et al.* [23]). Further decrease of the confinement reduces the shock train length to approximately $L/h = 8$. Figure 4.6 shows the shock train length L/h versus the level of flow confinement and figure 4.7 shows the wall shear stress.

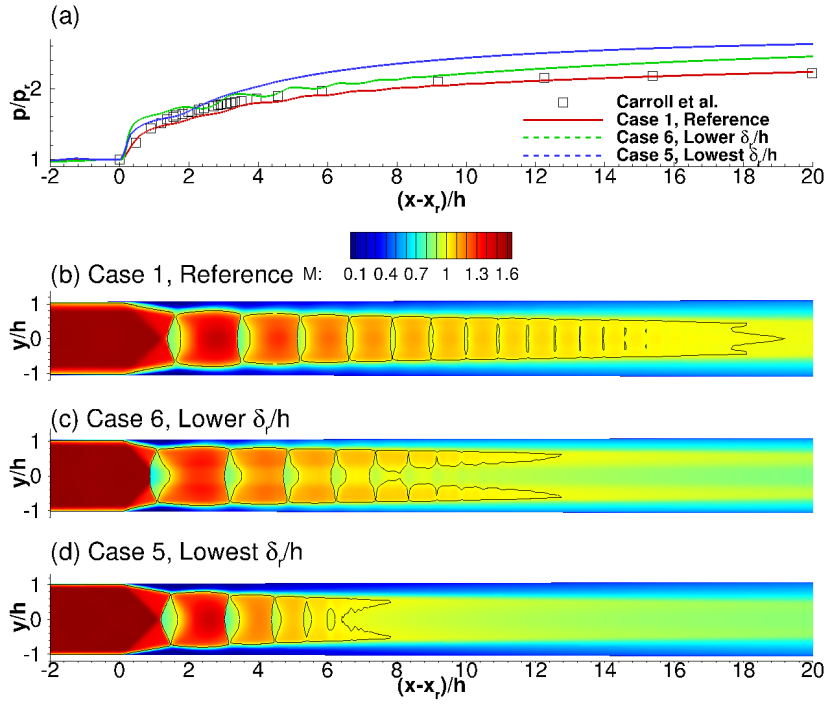

Figure 4.5: Wall pressure (top) and Mach number contours (bottom) for the reference and reduced δ_r/h cases of table 4.1.

The difference between the lower and lowest δ_r/h cases shown in Figure 4.7 can be attributed to the state of the upstream boundary layer. The shock train in the lowest δ_r/h case is close to the inlet of the domain where the boundary layer is not yet developed. As a result, the nature of the interaction is more "laminar" in that region. The shock train in the lower δ_r/h case, on the other hand, is at a location where the boundary layer is still developing (thinner, and not fully turbulent yet). The case at lower M_u has similar confinement to the case at lower δ_r/h - about 0.19. The difference in the pre-shock Mach numbers is about 7%. Nevertheless, both cases feature shorter shock trains with an initial shock that has a Mach stem. The pressure recovery for the lower δ_r/h case is $p_0/p_{0,u} = 0.783$, again taken at 20 dimensionless distance units after the start of the interaction. Figure 4.8 shows the sonic and separation iso-surfaces for the reference and lower δ_r/h cases. For the latter, the corner separations are larger. Since the size of the corner separation affects the centreline separation, and the structure of the

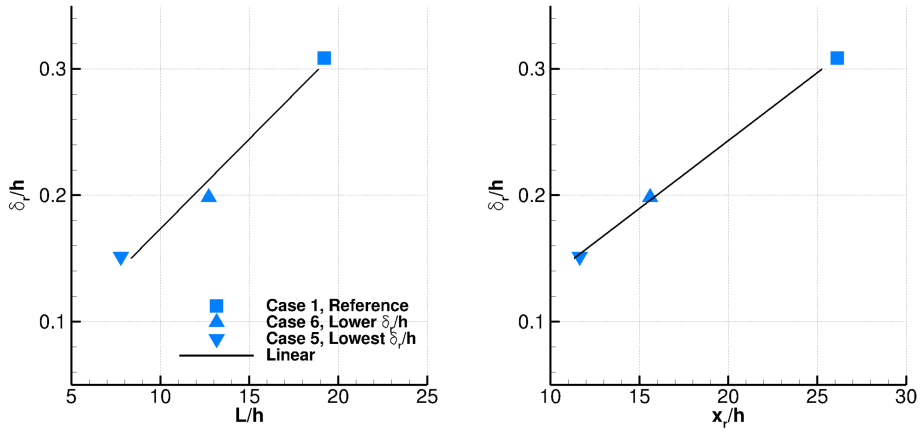

Figure 4.6: Shock train length L/h and onset x_r/h with respect to confinement level; L/h is obtained from the mid-plane slices at the location where the supersonic contours end.

initial shock, for cases with larger levels of flow confinement (reference and lower Re_h), the corner separations are small resulting in a larger separation at the centreline and no Mach stem.

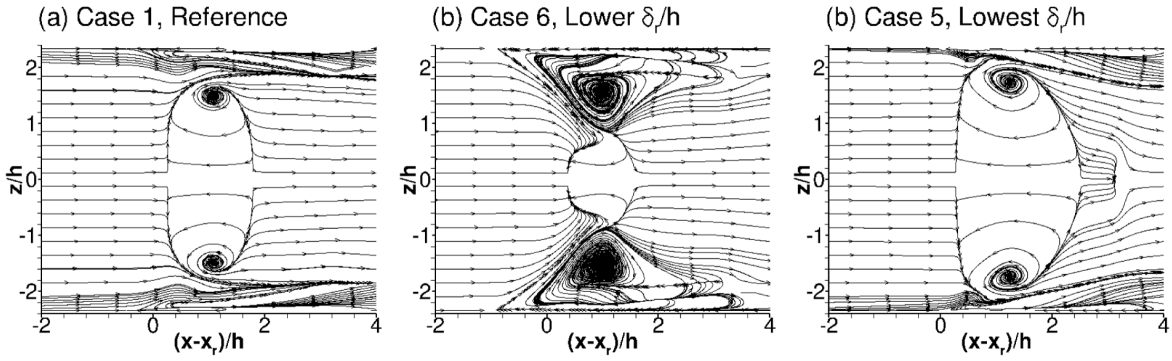

Figure 4.7: Visualisation of the wall shear stress using friction lines at the wall for cases 1, 6, and 5 of table 4.1.

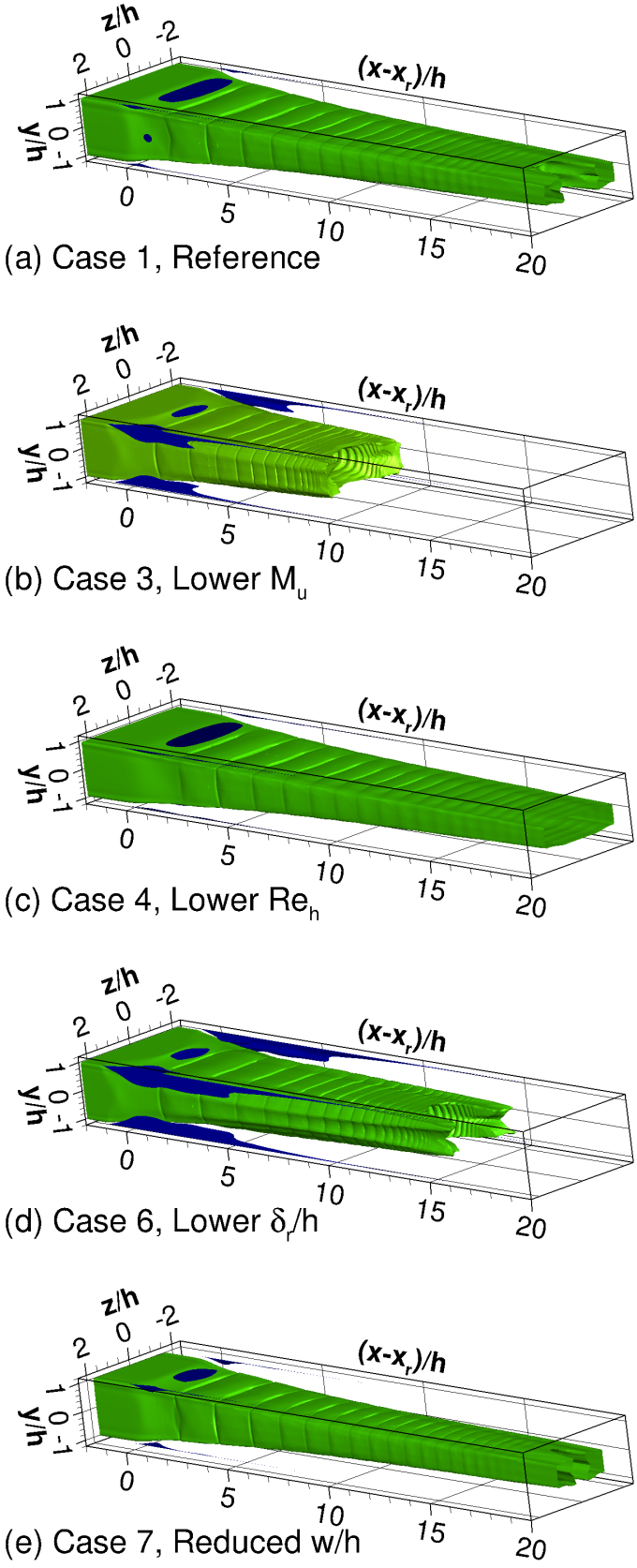

Figure 4.8: Iso-surfaces of $M = 1.0$ (green) and $u/V_u = 1 \times 10^{-3}$ (blue) for the reference, lower M_u, lower Re_h and lower δ_r/h cases of table 4.1.

4.4 Effect of aspect ratio

Reduction of the aspect ratio from $w/h = 2.34$ to $w/h = 1.76$ did not have a huge effect on the interaction. Figure 4.9 shows the wall pressure and Mach number contours for the reference and reduced w/h cases. A small Mach stem is present for the latter, resulting in the appearance of supersonic tongues and subsonic core flow. The difference between the onset of the interaction for the cases is $\approx 2\%$ of the domain length and the difference in pre-shock Mach number is $\approx 0.5\%$. The spanwise confinement (defined as δ_r/w where w is the half-width of the duct and δ_r is the boundary layer thickness in the mid-plane perpendicular to the side-wall) was $\delta_r/w = 0.13$ for the reference case and $\delta_r/w = 0.17$ for the reduced w/h case. A 25 % reduction of w/h resulted in 30.5% increase in δ_r/w. Although the percentage increase is large, the actual increase between the cases is not, $\Delta\delta_r/h = 0.04$. As stated earlier for the reduced w/h case the pre-shock train Mach number and the onset of the interaction do not vary considerably. The main difference observed from the Mach number contours is the appearance of supersonic tongues and a subsonic core (shown in 4.9 c). From the separation iso-surface, shown in Figure 4.8, it is observed that the corner separations are larger compared to the reference case and the centreline separation is smaller. Again, the smaller centreline separation results in an initial shock with a Mach stem.

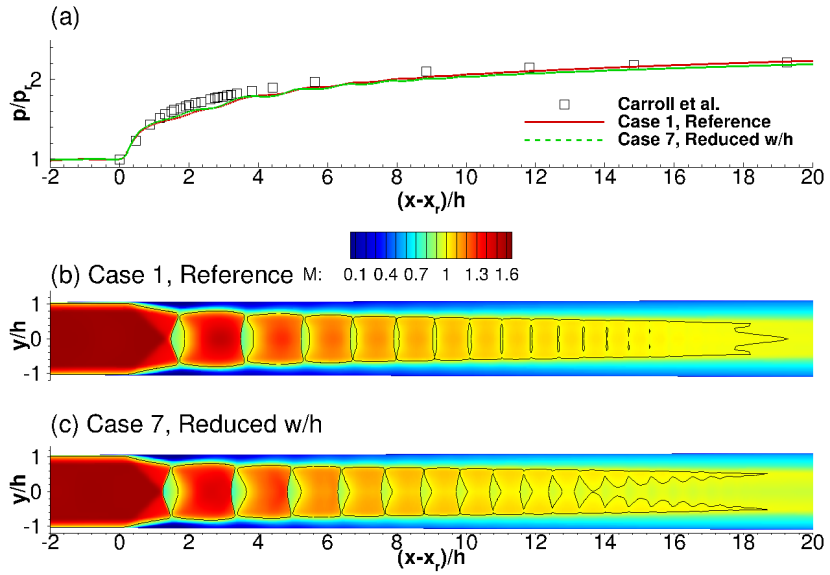

Figure 4.9: Wall pressure (a) and Mach number contours (b-c) for the reference and reduced w/h case of table 4.1.

The wall shear stress, shown in Figure 4.10, is qualitatively similar for both cases. Following the observations made form the separation iso-surfaces, the centreline separation is reduced.

The corner separations occupy approximately 4.06 % and 9.65 % of the duct width for the reference and reduced w/h cases respectively.

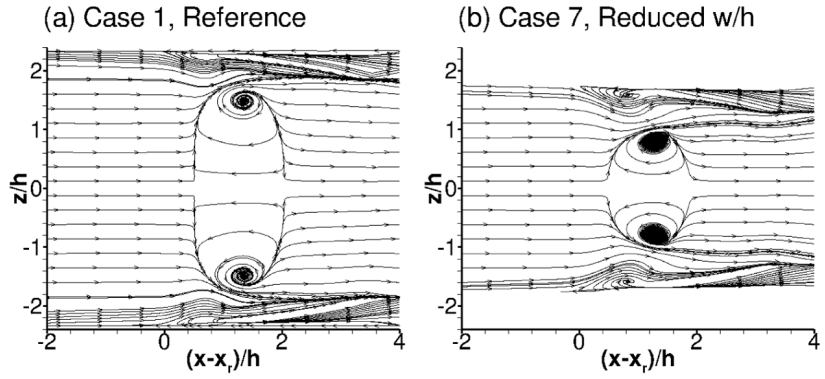

Figure 4.10: Visualisation of the wall shear stress using friction lines at the wall for cases 1 and 7 of table 4.1.

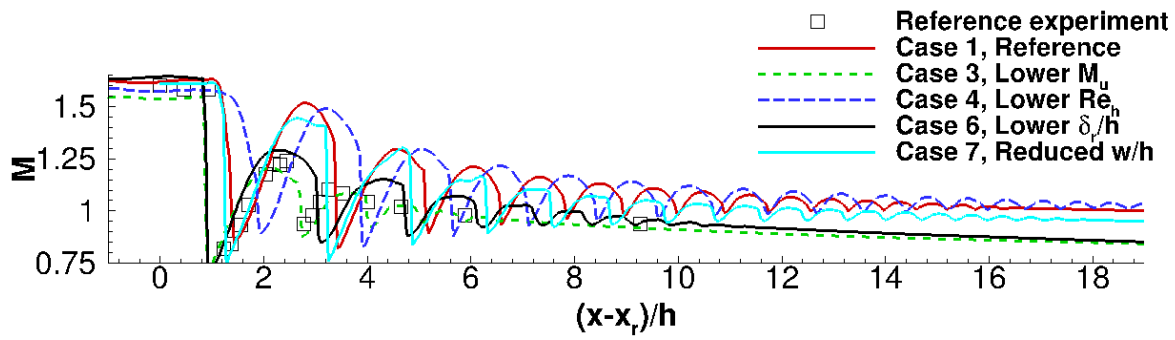

Figure 4.11: Centreline Mach number distributions for the cases of table 4.1.

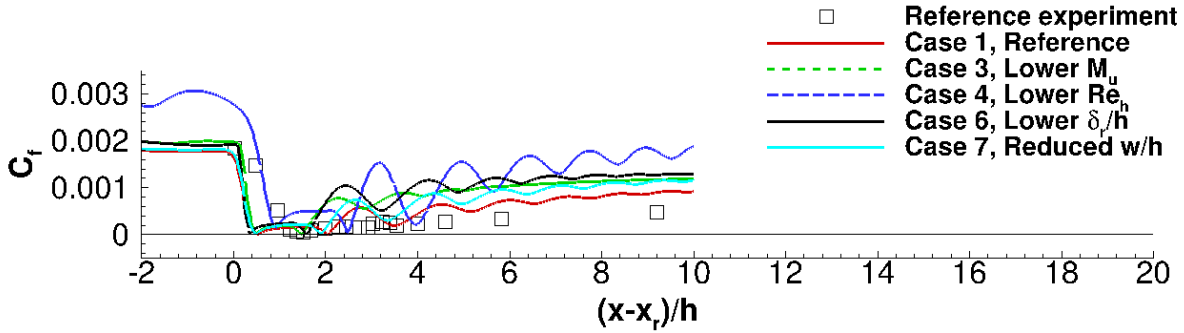

Figure 4.12: Skin friction coefficient distributions for the cases of table 4.1.

Figure 4.11 shows the centreline Mach number distribution. The lower M_u and lower δ_r/h cases, which feature an initial shock with a Mach stem, agree better with the experimental results. Although these cases are not at the experimental conditions, the results show the importance of the corner and centreline separation sizes and their effect on the initial shock structure and the centreline Mach number. The reference case gives the closest agreement with the experiment for the skin friction coefficient, as shown in Figure 4.12. Similarly to the wall pressure profiles, the C_f profiles exhibit "oscillations". The increase in C_f is associated with the "recovery" of the boundary layer profile after an interaction with a shock in the shock train. A rapid decrease in C_f is observed upstream of each shock location due to the adverse pressure gradient imparted by the shock. Both the lower M_u and lower δ_r/h cases have considerably larger C_f after the onset of the interaction compared to the experiment.

4.5 Matching pre-shock Mach number

Figure 4.13 compares the wall pressure and Mach number contours of the lower δ_r/h and Re_h cases, both having M_r of approximately 1.61. The inlet-outlet pressure ratio was kept constant while the inlet Mach number varied. Note that for the lower δ_r/h case the outlet pressure is 12 % higher.

As the pre-shock Mach number was approximately $M_r = 1.61$ for all three cases, the sole effect of confinement on the interaction was investigated. For the lowest level of confinement, an initial shock with a Mach stem was observed. As the confinement was increased, the Mach stem reduced in size and disappeared (for both the reference and lower Re_h cases). For the case at lower Re_h, the confinement was $\delta_r/h = 0.37$ which resulted in weak crossing oblique shocks followed by a weak normal shock. From the wall pressure, it was observed that the increasing confinement smeared the pressure gradient mainly by altering the initial shock structure. The increase of the confinement level was accompanied by a reduction of the corner separations and an increase of the shock train length, as seen from Figure 4.15. The shock train is longest for the lower Re_h case. From the figure, it can also be seen that the shock train cross-sectional shape is rectangular for cases 1 and 9. For case 8, the shock train cross-sectional shape resembles an octagon. The distinct gap between the iso-surfaces at the centerline (cases 1 and 8) indicates the presence of a subsonic core. The subsonic core is a sign of a strong initial shock (figure 4.13b, c). The onset of the interaction for the Reference (case 1) and Lower Re_h (case 9) cases is at $20.1 < x_r/h < 26.1$. The boundary layer for both cases has approximately 20 non-dimensional streamwise units to develop. As a result, both cases share similar wall shear stress visualisations. Figure 4.14 shows the visualisations. The higher smearing of the pressure gradient observed for the Lower Re_h case results in longer

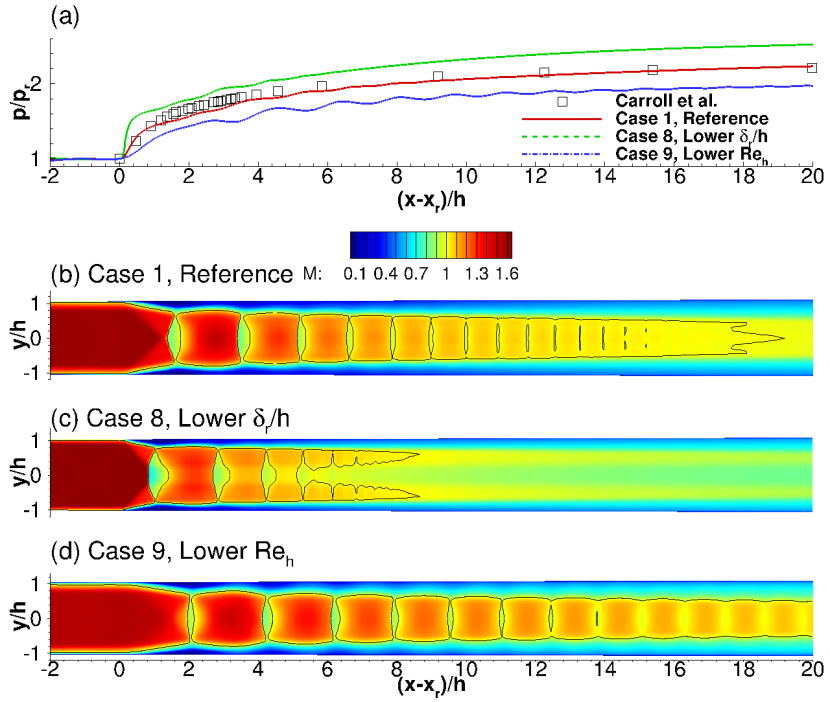

Figure 4.13: Wall pressure (top) and Mach number contours (bottom) for the reference and lower δ_r/h and Re_h cases of table 4.1.

corner separations that extend less into the flow compared to the ones in the Reference case. Both the flow confinement and the Reynolds number were observed to affect the shock train length. The flow confinement has a stronger effect on the shock train length, which is in accordance with the experiments.

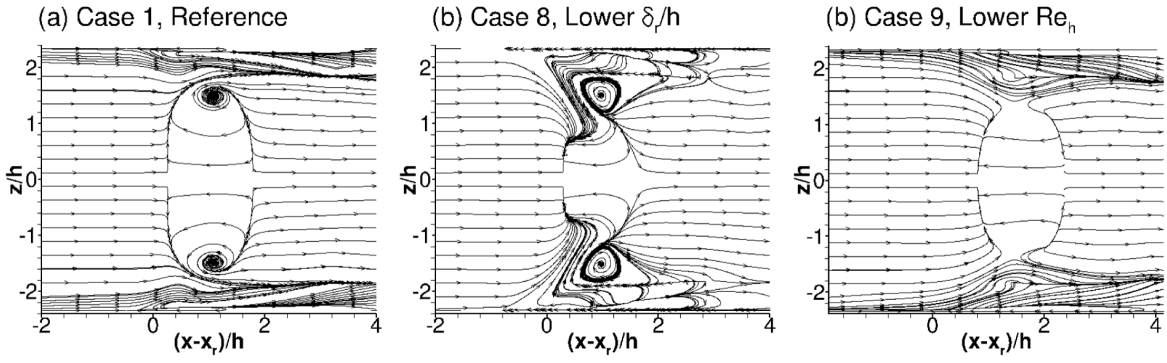

Figure 4.14: Visualisation of the wall shear stress using friction lines on the wall for cases 1, 8, and 9 of table 4.1.

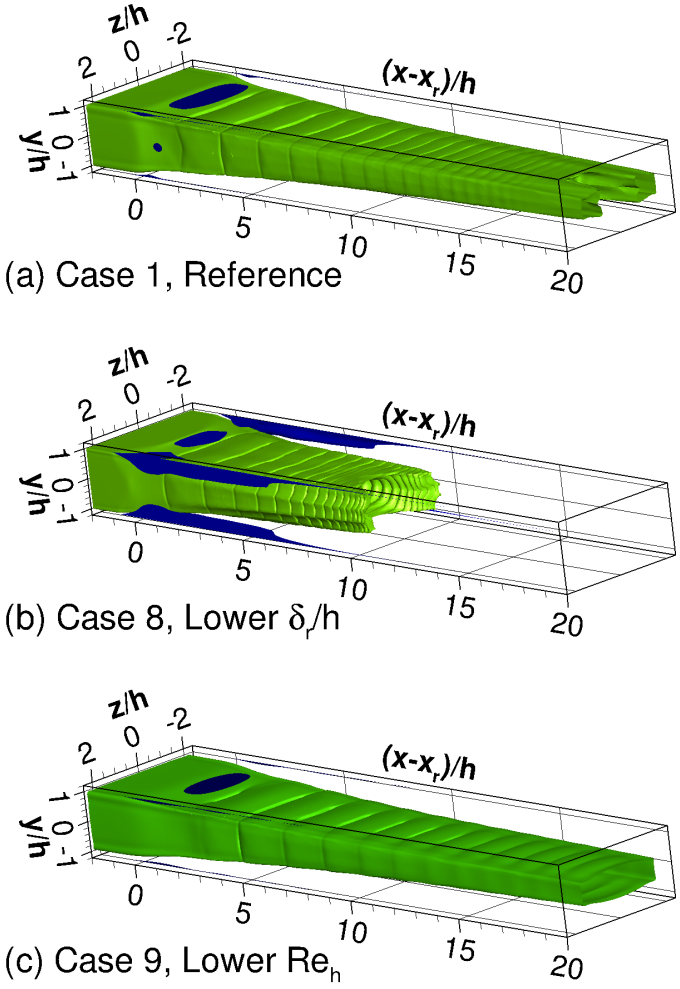

Figure 4.15: Iso-surfaces of $M = 1.0$ (shaded green) and $u/V_u = 1 \times 10^{-3}$ (shaded blue) for the reference and lower δ_r/h and Re_h cases of table 4.1.

4.6 Effect of cross-section

In addition to investigating the effects of upstream and downstream conditions, the effects of changing the cross-section of the duct were also investigated. Two cross-sections were considered - a circular one and one with rounded corners. The grids created for these geometries are shown in figure 4.2. Both grids - C and D were non-dimensionalised with the duct half-height at the inlet $h = 16.275$ mm. The Reynolds number based on the duct half-height, the inlet Mach number, and the pressure ratio were kept the same as for the reference case. Figure 4.16 shows the wall pressure and the Mach contours.

Both geometries moved x_r downstream by approximately 16% compared to the reference case. The boundary layer and the confinement before the start of the interaction was close

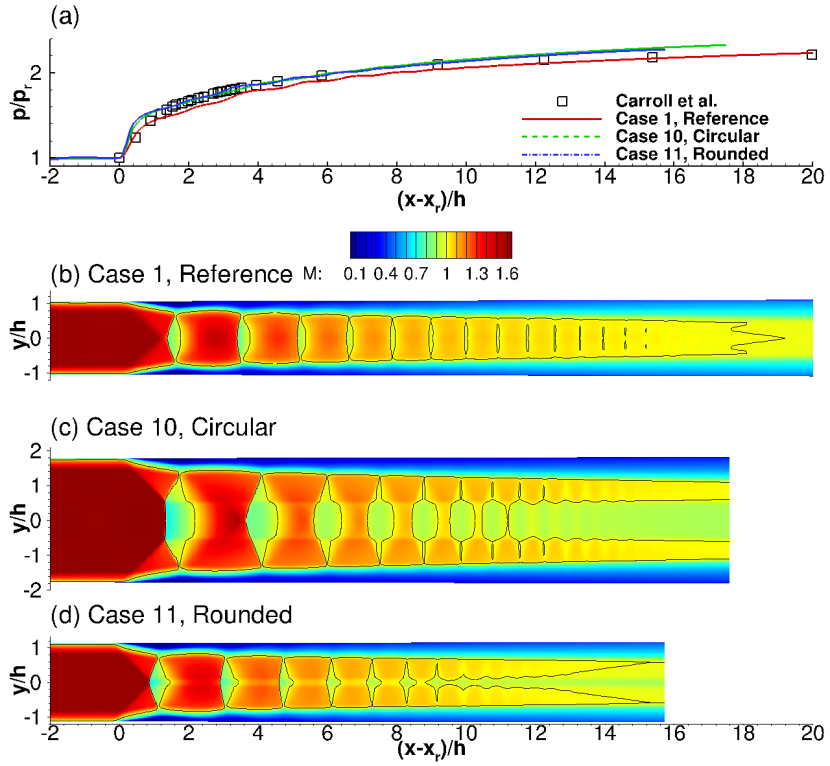

Figure 4.16: Wall pressure (top) and Mach number contours (bottom) for the reference, circular, and rounded geometry cases of table 4.1.

to the one observed in the experiment - $\delta_r \approx 5.4$ mm and $\delta_r/h = 0.32$. Although the Mach number was slightly higher than the experimental one, $M_r = 1.61$, the circular and round geometries predicted a different shock train structure compared to the one in the rectangular geometry. The spacing between subsequent shocks was smaller and the initial shock in each case feature a Mach stem. No corner separations were present in the rounded geometry. Interestingly, separations were observed on all four walls. Figure 4.17 shows the separation and sonic iso-surfaces for the two geometries.

The absence of corner separations for the rounded geometry can be attributed to the reduced streamwise vorticity in the corner region of the duct. In chapter 3 it was observed that high regions of vorticity were related to the presence of corner flows. In a rectangular duct, the momentum near the corner is significantly reduced due to the interaction of the two adjacent wall boundary layers. As a result, the flow near the corners separates first. The separation causes weak oblique shock waves that propagate into the flowfield. The waves act to smear the streamwise pressure gradient. If one of the wall dimensions of the duct is smaller, the smearing can be sufficient to suppress the centreline separation on that wall. For a rounded corners

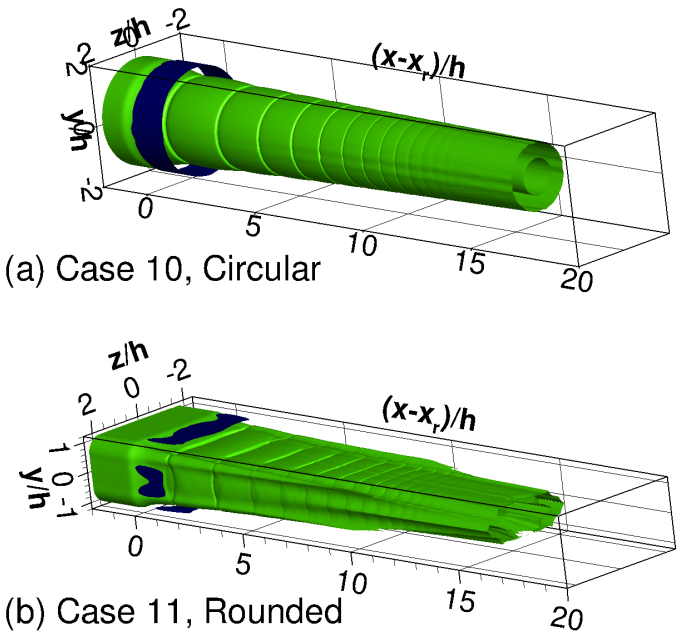

Figure 4.17: Iso-surfaces of $M = 1.0$ (green) and $u/V_u = 1 \times 10^{-3}$ (blue) for the reference, circular, and rounded geometry cases of table 4.1.

duct, the corner flows are weaker, as indicated by the streamwise vorticity contours in figure 4.18. Regions of positive and negative vorticity separated by $\Delta/h \approx 0.5$ non-dimensional units are present near the rounded corner (figure 4.18c). The vorticity magnitude in these regions is considerably smaller compared to the rectangular duct (figure 4.18a). The circular geometry shows even smaller vorticity magnitudes. Unlike the previous geometries, the circular one results in a flow topology similar to a two-dimensional normal shock interaction. The separation at the foot of the first shock is relatively uniform around the circumference of the duct. As the radius r_c is considerably greater than the reference h, Mach stem is present. Due to the presence of a Mach stem the flow decelerates more and the length of the shock train is reduced. The slip line emanating from the triple point can be identified. Below it the flow remains supersonic for longer distances downstream, creating the so-called supersonic "tongues".

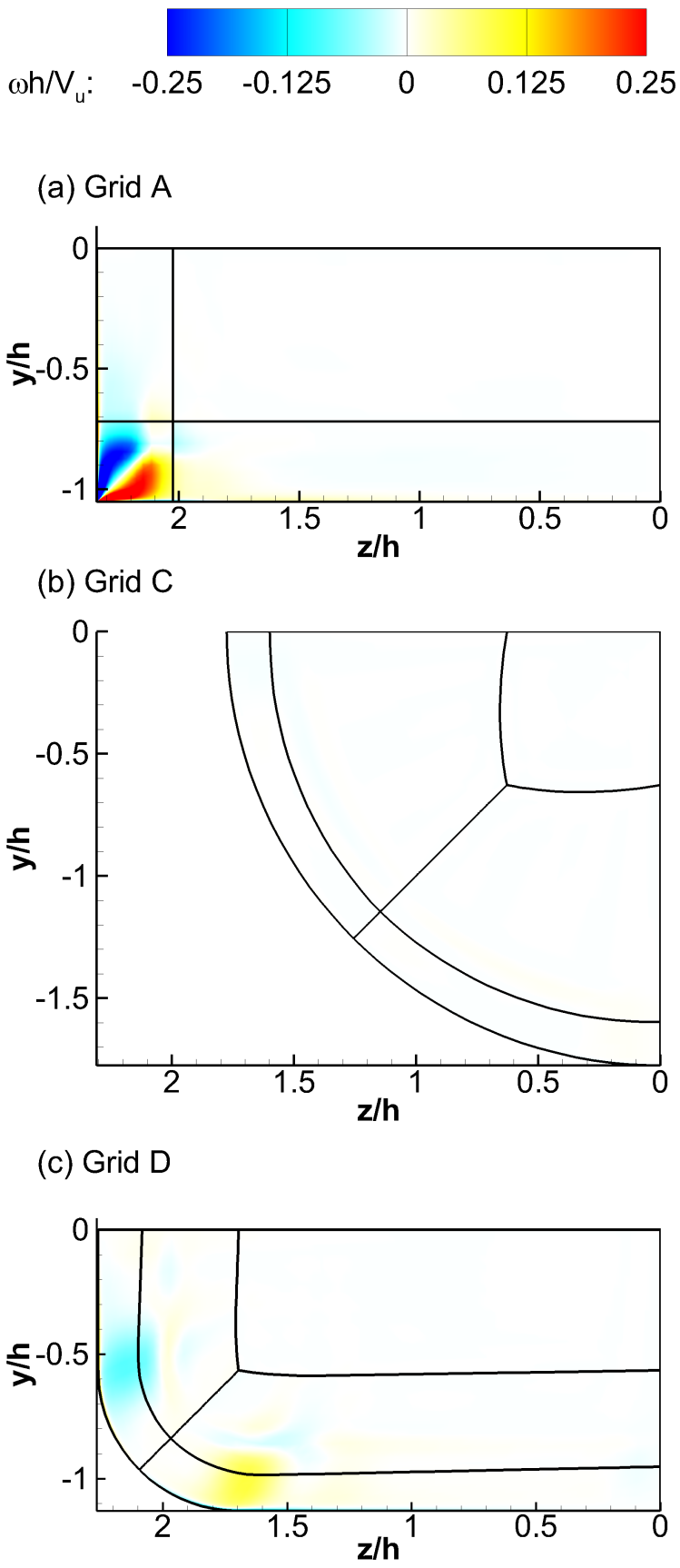

Figure 4.18: Streamwise vorticity contours for the reference, circular, and rounded geometry cases of table 4.1

4.7 Efficiency metrics

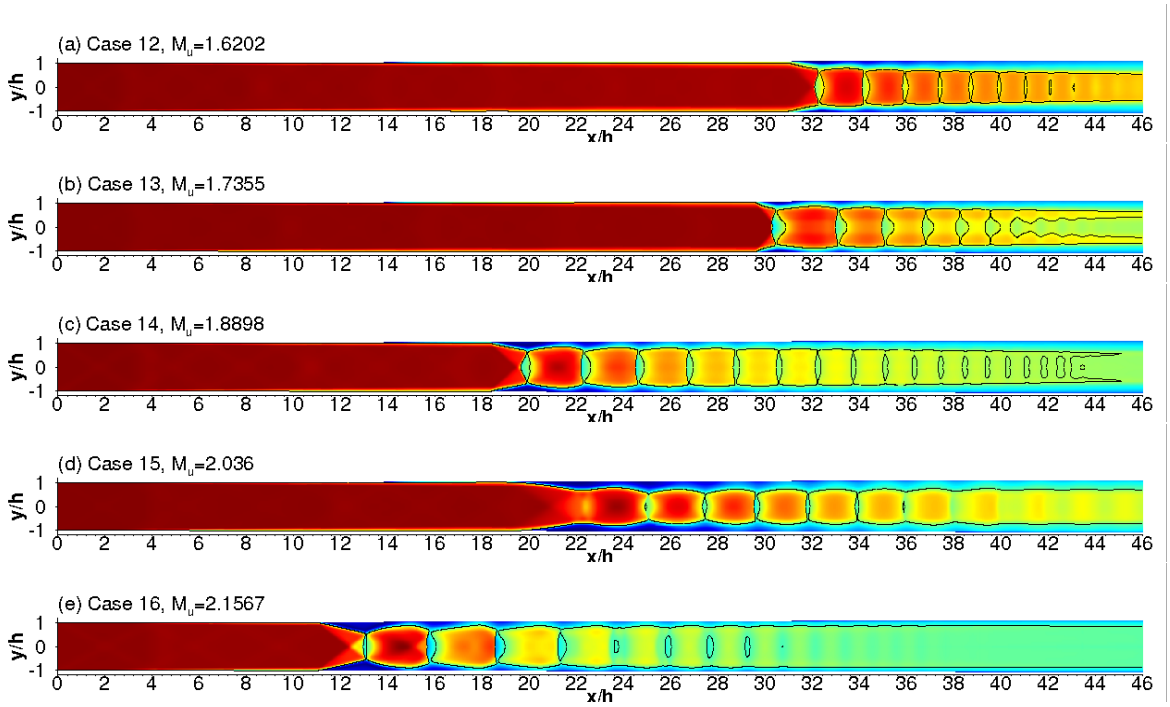

Figure 4.19: Mach number contours for cases 12 to 16 of table 4.1.

Figure 4.19 shows the Mach number contours for the remaining MSWBLI cases - 12 to 16 of table 4.1. For the shock train at $M_u = 1.736$ (case 13) the initial shock features a Mach stem. Absence of a Mach stem is observed for the shock train at $M_u = 1.62$ (case 12) although the pre-shock Mach number is lower. The difference in the pre-shock Mach number amounts to $\approx 8\%$. Comparing the confinement ratios shows that case 12 has higher confinement ($\delta_r/h = 0.36$) than case 13 ($\delta_r/h = 0.31$). The corner separations for case 12 are smaller giving rise to a larger centreline separation which affects the initial shock structure. Cases 14, 15 and 16 have lower levels of flow confinement than cases 12 and 13. However, the shock train is formed by two crossing oblique shocks followed by a series of normal shocks. According to Matsuo *et al.* [83] for Mach numbers M_r larger than 1.8-2.2, oblique shock trains are mostly observed, depending on the state of the boundary layers. The pre-shock Mach number for cases 14, 15 and 16 fall within this range. Case 14 features an initial shock with a very small Mach stem, whereas case 16 features two crossing oblique shocks terminated by a normal shock. The crossing of the oblique shocks for case 15 is significant and as a result there is no subsonic flow downstream of the crossing. In all cases, the downstream shocks in the shock train are concave facing upstream. All cases without a Mach stem, do not have supersonic tongues (reference, lower Re_h, case 12, case 15, case

16). Cases featuring an initial shock with a Mach stem and a triple point have supersonic tongues (lower M_u, lower δ_r/h, case 11). The flow near the slip-line emanating from the triple point of the initial shock remains supersonic for longer distances downstream. As these points move closer to the centreline, the core flow after the shock train remains supersonic. The efficiency metrics commonly used for high-speed intakes are the flow distortion (FD), and the total pressure recovery (TPR). The FD and TPR are given by

$$FD = \frac{p_{0,max} - p_{0,min}}{p_{0,average}}, \tag{4.1}$$

$$TPR = \frac{p_{0,average}}{p_{0,u}}, \tag{4.2}$$

where $p_{0,average}$ is the total averaged pressure at the engine face and $p_{0,u}$ is the total pressure of the free-stream. The effect of pseudo-shock length on the total pressure recovery was investigated by Mahoney [81] who showed that maximum total pressure recovery is achieved when the throat length of the intake equals or is slightly greater than the pseudo-shock length. For maximum total pressure recovery at off-design conditions e.g. increase/decrease of the design Mach number or non-uniform flow due to change in the angle of attack or sideslip, it was concluded that the length of the throat section (figure 1.15) should be sufficient to account for changes in the pseudo-shock length. Table 4.1 lists the TPR and FD efficiency metrics for all shock train cases and figures 4.21 and 4.20 show quadratic surface fits for the TPR and FD. For the first 9 cases in table 4.1, the efficiency metrics are evaluated at 20 dimensionless distance units after the onset of the interaction (x_r). The TPR for the reference case is approximately 11.9 % lower than the reference TPR, taken as the TPR across a normal shock with a pre-shock Mach number of M_r. As the confinement is decreased (lower δ_r/h case with matching M_r) the TPR increases and the flow distortion decreases). The lower δ_r/h case with matching M_r has an initial shock with a Mach stem due to the smaller centreline separation and larger corner separations. The extent of the centreline separation in the streamwise direction is about $L_{sep}/h = 1.30$. Both the reference and low Re_h cases have larger separations in the streamwise direction, of $L_{sep}/h = 1.55$ and $L_{sep}/h = 1.61$, respectively. The increase of the separation is accompanied by a decrease of the TPR, and an increase in the FD. As the centreline separation is affected by the corner separations and itself affects the initial shock structure, the cases with smaller centreline separations exhibit higher TPR. Such cases are the lower δ_r/h with and without matching M_r, and the lower M_u case. For the lower δ_r/h case with a matching M_r the TPR increases by 6.2 % and the FD decreases by 17.8 % compared to the reference case. Similarly, FD and TPR are evaluated at 10 dimensionless distance units after the onset of the interaction for cases 10 to 14 in table 4.1. As the M_u, Re_h and p vary

for each case it is more difficult to draw similar conclusions. However, the variation of Re_h is moderate and all cases exhibit reduced TPR and increased FD. On average, the TPR is approximately 10% lower than the reference TPR for cases 12 to 16. Case 12, being at a similar Mach number to the reference case, shows that larger centreline separation resulting in a triple point closer to the centreline reduces TPR and increases FD. As the Mach number is increased for cases 13 to 16, the TPR continues to decrease and the FD to increase. Even though case 13 features a triple point below the centreline, due to the higher Mach number the TPR and FD are worse than for the lower M_u or lower δ_r/h cases. For cases 15 and 16, the FD is greater than one. The increase of the FD is due to the decrease in the minimum stagnation pressure ratio p/p_u at $x/h = 10$. For the higher Mach numbers cases (15 and 16) the difference between the maximum and minimum stagnation pressure at $x/h = 10$ is greater than the average stagnation pressure which results in FD> 1.

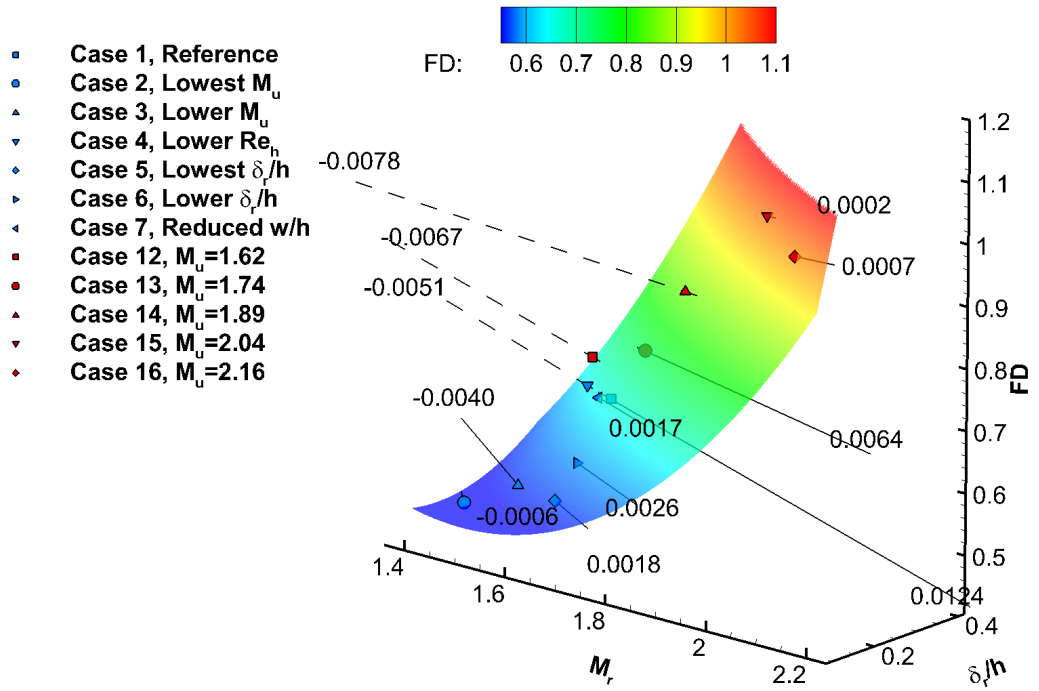

Figure 4.20: Quadratic surface fit for FD; $R^2 = 0.982$.

Flow distortion was also evaluated for the reference, lower Re_h and lower M_u cases at seven streamwise stations. The first station coincides with the onset of the pressure rise, $x_r/h = 0$. Subsequent stations are spaced at equal distances downstream with the last station placed at $x/h = 10$. The lowest M_u case has the lowest FD among the three cases. For the shock trains featuring an initial shock with a Mach stem, the FD has the highest rate of decrease. No significant differences in the rate of FD decrease or the FD are observed between the

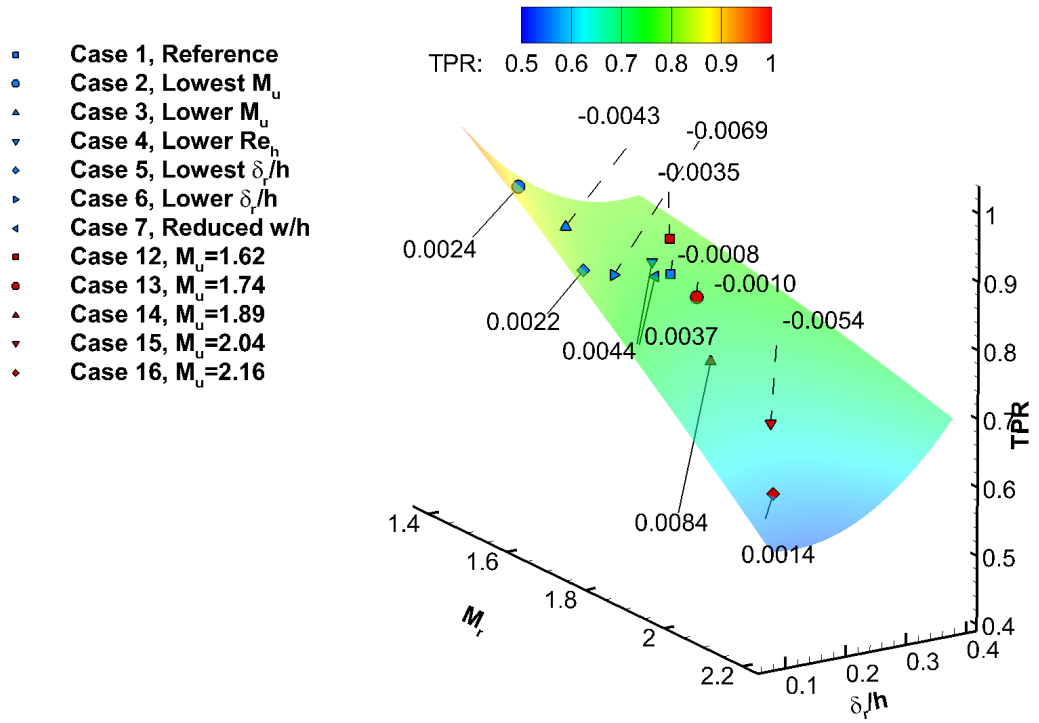

Figure 4.21: Quadratic surface fit for TPR; $R^2 = 0.994$.

reference and the lower Re_h cases which both have larger centreline separations and an initial shock without a Mach stem. Shock trains of this type were systematically observed to have a reduced TPR and increased FD. To minimise FD and maximise TPR one should aim for a shock train featuring an initial shock with a Mach stem, because of the smaller separation at its foot. Shock trains were observed for all combinations of Mach numbers, confinement levels, and Reynolds numbers. The lowest M_u ($M_u = 1.49$) case featured the shortest shock train. Further increase of the outlet pressure by approximately 3% for the lowest M_u case resulted in a single shock. This shows that even for low pre-shock Mach numbers in the range of $1.44 - 1.5$, and confinement levels greater than $\delta_r/h = 0.15$ shock trains are still present.

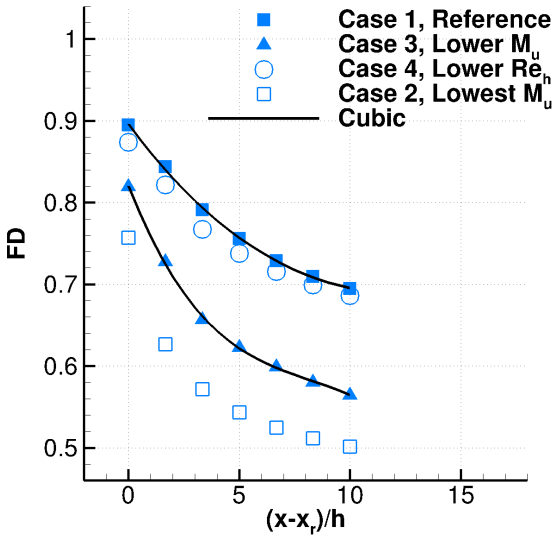

Figure 4.22: Flow distortion for the reference, lower M_u and lower Re_h cases.

4.8 Chapter summary

The shock train experiment by Carroll et al. [26] was used as a reference case in a parametric study investigating the effect of flow confinement, Reynolds number, and geometry changes. Reduction of confinement was achieved by increasing the exit (back) pressure, which relocates the shock train upstream where the boundary layer is thinner. Reduction of confinement significantly reduced the length of the shock train and improved the flow distortion and total pressure recovery efficiency metrics. Larger corner separations were observed at the reduced levels of confinement. Reduction of the pre-shock Mach number had a similar effect on the shock train - increased corner separations and significantly reduced shock train length. The length of the shock train was more sensitive to the Mach number which is in agreement with the literature. Reduction of the Reynolds number had an opposite effect - the shock train length was increased considerably and small corner separations were observed. The Mach stem disappeared in some cases due to the bigger separation at the foot of the first shock. The disappearance of the Mach stem correlated with increasing shock train lengths and disappearance of the supersonic tongues, otherwise present. Efficiency metrics based on the stagnation pressure were used to evaluate the "efficiency" of the interactions. Total pressure recovery (TPR) and flow distortion (FD) efficiency metrics were calculated at a specific location, downstream of the start of each interaction. Shock trains featuring an initial shock with a Mach stem resulted in higher TPR and lower FD. In order to maximise the former and minimise the latter, no supersonic flow should reach the location where the parameters

are calculated. Low Mach numbers and low levels of confinement are needed to achieve favourable efficiency metrics.

Chapter 5

MSWBLIs in high-speed pitot intakes *

With established confidence in the numerical method and after the study of parameters influencing the multiple-shock wave boundary layer interaction in a duct, a more realistic geometry was considered. This includes the intake of a store-like geometry at various incidence and roll angles with a non-linear Eddy viscosity model. The store-like geometry couples the external and internal flows. By doing so the ambiguity of the inlet conditions present in internal SWBLI/MSWBLI simulations is eliminated.

5.1 Fore-body intake geometry

Since the flow of interest is within the intake and the bulk of the flow around the store-like geometry is supersonic, only the forward section of the store-like geometry was considered. This forward section of the store is referred to here as the fore-body intake geometry. Figure 5.1 shows the geometry of the fore-body intake. The fore-body intake geometry consisted of a spherically blunted tangent ogive followed by a cylinder of constant diameter D. Four geometries were considered - one with a square intake, one with a kidney-shaped intake, one with a filleted intake, and one with an intake featuring a cross-sectional area that changes from rounded to circular. The geometries (or configurations) are referred to as A, B, C, and D in this chapter. Configuration A features an intake with a square profile of $h = w = 0.5H$ where $H = 0.5D$ and the thickness is $t = 0.03D$. The thickness t reduces towards the lips of the intake which are filleted. The diverter width is $0.1D$ and the intakes are oriented at 45deg with respect to the $x-y$ symmetry plane. Configuration B features a kidney shaped intake which was generated by filleting two concentric circles with radiuses $R_1 = D$ and

*The fore-body intake results in this chapter are published in K. Boychev *et al.* "Numerical Simulations of Multiple Shock Wave Boundary Layer Interactions", Proceedings of the AIAA Scitech 2021 Forum and Exposition, 11-15 January 2021, Orlando, Florida

$R_2 = 0.6D$. Configuration C is similar to configuration A apart from the intake having filleted corners with a fillet radius of $0.1D$. The intake geometries are shown in figure 5.1. The cross-sectional area of the configurations,was kept approximately constant at $A \approx 0.0019D^2$ and the intakes extended an additional $2D$ distances aft of the fore-body. The choice of diverter width and 45 degrees orientation with respect to the symmetry plane was driven by the findings of Goldsmith [59] who states that an intake aspect ratio of unity, diverter thickness of $0.1D$, and 45 degrees placement angle with respect to the vertical contributes to higher total pressure recovery. More detailed drawings of the fore-body geometry are presented in Appendix D.

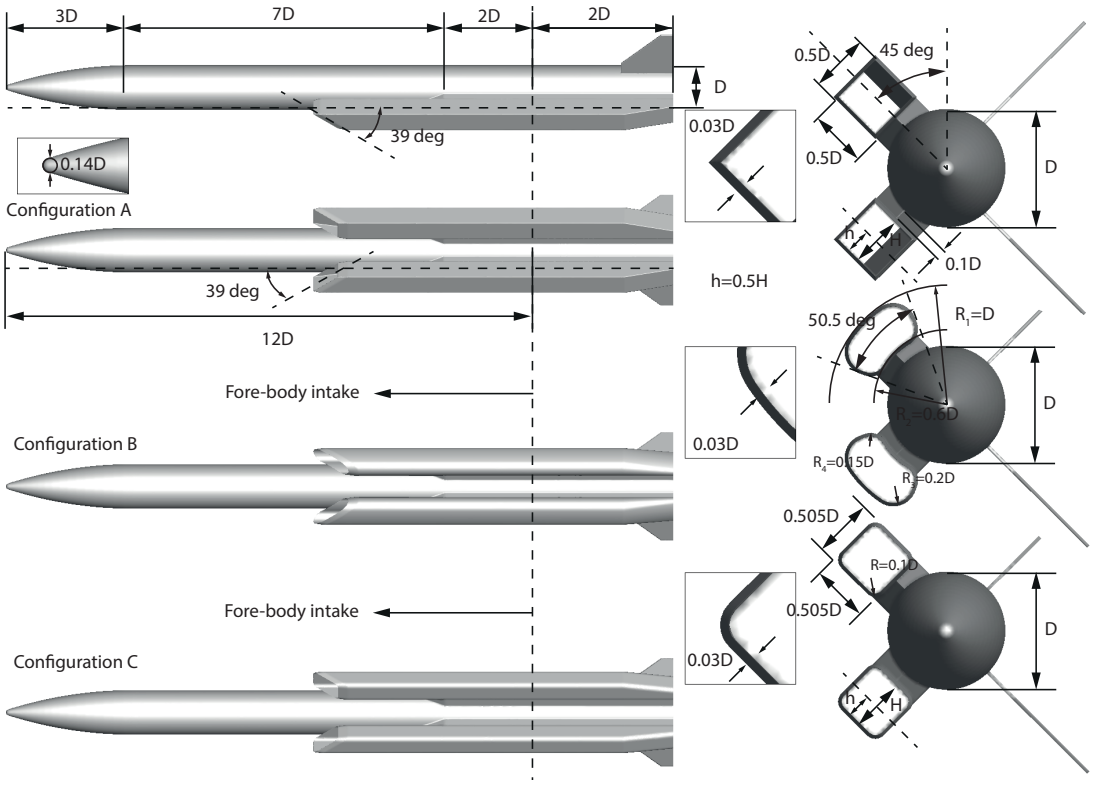

Figure 5.1: Fore-body intake geometry, configurations,A, B, and C. Schematic of the intake geometries is shown on the right.

To compare the efficiency of the pitot intakes in terms of total pressure recovery to that of a mixed compression intake, a mixed compression intake was designed using one-dimensional isentropic relations. The details are shown in table 5.1.

To compress the oncoming flow a thee-shock system was selected. The first shock was generated by a ramp of $\delta = 10$ deg. According to the isentropic relations for oblique shocks, a deflection angle of $\delta = 10$ deg corresponds to a shock angle β, of approximately 39 deg. The slant angle of all pitot intakes was based on this angle. A second oblique shock with an angle of $\beta = 49.4$ deg is then generated to satisfy the flow direction constraint. Finally,

Table 5.1: Total pressure recovery for mixed compression intake designed with one-dimensional isentropic relations.

Station (n)	M	δ deg	β deg	$p_{0,n}/p_{0,n-1}$	p_n/p_{n-1}	$p/(p_{ref}\gamma M_{ref}^2)$
1	2.00	10.0	39.31	1.0	1.0	0.1786
2	1.64	10.0	49.38	0.9846	1.7066	0.3047
3	1.28	-	-	0.9877	1.6426	0.5006
4	0.63	-	-	0.9819	1.7594	0.8807
Total				0.9549	4.9320	0.8807

the compression is completed by a weak terminal shock. The MIL-E-5008B relations which provide a reasonable initial estimate for TPR of an intake are used as a reference (Mattingly et al. [84]). In the MIL-E-5008B relations, the TPR is expressed as a function of the reference Mach number, M_{ref}, and is given by

$$TPR = 1 - 0.075\left(M_{ref} - 1\right)^{1.35}, \quad 1 < M_{ref} < 5 \tag{5.1}$$

At $M_{ref} = 2.0$ the above relation predicts a TPR of 0.925, however, the total pressure recovery of the intake is usually less. The starting characteristics of the intake are as important as its total pressure recovery. The quasi-one-dimensional Kantrowitz method [76] is often used to characterise the starting characteristics of intakes and it is based on two assumptions:

- The intake is fully enclosed, i.e. the freestream velocity is normal to the intake capture plane.
- The flow is quasi-one-dimensional and quasi-steady, i.e. the freestream velocity changes so slowly that the flow inside the intake has ample time to adjust.

Under these assumptions, the Kantrowitz theory leads to three distinct regions on the $\frac{A_t}{A_c}/M_{ref}$ diagram (Figure 5.2). These regions are defined by the Kantrowitz line and the isentropic line. The Kantrowitz line is obtained by assuming a normal shock at the capture plane of the intake and calculating the isentropic area ratio that will produce sonic flow at the intake throat. The Kantrowitz area ratio is given by:

$$\begin{aligned}\left(\frac{A_t}{A_c}\right)_{Kantrowitz} = &\left(\frac{\gamma-1}{\gamma+1} + \frac{2}{(\gamma+1)M_c^2}\right)^{-\frac{1}{2}} \\ &\cdot \left(\frac{2\gamma}{\gamma-1} - \frac{\gamma-1}{(\gamma+1)M_c^2}\right)^{\frac{-1}{\gamma-1}},\end{aligned} \tag{5.2}$$

where A_c is the capture area, A_t is the throat area where $M_t = M^* = 1$ and M_c is the Mach number at the capture plane. In addition to the Kantrowitz line, the internal contraction ratio can be obtained from the isentropic line in the absence of a normal shock at the entrance of the intake. The isentropic area ratio is given by the following equation:

$$\left(\frac{A_t}{A_c}\right)_{isentropic} = \frac{\left(\frac{\gamma+1}{2}\right)^{\frac{-(\gamma+1)}{2(\gamma-1)}} \left(1+\frac{\gamma-1}{2}M_c^2\right)^{\frac{\gamma+1}{2(\gamma-1)}}}{M_c}, \tag{5.3}$$

where A_c is the throat area where $M_t = M^* = 1$ and M_c is Mach number at the capture plane. Figure 5.2 shows the Kantrowitz and isentropic lines for $0.01 < M_{ref} < 6$.

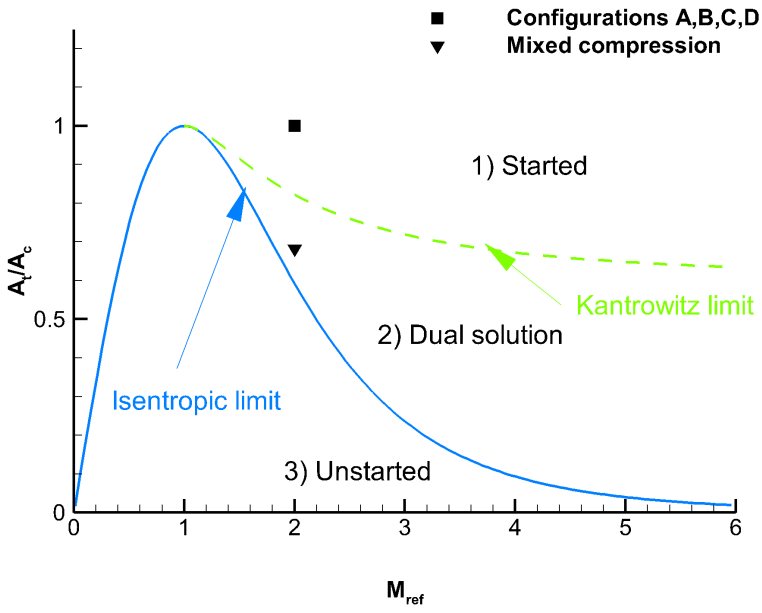

Figure 5.2: Intake start/unstart limits based on the Kantrowitz and isentropic contraction limits.

Above the Kantrowitz line, the intake will start spontaneously, i.e. steady supersonic flow in the intake can be established by a quasi-steady acceleration of the intake from zero velocity to the reference Mach number M_{ref}. Below the isentropic line, steady supersonic adiabatic flow in the intake is not possible, since its existence would require a decrease in entropy. The steady flow would pass through an area less than its sonic area. The only possible solution in this region, below the isentropic line, is a non-started one - a bow shock and a subsonic flow throughout the intake. In the area above the isentropic line and below the Kantrowitz line both started and non-started solutions are possible. If this region is entered from above

the Kantrowitz line, either by a Mach number or area ratio decrease the started solution will be maintained. An entry from below the isentropic line will result in a non-started solution. One way to start an intake is to bring the $\frac{A_t}{A_c}$ ratio above the Kantrowitz line by overspeeding, increasing M_{ref}. Another way is to increase the throat area A_t or decrease the capture area A_c. The intake may also be designed in such a way that it is not fully enclosed. For the designed mixed compression intake the ratio of the throat to capture area is $A_t/A_c = 0.8823$, where A_c is the area perpendicular to the compression ramp. This leads to an effective reduction of the Kantrowitz line for the overall intake. All configurations are above the Kantrowitz limit as $A_t/A_c \approx 1$ for all. The designed mixed compression intake has a ratio of $A_t/A_c = 0.8823$ and is not fully enclosed. Stared operations of the intakes are possible since the ratios are in the started and dual solution regions.

5.2 Grids and numerical setup

Since the external flow is predominantly supersonic, only the fore-body intake section of each store-like configuration was simulated. The aft-body, containing the fins and the nozzle was discarded. The fore-body extends from $x = 0$ to $x = 12D$ and its total length is $L = 12D$. The numerical domain, shown in 5.3 below, is non-dimensionalised with the fore-body length $L = 12D$ which gives a non-dimensional fore-body length of 1.

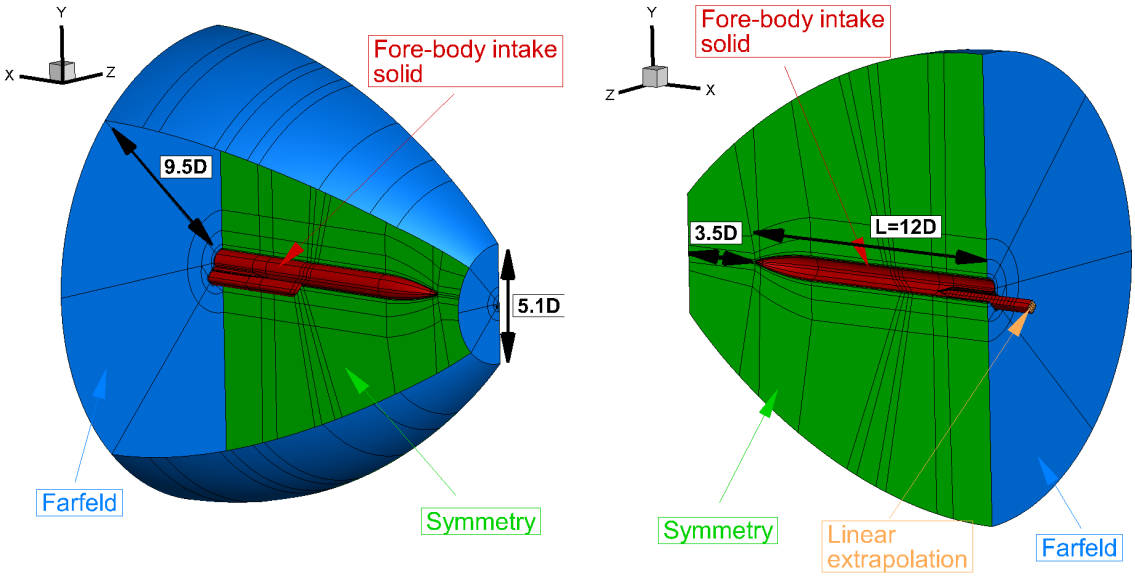

Figure 5.3: Fore-body intake numerical domain and boundary conditions.

For cases at zero roll angle, only half of the domain was considered with symmetry boundary condition applied at the $x-z$ plane. Far-field boundary conditions were applied at the far-field

boundaries and extrapolation boundary conditions, except where the flow is subsonic, were applied at the engine face. Adiabatic non-slip wall boundary conditions were applied at the surface of the fore-body intake. Fully-matched multiblock structured grids of the numerical domain were created using ICEM CFD by employing O-topologies around the intake and the fore-body. The blocks adjacent to the surface had a height of $0.005D$. The grids consisted of approximately 890 blocks and the topology of the grids varied slightly for each configuration. Figure 5.4 shows the grid and blocking topology for configuration C. The minimum wall distance was $2.5 \times 10^{-6}D$ which ensured a $y^+ < 1$. The minimum wall distance value was based on the one used in the isolated shock train simulations. In these simulations, a minimum distance of 1×10^{-5} with respect to the half-height of the duct was sufficient to achieve y^+ values of less than 1. Hyperbolic grid stretching was employed towards the far-field boundaries of the numerical domain. As the boundaries are far away from the fore-body and the flow is supersonic, stretching had a little effect on the solution. The grid parameters are shown in table 5.2.

Table 5.2: Grid parameters for the fore-body intake.

Grid	Min dist.	Intake points	Total points	Total cells
A	$2.5\times10^{-6}D$	26.82×10^{6}	60.04×10^{6}	57.40×10^{6}
B	$2.5\times10^{-6}D$	15.65×10^{6}	60.07×10^{6}	54.41×10^{6}
C	$2.5\times10^{-6}D$	15.65×10^{6}	60.07×10^{6}	54.41×10^{6}

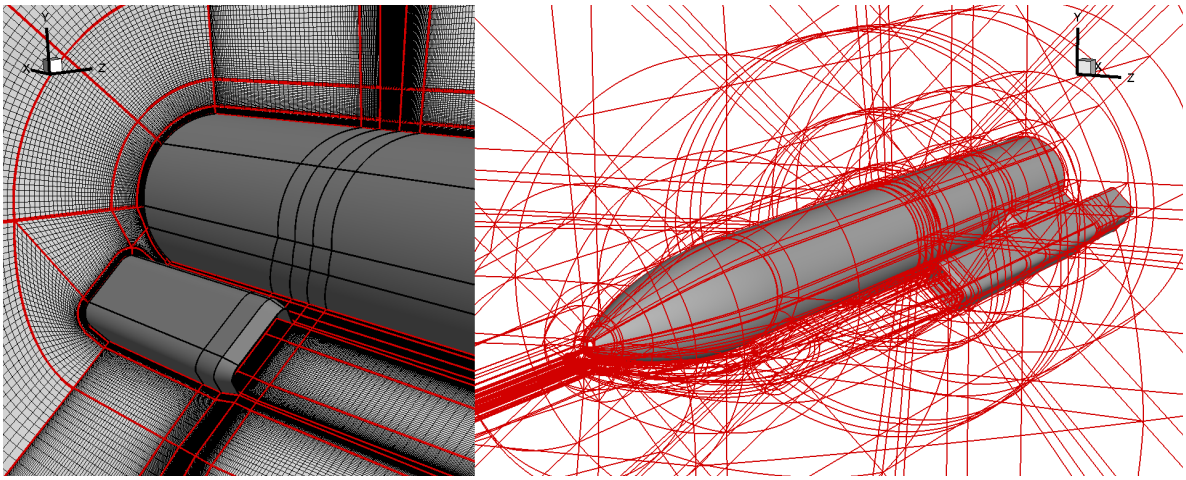

Figure 5.4: Configuration C grid (left) and blocking (right).

5.3 Cases

Numerical simulations of the configurations were performed with the $k-\omega$ SST and EARSM turbulence models. As shown previously in chapter 3, the choice of a turbulence model can have a significant impact on the solution. If the model accounts for the secondary flows, which are present near corners, corner separations will be suppressed by the higher momentum flow supplied by the corner flows. The suppression of the corner flows affects the centreline separation and the subsequent shock train structure by increasing the λ-foot of the first shock. If the separation is large the λ-foots on adjacent walls merge to form a χ shock train structure. The effect of the total incidence angle, σ and the roll angle λ on the total pressure recovery (TPR) and flow distortion (FD) efficiency metrics were investigated. Both metrics were evaluated at the engine face of the fore-body intake. Figure 5.5 shows the definitions of σ and λ.

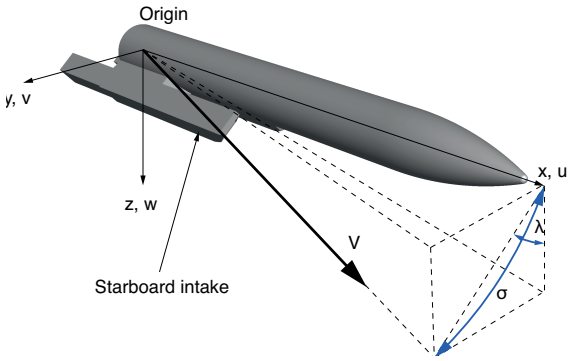

Figure 5.5: Fore-body intake axis definitions.

Freestream conditions at $M = 2.0$ and altitude of 8000 m were assumed. The international standard atmosphere model (ISA) was used to obtain the values of the density speed of sound and viscosity - $\rho_{ref} = 0.5252$ kg/m^3, $a_{ref} = 308.0627$ m/s, $\mu_{ref} = 1.5268 \times 10^{-5}$. The Reynolds number based on the fore-body diameter $D = 0.1$ m was $Re_D = 2.24 \times 10^6$. Based on the intake half-height h the Reynolds number was $Re_h = 5.3 \times 10^5$, and was comparable to the Reynolds numbers of the isolated shock train case of Carroll *et al.* [26] presented in chapter 3. Two incidence and one roll angles were considered. The velocity vector components in the body-fixed reference frame are given by

$$\vec{V} = (u,v,w) = \begin{cases} (0.996, 0, 0.087) & \text{for } \sigma = 5 \text{ and } \lambda = 0 \\ (0.985, 0, 0.174) & \text{for } \sigma = 10 \text{ and } \lambda = 0 \\ (0.996, 0.005, 0.087) & \text{for } \sigma = 5 \text{ and } \lambda = 3 \end{cases} \tag{5.4}$$

Table 5.3 lists the simulation parameters. The TPR and FD of the port and starboard intakes are separated by the colon symbol. Port TPR is on the left of the colon symbol and starboard TPR is on the right. All simulations were initialised with an inviscid shock placed at the end of the intake. The MUSCL 3rd order scheme was used and simulations were run until the axial force coefficient, C_X settled. The $k-\omega$ EARSM simulations at $\sigma = 0$ deg and $\lambda = 0$ deg used the $k-\omega$ SST as an initial solution.

Table 5.3: Fore-body intake cases.

Grid	M_{ref}	Symm.	σ (deg)	λ (deg)	TPR	FD	η	Model
A	2.00	Y	0	0	0.6568	0.7044	3.375	$k-\omega$ SST
A	2.00	Y	0	0	0.6527	0.8044	3.375	$k-\omega$ EARSM
A	2.00	Y	0	0	0.6696	0.6469	3.825	$k-\omega$ EARSM
A	2.00	Y	5	0	0.7122	0.6854	3.825	$k-\omega$ EARSM
A	2.00	N	5	3	0.7136 : 0.7095	0.6799 : 0.6778	3.825	$k-\omega$ EARSM
B	2.00	Y	0	0	0.6718	0.4649	3.825	$k-\omega$ SST
B	2.00	Y	0	0	0.6738	0.7379	3.825	$k-\omega$ EARSM
B	2.00	Y	5	0	0.7166	0.6873	3.825	$k-\omega$ EARSM
B	2.00	N	5	3	0.7191 : 0.7147	0.7074 : 0.7109	3.825	$k-\omega$ EARSM
C	2.00	Y	0	0	0.6706	0.5039	3.825	$k-\omega$ SST
C	2.00	Y	0	0	0.6737	0.7043	3.825	$k-\omega$ EARSM
C	2.00	Y	5	0	0.7172	0.6820	3.825	$k-\omega$ EARSM
C	2.00	N	5	3	0.7186 : 0.7147	0.6840 : 0.6830	3.825	$k-\omega$ EARSM

5.4 Investigating turbulence modelling

The effect of the turbulence model on the flowfied inside the intake was significant. The results from configuration C will be used to show the differences in the flowfied, however, similar observations were made for the other configurations. They are discussed at the end of this section. Figure 5.6 shows the wall pressure and Mach number contours for configuration C predicted by the $k-\omega$ SST turbulence model (top) and by the $k-\omega$ EARSM turbulence model (bottom). The Mach number contours in subfigure (a) are of a slice taken at 45 deg with respect to the vertical plane and are spaced at $\Delta M = 0.2$ starting from $M = 1$ (the sonic contour). The Mach number contours in subfigure (c) are of a slice taken at the mid-plane of the intake, perpendicular to the 45 deg slice. The intake is non-dimensionalised with a half-height of $h = 0.22D$ and the origin is shifted to the upper intake lip. The $k-\omega$ SST model predicts a single shock located at approximately $x/h \approx 19.6$ downstream of the lip of the intake. The upper and lower wall pressures are mostly symmetrical downstream of the onset of the interaction. The bottom wall pressure profile exhibits stronger pressure oscillations than the top one, upstream of the interaction. The oscillations are attributed to the oblique

shock generated by the upper intake lip which impinges the lower wall and its reflection then propagates downstream in the intake.

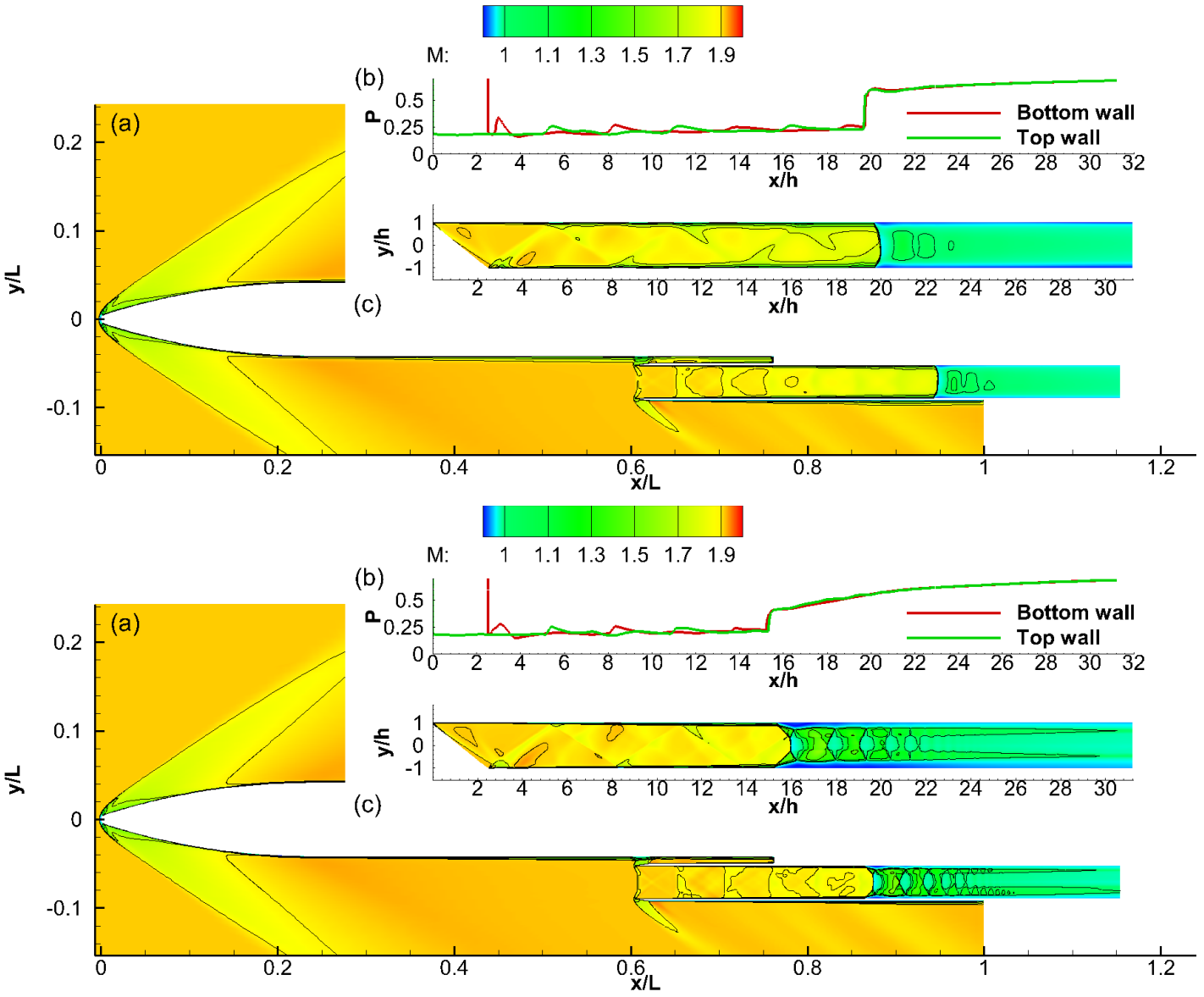

Figure 5.6: Wall pressure (b) and Mach number contours (a,c) for configuration C $k-\omega$ SST (top) and $k-\omega$ EARSM (bottom).

At the onset of the interaction, $x_r/h \approx 19.6$, the pre-shock Mach number is approximately $M_r = 1.82$ and the average stagnation pressure approximately $p_{0,average} = 0.98$. Based on 99% average stagnation pressure value, the average boundary layer thickness on the sidewalls is $\delta_{r,1} = 5.06$ mm and on the top and bottom walls $\delta_{r,2} = 4.4$ mm ($h = 0.22D$, $D = 0.1$ m). Since the half-height of the intake is $h = 22$ mm, this amounts to confinement levels of $\delta_{1,r}/h = 0.23$ and $\delta_{2,r}/h = 0.20$. Supersonic regions downstream of the first shock are observed, however, the Mach number in these regions is very close to 1 and as a result, there are no subsequent shocks. Since the flow is subsonic at the engine face the FD is relatively low - $FD = 0.5039$. This is not the case for the $k-\omega$ EARSM model which predicts a shock train within the intake. As shown in chapter 4 the existence of supersonic regions near the engine face, or the plane at which the flow distortion is evaluated, increases the flow distortion parameter. There is a 40% increase in the FD when a shock train is established inside the intake. The change in the total pressure recovery is negligible. The onset of the interaction is located at $x_r \approx 15.2$ which amounts to 30% relative upstream shift compared to the $k-\omega$ SST . At that location, the average stagnation pressure and centreline pre-shock Mach number are $p_{0,average}/p_{0,ref} = 0.8620$ and $M_r = 1.8240$. The levels of confinement are $\delta_{1,r}/h = 0.152$ and $\delta_{2,r}/h = 0.136$ which are approximately 33% smaller than the ones predicted by the $k-\omega$ SST . Table 5.4 shows the confinement levels.

Table 5.4: Confinement levels for configuration C at $\sigma = 0$ deg predicted by the $k-\omega$ SST and $k-\omega$ EARSM turbulence models.

x_r	M_r	δ_1/h	δ_1/h	Model
19.6	1.819	0.23	0.20	$k-\omega$ SST
15.2	1.824	0.15	0.14	$k-\omega$ EARSM

The shock train features the distinctive λ-foot structure with a large Mach stem and is comprised of three shocks which are concave facing upstream. The increased flow distortion at the engine face is attributed to the supersonic tongues which extend all the way up to the engine face. Like the $k-\omega$ SST model, there is no symmetry with respect to the $y-x$ and the $z-x$ planes. No separations at the corners are observed for the $k-\omega$ EARSM model. The $k-\omega$ SST model on the other hand predicts separations in all corners. Unlike configuration C, the $k-\omega$ SST model predicted a shock train in configuration A. The wall pressure featured significant oscillations which indicated the presence of large corner separations. Chapter 3 showed that pressure oscillations are mainly caused by the overprediction of the corner separations and the resulting stronger re-acceleration of the flow behind the first shock. Further visualisations of the flow field indeed showed that each corner featured a large separation. The separations at the top wall corners were slightly bigger. The difference in the top and bottom wall corner separation sizes contributed to a slight flow asymmetry in the

x-y plane. No flow asymmetry was observed in the x-z plane. Similarly to configuration C, configuration B did not feature a shock train when the $k-\omega$ SST model was used. A single normal shock was present without noticeable λ-foot structures. As in configuration C, the reduced upstream Mach number and the thicker boundary layer were the cause. The $k-\omega$ EARSM model predicted shock trains in all configurations and was used for all subsequent calculations. A detailed description of the flowfied in configurations A and B, predicted by the $k-\omega$ EARSM model, is provided in the next section.

5.5 Effect of total angle, σ

The effect of total angle was investigated by changing σ from 0 deg to 5 deg and keeping the roll angle $\lambda = 0$ deg. Description of the flow field and comparison of the efficiency metrics for all configurations, follows. First, the flow-field of each fore-body configuration is described by comparing Mach number contours and wall pressures. Then, the flow efficiency metrics - total pressure recovery and flow distortion are evaluated and compared.

5.5.1 Configuration A

Figure 5.8 compares the wall pressure (b) and Mach number contours in $x-y$ (c) and $x-z$ (a) wall planes of configuration A at $\sigma = 0$ deg and $\sigma = 5$ deg. At zero incidence angle, the rise of the top and bottom wall pressure begins at approximately $x_r/h = 14.1$ and $x_r/h = 14.4$. The relative difference of 2% between the two indicates that asymmetry in the flow is present. The first shock in the shock train features a Mach stem and two λ-foot structures - one adjacent to the bottom wall and one to the top wall. The top wall structure is bigger and as a result, the pressure rise on the top wall occurs earlier than the one on the bottom wall. As the λ-foot slows the flow less than the normal portion of the shock, regions of supersonic flow below the slip line are present and extend up to $x/h = 30$. Such regions were also observed for the internal interactions and are often termed supersonic tongues. The shock train exhibits symmetry in the port-starboard wall plane. The size of the λ-foot structures is almost identical. As the angle is increased the shock train becomes highly asymmetrical. It is difficult to agree on the exact structure of the first shock. It is theorised that the two λ-foot structures join and the Mach stem, otherwise present, disappears. Due to the absence of the Mach stem, the flow is faster (there is less deceleration) and as a result, a large supersonic region extends all the way up to the engine face $x/h = 30$. The presence of supersonic flow at the engine face is expected to increase the flow distortion.

5.5.2 Configuration B

Figure 5.9 compares the wall pressure (b) and Mach number contours in the $x-y$ (c) and $x-z$ (a) wall planes of configuration B at $\sigma = 0$ deg and $\sigma = 5$ deg. At both incidence angles, the interaction in the intake is highly-asymmetrical. Although the rise in the top and bottom wall pressure begins at $x_r/h \approx 12.5$ and $x_r/h \approx 13$ at $\sigma = 0$ deg it is not the cause for the asymmetry. The case for the asymmetry is the large separation on the bottom wall. The initial shock features an asymmetrical λ-foot structure with the bigger λ-foot adjacent to the bottom wall. The large region of subsonic flow downstream of the Mach stem is accelerated to supersonic speeds. However, the absence of contours bunching downstream indicates that the shocks in the region, if any, are weak. A presence of a shock is suggested by the bunching of the contours at $x/h \approx 16$. This shock does not propagate to the opposite wall but terminates below the centreline. When the incidence angle is increased, the separation region relocates further upstream. The relocation of the region is accompanied by an increase in the λ-foot structure adjacent to the bottom wall. The size of the Mach stem reduces significantly. Reduction of the centreline Mach number is also observed, due to the stronger oblique interaction forming at the entrance of the intake. The increase of the bottom wall λ-foot structure relocates the bottom wall pressure rise further upstream, resulting in approximately 13% difference in x_r/h between the top and bottom walls. The Mach number contours in the $x-z$ wall plane are shown in figure 5.9 (a). The contours in this plane are more symmetric compared to the ones in the $x-y$ wall plane. Supersonic regions are present at the location of the engine face, $x/h = 30$, which is expected to result in greater flow distortion values. Compared to the other configurations, the intake of configuration B has an unequal aspect ratio. Its height is considerably larger than its width. In addition, the intake does not feature any straight walls - every wall is curved. In chapter 4, lower levels of streamwise vorticity were observed in all of the rounded geometries. Lower vorticity levels are associated with weaker secondary flows that bring less momentum to the corners. Less momentum often results in increased corner separations. As rounded geometries do not result in well-defined corner separations (if the rounding is considerable), the adverse pressure gradient at the location of the first shock is expected to be stronger. In chapter 1, it was shown that the corner separations give rise to weak oblique waves that propagate into the flow, and as a result, smear the adverse pressure gradient at the start of the interaction. The absence of well-defined corner separations in the all-rounded intake geometry of configuration B and the unequal aspect ratio is considered the main contributors to the large separation at the bottom wall.

5.5.3 Configuration C

Figure 5.10 compares the wall pressure (b) and Mach number contours in the $x-y$ (c) and $x-z$ (a) wall planes of configuration C at $\sigma = 0$ deg and $\sigma = 5$ deg. The onset at zero incidence angle is approximately $x_r/h \approx 15.2$, and a slightly asymmetrical shock train with a λ-foot structure is observed. The supersonic regions below the slip line at $\sigma = 0$ deg extend to the engine face ($x/h = 30$). The presence of supersonic regions at the location where efficiency metrics are evaluated often lead to higher values of FD. At the higher incidence angle, the λ-foot structure on the bottom wall grows significantly in size. This is indicated by the interaction onsets on the top and bottom wall which are located at $x_r \approx 14.1$ and $x_r/h = 13.3$. The relative difference is approximately 5.7%. The difference is caused by the large λ-foot structure on the bottom wall. The centreline Mach number is reduced to $M_r \approx 1.74$. This amounts to a reduction of $\Delta M_r \approx 0.1$ when compared to the pre-shock Mach number at $\sigma = 0$ deg. The cause for the reduction is the stronger oblique interaction occurring at the entrance of the intake. As the flow behind the λ-foot structure is faster, a bigger region of supersonic flow is present at the engine face which is expected to reduce the flow distortion efficiency metric. The $x-z$ wall contours, shown in figure 5.10 (a) are relatively symmetrical at $\sigma = 0$. The symmetry is reduced at $\sigma = 5$ deg, however, the Mach number contours are not as distorted as the contours in the $x-y$ wall plane.

5.5.4 Efficiency metrics

Figure 5.7 compares the total pressure recovery and the flow distortion for the three configurations,at $\sigma = 0$ deg and $\sigma = 5$ deg. The total pressure recoveries for the three configurations, are comparable at both incidence angles, although configurations B and C result in slightly higher recoveries. At zero incidence, the variation in the flow distortion between the configurations,is significant. Since the flow distortion is defined as the ratio of the difference in the maximum and minimum stagnation pressures and the average stagnation at the engine face, larger $p_{0,max} - p_{0,min}$ or smaller $p_{0,avarage}$ will increase the FD. Higher $p_{0,max}$ is associated with higher velocities since bringing the flow to stagnation conditions isentropically from a higher velocity will result in a greater p_0. Table 5.5 compares the average, minimum, and maximum stagnation pressures of the three configurations, at $\sigma = 0$ deg and $\sigma = 5$ deg.
Configuration A has the smallest $p_{0,max} - p_{0,min}$ difference and the average TPR for the three configurations is approximately $p_{0,average} \approx 0.94$. The average streamwise velocity is also similar and approximately $u_{average} = 0.42$. The main contributing factor to the FD is the $p_{0,max} - p_{0,min}$ difference. Decreasing $p_{0,max}$ will improve the FD efficiency metric.

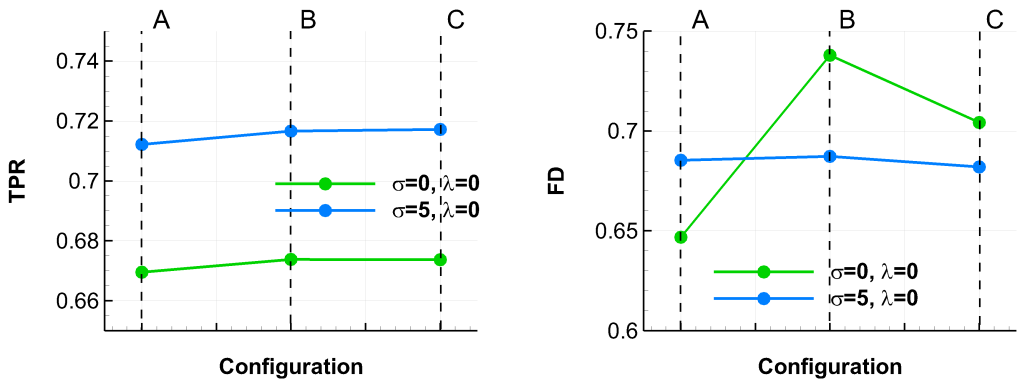

Figure 5.7: Total pressure recovery (left) and flow distortion (right) efficiency metrics at $\sigma = 0$ deg and $\sigma = 5$ deg.

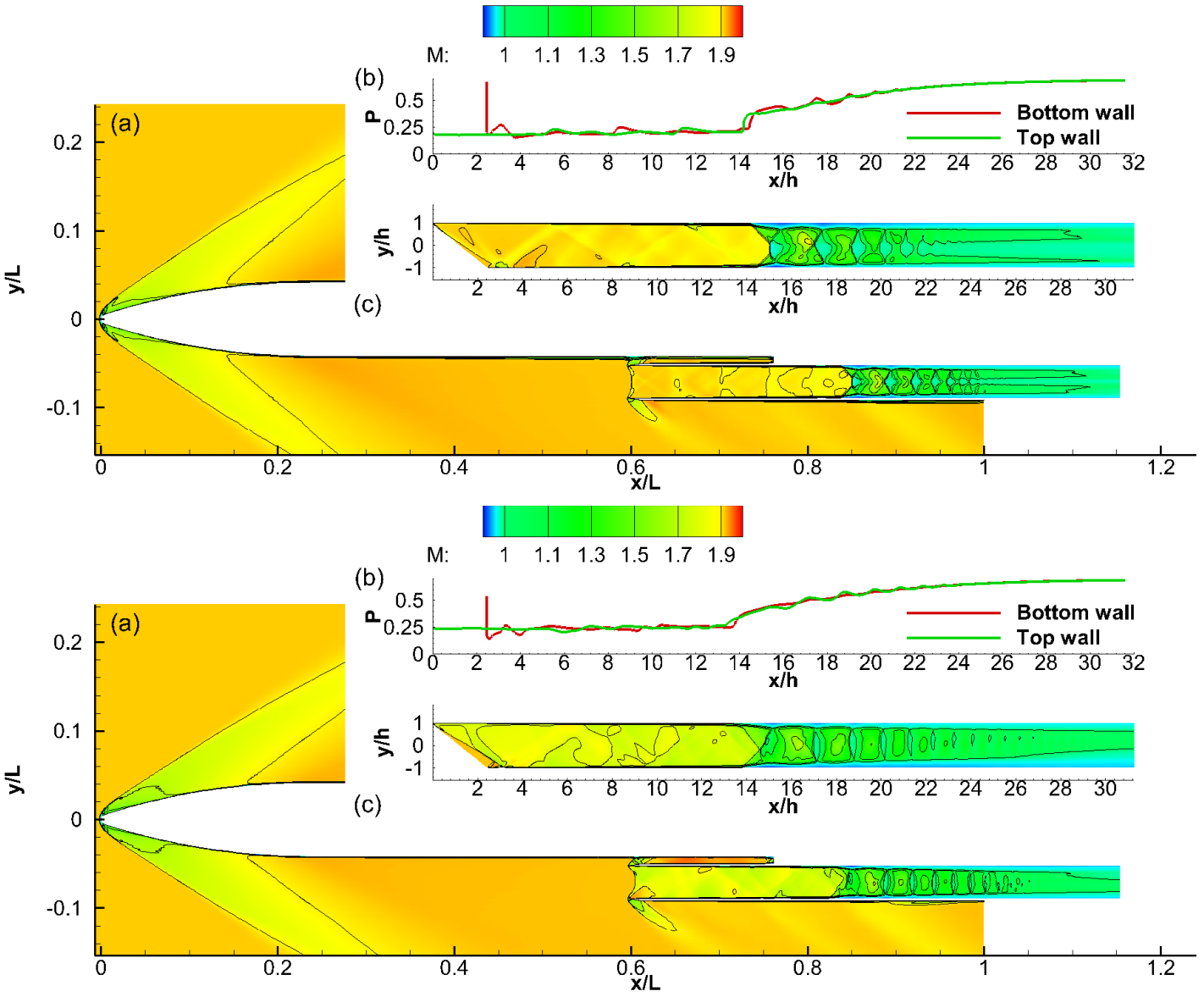

Figure 5.8: Wall pressure (b) and Mach number contours (a,c) for configuration A at $\sigma = 0$ deg (top) and $\sigma = 5$ deg (bottom).

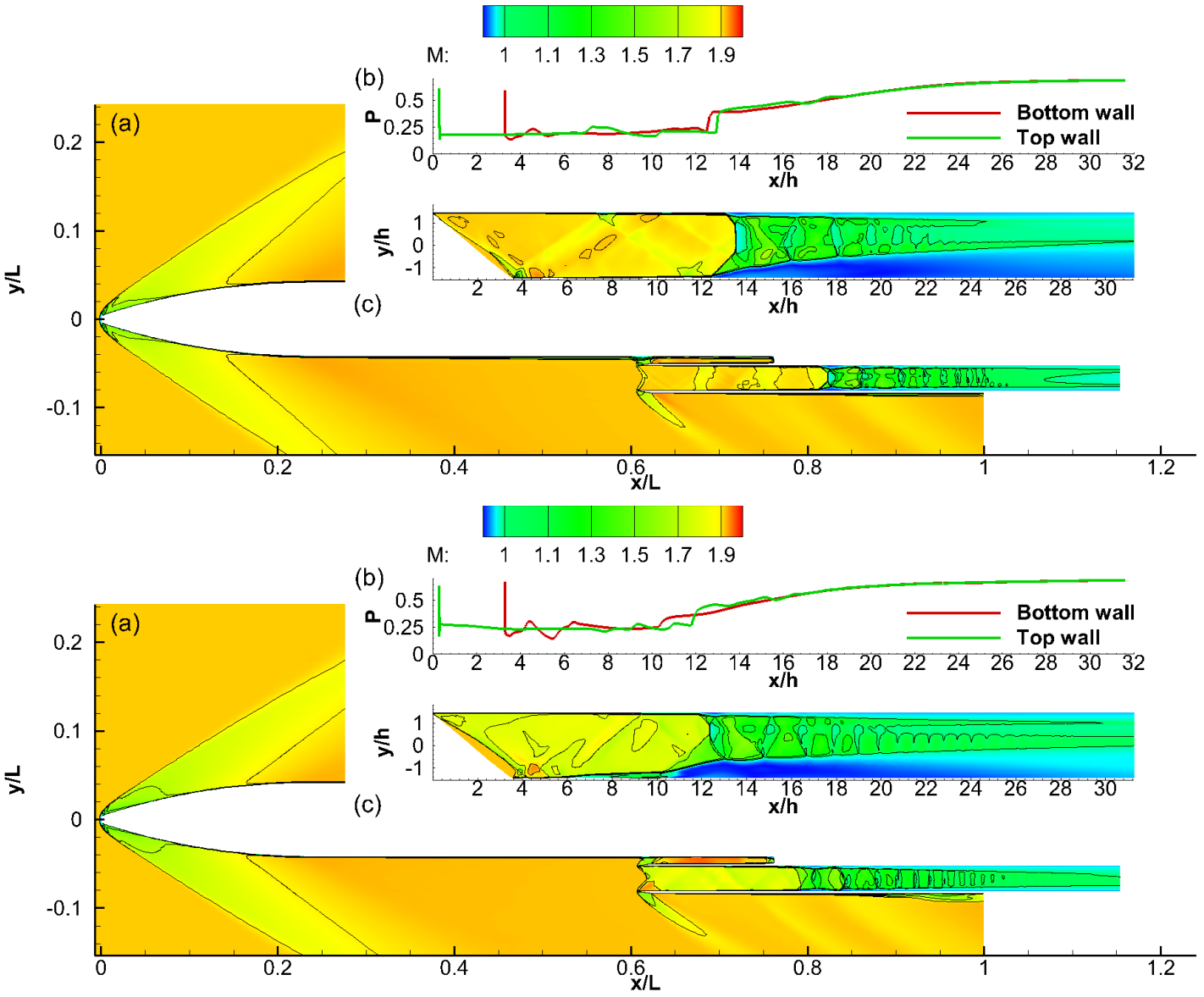

Figure 5.9: Wall pressure (b) and Mach number contours (a,c) for configuration B at $\sigma = 0$ deg (top) and $\sigma = 5$ deg (bottom).

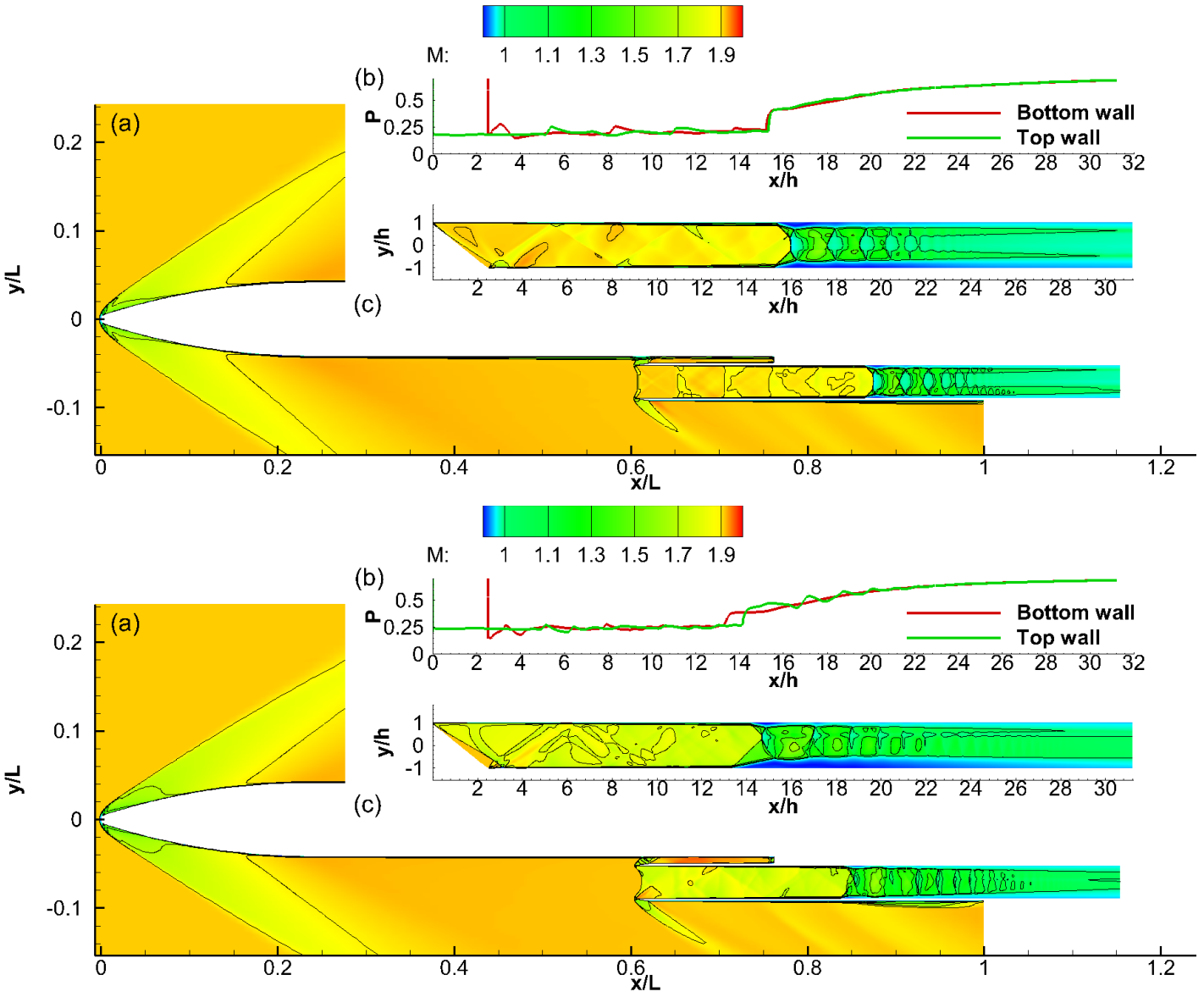

Figure 5.10: Wall pressure (b) and Mach number contours (a,c) for configuration C at $\sigma = 0$ deg (top) and $\sigma = 5$ deg (bottom).

Table 5.5: Stagnation pressures at $x/h = 30$ (engine face).

Configuration	σ deg	$p_{0,avg}$	$p_{0,max}$	$p_{0,min}$	$p_{0,max} - p_{0,min}$	$u_{average}$
A	0	0.9355	1.2853	0.6802	0.6051	0.4217
B	0	0.9415	1.3781	0.6834	0.6947	0.4165
C	0	0.9413	1.3421	0.6791	0.6630	0.4203
A	5	0.9951	1.3602	0.6782	0.6820	0.4515
B	5	1.0013	1.3705	0.6823	0.6882	0.4564
C	5	1.0021	1.3644	0.6810	0.6834	0.4557

At σ the differences in the $p_{0,max} - p_{0,min}$ ratios and the average stagnation pressure $p_{0,average}$ are insignificant, resulting in a flow distortion of $FD \approx 0.68$. Further investigations of the TPR and FD with respect to the incidence angle were performed for configuration A. Figure 5.11 shows the TPR and FD as a function of the incidence angle σ. The incidence angle was varied from $\sigma = -3$ deg to $\sigma = 10$ deg. At the negative incidence angle, the flow within the intake was completely unstarted. The FD was minimum at this condition as the resulting flow velocities in the intake were small. At higher incidence angles, the FD increased up to a maximum value at $\sigma = 5$ deg and reduced as an incidence angle of 10 deg was reached. The reduction of the flow distortion was attributed to the stronger interaction taking place at the entrance of the intake. As the interaction at the entrance of the intake was oblique in nature it reduced the flow velocities more efficiently. As a result, the pre-shock Mach number was lower for subsequent stronger interactions occurring in the intake, the FD was decreased and the TPR increased. The maximum TPR was observed at $\sigma = 10$ deg. The TPRs and FDs of configurations,B and C are compared once again and show that the TPR of the configurations,is comparable at $\sigma = 0$ and $\sigma = 5$ deg. The FD of the configurations,is comparable only at $\sigma = 5$ deg.

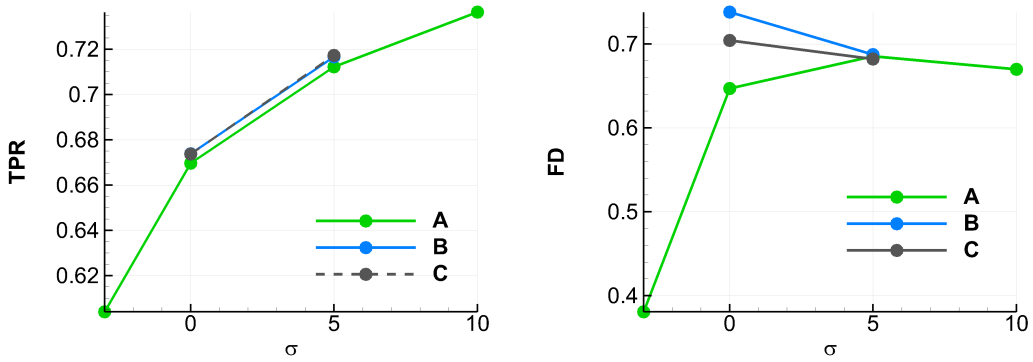

Figure 5.11: Total pressure recovery (left) and flow distortion (right) efficiency metrics at $\sigma = -3, 0, 5,$ and 10 deg.

5.6 Effect of roll angle, λ

The effect of the roll angle, on the flow field inside the intake and the efficiency metrics, was investigated by introducing a positive roll angle of $\lambda = 3$ deg while keeping the incidence angle fixed at $\sigma = 5$ deg. An incidence angle of 5 deg was selected, as, at higher incidence angles, the oblique interaction at the intake entrance was responsible for most of the flow deceleration. The strong oblique interaction was the cause for higher TPR values at $\sigma = 10$ deg. Since we are interested in the flow deceleration across the shock train, a weak oblique interaction at the intake entrance is preferred.

5.6.1 Configuration A

Figure 5.12 compares the Mach number contours and wall pressures for configuration A at zero and three degrees roll angle. The starboard intake at $\lambda = 3$ is compared to the port intake at $\lambda = 0$ deg. Since symmetry boundary conditions were employed at $\lambda = 0$ deg the flow field in the port and starboard intakes is the same. At $\lambda = 3$ deg the shock train features a well-defined initial shock structure which is followed by several vanishingly weak shock structures. The flow fields of the port (not shown) and starboard intake were similar. Both featured initial shocks with asymmetric λ-foot structures. The larger λ-foot structure was adjacent to the starboard wall in both intakes. Based on the upper and lower wall pressure the onset of the interaction in the port intake was located at approximately $x_r/h \approx 17.7$ non-dimensional distances. Both wall pressures exhibited oscillations, an indication of a stronger interaction near the wall. The onset of the interaction in the starboard intake occurred at approximately $x_r/h \approx 17.917$ non-dimensional distances which amounted to 1.1% relative difference. The average difference between the onset on the upper and lower walls of both intakes was approximately $\Delta x_r/h = 0.22$. Compared to the flow field at $\sigma = 5$ deg and $\lambda = 0$ deg the flowfield within the intakes at $\lambda = 3$ exhibited greater similarity to the isolated shock train interactions. The main effect of the roll angle was to move the shock train downstream the intake. Such movement is not beneficial as the interaction gets closer to the engine face and degrades the flow distortion efficiency metric. The relative movement of the shock train was approximately 32.2 %.

5.6.2 Configuration B

The difference between the onset of the interaction on the upper and lower wall as well as the difference between the onset of the interaction at $\lambda = 0$ and $\lambda = 3$ deg was significant for configuration B. Figure 5.13 shows the wall pressure and Mach number contours. At $\lambda = 0$

deg the relative $\Delta x_r/h$ is approximately 14.7 %. At the higher roll angle, $\lambda = 3$ deg, the $\Delta x_r/h$ decreases to 5.2 %. The average onset x_r/h is approximately 10.9 at $\lambda = 0$ and 17.5 at $\lambda = 3$ deg. As the roll angle is increased the onset translates downstream by approximately 6.6 non-dimensional distances. The large plateau regions in the lower wall pressures are the result of the larger flow separation occurring at the lower wall of the intake. The difference in the wall pressure profiles visualises the significant degree of flow asymmetry. The oscillations in the top wall pressure hint that the interactions are stronger near the upper intake wall. Again, the downstream movement of the shock train is not favourable as the flow has less time uniformise before it reaches the engine face.

5.6.3 Configuration C

Figure compares the Mach number contours and wall pressure for configuration C at zero and three degrees roll angle. Again the flow in the starboard intake is compared to the flow at $\lambda = 0$ deg. The plateau-type region in the wall pressure distributions on the bottom wall of the intakes indicates the presence of a large separated region at both $\lambda = 3$ deg and $\lambda = 0$ deg. The sharp pressure rise at the top walls and the subsequent pressure oscillations indicate stronger interactions and supersonic flow regions close to the wall. The difference in the onset of interaction between the upper and lower walls is caused by the larger separation at the lower wall. The larger separation displaces the start on the interaction further upstream. On average the relative difference between the upper and lower wall pressure onset was 6.1% at $\lambda = 0$ deg and 3.1% at $\lambda = 3$ deg. The relative movement of the average onset at $\lambda = 0$ and at $\lambda = 3$ deg amounted to 21.1%. Similarly to configuration A, the initial shock was more well defined at $\lambda = 3$ deg than at $\lambda = 0$. The large separation at the bottom wall of the intake was the reason for the absence of a well-defined Mach stem. The initial shock was followed by several vanishingly weak shocks. Two smaller separated regions on the sidewalls of each intake at the location of the initial shock were also present.

5.6.4 Efficiency metrics

Figure 5.15 compares the total pressure recovery and the flow distortion of the three configurations,at an incidence angle of $\sigma = 5$ deg and a roll angle of $\lambda = 3$ deg. For all configurations, the TPR in the port intake increases and the TPR in the starboard intake decreases. The largest decrease in TPR was observed in configurations,C and A where the TPR in the starboard intake was on average 0.5% lower than the reference TPR at $\lambda = 0$ deg. Configuration B resulted in the largest increase in TPR which amounted to 0.3%. The increase or decrease in the TPR as observed from the averages, however, is negligible, as it is less than 1%. This

shows that introduction of a positive roll angle has little impact on the TPR characteristics of the intakes. As detailed in the flow descriptions the introduction of a positive roll angle relocated the shock train downstream. Table 5.6 compares the average, minimum, and maximum stagnation pressures of the three configurations,at $\lambda = 0$ deg and $\lambda = 3$ deg.

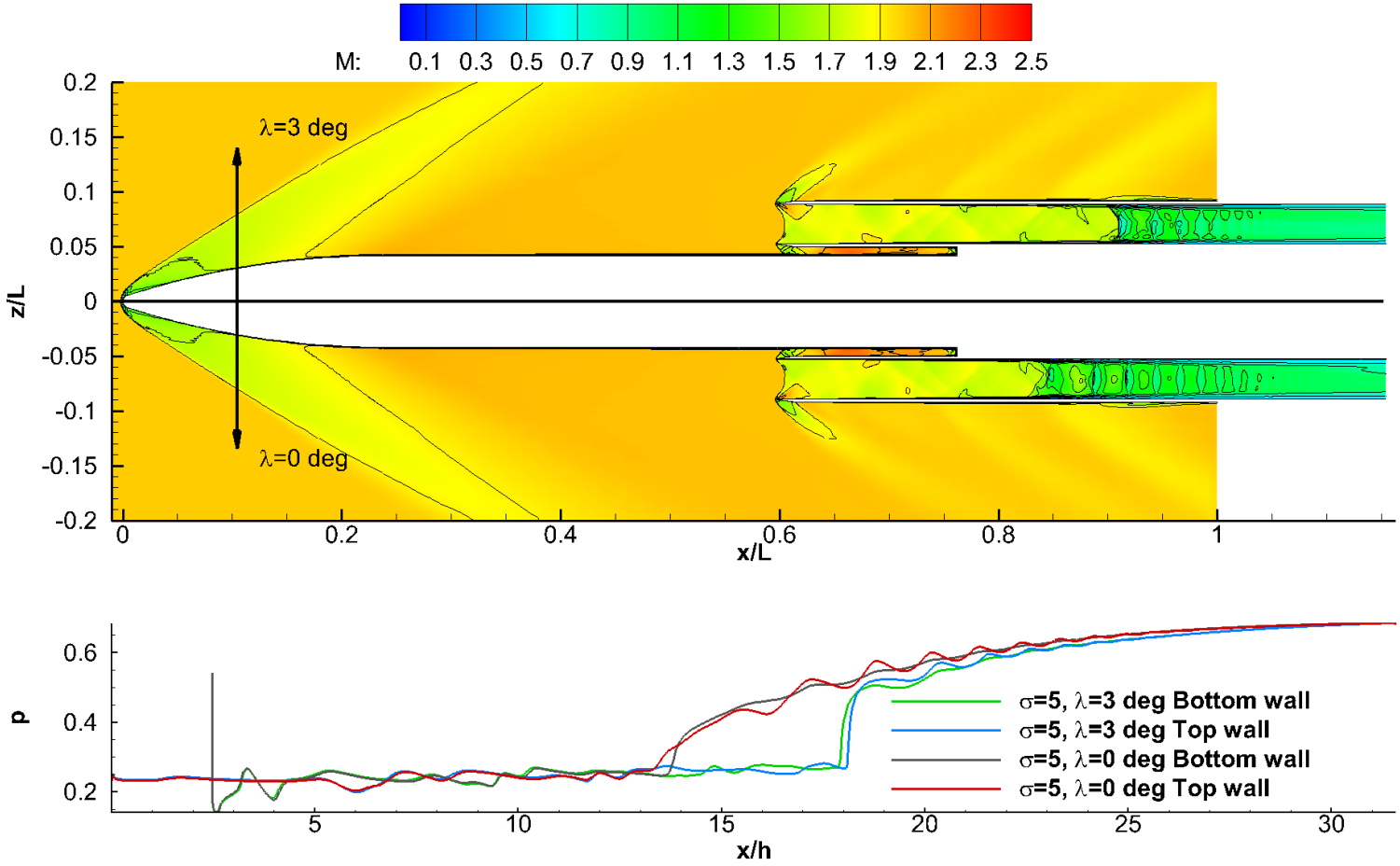

Figure 5.12: Configuration A Mach number contours (top) and wall pressures (bottom) at $\lambda = 3$ deg and $\lambda = 0$ deg.

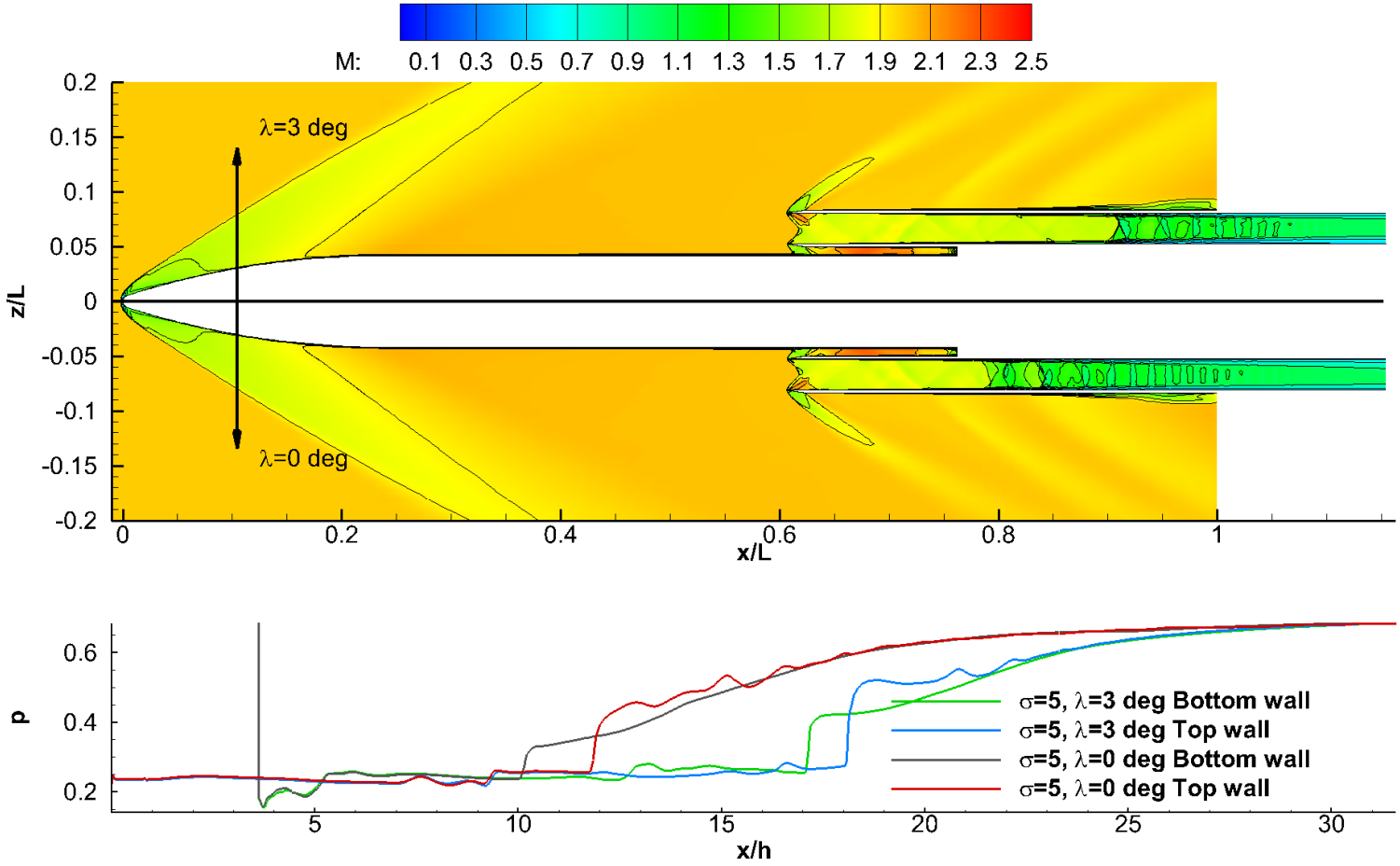

Figure 5.13: Configuration B Mach number contours (top) and wall pressures (bottom) at $\lambda = 3$ deg and $\lambda = 0$ deg.

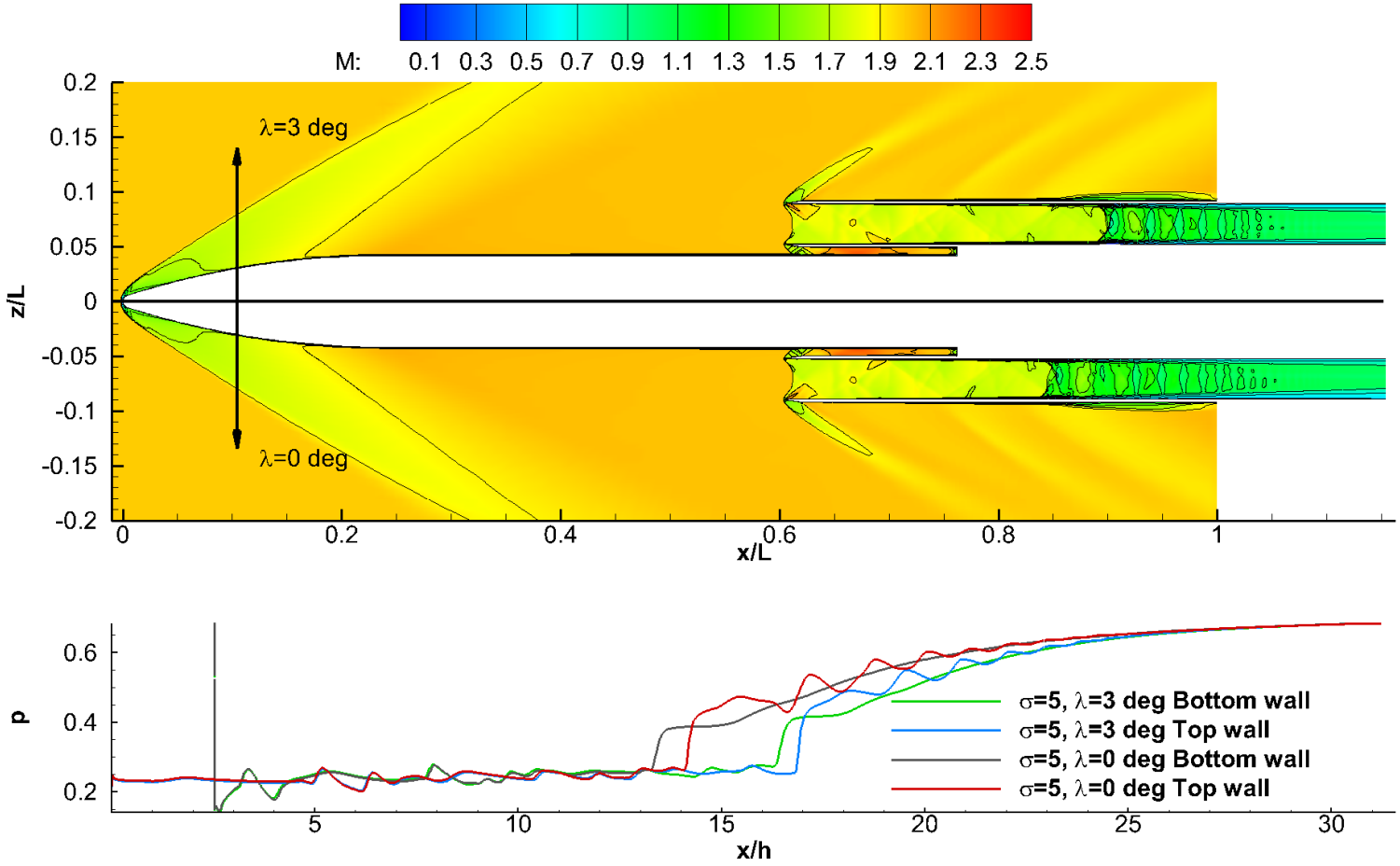

Figure 5.14: Configuration C Mach number contours (top) and wall pressures (bottom) at $\lambda = 3$ deg and $\lambda = 0$ deg.

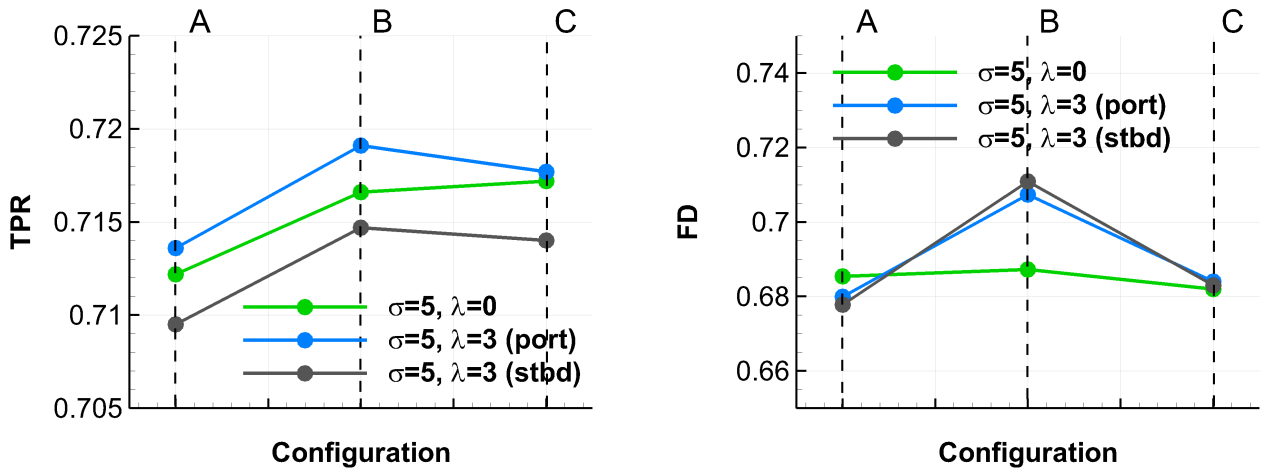

Figure 5.15: Total pressure recovery (left) and flow distortion (right) efficiency metrics at $\sigma = 5$ deg and $\lambda = 3$ deg.

Table 5.6: Stagnation pressures at $x/h = 30$ (engine face).

Configuration	σ deg	λ deg	$p_{0,avg}^{port}$	$p_{0,max}^{port}$	$p_{0,min}^{port}$	$p_{0,max}^{port} - p_{0,min}^{port}$	$u_{average}^{port}$	$p_{0,avg}^{stbd}$	$p_{0,max}^{stbd}$	$p_{0,min}^{stbd}$	$p_{0,max}^{stbd} - p_{0,min}^{stbd}$	$u_{average}^{stbd}$
A	5	0	0.9951	1.3602	0.6782	0.6820	0.4515	0.9951	1.3602	0.6782	0.6820	0.4515
B	5	0	1.0013	1.3705	0.6823	0.6882	0.4564	1.0013	1.3705	0.6823	0.6882	0.4564
C	5	0	1.0021	1.3644	0.6810	0.6834	0.4557	1.0021	1.3644	0.6810	0.6834	0.4557
A	5	3	0.9971	1.3557	0.6777	0.6780	0.4515	0.9913	1.3509	0.6789	0.6720	0.4497
B	5	3	1.0047	1.3911	0.6804	0.7107	0.4508	0.9985	1.3913	0.6814	0.7099	0.4484
C	5	3	1.0041	1.3681	0.6813	0.6868	0.4549	0.9987	1.3633	0.6812	0.6821	0.4519

The flow distortion of configurations,B and C increased when a positive roll angle was introduced. The average stagnation pressure $p_{0,avg}$ was observed to increase in the port intake and decrease in the starboard intake. Increased difference between the maximum and minimum stagnation pressure at the engine face was also observed in both intakes. The increase of $p_{0,max} - p_{0,min}$ and the decrease of $p_{0,avg}$ results in higher flow distortion values. The values between the two intakes (port and starboard) were comparable. The flow distortion values for configuration A remained close to the values at $\lambda = 0$ deg. The slight reduction of the FD values resulted from the slight increase of $p_{0,avg}$ and the slight decrease of $p_{0,max}$ at the engine face. Like configurations B and C, no significant differences between the values of the port and starboard intakes was observed. The downstream movement of the onset of the interaction, x_r, in configuration B, results in supersonic regions near the engine face. In addition, the "plateau" regions observed in the top and bottom wall pressure distributions indicate long separations on both walls (figure 5.13). The proximity of the supersonic regions to the engine face and the increased sizes of the separated zones cause a higher flow distortion for configuration B. Although the separated zones in the intakes of configurations B and C were concentrated at the bottom and/or sidewalls of the intake, their larger size contributed to the increased flow distortion comapred to configuration A. In comparison, configuration A had smaller, more irregular separated zones concentrated at the corners. Since the stagnation pressure values in separated zones are low, larger separated zones are more likely to contribute to higher flow distortion values. A lower $p_{0,min}$ value at the engine face, increases the $p_{0,max} - p_{0,min}$ difference which in turn increases the flow distortion value. Reducing the size of the separated zone and improving the flow uniformity by means of flow control or varying geometry can reduce the flow distortion and increase the performance of the intake.

5.7 Chapter summary

A store with an intake geometry was created and used to couple internal and external supersonic flows to investigate shock trains in a more realistic geometry. Only the fore-body of the store was simulated and the effect of different incidence and roll angles on the total pressure recovery and flow distortion efficiency metrics was evaluated. The $k-\omega$ SST turbulence model was found to predict single shocks within the intakes of configurations,featuring rounded corners. Only the configuration featuring sharp corners, similarly to the isolated shock train experiments, featured a shock train when the $k-\omega$ SST model was used. The cause was the more organised flow topology resulting from the sharp corners. In contrast, the non-linear $k-\omega$ EARSM model predicted shock trains in all configurations. The choice of turbulence model was shown to affect the flow distortion performance metric. If the model predicted a

single normal shock the resulting flow distortion at the engine face of the intake was small. As the flow behind a single normal shock is significantly decelerated, and there is no further flow re-acceleration, caused by confinement effects, the average downstream Mach number is lower. If the model predicted a shock train, however, the presence of supersonic regions in the vicinity of the engine face resulted in higher average Mach numbers. The higher average values resulted in higher FD values at the engine face. Opposite to the FD, the sensitivity of the total pressure recovery to the turbulence model and the intake shape was small. All configurations had similar total pressure recoveries at $\sigma = 0$ and $\sigma = 5$ deg. This shows that the shape of the intake affects the TPR less than the FD. Due to the organised flow topology, and relatively small separation configuration A had favourable TPR and FD metrics. Increase of the incidence angle beyond 5 degrees resulted in a further increase in TPR which was attributed to the lower centreline Mach numbers in the intake. The reduction of the centreline Mach number was caused by an oblique interaction at the entrance of the intake which increased in strength with increasing incidence angle. The introduction of a roll angle did not affect the performance metrics significantly, however, the onset of the interactions was moved downstream. From the three configurations, only configuration A showed similar total pressure and flow distortion metrics to the ones at zero roll angle. The other two configurations,resulted in higher FD values at $\lambda = 3$ deg. The sensitivity of the FD metric shows the importance of using non-linear turbulence models for internal, highly-confined shock wave boundary layer simulations. Although the results presented in this chapter apply strictly to pitot intakes, they show that the use of linear turbulence models can lead to conservative predictions of the flow distortion efficiency metric. Since this metric is very important conservative predictions can have a negative impact on the performance of the engine.

Chapter 6

Conclusions and future work

6.1 Conclusions

This work systematically investigated the shock train phenomenon occurring in confined (internal) supersonic flows. Its aim was to propose the best RANS methods, turbulence models, and modelling techniques for simulating shock trains by answering the following research questions arising from the thesis objectives in Chapter 1:

1. What is the best modelling technique to match the experimental conditions in a shock train simulation?
2. Do non-linear models improve the flowfield predictions for shock trains?
3. Can simplified non-linear models using quadratic constitutive relations achieve similar improvements?
4. How do the total pressure recovery and flow distortion across a shock train change with respect to changing freestream parameters?
5. How does the corner geometry affect the shock train structure?
6. What is the shock train structure in a geometry representative of a high-speed intake, and how it is affected by freestream parameters?

Existing simulations of shock trains by other researchers do not extensively detail what modelling technique was used to match the experimental conditions. Therefore questions as to what the best modelling technique is might arise if one tries to perform such simulations (first research question). To answer the first research question, simulations of the shock train experiment by Carroll *et al.* [26] outlined in 3 were performed. As explained in the chapter 3

the experiment by Carroll et al. was selected because it was one of the few experiments that featured detailed flow measurements. After evaluating the success of different techniques the following technique is proposed:

- The domain must be three-dimensional to account for the spanwise flow confinement.
- The domain is elongated so that the boundary layer can develop from freestream (reference) conditions. Several iterations might be needed in order to determine by how much the domain needs to be elongated.
- The Mach number at the inlet of the domain must be increased to take into account the decrease of the Mach number due to the boundary layer growth.
- The exit (back) pressure must be adjusted so that the shock train is positioned at a location where δ_r/h matches the experimental one.

Many of the shock train simulations performed by researchers listed in Chapter 1 neglect the three-dimensionality of the flow. Although the agreement with the experiments is often favourable, neglecting the three-dimensionality of the flow should be avoided. In some cases, the favourable agreement can be misleading as the shock train forms at a location where the boundary layer is thicker (compared to the experiment). The increased thickness (increased confinement) compensates for the confinement that would otherwise arise if three-dimensional effects are considered.

Several non-linear models were implemented in the HMB3 solver to answer the second and third research questions - the k-ω EARSM, and the k-ω SST with different Quadratic Constitutive Relations (QCRs). Two different QCR versions were added to the k-ω SST - the original QCR by Spalart [122] (k-ω SST V1) and a more recent QCR by Sabnis [113] (k-ω SST V2). The non-linear models removed the wall pressure oscillations and predicted wall pressure profiles in closer agreement with the experiments compared to the linear models. Additional modifications of the C_{cr1} coefficient of the $k-\omega$ SST QCR V1 model showed that an increased value of $C_{cr1} = 0.4$ improves the predictions even further. Although the wall pressure was in good agreement, the spacing between the second and third shocks in the shock train was overpredicted by up to 17%. Further adjustments of the back pressure to reduce the confinement and bring it closer to the experimental one reduced the overprediction to 5%. The following points summarise the finding obtained with the non-linear models:

- Linear models overpredict the corner separations due to their inability to account for the secondary (corner) flows.

- Secondary (corner) flows can be accounted for by adding quadratic (or higher) terms of strain and/or vorticity.
- The newly implemented k-ω SST models using constitutive relations (QCR V1 and V2) improve the predictions significantly.

Further investigation of the effects of limiting the turbulent kinetic energy production term in regions with high velocity gradients showed that the limiting has a little effect within the boundary layer. At the centreline, the high values of k were removed without any difference in the wall pressure or the onset of the interaction x_r.

The fourth and fifth research questions were answered by the parametric studies in Chapter 4. The studies showed that flow distortion, evaluated at different streamwise planes starting from the onset of the interaction, decreases rapidly. Shock trains that feature an initial shock with a λ-foot structure were found to be more "efficient" as they had higher total pressure recovery and lower flow distortion. When supersonic regions were present at the plane where the flow distortion was evaluated, higher values of flow distortion were observed. Shock trains at lower confinement levels and Mach numbers are preferred if one aims to achieve higher efficiency metrics.

Shock train simulations by previous researchers often consider simplified geometries. Such geometries include rectangular, square or circular ducts. Although these geometries are suitable for investigating the flow physics of shock trains, they do not represent practical geometries found in high-speed intakes. Chapter 5 compares the flowfield predictions from linear and non-linear turbulence models in geometry representative of a high-speed intake to answer the sixth and last research question. A fore-body intake geometry, consisting of a spherically blunted tangent ogive followed by a constant radius cylinder was used to couple external and internal supersonic flows. Different configurations of the geometry were considered each having an intake with a specific cross-sectional area and shape. The importance of non-linear models was once again highlighted as some linear models did not predict shock trains in the intakes. At zero incidence angle, the most efficient geometry was the one featuring a square intake with perfectly sharp corners. The flow within the intake resembled the idealised shock trains although asymmetries were present. The asymmetries originated from the slant angle of the intake as the transverse flow affects the corner flows and the subsequent corner separations. Insignificant differences in the total pressure recovery and flow distortion between the intakes were observed at higher incidence angles. At these conditions, the flow was highly asymmetric and shared little similarity with the flow observed in the idealised interactions.

Introduction of a roll angle displaced the shock trains downstream even though the back (exit) pressure was kept constant. The additional calculations detailed in Appending A and in [134] further showed the importance of using non-linear models for external high-speed flows. The predicted loads agreed better when non-linear models were used. Coupled with the findings for internal flows in this work, it shows that non-linear models should be used where strong vortices or secondary flows are expected.

6.2 Future work

The summary of the different shock train experiments in Chapter 1 shows the need for detailed shock train experimental studies, measuring not only the wall pressure but also the turbulence statistics. Additional insight into how well the non-linear models predict the corner flows can be obtained by performing measurements in the corner of the test section at various streamwise locations. Such measurements can determine whether RANS methods, with properly calibrated models capable of resolving the corner separations, are sufficient.

The synthetic eddy method (SEM) implemented and tested in Appendix A provides a viable alternative to inflow turbulence generation. Compared to the recycling-rescaling method and the pre-cursor simulation method the SEM is computationally efficient and is capable of reproducing prescribed Reynolds stresses. Coupling of an SEM with a hybrid RANS/LES method, capable of resolving the larger turbulent structures in the outer part of the boundary layer may provide further insight into the modelling fidelity of shock trains. The hybrid method can offer an alternative to the wall resolved and wall modelled LES without the need for reduction of the Reynolds number or the use of simplified wall models.

Appendix A

Jarrin's synthetic turbulence method implementation

The generation of inflow data for spatially developing turbulent flows is still a challenge and must be addressed in the application of hybrid RANS/LES and LES methods to internal flows. Internal flows often feature shallow separation regions which are not strong enough to trigger the LES mode of a hybrid RANS/LES method. Often, some form of forcing at the inlet of the internal flow simulation is required, either in the form of a precursor LES simulation, recycling-rescaling approach, or synthetic turbulence generation.

A.1 The synthetic eddy method

The Synthetic Eddy Method (SEM) was proposed by Jarrin *et al.* [74] and it is often used to generate realistic turbulent inflow conditions for scale-resolving simulations. A control volume populated by a uniform random distribution of eddies surrounds the inflow plane. At each time step, every Eddy located at x_k creates a velocity perturbation at location x given by

$$u_i'^k = \frac{1}{N_{eddies}} A_{ij} \varepsilon_j^k f_\sigma \left(x_i^k - x_i \right), \tag{A.1}$$

where N_{eddies} is the number of eddies given by $\frac{V_{eddies}}{\sigma_x \sigma_y \sigma_z}$ and ε_j^k is a randomly assigned sign. The volume occupied by the eddies is given by $V_{eddies} = 2\sigma_x \left(L_y + 2\sigma_y\right)\left(L_z + 2\sigma_z\right)$, where σ_x, σ_y, and σ_z are the eddy sizes in the x, y, and z-direction and L_y and L_z are the inflow sizes in the y and z-directions. Figure A.1 shows the reference frame and the definition of the eddy sizes. The A_{ij} is the Cholesky decomposition of the Reynolds stress tensor τ_{ij} and is given by:

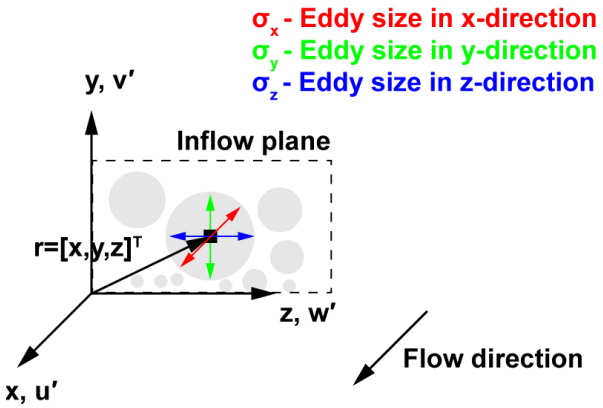

Figure A.1: Reference frame and definition of the eddy sizes

$$A = \begin{bmatrix} \sqrt{\overline{u'u'}} & 0 & 0 \\ \frac{\overline{v'u'}}{A_{11}} & \sqrt{\overline{v'v'} - A_{21}^2} & 0 \\ \frac{\overline{w'u'}}{A_{11}} & \frac{\overline{w'v'} - A_{21}A_{31}}{A_{22}} & \sqrt{\overline{w'w'} - A_{31}^2 - A_{32}^2}. \end{bmatrix} \tag{A.2}$$

The velocity perturbation from each eddy is defined by $f_\sigma\left(x_i^k - x_i\right)$ and depends on the shape of the eddies, defined by a characteristic length for each direction σ as follows:

$$\begin{aligned} f_\sigma\left(x_i^k - x_i\right) &= \sqrt{\frac{V_{eddies}}{\sigma_x \sigma_y \sigma_z}} f\left(\frac{x^k - x}{\sigma_x}\right) f\left(\frac{y^k - y}{\sigma_y}\right) f\left(\frac{z^k - z}{\sigma_z}\right) \\ f(x) &= \begin{cases} \sqrt{\frac{3}{2}}\left(1 - |x|\right), & \text{if } |x| < 1 \\ 0, & \text{if } |x| > 1 \end{cases}. \end{aligned} \tag{A.3}$$

In the above equation, the shape of the eddy is defined by a tent function. The resulting velocity perturbation at each location x is given by:

$$u_i = \overline{u}_i + \sum_{k=1}^{N_{eddies}} u_i'^k. \tag{A.4}$$

For each time step, each eddy is convected in the streamwise direction by

$$x_i^k\left(t + \Delta t\right) = x_i^k\left(t\right) + \overline{u}_i \Delta t \tag{A.5}$$

If an eddy leaves the control volume it is regenerated upstream at a location selected by a uniform random distribution. The values of the Reynolds stresses determine the resulting standard deviation in the turbulent velocities generated for each axis and the shape of the eddies determines the length scale of turbulence and therefore the spatial correlation between turbulent velocities at two different locations.

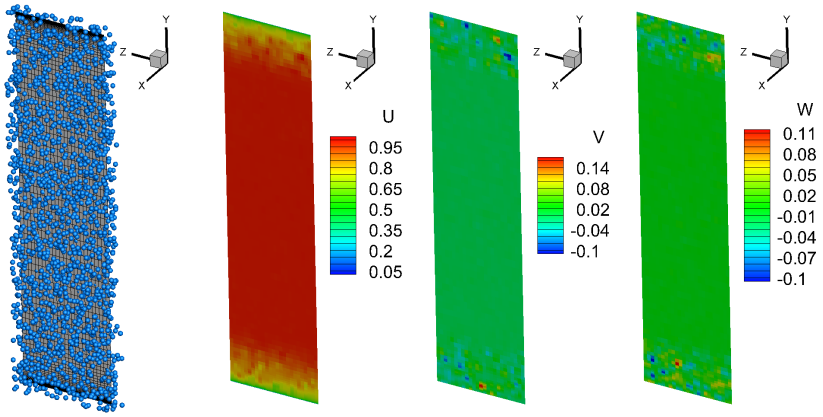

Figure A.2: Eddies, inlet plane grid, and resulting velocity components

A.2 Numerical implementation

A C++ program implementing the synthetic eddy method, outlined above, was created. The purpose of the program was to test the SEM method and to create velocity profiles that can be used as boundary conditions by the HMB3 flow solver. The program creates a box of eddies with a size of $2(L_y+\sigma_y)$, $2(L_z+\sigma_z)$, and $2\sigma_x$ where L_y and L_z are the dimensions of the inlet. Since the program reads an HMB3 profile file which contains the mean flow and Reynolds stress quantities - ρ, u, v, w, p, k, ω, $\overline{u'u'}$, $\overline{u'v'}$, $\overline{u'w'}$, $\overline{v'v'}$, $\overline{v'w'}$, and $\overline{w'w'}$, the SEM method can reconstruct the stresses at every point of the inlet plane. Figure A.2 shows the resulting velocity perturbations superimposed on the mean velocities for an inlet featuring a turbulent boundary layer. The eddy sizes were $\sigma_x=\sigma_y=\sigma_z=0.05$ and were considered to be of constant size over the entire inlet plane. At $y/h\approx-0.84$ the Reynolds stresses were:

$$\overline{u_i'u_j'}=\begin{bmatrix}\overline{u'u'} & \overline{u'v'} & \overline{u'w'}\\ \overline{v'u'} & \overline{v'v'} & \overline{v'w'}\\ \overline{w'u'} & \overline{w'v'} & \overline{w'w'}\end{bmatrix}=\begin{bmatrix}0.00012 & -9.7\times10^{-5} & 2.7\times10^{-5}\\ & 0.00024 & -8.0\times10^{-6}\\ \text{Symmetric} & & 0.00021\end{bmatrix}. \tag{A.6}$$

A total of 1000 timesteps were performed with a timestep size of $\Delta t=0.01$. All of the quan-

tities are in non-dimensional form, following the non-dimensionalisation detailed in Chapter 2 of the thesis. The instantaneous velocities at $y/h \approx -0.84$ are reported below. Their time history and the spectrum of the turbulent kinetic energy are shown in figure A.3.

y=−0.839866
<u'>=2.07625e−20
<v'>=−1.83382e−18
<w'>=−4.18068e−19
<u'u'>=0.000116081
<v'v'>=0.000243611
<w'w'>=0.000210046
<u'v'>=−9.69167e−05
<u'w'>=2.70812e−05
<v'w'>=−8.01145e−06
k/<V>^2=0.000284869
I=0.0137809

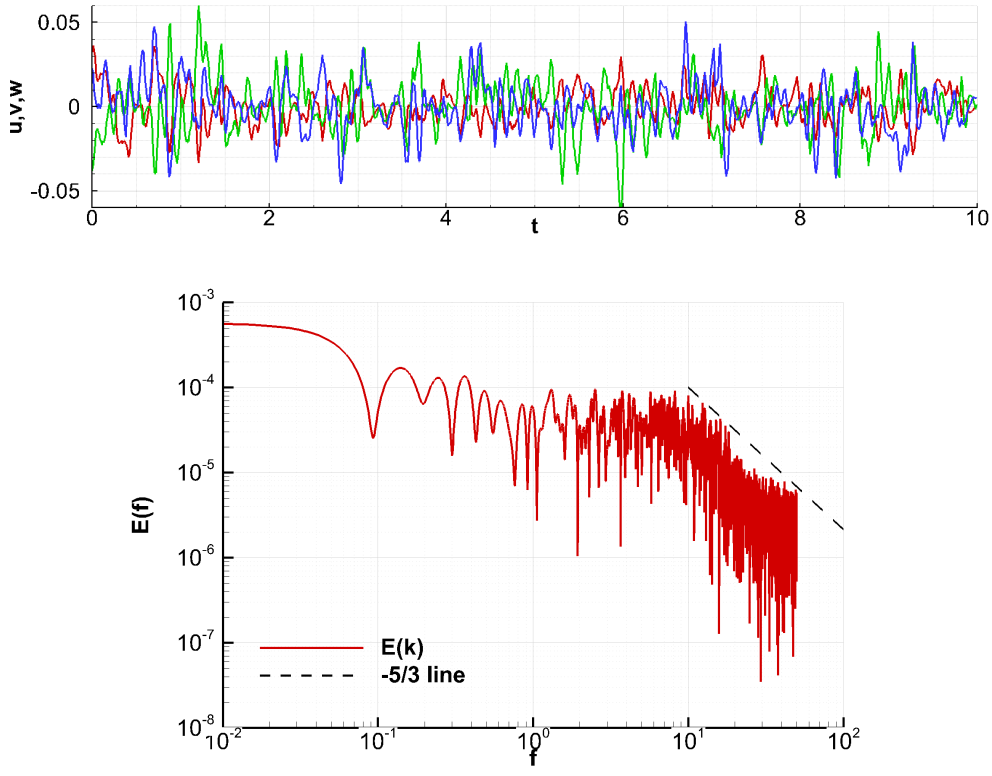

Figure A.3: Instantaneous velocity time history (top) and turbulent kinetic energy spectrum (bottom)

As seen from the output, the SEM method is capable of reconstructing the specified Reynolds stresses and predicts correctly the slope of the turbulent kinetic energy spectrum. The source code of the SEM program is listed below

```
1  #include <iostream>
2  #include <fstream>
3  #include <string>
4  #include <iomanip>
5  #include <vector>
6  #include <random>
7  #include <sstream>
8  #define pi 3.14159265358979323846264338327950288 4
9  double crand()
10 {
11         return (double)rand() / (double)RAND_MAX;
12 }
13 //
       ////////////////////////////////////////////////////////////////////////////

14 double sign(double a)
15 {
16         if (a > 0.5)
17         {
18                 return 1.0;
19         }
20         return -1.0;
21 }
22 //
       ////////////////////////////////////////////////////////////////////////////

23 double min(double a, double b)
24 {
25         if (a > b)
26         {
27                 return b;
28         }
29         return a;
30 }
31 //
       ////////////////////////////////////////////////////////////////////////////

32 double shape_function(double x, double sigma, int type)
33 {
34         double f;
```

```
35          f = 0.0;
36          x /= sigma;
37          if (type == 0)
38          {
39                  if (std::abs(x) < 1.0)
40                  {
41                          //tent
42                          f = std::sqrt(3.0 / 2.0) * (1.0 - std::abs(x));
43                  }
44          }
45          if (type == 1)
46          {
47                  if (std::abs(x) < 1.0)
48                  {
49                          //gaussian
50                  }
51          }
52          return f;
53  }
54  //
        ////////////////////////////////////////////////////////////////////////

55  class eddy
56  {
57  public:
58          double x;
59          double y;
60          double z;
61          double eps_x;
62          double eps_y;
63          double eps_z;
64          eddy();
65          ~eddy();
66  };
67  eddy::eddy() {}
68  eddy::~eddy() {}
69  //
        ////////////////////////////////////////////////////////////////////////

70  class probe
71  {
72  public:
73          double x;
74          double y;
```

```
75          double z;
76          double R[9];
77          std::vector<double> u;
78          std::vector<double> v;
79          std::vector<double> w;
80          std::vector<double> t;
81          probe();
82          ~probe();
83  };
84  probe::probe() {}
85  probe::~probe() {}
86  //
        ////////////////////////////////////////////////////////////////////////

87  double get_mean(std::vector<double> &x)
88  {
89          double mean_x = 0.0;
90          for (unsigned i = 0; i < x.size(); i++)
91          {
92                  mean_x += x[i];
93          }
94          mean_x /= x.size();
95          return mean_x;
96  };
97  //
        ////////////////////////////////////////////////////////////////////////

98  double get_variance(std::vector<double> &x, std::vector<double> &y)
99  {
100         double variance_xy = 0.0;
101         if (x.size() != y.size())
102         {
103                 std::cout << "Vectors must be of same length!" << std::
                        endl;
104                 std::exit(0);
105         }
106         for (unsigned i = 0; i < x.size(); i++)
107         {
108                 variance_xy += x[i] * y[i];
109         }
110         variance_xy /= x.size();
111         return variance_xy;
112 };
113 //
```

```
    ////////////////////////////////////////////////////////////////////////

114 double get_rms(double variance_xy)
115 {
116         if (variance_xy < 0)
117         {
118                 std::cout << "Variance must be greater or equal to 0!" <<
                        std::endl;
119                 std::exit(0);
120         }
121         return std::sqrt(variance_xy);
122 };
123 //
    ////////////////////////////////////////////////////////////////////////

124 int main(int argc, char *argv[])
125 {
126         std::srand(std::time(nullptr));
127         std::cout << "3D Synthetic Eddy Method [Version 3.0.0]" << std::
              endl;
128         int N_timesteps, N_eddys, N_probes;
129         double Ly, Lz, x, y, z;
130         double sigma_x, sigma_y, sigma_z, sigma, V_sigma, f;
131         double u_bar, v_bar, w_bar, V_bar;
132         double dt, t;
133         double a[9], R[9];
134         std::fstream eddy_file;
135         Ly = 1.04537;
136         Lz = 2.34113;
137         x = 0.0;
138         y = 0.0;
139         z = 0.0;
140         N_timesteps = 1000;
141         sigma_x = 0.05;
142         sigma_y = 0.05;
143         sigma_z = 0.05;
144         sigma = 1.0 / 3.0 * (sigma_x + sigma_y + sigma_z);
145         V_sigma = (Ly + 2 * sigma_y) * (Lz + 2 * sigma_z) * 2 * sigma_x;
146         N_eddys = ceil(V_sigma / (sigma_x * sigma_y * sigma_z));
147         u_bar = 1.0;
148         v_bar = 0;
149         w_bar = 0;
150         V_bar = std::sqrt(std::pow(u_bar, 2) + std::pow(v_bar, 2) + std::
              pow(w_bar, 2));
```

```
151         dt = 0.01;
152         std::cout << "Ly=" << Ly << std::endl;
153         std::cout << "Lz=" << Lz << std::endl;
154         std::cout << "N_timesteps=" << N_timesteps << std::endl;
155         std::cout << "N_eddys=" << N_eddys << std::endl;
156         std::cout << "sigma_x=" << sigma_x << std::endl;
157         std::cout << "sigma_y=" << sigma_y << std::endl;
158         std::cout << "sigma_z=" << sigma_z << std::endl;
159         std::cout << "sigma=" << sigma << std::endl;
160         std::cout << "V_sigma=" << V_sigma << std::endl;
161         std::cout << "u_bar=" << u_bar << std::endl;
162         std::cout << "v_bar=" << v_bar << std::endl;
163         std::cout << "w_bar=" << w_bar << std::endl;
164         std::cout << "V_bar=" << V_bar << std::endl;
165         std::cout << "dt=" << dt << std::endl;
166         //
              ////////////////////////////////////////////////////////////////////////

167         //
              ////////////////////////////////////////////////////////////////////////

168         std::cout << "Creating␣eddys..." << std::endl;
169         std::vector<eddy> eddys;
170         eddy_file.open("eddys.dat", std::fstream::out);
171         for (unsigned l = 0; l < N_eddys; l++)
172         {
173                 eddy eddy;
174                 eddy.x = -sigma_x + (2.0 * sigma_x) * crand();
175                 eddy.y = (-sigma_y + (Ly + 2.0 * sigma_y) * crand()) - Ly
                        ;
176                 eddy.z = -sigma_z + (Lz + 2.0 * sigma_z) * crand();
177                 eddy.eps_x = sign(crand());
178                 eddy.eps_y = sign(crand());
179                 eddy.eps_z = sign(crand());
180                 eddys.push_back(eddy);
181                 eddy_file << eddy.x << "␣" << eddy.y << "␣" << eddy.z <<
                        "␣" << eddy.eps_x << "␣" << eddy.eps_y << "␣" << eddy.
                        eps_z << std::endl;
182         }
183         eddy_file.close();
184         std::cout << "Created␣" << N_eddys << "␣eddys." << std::endl;
185         //
              ////////////////////////////////////////////////////////////////////////
```

```
186         //
                ////////////////////////////////////////////////////////////////////////

187         std::cout << "Creating probes..." << std::endl;
188         std::stringstream file_line_stream;
189         std::string file_line;
190         std::fstream file;
191         std::vector<probe> probes;
192         file.open("source_profile.csv", std::ios::in);
193         if (!file.is_open())
194         {
195                 std::cout << "Failed to open source_profile.csv" << std::
                        endl;
196                 return 1;
197         }
198         while (std::getline(file, file_line))
199         {
200                 file_line_stream.clear();
201                 file_line_stream.str(file_line);
202                 double y, uu, uv, uw, vv, vw, ww;
203                 file_line_stream >> y >> uu >> uv >> uw >> vv >> vw >> ww
                        ;
204                 probe probe;
205                 probe.x = 0;
206                 probe.y = y;
207                 probe.z = 1e-3;
208                 probe.R[0] = probe.R[1] = probe.R[2] = probe.R[3] = probe
                        .R[4] = probe.R[5] = probe.R[6] = probe.R[7] = probe.R
                        [8] = 0.0;
209                 probe.R[0] = uu; //uu
210                 probe.R[1] = uv; //uv
211                 probe.R[2] = uw; //uu
212                 probe.R[3] = uv; //vu
213                 probe.R[4] = vv; //vu
214                 probe.R[5] = vw; //vw
215                 probe.R[6] = uw; //wu
216                 probe.R[7] = vw; //wv
217                 probe.R[8] = ww; //ww
218                 probes.push_back(probe);
219         }
220         file.close();
221         N_probes = probes.size();
222         for (unsigned 1 = 0; 1 < N_probes; 1++)
223         {
```

```
224                 probes[1].t.resize(N_timesteps);
225                 probes[1].u.resize(N_timesteps);
226                 probes[1].v.resize(N_timesteps);
227                 probes[1].w.resize(N_timesteps);
228                 a[0] = sqrt(probes[1].R[0]);
229                 a[3] = probes[1].R[3] / a[0];
230                 a[4] = sqrt(probes[1].R[4] - a[3] * a[3]);
231                 a[6] = probes[1].R[6] / a[0];
232                 a[7] = (probes[1].R[7] - a[3] * a[6]) / a[4];
233                 a[8] = sqrt(probes[1].R[8] - a[6] * a[6] - a[7] * a[7]);
234                 std::cout << std::endl;
235                 std::cout << "Probe " << 1 << std::endl;
236                 std::cout << "[R]=" << probes[1].R[0] << "," << probes[1
                        ].R[1] << "," << probes[1].R[2] << std::endl;
237                 std::cout << "    " << probes[1].R[3] << "," << probes[1
                        ].R[4] << "," << probes[1].R[5] << std::endl;
238                 std::cout << "    " << probes[1].R[6] << "," << probes[1
                        ].R[7] << "," << probes[1].R[8] << std::endl;
239                 std::cout << "[a]=" << a[0] << "," << a[1] << "," << a[2]
                         << std::endl;
240                 std::cout << "    " << a[3] << "," << a[4] << "," << a[5]
                         << std::endl;
241                 std::cout << "    " << a[6] << "," << a[7] << "," << a[8]
                         << std::endl;
242                 std::cout << std::endl;
243         }
244         std::cout << "Created " << N_probes << " probes." << std::endl;
245         //
              ////////////////////////////////////////////////////////////////////////

246         //
              ////////////////////////////////////////////////////////////////////////

247         for (unsigned n = 0; n < N_timesteps; n++)
248         {
249                 t = dt * n;
250                 std::cout << "Step " << n << " t=" << t << std::endl;
251                 for (unsigned m = 0; m < N_probes; m++)
252                 {
253                         a[0] = sqrt(probes[m].R[0]);
254                         a[3] = probes[m].R[3] / a[0];
255                         a[4] = sqrt(probes[m].R[4] - a[3] * a[3]);
256                         a[6] = probes[m].R[6] / a[0];
257                         a[7] = (probes[m].R[7] - a[3] * a[6]) / a[4];
```

```
258                         a[8] = sqrt(probes[m].R[8] - a[6] * a[6] - a[7] *
                                a[7]);
259                         probes[m].t[n] = t;
260                         probes[m].u[n] = 0.0;
261                         probes[m].v[n] = 0.0;
262                         probes[m].w[n] = 0.0;
263                         for (unsigned l = 0; l < N_eddys; l++)
264                         {
265                                 f = 1.0;
266                                 f *= shape_function(probes[m].x - eddys[l
                                        ].x, sigma_x, 0);
267                                 f *= shape_function(probes[m].y - eddys[l
                                        ].y, sigma_y, 0);
268                                 f *= shape_function(probes[m].z - eddys[l
                                        ].z, sigma_z, 0);
269                                 probes[m].u[n] += (a[0] * eddys[l].eps_x
                                    + a[1] * eddys[l].eps_y + a[2] * eddys
                                    [l].eps_z) * f;
270                                 probes[m].v[n] += (a[3] * eddys[l].eps_x
                                    + a[4] * eddys[l].eps_y + a[5] * eddys
                                    [l].eps_z) * f;
271                                 probes[m].w[n] += (a[6] * eddys[l].eps_x
                                    + a[7] * eddys[l].eps_y + a[8] * eddys
                                    [l].eps_z) * f;
272                         }
273                         probes[m].u[n] *= std::sqrt(V_sigma / (N_eddys *
                                sigma_x * sigma_y * sigma_z));
274                         probes[m].v[n] *= std::sqrt(V_sigma / (N_eddys *
                                sigma_x * sigma_y * sigma_z));
275                         probes[m].w[n] *= std::sqrt(V_sigma / (N_eddys *
                                sigma_x * sigma_y * sigma_z));
276                 }
277                 for (unsigned l = 0; l < N_eddys; l++)
278                 {
279                         eddys[l].x += dt * u_bar;
280                         if (eddys[l].x > sigma_x)
281                         {
282                                 eddys[l].x = (-1.0 * sigma_x);
283                                 eddys[l].y = -sigma_y + (Ly + 2.0 *
                                        sigma_y) * crand() - Ly;
284                                 eddys[l].z = -sigma_z + (Lz + 2.0 *
                                        sigma_z) * crand();
285                                 eddys[l].eps_x = sign(crand());
286                                 eddys[l].eps_y = sign(crand());
```

```
287                                     eddys[l].eps_z = sign(crand());
288                             }
289                     }
290             }
291             //
                    ////////////////////////////////////////////////////////////////////////////

292             //
                    ////////////////////////////////////////////////////////////////////////////

293             std::fstream probe_file;
294             probe_file.open("probes.dat", std::fstream::out);
295             probe_file << "TITLE     = \"Time history of the loads for the
                    fine , veryfine , and extrafine grids\"\n";
296             probe_file << "VARIABLES = \" Y \",\" UU \",\" UV \",\" UW \",\"
                    VV \",\" VW \",\" WW \",\" UU_REF \",\" UV_REF \",\" UW_REF
                    \",\" VV_REF \",\" VW_REF \",\" WW_REF \"\n";
297             probe_file << "ZONE I=" << N_probes << ", F=POINT\n";
298             for (unsigned m = 0; m < N_probes; m++)
299             {
300                     double k, I, mean_u, mean_v, mean_w, mean_uu, mean_uv,
                            mean_uw, mean_vv, mean_vw, mean_ww;
301                     mean_u = get_mean(probes[m].u);
302                     mean_v = get_mean(probes[m].v);
303                     mean_w = get_mean(probes[m].w);
304                     for (unsigned l = 0; l < probes[m].u.size(); l++)
305                     {
306                             probes[m].u[l] -= mean_u;
307                             probes[m].v[l] -= mean_v;
308                             probes[m].w[l] -= mean_w;
309                     }
310                     mean_uu = get_variance(probes[m].u, probes[m].u);
311                     mean_uv = get_variance(probes[m].u, probes[m].v);
312                     mean_uw = get_variance(probes[m].u, probes[m].w);
313                     mean_vv = get_variance(probes[m].v, probes[m].v);
314                     mean_vw = get_variance(probes[m].v, probes[m].w);
315                     mean_ww = get_variance(probes[m].w, probes[m].w);
316                     std::cout << std::endl;
317                     std::cout << "Probe " << m << std::endl;
318                     std::cout << "y=" << probes[m].y << std::endl;
319                     std::cout << "<u'>=" << get_mean(probes[m].u) << std::
                            endl;
320                     std::cout << "<v'>=" << get_mean(probes[m].v) << std::
                            endl;
```

```
321                     std::cout << "<w'>=" << get_mean(probes[m].w) << std::
                            endl;
322                     std::cout << "<u'u'>=" << mean_uu << std::endl;
323                     std::cout << "<v'v'>=" << mean_vv << std::endl;
324                     std::cout << "<w'w'>=" << mean_ww << std::endl;
325                     std::cout << "<u'v'>=" << mean_uv << std::endl;
326                     std::cout << "<u'w'>=" << mean_uw << std::endl;
327                     std::cout << "<v'w'>=" << mean_vw << std::endl;
328                     k = 1.0 / 2.0 * (mean_uu + mean_vv + mean_ww);
329                     I = std::sqrt(2.0 / 3.0 * k) / V_bar;
330                     std::cout << "k/<V>^2=" << k << std::endl;
331                     std::cout << "I=" << I << std::endl;
332                     probe_file << probes[m].y << "␣" << mean_uu << "␣" <<
                            mean_uv << "␣" << mean_uw << "␣" << mean_vv << "␣" <<
                            mean_vw << "␣" << mean_ww << "␣" << probes[m].R[0] <<
                            "␣" << probes[m].R[1] << "␣" << probes[m].R[2] << "␣"
                            << probes[m].R[4] << "␣" << probes[m].R[5] << "␣" <<
                            probes[m].R[8] << std::endl;
333             }
334             probe_file.close();
335             //
                    ////////////////////////////////////////////////////////////////////////

336             //
                    ////////////////////////////////////////////////////////////////////////

337             int l = 60;
338             probe_file.open("probe_" + std::to_string(l) + ".dat", std::
                    fstream::out);
339             std::cout << "y=" << probes[l].y << std::endl;
340             for (unsigned m = 0; m < probes[l].u.size(); m++)
341             {
342                     probe_file << probes[l].t[m] << "␣" << probes[l].u[m] <<
                            "␣" << probes[l].v[m] << "␣" << probes[l].w[m] << std
                            ::endl;
343             }
344             probe_file.close();
345             return 0;
346     }
```

Appendix B

Generation of mean inflow profiles

The velocity perturbations from the SEM method detailed in Appendix A are ofter superimposed on a mean velocity profile. For internal flow simulations, a mean boundary layer velocity profile having a specific thickness (or another parameter) is usually specified at the inlet. As shown in Appendix A, the mean inflow profile is obtained either from a pre-cursor RANS simulation preferably employing a non-linear Eddy viscosity model to account for the normal Reynolds stress anisotropy or from a van Driest transformed mean velocity distribution. This section details a C++ and Matlab programs for generating three-dimensional mean inflow profiles from one-dimensional mean inflow profiles which are obtained from existing simulations or are generated by a pre-defined van Driest transformed mean velocity distribution.

B.1 Generation of a one-dimensional mean velocity profile

If pre-cursor simulations are not available, the van Driest transformation [140] can be used to generate a one-dimensional mean velocity profile. The van Driest transformed mean velocity profile of Musker's [96] law-of-the wall and law-of-the wake is given by

$$u_c^+ = \begin{cases} 5.424 tan^{-1}\left[\frac{2y^+-8.15}{16.7}\right] + log_{10}\left[\frac{\left(y^++10.6\right)^{9.6}}{\left(y^{+2}+8.15y^++86\right)^2}\right] \\ -3.52+2.44\left\{\Pi\left[6\left(\frac{y}{\delta}\right)^2-4\left(\frac{y}{\delta}\right)^3\right]+\left(\frac{y}{\delta}\right)^2\left(1-\frac{y}{\delta}\right)\right\}, y \leq \delta \\ u_{ce}/u_\tau, y \geq \delta \end{cases} \tag{B.1}$$

where y is the wall-normal coordinate and $\Pi = 0.55\left[1-exp\left(-0.24\sqrt{Re_\theta}-0.298Re_\theta\right)\right]$. The pressure across the boundary layer is assumed to be constant and the mean density is

calculated from the Crocco-Busemann relation [29]. Full details of the procedure are detailed by Zhang *et al.* [153] who improved the approach of Huang *et al.* [68]. Figure B.1 shows the generated van Driest transformed mean velocity u_c^+ in wall units for a boundary layer with a thickness of $\delta = 5.4$ mm and a Reynolds number of $Re_\theta = 12.85 \times 10^3$.

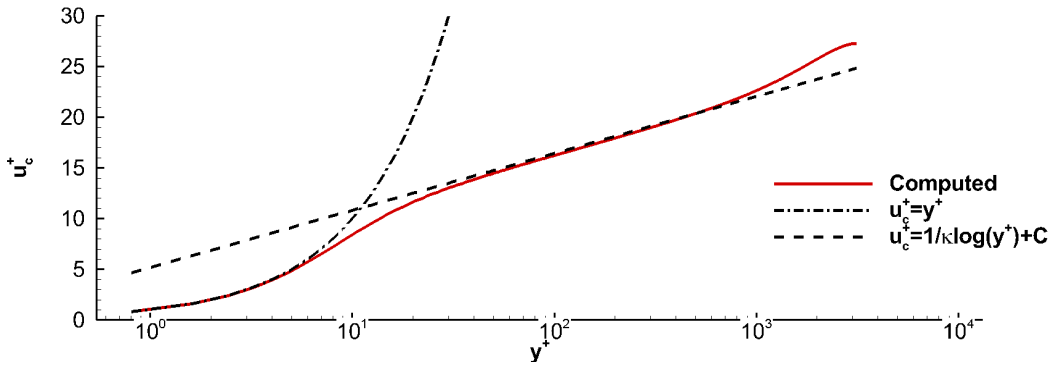

Figure B.1: Generated van Driest transformed mean velocity u_c^+ of Musker's [96] law-of-the wall and law-of-the wake

B.2 Generation of three-dimensional mean inflow profiles

A three-dimensional inflow profile can be created form a one-dimensional inflow profile by considering the normal distances to each wall at the inlet plane. Inverse distance weighting is used for the coupling with a weighting function W_n given by

$$W_n = \frac{1}{d_n^2} \left(\sum_{m=1}^{N_{walls}} \frac{1}{d_m^2} \right)^{-1}, \tag{B.2}$$

where the number of walls at the inlet is specified by N_{walls} and d_n and d_m are the distances to walls n and m respectively. The mean streamwise velocity (or any other mean quantity) at an arbitrary point y,z is obtained from the following relation

$$\overline{u}(y,z) = \sum_{n=1}^{N_{walls}} W_n \overline{u}_{interp}, \tag{B.3}$$

where $\overline{u}_{interp}$ is the interpolated mean streamwise velocity. The interpolated mean streamwise velocity is obtained from the one-dimensional mean inflow profile. To define the walls a .wall file which contains the centroid of each wall and its unit normal vector, which points away

from the domain as shown in figure B.2 is specified. The mean streamwise velocity at y, z can be obtained by calculating the weighting function W_n which requires the distances to each wall. Each distance is simply the dot product of the wall-normal vector with Δ_n - the distance between y, z and the centroid of the n-th wall.

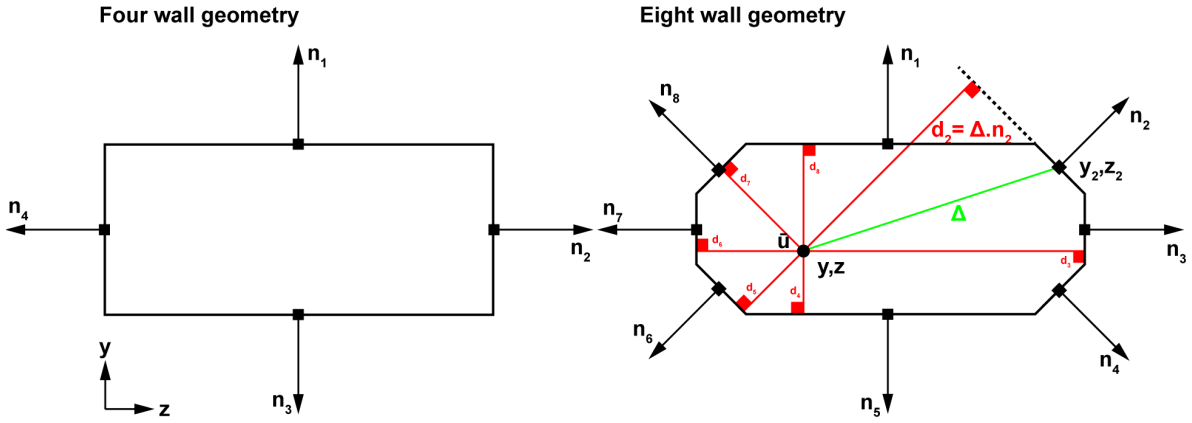

Figure B.2: Definition of the wall-normal distances

Below are the contents of a .wall file which specifies two walls having centroids $y = 0$, $z = 2.3411$, and $y = -1$, $z = 0$. The wall-normal vectors point in the negative y and positive z-directions. Each line contains the y and z coordinates of the wall centroid and the y and z components of the wall unit normal vector.

```
1   0.0000  2.3411  0.0000  1.0000
2  -1.0000  0.0000  -1.0000  0.0000
```

Figure B.3 shows the mean streamwise velocity profile for a rectangular inlet with two walls. The program couples the mean quantities of adjacent walls near the corner through the weighting function W_n and outputs a profile file that can be used by the HMB3 solver. The coupling is weak as it does not consider the presence of the corner flow in this region. To achieve strong coupling, a pre-cursor simulation must first be performed and the entire inflow plane must then be extracted.

```
1  #include <iostream>
2  #include <fstream>
3  #include <string>
4  #include <iomanip>
5  #include <vector>
6  #include <sstream>
7  #include <algorithm>
8  #include <cstdlib>
9  #include <iostream>
10 #include <ctime>
```

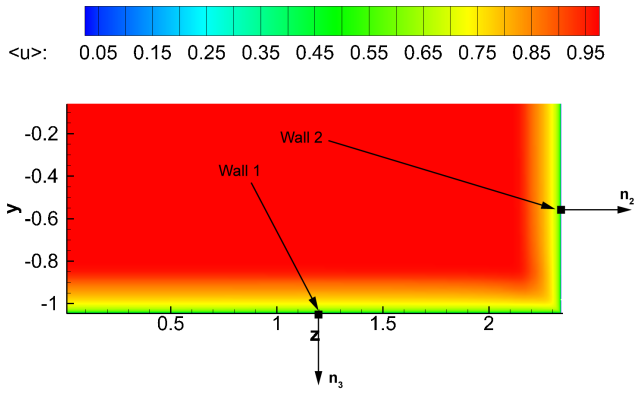

Figure B.3: Mean streamwise velocity profile for a rectangular inlet with two walls

```
11 // 1D interpolation
12 //
    ////////////////////////////////////////////////////////////////////////////////
13 double interp1(std::vector<double> &x, std::vector<double> &y, double &
       x_interp)
14 {
15     double x_min = *std::min_element(x.begin(), x.end());
16     double x_max = *std::max_element(x.begin(), x.end());
17     int i = 0;
18     if (x_interp >= x_min && x_interp <= x_max)
19     {
20         for (; i < x.size(); i++)
21         {
22             if (x_interp >= x[i] && x_interp <= x[i + 1])
23             {
24                 break;
25             }
26         }
27     }
28     else
29     {
30         if (x_interp > x_max)
31         {
32             return y.back();
33         }
34         if (x_interp < x_min)
35         {
36             return y[0];
37         }
```

```
38      }
39      double y_interp = y[i] + ((x_interp - x[i]) / (x[i + 1] - x[i])) * (y
            [i + 1] - y[i]);
40      return y_interp;
41  }
42  //Structure containing grid block data
43  //
        ////////////////////////////////////////////////////////////////////////////////

44  struct block
45  {
46      int Nx;
47      int Ny;
48      int Nz;
49      std::vector<std::vector<std::vector<double>>> x;
50      std::vector<std::vector<std::vector<double>>> y;
51      std::vector<std::vector<std::vector<double>>> z;
52      std::vector<std::vector<double>> yc;
53      std::vector<std::vector<double>> zc;
54      std::vector<std::vector<double>> rhoc;
55      std::vector<std::vector<double>> uc;
56      std::vector<std::vector<double>> vc;
57      std::vector<std::vector<double>> wc;
58      std::vector<std::vector<double>> pc;
59      std::vector<std::vector<double>> kc;
60      std::vector<std::vector<double>> omegac;
61      std::vector<std::vector<double>> uuc;
62      std::vector<std::vector<double>> uvc;
63      std::vector<std::vector<double>> uwc;
64      std::vector<std::vector<double>> vvc;
65      std::vector<std::vector<double>> vwc;
66      std::vector<std::vector<double>> wwc;
67      std::vector<int> orientation;  //orientation
68      std::vector<int> connectivity; //flags
69      std::vector<int> flags;        //flags
70      int profile;                   //is block profile
71  };
72  //Structure containing .walls file data
73  //
        ////////////////////////////////////////////////////////////////////////////////

74  struct wall
75  {
76      double ny;
```

```
77      double nz;
78      double y;
79      double z;
80  };
81  //Structure containing .profile file data
82  //
        ////////////////////////////////////////////////////////////////////////////////

83  struct profile
84  {
85      std::vector<double> y;
86      std::vector<double> rho;
87      std::vector<double> u;
88      std::vector<double> v;
89      std::vector<double> w;
90      std::vector<double> p;
91      std::vector<double> k;
92      std::vector<double> omega;
93      std::vector<double> uu;
94      std::vector<double> uv;
95      std::vector<double> uw;
96      std::vector<double> vv;
97      std::vector<double> vw;
98      std::vector<double> ww;
99  };
100 //Main
101 //
        ////////////////////////////////////////////////////////////////////////////////

102 int main(int argc, char *argv[])
103 {
104     if (argc < 4)
105     {
106         std::cout << "Usage: gen_profile <grid> <profile> <walls> <
                stresses>" << std::endl;
107         return -1;
108     }
109     std::cout << "Profile Generator [Version 1.0.0]" << std::endl;
110     int include_stresses = 0;
111     std::string grid_file_name, profile_file_name, walls_file_name;
112     grid_file_name = argv[1];
113     profile_file_name = argv[2];
114     walls_file_name = argv[3];
115     if (argc == 5)
```

```
116     {
117         include_stresses = std::stoi(argv[4]);
118         if (include_stresses != 1 && include_stresses != 0)
119         {
120             std::cout << "Include␣stresses␣must␣be␣0␣or␣1!" << std::endl;
121             std::exit(-1);
122         }
123     }
124     int N_blocks;
125     std::vector<block> blocks;
126     std::fstream grid_file;
127     grid_file.open(grid_file_name, std::ios::in);
128     if (!grid_file.is_open())
129     {
130         std::cout << "Failed!" << std::endl;
131         std::cout << "Error␣while␣opening␣grid␣file␣for␣reading!" << std
                ::endl;
132         std::exit(-1);
133     }
134     std::string file_line;
135     std::stringstream file_line_stream;
136     std::getline(grid_file, file_line);
137     N_blocks = std::stoi(file_line);
138     blocks.resize(N_blocks);
139     std::cout << "Reading␣blocks...";
140     for (int i = 0; i < N_blocks; i++)
141     {
142         std::getline(grid_file, file_line);
143         file_line_stream.clear();
144         file_line_stream.str(file_line);
145         file_line_stream >> blocks[i].Nx >> blocks[i].Ny >> blocks[i].Nz;
146         blocks[i].x = std::vector<std::vector<std::vector<double>>>(
                blocks[i].Nx, std::vector<std::vector<double>>(blocks[i].Ny,
                std::vector<double>(blocks[i].Nz, 0)));
147         blocks[i].y = std::vector<std::vector<std::vector<double>>>(
                blocks[i].Nx, std::vector<std::vector<double>>(blocks[i].Ny,
                std::vector<double>(blocks[i].Nz, 0)));
148         blocks[i].z = std::vector<std::vector<std::vector<double>>>(
                blocks[i].Nx, std::vector<std::vector<double>>(blocks[i].Ny,
                std::vector<double>(blocks[i].Nz, 0)));
149     }
150     int c;
151     for (int i = 0; i < N_blocks; i++)
152     {
```

```
153             std::getline(grid_file, file_line);
154             file_line_stream.clear();
155             file_line_stream.str(file_line);
156             while (file_line_stream >> c)
157             {
158                 blocks[i].connectivity.push_back(c);
159             }
160             std::getline(grid_file, file_line);
161             file_line_stream.clear();
162             file_line_stream.str(file_line);
163             while (file_line_stream >> c)
164             {
165                 blocks[i].orientation.push_back(c);
166             }
167             std::getline(grid_file, file_line);
168             file_line_stream.clear();
169             file_line_stream.str(file_line);
170             while (file_line_stream >> c)
171             {
172                 blocks[i].flags.push_back(c);
173             }
174             blocks[i].profile = -1;
175             for (int j = 0; j < blocks[i].flags.size(); j++)
176             {
177                 if (blocks[i].flags[j] == 10007 || blocks[i].flags[j] ==
                        10321)
178                 {
179                     blocks[i].profile = j;
180                 }
181             }
182         }
183         for (int i = 0; i < N_blocks; i++)
184         {
185             std::getline(grid_file, file_line);
186         }
187         for (int n = 0; n < N_blocks; n++)
188         {
189             for (int k = 0; k < blocks[n].Nz; k++)
190             {
191                 for (int j = 0; j < blocks[n].Ny; j++)
192                 {
193                     for (int i = 0; i < blocks[n].Nx; i++)
194                     {
195                         std::getline(grid_file, file_line);
```

```
196                     file_line_stream.clear();
197                     file_line_stream.str(file_line);
198                     file_line_stream >> blocks[n].x[i][j][k];
199                     file_line_stream >> blocks[n].y[i][j][k];
200                     file_line_stream >> blocks[n].z[i][j][k];
201                 }
202             }
203         }
204     }
205     grid_file.close();
206     for (int i = 0; i < N_blocks; i++)
207     {
208         if (blocks[i].profile != -1)
209         {
210             if (blocks[i].profile == 1 || blocks[i].profile == 3)
211             {
212                 blocks[i].yc = std::vector<std::vector<double>>(blocks[i
                        ].Ny - 1, std::vector<double>(blocks[i].Nz - 1, 0));
213                 blocks[i].zc = std::vector<std::vector<double>>(blocks[i
                        ].Ny - 1, std::vector<double>(blocks[i].Nz - 1, 0));
214                 blocks[i].rhoc = std::vector<std::vector<double>>(blocks[
                        i].Ny - 1, std::vector<double>(blocks[i].Nz - 1, 0));
215                 blocks[i].uc = std::vector<std::vector<double>>(blocks[i
                        ].Ny - 1, std::vector<double>(blocks[i].Nz - 1, 0));
216                 blocks[i].vc = std::vector<std::vector<double>>(blocks[i
                        ].Ny - 1, std::vector<double>(blocks[i].Nz - 1, 0));
217                 blocks[i].wc = std::vector<std::vector<double>>(blocks[i
                        ].Ny - 1, std::vector<double>(blocks[i].Nz - 1, 0));
218                 blocks[i].pc = std::vector<std::vector<double>>(blocks[i
                        ].Ny - 1, std::vector<double>(blocks[i].Nz - 1, 0));
219                 blocks[i].kc = std::vector<std::vector<double>>(blocks[i
                        ].Ny - 1, std::vector<double>(blocks[i].Nz - 1, 0));
220                 blocks[i].omegac = std::vector<std::vector<double>>(
                        blocks[i].Ny - 1, std::vector<double>(blocks[i].Nz -
                        1, 0));
221                 blocks[i].uuc = std::vector<std::vector<double>>(blocks[i
                        ].Ny - 1, std::vector<double>(blocks[i].Nz - 1, 0));
222                 blocks[i].uuc = std::vector<std::vector<double>>(blocks[i
                        ].Ny - 1, std::vector<double>(blocks[i].Nz - 1, 0));
223                 blocks[i].uvc = std::vector<std::vector<double>>(blocks[i
                        ].Ny - 1, std::vector<double>(blocks[i].Nz - 1, 0));
224                 blocks[i].uwc = std::vector<std::vector<double>>(blocks[i
                        ].Ny - 1, std::vector<double>(blocks[i].Nz - 1, 0));
225                 blocks[i].vvc = std::vector<std::vector<double>>(blocks[i
```

```
                    ].Ny - 1, std::vector<double>(blocks[i].Nz - 1, 0));
226                 blocks[i].vwc = std::vector<std::vector<double>>(blocks[i
                    ].Ny - 1, std::vector<double>(blocks[i].Nz - 1, 0));
227                 blocks[i].wwc = std::vector<std::vector<double>>(blocks[i
                    ].Ny - 1, std::vector<double>(blocks[i].Nz - 1, 0));
228             }
229             else
230             {
231                 std::cout << blocks[i].profile << std::endl;
232                 std::cout << "Profiles can be specified on faces 2 and 4
                    only!" << std::endl;
233                 std::exit(-1);
234             }
235         }
236     }
237     std::cout << "Done!" << std::endl;
238     std::cout << "N_blocks=" << N_blocks << std::endl;
239     //
        ////////////////////////////////////////////////////////////////////////////////

240     //
        ////////////////////////////////////////////////////////////////////////////////

241     //
        ////////////////////////////////////////////////////////////////////////////////

242     //
        ////////////////////////////////////////////////////////////////////////////////

243     std::cout << "Listing profile blocks...";
244     int N_profile_blocks = 0;
245     for (int n = 0; n < N_blocks; n++)
246     {
247         if (blocks[n].profile != -1)
248         {
249             std::cout << std::endl;
250             std::cout << "Block " << (n + 1) << std::endl;
251             int i = 0; //if face is 4 i=0, howver, if face is 2 i=Nx-1
252             if (blocks[n].profile == 1)
253             {
254                 i = blocks[n].Nx - 1;
255             }
256             for (int k = 0; k < blocks[n].Nz - 1; k++)
257             {
```

```
258                 for (int j = 0; j < blocks[n].Ny - 1; j++)
259                 {
260                     double yc, zc;
261                     yc = 1.0 / 4.0 * (blocks[n].y[i][j][k] + blocks[n].y[
                            i][j + 1][k] + blocks[n].y[i][j + 1][k + 1] +
                            blocks[n].y[i][j][k + 1]);
262                     zc = 1.0 / 4.0 * (blocks[n].z[i][j][k] + blocks[n].z[
                            i][j + 1][k] + blocks[n].z[i][j + 1][k + 1] +
                            blocks[n].z[i][j][k + 1]);
263                     blocks[n].yc[j][k] = yc;
264                     blocks[n].zc[j][k] = zc;
265                 } // profile grid block j loop
266             }     // profile grid block k loop
267             std::cout << "Nx=" << blocks[n].Nx << std::endl;
268             std::cout << "Ny=" << blocks[n].Ny << std::endl;
269             std::cout << "Nz=" << blocks[n].Nz << std::endl;
270             std::cout << "profile_face=" << blocks[n].profile + 1 << std
                    ::endl;
271             std::cout << "min(y)=" << blocks[n].y[i][0][0] << std::endl;
272             std::cout << "max(y)=" << blocks[n].y[i][(blocks[n].Ny - 1)
                    ][0] << std::endl;
273             std::cout << "min(z)=" << blocks[n].z[i][0][0] << std::endl;
274             std::cout << "max(z)=" << blocks[n].z[i][0][(blocks[n].Ny -
                    1)] << std::endl;
275             std::cout << std::flush;
276             N_profile_blocks++;
277         }
278     }
279     std::cout << "Done!" << std::endl;
280     std::cout << "N_profile_blocks=" << N_profile_blocks << std::endl;
281     //
        ////////////////////////////////////////////////////////////////////////////////

282     //
        ////////////////////////////////////////////////////////////////////////////////

283     //
        ////////////////////////////////////////////////////////////////////////////////

284     //
        ////////////////////////////////////////////////////////////////////////////////

285     std::cout << std::endl;
286     std::cout << "Loading␣walls␣file ...";
```

```
287     int N_walls;
288     std::vector<wall> walls;
289     std::fstream walls_file;
290     walls_file.open(walls_file_name, std::ios::in);
291     if (walls_file.is_open())
292     {
293         while (std::getline(walls_file, file_line))
294         {
295             wall wall;
296             file_line_stream.clear();
297             file_line_stream.str(file_line);
298             file_line_stream >> wall.y;
299             file_line_stream >> wall.z;
300             file_line_stream >> wall.ny;
301             file_line_stream >> wall.nz;
302             walls.push_back(wall);
303             std::cout << std::endl;
304             std::cout << "Wall " << walls.size() << std::endl;
305             std::cout << "y=" << wall.y << std::endl;
306             std::cout << "z" << wall.z << std::endl;
307             std::cout << "ny=" << wall.ny << std::endl;
308             std::cout << "nz=" << wall.nz << std::endl;
309             std::cout << std::endl;
310         }
311         walls_file.close();
312     }
313     else
314     {
315         std::cout << "Failed!" << std::endl;
316         std::cout << "Error while opening walls file!" << std::endl;
317         std::exit(-1);
318     }
319     N_walls = walls.size();
320     std::cout << "Done!" << std::endl;
321     std::cout << "N_walls=" << N_walls << std::endl;
322     //
        ////////////////////////////////////////////////////////////////////////////////

323     //
        ////////////////////////////////////////////////////////////////////////////////

324     //
        ////////////////////////////////////////////////////////////////////////////////
```

```
325     //
            ////////////////////////////////////////////////////////////////////////////////

326     std::cout << std::endl;
327     std::cout << "Loading␣boundary␣layer␣profile␣file...";
328     profile profile;
329     std::fstream profile_file;
330     profile_file.open(profile_file_name, std::ios::in);
331     if (profile_file.is_open())
332     {
333         while (std::getline(profile_file, file_line))
334         {
335             char c;
336             double y, rho, u, v, w, p, k, omega, uu, uv, uw, vv, vw, ww;
337             file_line_stream.clear();
338             file_line_stream.str(file_line);
339             file_line_stream >> y >> rho >> u >> v >> w >> p >> k >>
                    omega;
340             profile.y.push_back(y);
341             profile.rho.push_back(rho);
342             profile.u.push_back(u);
343             profile.v.push_back(v);
344             profile.w.push_back(w);
345             profile.p.push_back(p);
346             profile.k.push_back(k);
347             profile.omega.push_back(omega);
348             if (include_stresses)
349             {
350                 if (!(file_line_stream >> uu >> uv >> uw >> vv >> vw >>
                        ww))
351                 {
352                     std::cout << "Failed!" << std::endl;
353                     std::cout << "Include␣stresses␣is␣set␣to␣1,␣howver,␣
                            the␣profile␣file␣does␣not␣contain␣stresses!" <<
                            std::endl;
354                     std::exit(-1);
355                 }
356                 profile.uu.push_back(uu);
357                 profile.uv.push_back(uv);
358                 profile.uw.push_back(uw);
359                 profile.vv.push_back(vv);
360                 profile.vw.push_back(vw);
361                 profile.ww.push_back(ww);
362             }
```

```
363             }
364             profile_file.close();
365         }
366         else
367         {
368             std::cout << "Failed!" << std::endl;
369             std::cout << "Error while opening boundary layer profile file!"
                    << std::endl;
370             std::exit(-1);
371         }
372         std::cout << "Done!" << std::endl;
373         std::cout << std::endl;
374         //
            ////////////////////////////////////////////////////////////////////////////////

375         //
            ////////////////////////////////////////////////////////////////////////////////

376         //
            ////////////////////////////////////////////////////////////////////////////////

377         //
            ////////////////////////////////////////////////////////////////////////////////

378         std::cout << "Creating inlet profile...";
379         std::cout << std::flush;
380         for (int n = 0; n < N_blocks; n++)
381         {
382             if (blocks[n].profile != -1)
383             {
384                 for (int k = 0; k < blocks[n].Nz - 1; k++)
385                 {
386                     for (int j = 0; j < blocks[n].Ny - 1; j++)
387                     {
388                         double dl, Wl, phil;
389                         for (int l = 0; l < N_walls; l++)
390                         {
391                             double dm, sum_dm;
392                             dl = (walls[l].y - blocks[n].yc[j][k]) * walls[l
                                    ].ny + (walls[l].z - blocks[n].zc[j][k]) *
                                    walls[l].nz;
393                             Wl = 1.0 / (dl * dl);
394                             sum_dm = 0;
395                             for (int m = 0; m < N_walls; m++)
```

```
396                         {
397                             dm = (walls[m].y - blocks[n].yc[j][k]) *
                                    walls[m].ny + (walls[m].z - blocks[n].zc[j
                                    ][k]) * walls[m].nz;
398                             sum_dm += 1.0 / (dm * dm);
399                         }
400                         Wl = Wl * 1.0 / sum_dm;
401                         phil = interp1(profile.y, profile.rho, dl); //
                            density
402                         blocks[n].rhoc[j][k] += Wl * phil;
403                         phil = interp1(profile.y, profile.u, dl); //x
                            component of velocity
404                         blocks[n].uc[j][k] += Wl * phil;
405                         phil = interp1(profile.y, profile.v, dl); //y
                            component of velocity
406                         blocks[n].vc[j][k] += Wl * phil;
407                         phil = interp1(profile.y, profile.w, dl); //z
                            component of velocity
408                         blocks[n].wc[j][k] += Wl * phil;
409                         phil = interp1(profile.y, profile.p, dl); //
                            pressure
410                         blocks[n].pc[j][k] += Wl * phil;
411                         phil = interp1(profile.y, profile.k, dl); //
                            turbulent kintetic energy
412                         blocks[n].kc[j][k] += Wl * phil;
413                         phil = interp1(profile.y, profile.omega, dl); //
                            specific dissipation rate
414                         blocks[n].omegac[j][k] += Wl * phil;
415                         if (include_stresses)
416                         {
417                             phil = interp1(profile.y, profile.uu, dl); //
                                <u'u'> Reynolds stress
418                             blocks[n].uuc[j][k] += Wl * phil;
419                             phil = interp1(profile.y, profile.uv, dl); //
                                <u'v'> Reynolds stress
420                             blocks[n].uvc[j][k] += Wl * phil;
421                             phil = interp1(profile.y, profile.uw, dl); //
                                <u'w'> Reynolds stress
422                             blocks[n].uwc[j][k] += Wl * phil;
423                             phil = interp1(profile.y, profile.vv, dl); //
                                <v'v'> Reynolds stress
424                             blocks[n].vvc[j][k] += Wl * phil;
425                             phil = interp1(profile.y, profile.vw, dl); //
                                <v'w'> Reynolds stress
```

```
426                                 blocks[n].vwc[j][k] += Wl * phil;
427                                 phil = interp1(profile.y, profile.ww, dl); //
                                        <w'w'> Reynolds stress
428                                 blocks[n].wwc[j][k] += Wl * phil;
429                             }
430                         }
431                     }
432                 }
433             }
434         }
435         //
              ////////////////////////////////////////////////////////////////////////////////

436         //
              ////////////////////////////////////////////////////////////////////////////////

437         //
              ////////////////////////////////////////////////////////////////////////////////

438         //
              ////////////////////////////////////////////////////////////////////////////////

439         profile_file.open("profile.dat", std::ios::out);
440         if (!profile_file.is_open())
441         {
442             std::cout << "Failed!" << std::endl;
443             std::cout << "Error while opening profile file!" << std::endl;
444             std::exit(-1);
445         }
446         profile_file << std::fixed;
447         profile_file << std::showpoint;
448         profile_file << std::setprecision(6);
449         profile_file << std::setfill('0');
450         if (include_stresses)
451         {
452             profile_file << "VARIABLES = \"X\", \"Y\", \"Z\", \"RHO\", \"U\",
                  \"V\", \"W\", \"P\", \"K\", \"O\", \"U'U'\", \"U'V'\", \"
                  U'W'\", \"V'V'\", \"V'W'\", \"W'W'\"" << std::endl;
453         }
454         else
455         {
456             profile_file << "VARIABLES = \"X\", \"Y\", \"Z\", \"RHO\", \"U\",
                  \"V\", \"W\", \"P\", \"K\", \"O\"" << std::endl;
457         }
```

```
458     for (int n = 0; n < N_blocks; n++)
459     {
460         if (blocks[n].profile != -1)
461         {
462             profile_file << "ZONE␣N=" << (4 * (blocks[n].Ny - 1) * (
                    blocks[n].Nz - 1)) << ",␣E=" << (blocks[n].Ny - 1) * (
                    blocks[n].Nz - 1) << "␣,␣DATAPACKING=POINT,␣ZONETYPE=
                    FEQUADRILATERAL\n";
463             int i = 0; //if face is 4 i=0, howver, if face is 2 i=Nx-1
464             if (blocks[n].profile == 1)
465             {
466                 i = blocks[n].Nx - 1;
467             }
468             for (int k = 0; k < blocks[n].Nz - 1; k++)
469             {
470                 for (int j = 0; j < blocks[n].Ny - 1; j++)
471                 {
472                     profile_file << "\t";
473                     profile_file << blocks[n].x[i][0][0] << "\t";
474                     profile_file << blocks[n].y[i][j][k] << "\t";
475                     profile_file << blocks[n].z[i][j][k] << "\t";
476                     profile_file << blocks[n].rhoc[j][k] << "\t";
477                     profile_file << blocks[n].uc[j][k] << "\t";
478                     profile_file << blocks[n].vc[j][k] << "\t";
479                     profile_file << blocks[n].wc[j][k] << "\t";
480                     profile_file << blocks[n].pc[j][k] << "\t";
481                     profile_file << blocks[n].kc[j][k] << "\t";
482                     if (include_stresses)
483                     {
484                         profile_file << blocks[n].omegac[j][k] << "\t";
485                         profile_file << blocks[n].uuc[j][k] << "\t";
486                         profile_file << blocks[n].uvc[j][k] << "\t";
487                         profile_file << blocks[n].uwc[j][k] << "\t";
488                         profile_file << blocks[n].vvc[j][k] << "\t";
489                         profile_file << blocks[n].vwc[j][k] << "\t";
490                         profile_file << blocks[n].wwc[j][k] << "\n";
491                     }
492                     else
493                     {
494                         profile_file << blocks[n].omegac[j][k] << "\n";
495                     }
496                     profile_file << "\t";
497                     profile_file << blocks[n].x[i][0][0] << "\t";
498                     profile_file << blocks[n].y[i][j + 1][k] << "\t";
```

```
499                     profile_file << blocks[n].z[i][j + 1][k] << "\t";
500                     profile_file << blocks[n].rhoc[j][k] << "\t";
501                     profile_file << blocks[n].uc[j][k] << "\t";
502                     profile_file << blocks[n].vc[j][k] << "\t";
503                     profile_file << blocks[n].wc[j][k] << "\t";
504                     profile_file << blocks[n].pc[j][k] << "\t";
505                     profile_file << blocks[n].kc[j][k] << "\t";
506                     if (include_stresses)
507                     {
508                         profile_file << blocks[n].omegac[j][k] << "\t";
509                         profile_file << blocks[n].uuc[j][k] << "\t";
510                         profile_file << blocks[n].uvc[j][k] << "\t";
511                         profile_file << blocks[n].uwc[j][k] << "\t";
512                         profile_file << blocks[n].vvc[j][k] << "\t";
513                         profile_file << blocks[n].vwc[j][k] << "\t";
514                         profile_file << blocks[n].wwc[j][k] << "\n";
515                     }
516                     else
517                     {
518                         profile_file << blocks[n].omegac[j][k] << "\n";
519                     }
520                     profile_file << "\t";
521                     profile_file << blocks[n].x[i][0][0] << "\t";
522                     profile_file << blocks[n].y[i][j + 1][k + 1] << "\t";
523                     profile_file << blocks[n].z[i][j + 1][k + 1] << "\t";
524                     profile_file << blocks[n].rhoc[j][k] << "\t";
525                     profile_file << blocks[n].uc[j][k] << "\t";
526                     profile_file << blocks[n].vc[j][k] << "\t";
527                     profile_file << blocks[n].wc[j][k] << "\t";
528                     profile_file << blocks[n].pc[j][k] << "\t";
529                     profile_file << blocks[n].kc[j][k] << "\t";
530                     if (include_stresses)
531                     {
532                         profile_file << blocks[n].omegac[j][k] << "\t";
533                         profile_file << blocks[n].uuc[j][k] << "\t";
534                         profile_file << blocks[n].uvc[j][k] << "\t";
535                         profile_file << blocks[n].uwc[j][k] << "\t";
536                         profile_file << blocks[n].vvc[j][k] << "\t";
537                         profile_file << blocks[n].vwc[j][k] << "\t";
538                         profile_file << blocks[n].wwc[j][k] << "\n";
539                     }
540                     else
541                     {
542                         profile_file << blocks[n].omegac[j][k] << "\n";
```

```
543                     }
544                     profile_file << "\t";
545                     profile_file << blocks[n].x[i][0][0] << "\t";
546                     profile_file << blocks[n].y[i][j][k + 1] << "\t";
547                     profile_file << blocks[n].z[i][j][k + 1] << "\t";
548                     profile_file << blocks[n].rhoc[j][k] << "\t";
549                     profile_file << blocks[n].uc[j][k] << "\t";
550                     profile_file << blocks[n].vc[j][k] << "\t";
551                     profile_file << blocks[n].wc[j][k] << "\t";
552                     profile_file << blocks[n].pc[j][k] << "\t";
553                     profile_file << blocks[n].kc[j][k] << "\t";
554                     if (include_stresses)
555                     {
556                         profile_file << blocks[n].omegac[j][k] << "\t";
557                         profile_file << blocks[n].uuc[j][k] << "\t";
558                         profile_file << blocks[n].uvc[j][k] << "\t";
559                         profile_file << blocks[n].uwc[j][k] << "\t";
560                         profile_file << blocks[n].vvc[j][k] << "\t";
561                         profile_file << blocks[n].vwc[j][k] << "\t";
562                         profile_file << blocks[n].wwc[j][k] << "\n";
563                     }
564                     else
565                     {
566                         profile_file << blocks[n].omegac[j][k] << "\n";
567                     }
568                 }
569             }
570             for (int i = 0; i < (blocks[n].Ny - 1) * (blocks[n].Nz - 1);
                    i++)
571             {
572                 profile_file << "\t";
573                 profile_file << (4 * (i + 1) - 3) << "\t";
574                 profile_file << (4 * (i + 1) - 2) << "\t";
575                 profile_file << (4 * (i + 1) - 1) << "\t";
576                 profile_file << (4 * (i + 1)) << "\n";
577             }
578         }
579     }
580     profile_file.close();
581     profile_file.open("profile", std::ios::out);
582     if (!profile_file.is_open())
583     {
584         std::cout << "Failed!" << std::endl;
585         std::cout << "Error while opening profile file!" << std::endl;
```

```
586             std::exit(-1);
587         }
588         profile_file << std::fixed;
589         profile_file << std::scientific;
590         profile_file << std::setprecision(6);
591         profile_file << std::setfill('0');
592         profile_file << N_profile_blocks << std::endl;
593         for (int n = 0; n < N_blocks; n++)
594         {
595             if (blocks[n].profile != -1)
596             {
597                 profile_file << (n + 1) << " " << (blocks[n].profile + 1) <<
                        " " << (blocks[n].Ny - 1) << " " << (blocks[n].Nz - 1) <<
                        std::endl;
598             }
599         }
600         for (int n = 0; n < N_blocks; n++)
601         {
602             if (blocks[n].profile != -1)
603             {
604                 for (int k = 0; k < blocks[n].Nz - 1; k++)
605                 {
606                     for (int j = 0; j < blocks[n].Ny - 1; j++)
607                     {
608
609                         profile_file << blocks[n].rhoc[j][k] << " " << blocks
                                [n].uc[j][k] << " " << blocks[n].vc[j][k] << " "
                                << blocks[n].wc[j][k] << " " << blocks[n].pc[j][k]
                                 << " " << blocks[n].kc[j][k] << " " << blocks[n].
                                omegac[j][k];
610                         if (include_stresses)
611                         {
612                             profile_file << " " << blocks[n].uuc[j][k] << " "
                                    << blocks[n].uvc[j][k] << " " << blocks[n].
                                    uwc[j][k] << " " << blocks[n].vvc[j][k] << " "
                                    << blocks[n].vwc[j][k] << " " << blocks[n].
                                    wwc[j][k];
613                         }
614                         profile_file << std::endl;
615                     }
616                 }
617             }
618         }
619         profile_file.close();
```

```
620     std::cout << "Done!" << std::endl;
621     std::cout << std::endl;
622     profile_file.open("profile_with_coordinates", std::ios::out);
623     if (!profile_file.is_open())
624     {
625         std::cout << "Failed!" << std::endl;
626         std::cout << "Error␣while␣opening␣profile␣file!" << std::endl;
627         std::exit(-1);
628     }
629     profile_file << std::fixed;
630     profile_file << std::scientific;
631     profile_file << std::setprecision(6);
632     profile_file << std::setfill('0');
633     profile_file << N_profile_blocks << std::endl;
634     for (int n = 0; n < N_blocks; n++)
635     {
636         if (blocks[n].profile != -1)
637         {
638             profile_file << (n + 1) << "␣" << (blocks[n].profile + 1) <<
                    "␣" << (blocks[n].Ny - 1) << "␣" << (blocks[n].Nz - 1) <<
                    std::endl;
639         }
640     }
641     for (int n = 0; n < N_blocks; n++)
642     {
643         if (blocks[n].profile != -1)
644         {
645             int i = 0; //if face is 4 i=0, howver, if face is 2 i=Nx-1
646             if (blocks[n].profile == 1)
647             {
648                 i = blocks[n].Nx - 1;
649             }
650             for (int k = 0; k < blocks[n].Nz - 1; k++)
651             {
652                 for (int j = 0; j < blocks[n].Ny - 1; j++)
653                 {
654                     double y1, y2, y3, y4, z1, z2, z3, z4;
655                     y1 = blocks[n].y[i][j][k];
656                     y2 = blocks[n].y[i][j + 1][k];
657                     y3 = blocks[n].y[i][j + 1][k + 1];
658                     y4 = blocks[n].y[i][j][k + 1];
659                     z1 = blocks[n].z[i][j][k];
660                     z2 = blocks[n].z[i][j + 1][k];
661                     z3 = blocks[n].z[i][j + 1][k + 1];
```

```
662                         z4 = blocks[n].z[i][j][k + 1];
663                         profile_file << y1 << "␣" << y2 << "␣" << y3 << "␣"
                               << y4 << "␣" << z1 << "␣" << z2 << "␣" << z3 << "␣
                               " << z4 << "␣";
664                         profile_file << blocks[n].yc[j][k] << "␣" << blocks[n
                               ].zc[j][k] << "␣" << blocks[n].rhoc[j][k] << "␣"
                               << blocks[n].uc[j][k] << "␣" << blocks[n].vc[j][k]
                                << "␣" << blocks[n].wc[j][k] << "␣" << blocks[n].
                               pc[j][k] << "␣" << blocks[n].kc[j][k] << "␣" <<
                               blocks[n].omegac[j][k];
665                         if (include_stresses)
666                         {
667                             profile_file << "␣" << blocks[n].uuc[j][k] << "␣"
                                   << blocks[n].uvc[j][k] << "␣" << blocks[n].
                                  uwc[j][k] << "␣" << blocks[n].vvc[j][k] << "␣"
                                   << blocks[n].vwc[j][k] << "␣" << blocks[n].
                                  wwc[j][k];
668                         }
669                         profile_file << std::endl;
670                     }
671                 }
672             }
673         }
674         profile_file.close();
675         std::cout << "Done!" << std::endl;
676         std::cout << std::endl;
677         return 0;
678 }
```

```
1  clear all;
2  close all;
3  clc;
4  % Huang, P.G. "Skin Friction and Velocity Profile Family for Compressible
       Turbulent Boundary Layers" AIAA Journal 1993 vol. 31 no. 9
5  % Huang, P.G. "Van Driest Transformation and Compressible Wall-Bounded
       Flows" AIAA Journal 1994 vol. 32 no. 10
6  % Zhang, J. and Morishita, E. "An Efficient Way of Specifying Profile
       Inflow Boundary Conditions"
7  %%%%%%%%%%%%%%%%%%%%%%%%%%%%%%%%%%%%%%%%%%%%%%%%%%%%%%%%%%%%%%%%%%%%%%%%%%%%
8  % kappa=0.41
9  % C=5.2
10 % u_c/u_tau=sqrt(B)*(asin((A+u)/D)-asin(A/D))/u_tau, where
11 % A=q_w/tau_w
12 % B=2*C_p*T_w/Pr_t
```

```
% D=sqrt(A^2+B)
% u_tau=sqrt(tau_w/rho_w)
% y_plus=u_tau*y/nu_w
% nu_w=mu_w/rho_w
% u/u_tau=1/R*sin(R*u_c/u_tau)-H*(1-cos(R*u_c/u_tau)), where
% R=u_tau/sqrt(B)
% H=A/u_tau
% T=T_w-Pr_t*q_w*u/(Cp*tau_w)-Pr_t*u^2/(2*Cp);
% Pr_t=0.9
% T_aw=T_inf*(1+r*(gamma-1)/2*M_inf^2);
% r=Pr_t=0.9;
%%%%%%%%%%%%%%%%%%%%%%%%%%%%%%%%%%%%%%%%
% Procedure
% At the inflow a van Driest transformed mean velocity is computed assuming
% a turbulent flat plate boundary layer profile. The mean velocity along
% the wall-binormal direction y is then obtained by an inverse van Driest
% transform. Coupling between adjacent walls is enforced through a
% weighting function based of the inverse squared wall distances. The
% pressure is assumed to be uniform and the mean density is determined from
% the Crocco-Busseman integral.

fprintf('\nConstants\n------------------------------\n');
kappa=0.41;
C=5.2;
Pr_t=0.90;
gamma=1.4;
Cp=1005;
Cv=Cp/gamma;
R=Cp-Cv;
fprintf('kappa:%0.4f␣-\n',kappa);
fprintf('C:%0.4f␣-\n',C);
fprintf('Cp:%0.4f␣-\n',Cp);
fprintf('gammma:%0.4f␣-\n',gamma);
fprintf('R:%0.4f␣-\n',R);
fprintf('Pr_t:%0.4f␣-\n',Pr_t);
fprintf('\nFreestream\n------------------------------\n');
L=(753.8-164.8)*10^(-3);
h=16.275e-3; %at inlet
p0_inf=206*10^3;
T0_inf=295;
M_inf=1.61;
p_inf=p0_inf/(1+(gamma-1)/2*M_inf^2)^(gamma/(gamma-1));
```

```
55 T_inf=T0_inf/(1+(gamma-1)/2*M_inf^2);
56 a_inf=sqrt(gamma*R*T_inf);
57 rho_inf=p_inf/(R*T_inf);
58 u_inf=M_inf*a_inf;
59 delta=5.4e-3;
60 Re_inf=3e+07;
61 Re_delta=Re_inf*delta;
62 Re_h=Re_inf*h;
63 mu_inf=(rho_inf*u_inf*delta)/Re_delta;
64 nu_inf=u_inf/Re_inf;
65 Re_t=10;
66 I_inf=0.01;
67 tau_inf=delta/u_inf;
68 t_inf=L/u_inf;
69 dt1=0.5*t_inf;
70 dt2=0.05*t_inf;
71 dt3=0.025*t_inf;
72 bar_p_inf=1/(gamma*M_inf^2);
73 bar_rho_inf=1;
74 bar_I_inf=0.01;
75 bar_k_inf=3/2*(I_inf)^2*Re_h;
76 bar_omega_inf=bar_k_inf/Re_t;
77 fprintf('M_inf:%0.4f -\n',M_inf);
78 fprintf('u_inf:%0.4f m/s\n',u_inf);
79 fprintf('p_inf:%0.4f Pa\n',p_inf);
80 fprintf('T_inf:%0.4f K\n',T_inf);
81 fprintf('rho_inf:%0.4f kg/m3\n',rho_inf);
82 fprintf('tau_inf:%0.4e s\n',tau_inf);
83 fprintf('Re_inf:%0.4f 1/m\n',Re_inf);
84 fprintf('Re_delta:%0.4f -\n',Re_delta);
85 fprintf('Re_h:%0.4f -\n',Re_h);
86 fprintf('mu_inf:%0.4e Pa.s\n',mu_inf);
87 fprintf('nu_inf:%0.4e Pa.s\n',nu_inf);
88 fprintf('mu_inf:%0.4e Pa.s\n',nu_inf*rho_inf);
89 fprintf('bar_p_inf:%0.4f -\n',bar_p_inf);
90 fprintf('bar_I_inf:%0.4f -\n',I_inf);
91 fprintf('bar_k_inf*Re_delta:%0.6f -\n',bar_k_inf);
92 fprintf('bar_omega_inf:%0.6f -\n',bar_omega_inf);
93 fprintf('t_inf (based on L):%0.4e s\n',t_inf);
94 fprintf('dt1=0.5*t_inf=:%0.4e s\n',dt1);
95 fprintf('dt2=0.05*t_inf=:%0.4e s\n',dt2);
96 fprintf('dt3=0.025*t_inf=:%0.4e s\n',dt3);
97 fprintf('\n');
98 fprintf('\nWall\n----------\n');
```

```
99  T_w=T_inf+Pr_t*u_inf^2/(2*Cp);
100 p_w=p_inf;
101 rho_w=p_w/(R*T_w);
102 S_mu=0.368;
103 T0T_inf=(1.0+(gamma-1.0)/2*M_inf^2);
104 mu_w=T_w/T_inf*sqrt(T_w/T_inf)*(1+T0T_inf*S_mu)/(T_w/T_inf+T0T_inf*S_mu)*
        mu_inf;
105 % mu_w=mu_inf*(T_w/T_inf)^(3/2)*(T_inf+110.4)/(T_w+110.4);
106 nu_w=mu_w/rho_w;
107 fprintf('T_w:%0.6f␣K\n',T_w);
108 fprintf('p_w:%0.6f␣Pa\n',p_w);
109 fprintf('rho_w:%0.6f␣kg/m3\n',rho_w);
110 fprintf('mu_w:%0.4e␣Pa.s␣\n',mu_w);
111 fprintf('nu_w:%0.4e␣m^2/s\n',nu_w);
112 fprintf('\nSolving␣for␣above␣profile␣parameters...');
113 A=0;
114 B=2*Cp*T_w/Pr_t;
115 D=sqrt(A^2+B);
116 u_tau=10;
117 u_tau_old=0;
118 theta_delta=0.01;
119 i=1;
120 R_u_tau=1;
121 while abs(R_u_tau) > 1e-6
122     theta=theta_delta*delta;
123     uc_delta_plus=sqrt(B)*(asin((A+u_inf)/D)-asin(A/D));
124     Re_delta2=(rho_inf*u_inf*theta)/mu_w;
125     PI=0.55*(1-exp(-0.24*sqrt(Re_delta2)-0.298*Re_delta2));
126     Re_deltaw=rho_w*uc_delta_plus*delta/mu_w;
127     delta_plus=(u_tau*delta)/nu_w;
128     uc_delta_plus=5.424*atan((2*delta_plus-8.15)/16.7)+log10((delta_plus
          +10.6)^(9.6)/(delta_plus^2-8.15*delta_plus+86)^2)-3.52+4.88*PI;
129     delta_plus=Re_deltaw/uc_delta_plus;
130     u_tau_old=u_tau;
131     u_tau=delta_plus*mu_w/(rho_w*delta);
132     Cf=2*(T_inf/T_w)*(u_tau/u_inf)^2;
133     R_u_tau=u_tau-u_tau_old;
134     eta=(logspace(0,1,1000)-1)/9;
135     for j=1:length(eta)
136         y=eta(j)*delta;
137         y_plus=(u_tau*y)/nu_w;
138         uc_plus=5.424*atan((2*y_plus-8.15)/16.7)+log10((y_plus+10.6)
              ^(9.6)/(y_plus^2-8.15*y_plus+86)^2)-3.52...
139         +2.44*(PI*(6*eta(j)^2-4*eta(j)^3)+eta(j)^2*(1-eta(j)));  %Musker's
```

```
                law-of-the-wall and law-of-the-wake profile
140             R=u_tau/sqrt(B);
141             H=A/u_tau;
142             u_plus=1/R*sin(R*uc_plus)-H*(1-cos(R*uc_plus)); %uc_plus to
                    u_plus (inverse van Driest)
143             u(j)=u_plus*u_tau/u_inf;
144             if u(j)<0
145                 u(j)=0;
146             end
147             T(j)=(T_w-Pr_t*(u(j)*u_inf)^2/(2*Cp))/T_inf;
148             rho(j)=1/T(j);
149         end
150         theta_delta=0;
151         delta_star_delta=0;
152         theta_delta_i=0;
153         delta_star_delta_i=0;
154         for j=1:(length(eta)-1)
155             theta_delta=theta_delta+1/2*(rho(j+1)*u(j+1)*(1-u(j+1))+rho(j)*u(
                    j)*(1-u(j)))*(eta(j+1)-eta(j));
156             delta_star_delta=delta_star_delta+1/2*((1-rho(j+1)*u(j+1))+(1-rho
                    (j)*u(j)))*(eta(j+1)-eta(j));
157             theta_delta_i=theta_delta_i+1/2*(u(j+1)*(1-u(j+1))+u(j)*(1-u(j)))
                    *(eta(j+1)-eta(j));
158             delta_star_delta_i=delta_star_delta_i+1/2*((1-u(j+1))+(1-u(j)))*(
                    eta(j+1)-eta(j));
159         end
160         i=i+1;
161     end
162     fprintf('Done!\n\n');
163     fprintf('\nR_u_tau:%0.4f - \n',R_u_tau);
164     fprintf('theta/delta:%0.4f -\n',theta_delta);
165     fprintf('delta_star/delta:%0.4f -\n',delta_star_delta);
166     fprintf('delta:%0.4f mm\n',delta*1000);
167     fprintf('theta:%0.4f mm\n',theta_delta*delta*1000);
168     fprintf('Re_theta:%0.4f -\n',(rho_inf*u_inf*theta)/mu_inf);
169     fprintf('delta_star:%0.4f mm\n',delta_star_delta*delta*1000);
170     fprintf('H:%0.4f -\n',delta_star_delta/theta_delta);
171     fprintf('theta_i:%0.4f mm\n',theta_delta_i*delta*1000);
172     fprintf('delta_star_i:%0.4f mm\n',delta_star_delta_i*delta*1000);
173     fprintf('H_i:%0.4f -\n',delta_star_delta_i/theta_delta_i);
174     dudy=(u(2)-u(1))/(eta(2)-eta(1));
175     tau_w=mu_w*dudy*u_inf/delta;
176     fprintf('mu_w:%0.6e Pa.s \n',mu_w);
177     fprintf('nu_w:%0.6e m^2/s\n',nu_w);
```

```
178 fprintf('tau_w:%0.4f␣\n',tau_w);
179 fprintf('u_tau:%0.4f␣m/s\n',sqrt(tau_w/rho_w));
180 fprintf('u_tau:%0.4f␣m/s\n',u_tau);
181 fprintf('u_tau/nu_w:%0.4e␣1/m\n',u_tau/nu_w);
182 y_plus=[0.1,1,5,6,7,8,9,10,15,20,30,40,60,100,200,300,500,700];
183 for i=1:length(y_plus)
184     fprintf('y:%0.8f␣@␣y+=%i\n',y_plus(i)*nu_w/u_tau*1/delta,y_plus(i));
185 end
186 y_plus=(u_tau*(eta*delta))/nu_w;
187 uc_plus_inner=y_plus;
188 uc_plus_outer=1/kappa*log(y_plus)+C;
189 uc_plus=sqrt(B)*asin((u*u_inf)/sqrt(B))/u_tau;
190 profile_file=fopen(sprintf('profile_%i_vandriest',M_inf*100),'w');
191 for i=1:length(eta)
192     fprintf(profile_file,'%0.6f␣%0.6f␣%0.6f␣%0.6f␣%0.6f␣%0.6f␣%0.6f␣%0.6f
        \n',eta(i),rho(i),u(i),0,0,bar_p_inf,bar_k_inf,bar_omega_inf);
193 end
194 fclose(profile_file);
195 figure(1);
196 hold on;
197 plot(y_plus,uc_plus,'Marker','s','LineStyle','-','Color',[0,0,0],'
    DisplayName','Generated␣(x=0)');
198 plot(y_plus,uc_plus_inner,'LineStyle','-.','Color',[0,0,0],'DisplayName',
    'u^{+}=y^{+}');
199 plot(y_plus,uc_plus_outer,'LineStyle','-.','Color',[0,0,0],'DisplayName',
    'u^{+}=1/\kappalog(y^{+})+C');
200 grid on;
201 ylabel('u_{c}^{+}␣(-)');
202 xlabel('y^{+}␣(-)');
203 set(gca,'XScale','log');
204 ylim([0,30]);
205 xlim([0,10000]);
206 legend show;
207 figure(2);
208 subplot(1,4,1);
209 hold on;
210 plot(u,eta,'LineStyle','-','Color',[0,0,0],'DisplayName','Generated');
211 grid on;
212 xlabel('u/u_{\infty}␣(-)');
213 ylabel('y/\delta␣(-)');
214 subplot(1,3,2);
215 hold on;
216 plot(T,eta,'LineStyle','-','Color',[0,0,0],'DisplayName','Generated');
217 grid on;
```

```
218 xlabel('T/T_{\infty}␣(-)');
219 subplot(1,3,3);
220 hold on;
221 plot(rho,eta,'LineStyle','-','Color',[0,0,0],'DisplayName','Generated');
222 grid on;
223 xlabel('\rho/\rho_{\infty}␣(-)');
```

Appendix C

Simulations of a store body at a high incidence angle *

Predicting the flowfield around a supersonic missile can be challenging as vortices and shocks are often present and interact with each other. The complexity of the problem is further increased by the presence of wing-body and wing-tail junctions as these can be the source of secondary flows. This section investigates the flowfield around the body of a supersonic missile at high incidence angle and comments on the grid convergence and the effect of non-linear turbulence models.

C.1 Geometry and conditions

The missile geometry was used in the NATO AVT-316 activity [3] and is shown in figure C.1. The total length of the body is $L_{ref} = 3.45$ m and the outer diameter of the body is $d_{ref} = 0.15$ m. The total length of the body was used as the characteristic length for the problem. The reference Mach number and the Reynolds number based on the missile length were $M_{ref} = 1.4$ and $Re_{L_{ref}} = 112.47 \times 10^6$. An incidence angle of $\sigma = 15$ deg and a roll angle of $\lambda = 2.5$ deg, as well as standard sea-level ISA atmospheric conditions, were assumed. Aerodynamic loads were reported in the body-fixed coordinate system located at $x/L_{ref} = 0.5$ (50% of the length of the body). The coordinate system and the definitions for the incidence σ and roll λ angles are shown in figure C.2. A strong interaction between the starboard wing vortex and the downstream fin 4 caused difficulties in obtaining grid converged results. This was confirmed by simulations from other partners [134]. In an attempt to investigate whether

*Some of this work is presented in N. Taylor *et al.* "The Prediction of Vortex Interactions on a Generic Missile Configuration Using CFD: Current Status of Activity in NATO AVT-316", Proceedings of the AVT-307 Research Symposium on Separated Flow: Prediction, Measurement and Assessment for Air and Sea Vehicles

grid convergence can be obtained a simplified geometry was created by removing the missile fins and wings.

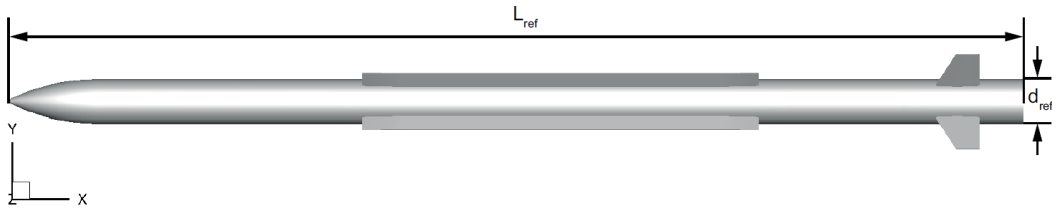

Figure C.1: Missile geometry.

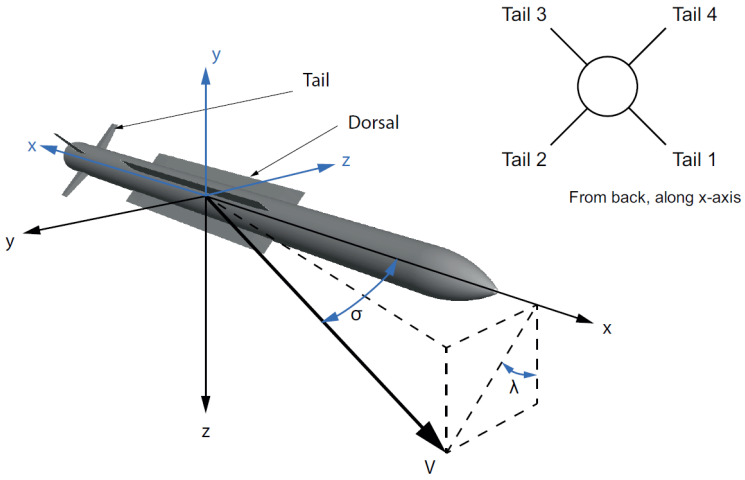

Figure C.2: Body-fixed coordinate system; the flow coordinate system is coloured in blue.

C.2 Grids and numerical setup

Multi-block structured grids of the store body were created with ANSYS ICEM CFD. Two blocking topologies were used - one for the background grid and one for the store body grid. Figure C.3 shows the blocking topologies of the background and the store body grid. A total of four grids were created - fine, very fine, extra-fine, and super-fine. The increase in node count in every direction was 8 for the store body grid and 5 for the background grid. The number of cells in the normal direction was kept constant only for the blocks adjacent to the body (the boundary layer blocks). A total of 1360 blocks were used. Table C.1 shows the grid parameters.

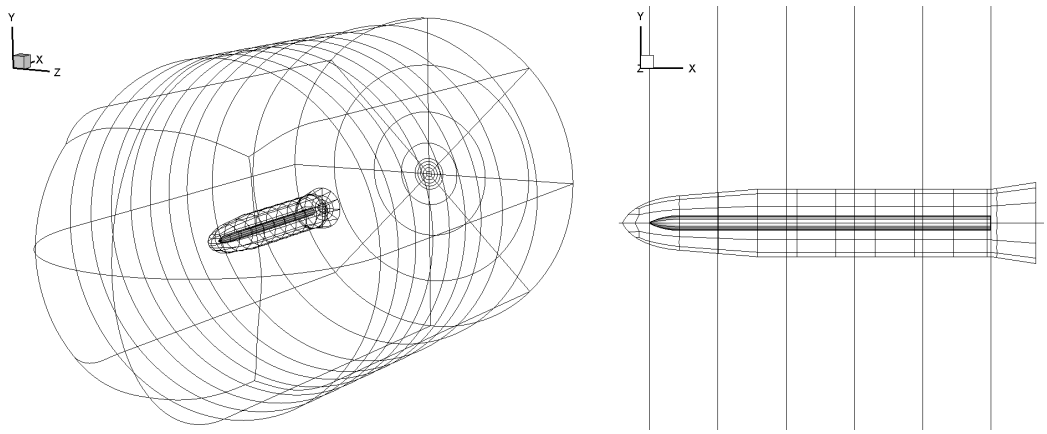

Figure C.3: Blocking topology of the store body grid.

Table C.1: Grid parameters (all dimensional quantities are given in millimetres).

Description	Fine	Very fine	Extra-fine	Super-fine
Domain size WxHxL	80.5x46x46d_{ref}^3	80.5x46x46d_{ref}^3	80.5x46x46d_{ref}^3	80.5x46x46d_{ref}^3
Wake length	$3.0d_{ref}$	$3.0d_{ref}$	$3.0d_{ref}$	$3.0d_{ref}$
Density radius	$1.8333d_{ref}$	$1.8333d_{ref}$	$1.8333d_{ref}$	$1.8333d_{ref}$
Total cells ($\times 10^6$)	43.1	80.0	127.8	190.7
Total nodes ($\times 10^6$)	47.2	86.4	136.0	201.5
First layer height	3.45×10^{-3}	3.45×10^{-3}	3.45×10^{-3}	3.45×10^{-3}

Figure C.4 shows the cell volume at $x/L_{ref} = 0.5$ of the very fine, extra-fine, and super-fine grids. The location of the Chimera interface was determined by the position of the vortices generated by the body. For both $\sigma = 5$ and $\sigma = 15$ deg incidence angles the body vortices remained within the body grid. Simulations with the $k-\omega$ SST model were performed on all grids at $\sigma = 5$ and $\sigma = 15$ deg. The effect of non-linear turbulence models was investigated on the extra-fine grid. Both the $k-\omega$ EARSM and the $k-\omega$ SST QCR V1 models were considered. Unsteady RANS with the $k-\omega$ SST model was also performed to investigate whether there is any unsteadiness in the flow. Table C.2 lists the simulation parameters and the aerodynamic loads.

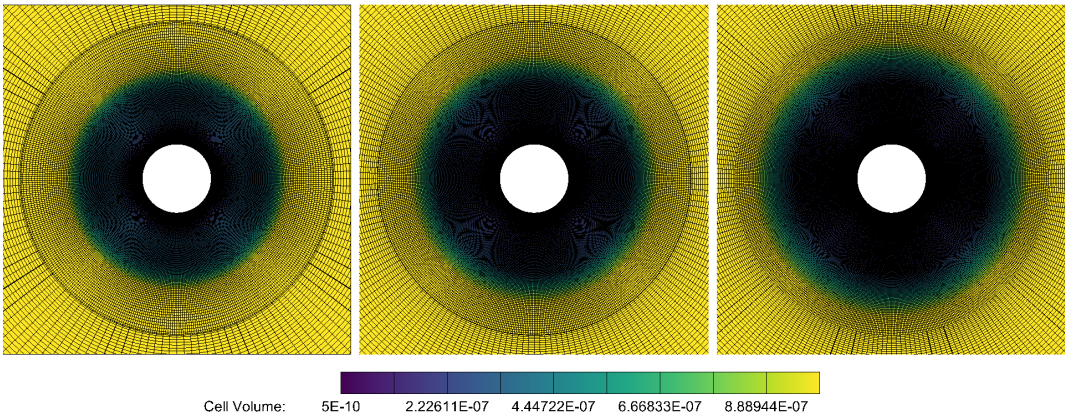

Figure C.4: Cell volume at $x/L_{ref} = 0.5$ for the very fine (left), extra-fine (middle), and super-fine (right) grids.

Table C.2: Simulation parameters.

Grid	σ deg	C_X	C_Y	C_Z	C_l	C_m	C_n	Turb. model
Fine	5.0	-0.609	0.000	-0.352	0.000	2.121	0.002	$k-\omega$ SST
Very fine	5.0	-0.608	-0.000	-0.337	0.000	2.086	-0.001	$k-\omega$ SST
Extra-fine	5.0	-0.607	-0.000	-0.327	-0.000	2.078	-0.000	$k-\omega$ SST
Super-fine	5.0	-0.607	0.000	-0.324	-0.000	2.057	0.000	$k-\omega$ SST
Very fine	15.0	-0.692	-0.000	-1.673	0.000	7.578	-0.000	$k-\omega$ SST
Extra-fine	15.0	-0.690	-0.000	-1.652	-0.000	7.563	0.001	$k-\omega$ SST
Super-fine	15.0	-0.689	-0.001	-1.640	-0.000	7.515	-0.002	$k-\omega$ SST
Very fine	15.0	-0.597	-0.000	-1.732	-0.000	7.056	-0.001	$k-\omega$ EARSM
Extra-fine	15.0	-0.596	0.000	-1.727	-0.000	7.093	-0.001	$k-\omega$ EARSM
Super-fine	15.0	-0.595	0.001	-1.726	-0.000	7.093	-0.005	$k-\omega$ EARSM
Extra-fine	15.0	-0.685	-0.001	-1.699	-0.000	7.491	-0.003	$k-\omega$ SST QCR V1

C.3 Results and discussion

C.3.1 Low incidence angle

First, simulations at a low incidence angle - $\sigma = 5$ deg were performed. Figures C.5 to C.7 show the iteration history of the aerodynamic loads. The large difference in C_Z between the fine, very fine, and extra-fine grid shows that grids of the same size as the very fine grid or larger must be used to accurately predict C_Z. A further increase of the grid size by 65.32×10^6 points reduced the difference in C_Z significantly. The C_X, C_Z, and C_m aerodynamic coefficients were observed to settle after approximately 30000 steps and exhibited monotonicity i.e. all values were increasing or decreasing. A total of 50000 steps were performed for the C_X, C_Z, and C_m to show iterative convergence.

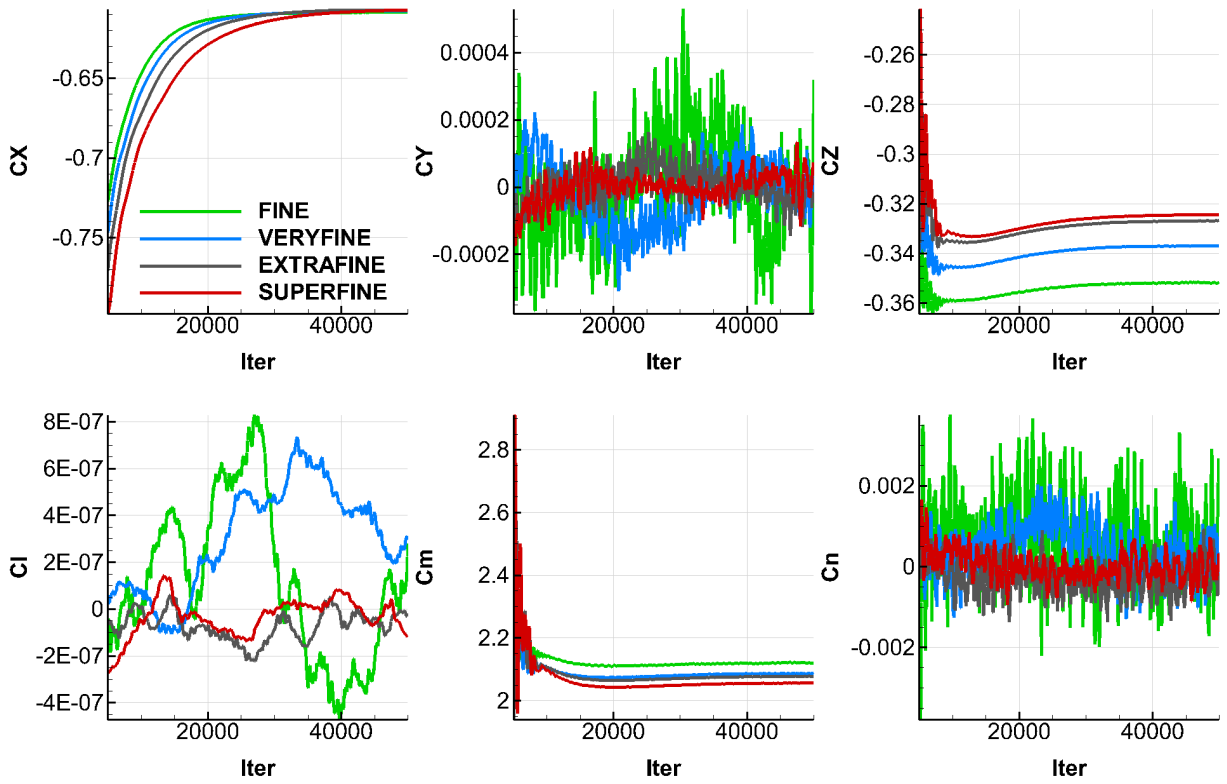

Figure C.5: Aerodynamic loads for the store body resulting from pressure and viscous contributions.

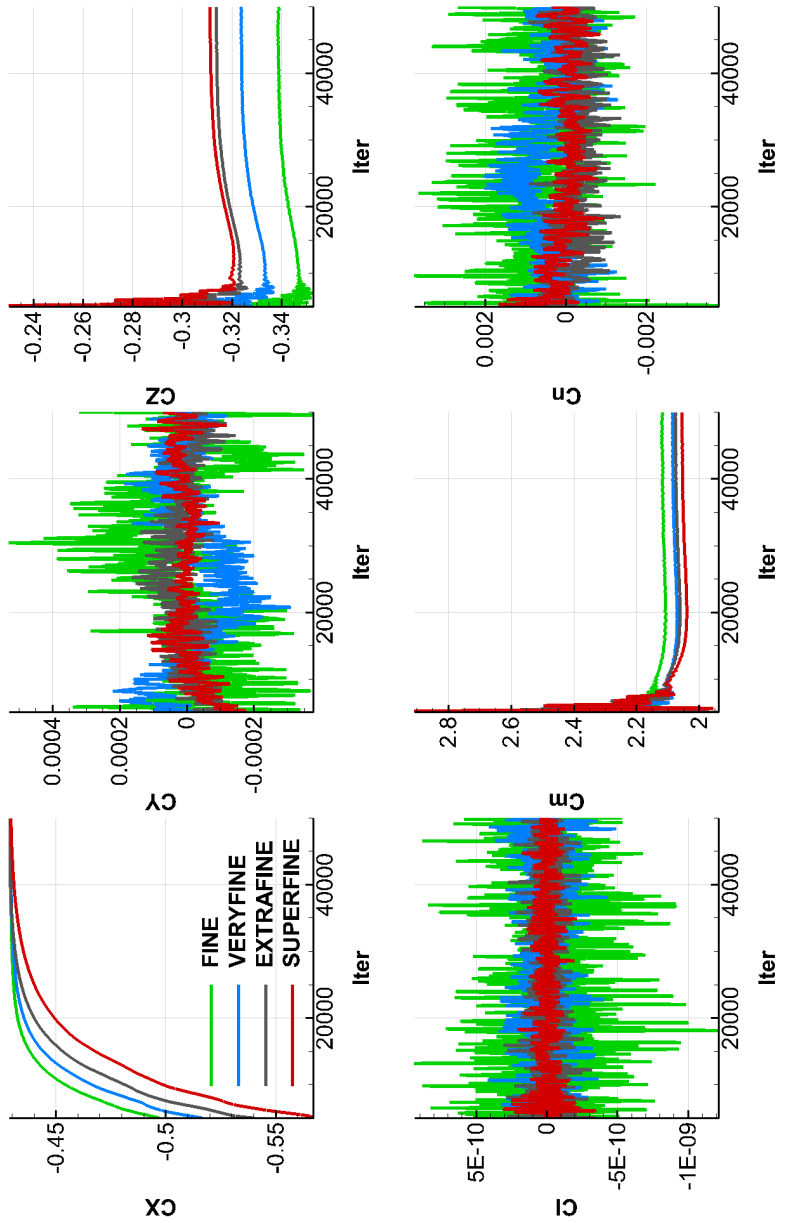

Figure C.6: Aerodynamic loads for the store body resulting from pressure contributions.

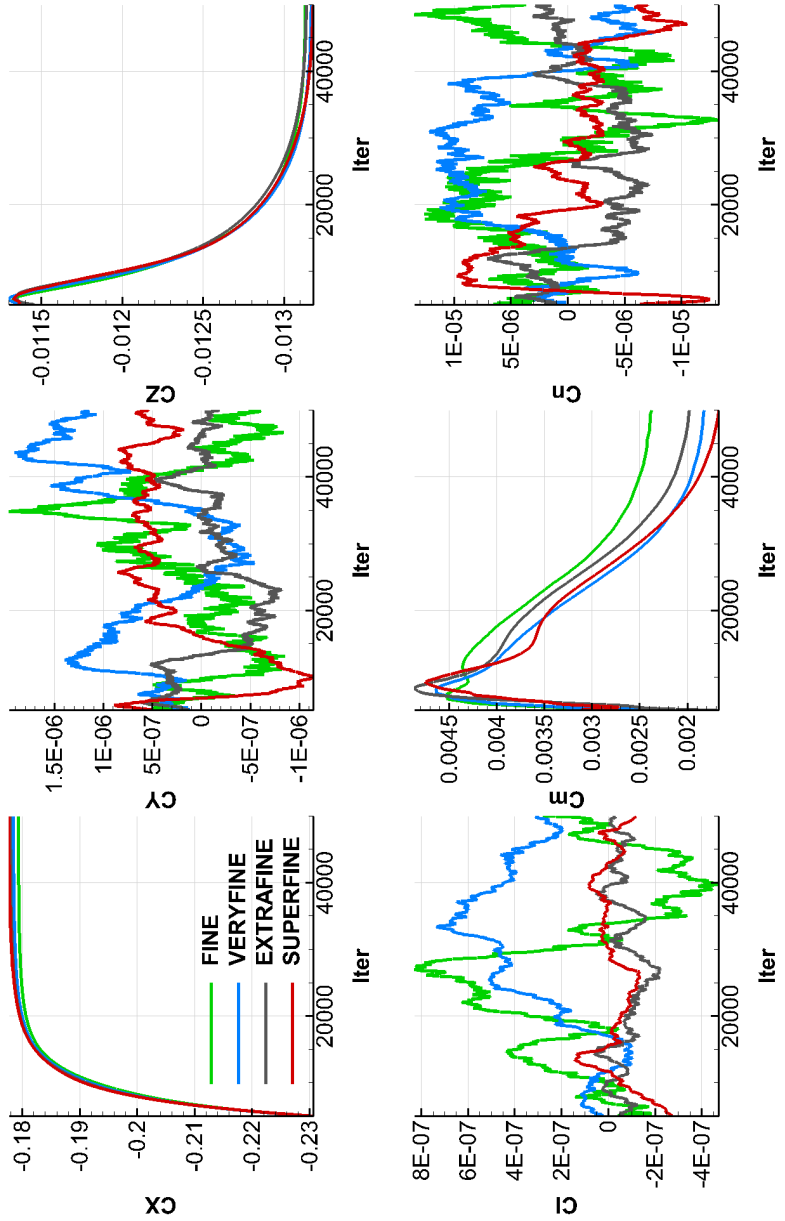

Figure C.7: Aerodynamic loads for the store body resulting from viscous contributions.

A non-monotonic behaviour was observed in the viscous C_Z and C_m values. The value of C_m on the very fine grid was less than the value on the extra-fine grid, which was greater than the value on the super-fine grid. Even though the viscous values for C_Z and C_m were non-monotonic the total values were, due to the small contribution of the viscous values. The difference in the total C_m value between the super-fine and extra-fine grid was greater than between the extra-fine and very fine grids. One would expect the difference in all aerodynamic coefficients to decrease as the grid is refined (C_Z is such an example). Further analysis of the C_m values per component (store body and base) and per contribution (pressure and viscous) showed that the difference in C_m originates from the store body. Grid convergence was investigated through the grid convergence index approach. The grid convergence index or GCI [108,109] presents a simple method for uniform reporting of grid convergence studies without any restriction to grid doubling. The GCI is based on generalised Richardson extrapolation involving comparison of discrete solutions at two different grid spacings. The error in a fine grid solution f_1 can be obtained by comparing it to the solution on a coarse grid f_2 and is defined as:

$$E^{fine} = \frac{\varepsilon_{12}}{(1-r^p)}, \tag{C.1}$$

where $\varepsilon_{12} = f_2 - f_1$, r is the refinement ratio and p is the observed order of accuracy. A second-order numerical algorithm will have $p = 2$, however, due to factors including but not limited to the grid the observed order of accuracy will be less. To account for the uncertainty in the generalised Richardson-based error estimates and to put the grid convergence studies on the same basis as grid doubling with a second-order numerical algorithm Roache incorporated a safety factor and defined the GCI as:

$$GCI^{fine} = F_s|E^{fine}|, \tag{C.2}$$

where F_s is a safety factor. The GCI is not an error estimator but F_s times the error estimator, representing error bands in a loose statistical sense. A value of $F_s = 3$ for two grids and $F_s = 1.25$ for three grids was recommended by Roache [109]. For three grids, having solutions f_1, f_2, and f_3, where f_1 corresponds to the solution on the finest grid, the observed order of convergence, p, is given by:

$$\frac{\varepsilon_{23}}{\left(r_{23}^{p}-1\right)} = r_{12}^{p}\left[\frac{\varepsilon_{12}}{\left(r_{12}^{p}-1\right)}\right]. \tag{C.3}$$

As the above equation is transcendental in p, an iterative method is required to solve it. For well behaved solutions simple substitution iteration with a relaxation factor of $\omega = 0.5$ works well.

$$\begin{aligned} \beta &= \frac{\left(r_{12}^{p^i}-1\right)}{\left(r_{23}^{p^i}-1\right)}\frac{\varepsilon_{23}}{\varepsilon_{12}} \\ p^{i+1} &= \omega p^i + (1-\omega)\frac{\ln(\beta)}{\ln(r_{12})}; \end{aligned} \tag{C.4}$$

A Matlab script employing the above approach was used to calculate the GCIs for the aerodynamic coefficients. The script is detailed at the end of this appendix. Table C.3 shows the GCIs for the C_Z coefficient. The GCIs between the last three grids in the grid convergence study were calculated. Although a small variation was present, the refinement ratio between the very-fine and extra-fine and the extra-fine and super-fine grids was approximately 1.464. The difference in C_Z between the grids was observed to reduce and resulted in small GCIs. The GCI between the super-fine and the extra-fine grid amounted to approximately 0.6%. The decrease with respect to the GCI between the very-fine and the extra-fine grid shows that the sensitivity of the solution with respect to the grid size decreases. Estimation of the observed order of convergence p resulted in a value of 2.96 which was close to the theoretical order of convergence ($p = 3$).

Table C.3: GCI for the C_Z aerodynamic coefficient.

	Very-fine (3)	Extra-fine (2)	Super-Fine (1)
Points ($\times 10^6$)	86.44	136.08	195.40
h	2.137	1.386	1.000
r_{12}		1.386	
r_{23}	1.542		
C_Z	-0.337	-0.327	-0.324
GCI_{12} %		0.564	
GCI_{23} %	1.482		
p		2.961	
$r_{12}^{p}\frac{GCI_{12}}{GCI_{23}}$		1.01	
$C_{Z,extr.}$		-0.323	

In addition the ratio between the GCIs was close to 1 indicating that the solution is in the asymptotic range of convergence. Using the observed order an extrapolated value for C_Z of -0.323 was obtained. Figure C.8 shows the stagnation pressure contours p_0/p_{ref} at the $x/d_{ref} = 21.5$ streamwise location (base). The TKE contours k/V_{ref}^2 are shown in figures C.8. Only the very fine, extra-fine, and super-fine grids are shown. The fine grid is omitted due to the large difference in the predicted C_Z value. No significant differences in the stagnation pressure and TKE contours were observed between the three grids. It is hard to identify the cause for the differences in the aerodynamic coefficients solely from the stagnation or TKE contour plots. A better comparison is shown in figure C.10. The figure shows the pressure contours on the surface of the store body. In the area of the nose, the pressure contours showed good agreement between the three grids. Downstream of the nose, however, noticeable differences were observed. The low-pressure region on the leeward side of the store body, extending to the port and starboard sides changed its shape slightly as the grid was refined. A change in the pressure region on the windward side was also observed. Since the pressure distribution on the windward and leeward sides is the main contributor to the pitching moment, differences in the pressure distribution in these areas between grids are expected to affect the pitching moment. The pressure contours on the base showed no significant differences, further supporting the component analysis which showed that the base is not contributing to the difference in C_m. To support the statement that pressure differences on the windward and leeward side of the store are the main contributor to the difference in pitching moment C_m, Figure C.11 shows the difference in the pressure coefficient between the fine and very fine, the very fine and extra-fine and the extra-fine and super-fine grids. The largest ΔC_p was observed near the nose of the store, downstream differences in C_p were insignificant. As the grid was refined, ΔC_p reduced, however, it was still identifiable. Figure C.12 shows the pressure coefficient C_p on the windward and leeward sides of the store body as a function of the store body length. Small oscillations in the C_p were observed on the windward side of the store. At $x/L_{ref} = -0.4$ the super-fine grid predicted a slightly higher C_p than the extra-fine grid. This difference may be the cause for the difference in the pitching moment coefficient C_m between the extra-fine and super-fine grids. Figure C.13 shows the vortex trajectories obtained with the Lambda2 vortex criterion.

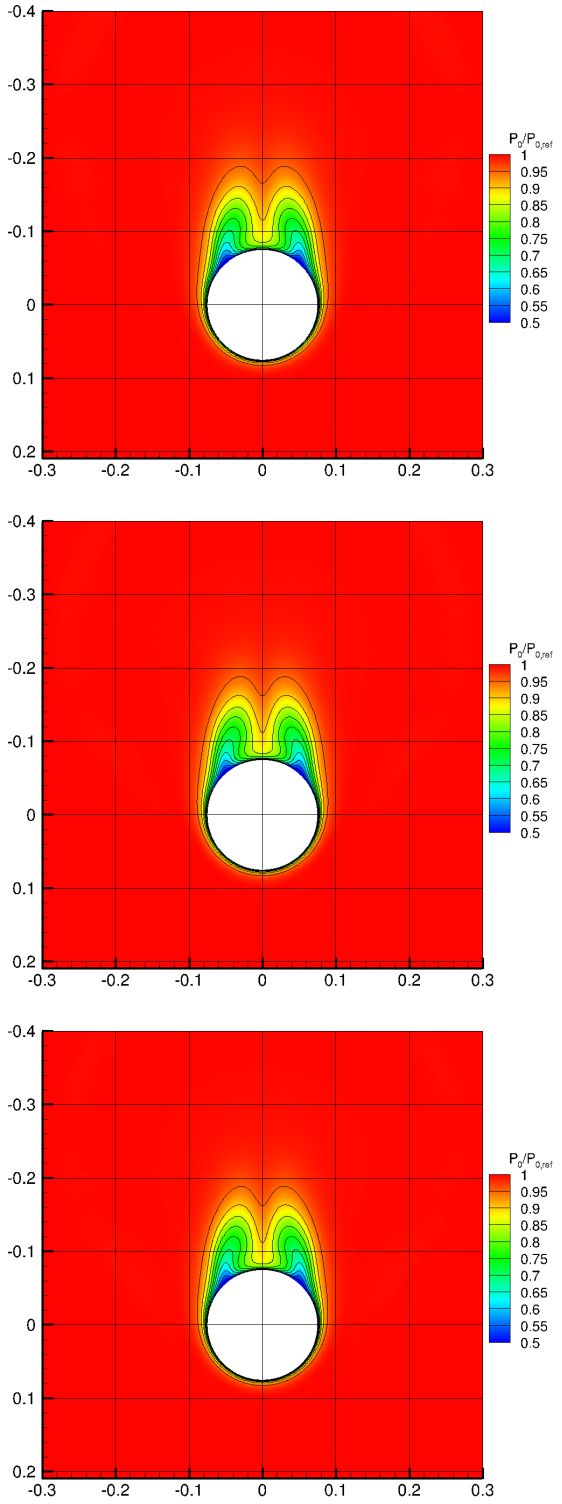

Figure C.8: Stagnation pressure for the $k-\omega$ SST model on the very fine (top), extra-fine (middle), and super-fine (bottom) grids at $x/d_{ref} = 21.5$.

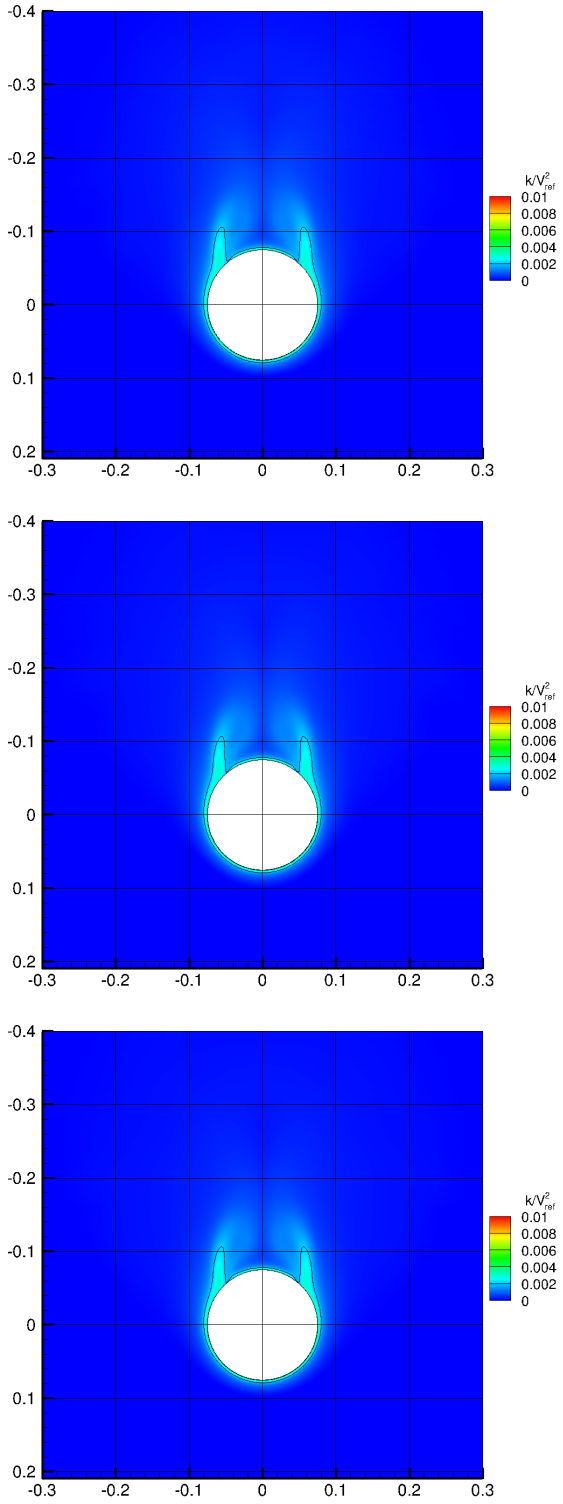

Figure C.9: Turbulent kinetic energy contours for the $k-\omega$ SST model on the very fine (top), extra-fine (middle), and super-fine (bottom) grids at $x/d_{ref} = 21.5$.

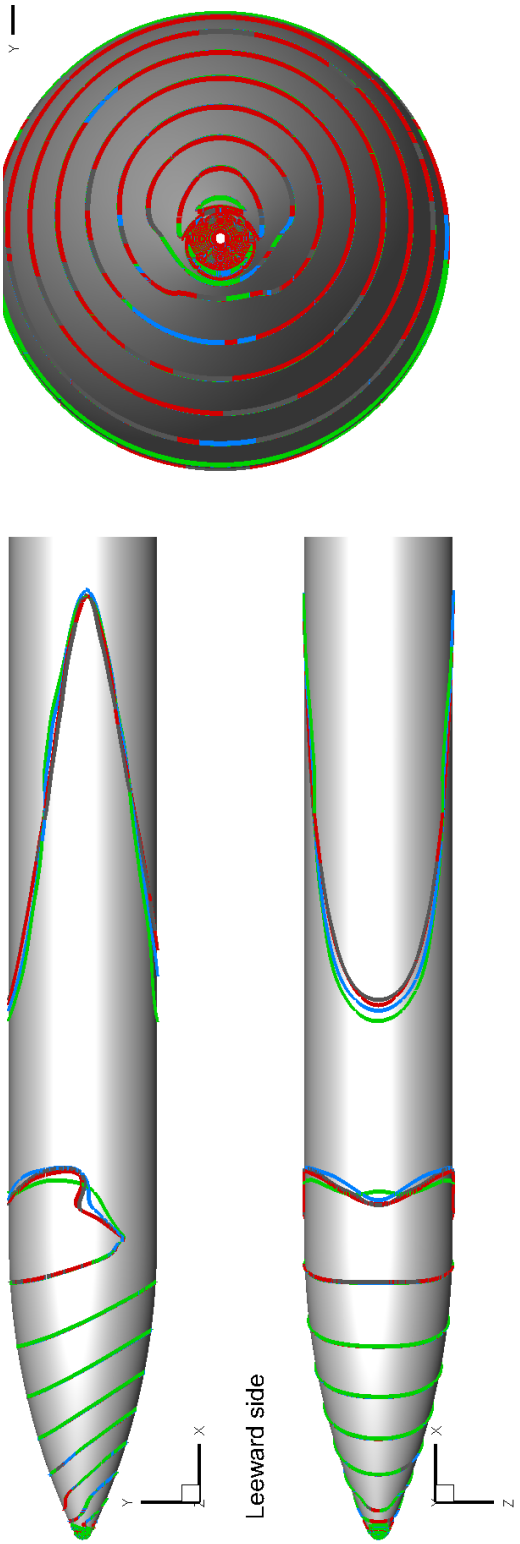

Figure C.10: Surface pressure contours for the $k-\omega$ SST model on the fine (green) very fine (blue), extra-fine (grey), and super-fine (red) grids.

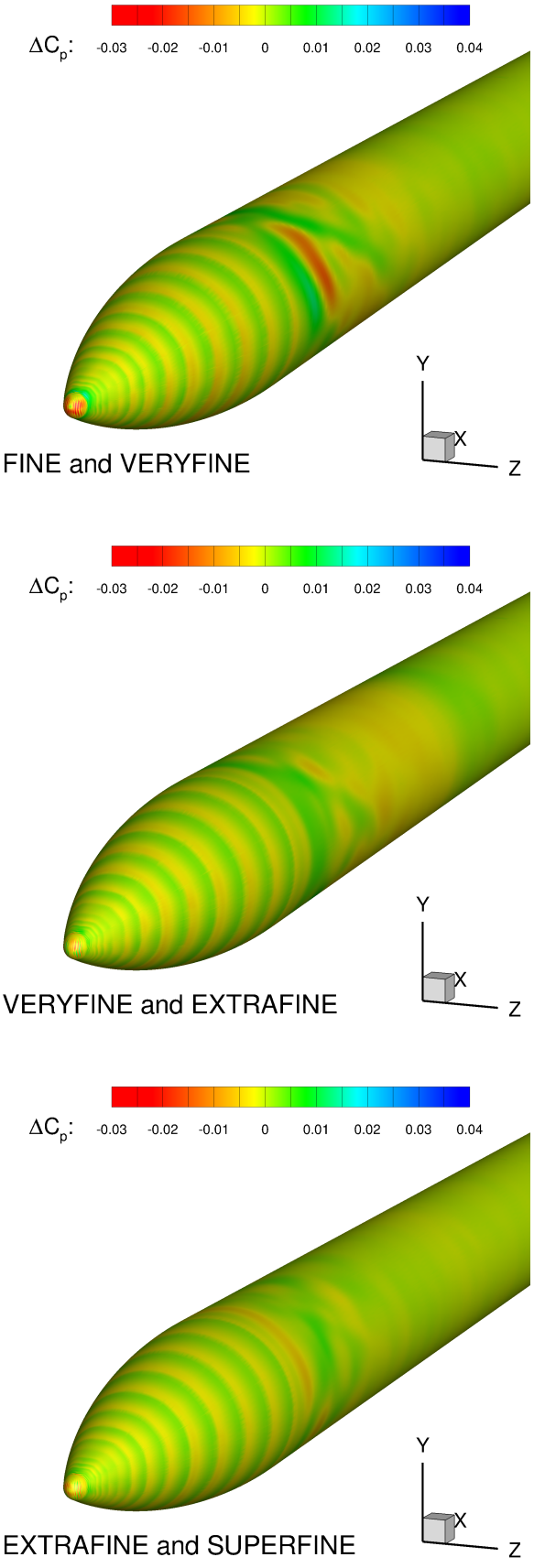

Figure C.11: Difference in the pressure coefficient ΔC_p between grids.

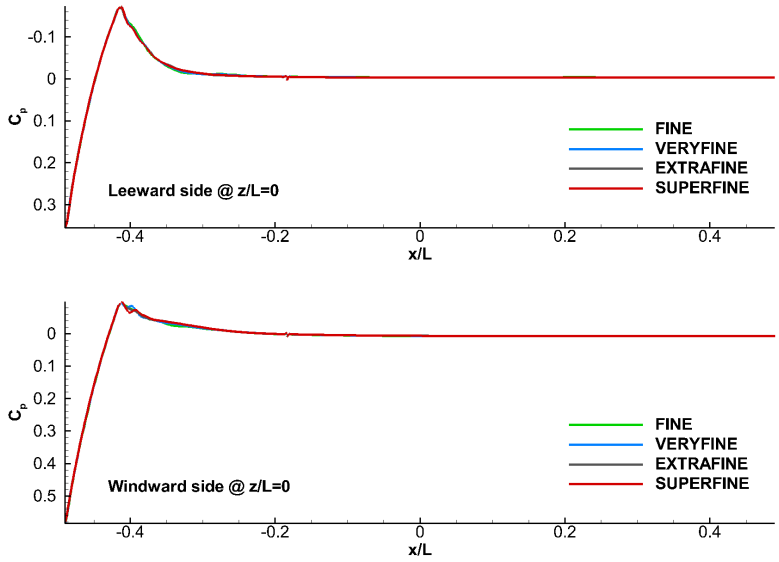

Figure C.12: Difference in the pressure coefficient ΔC_p between grids.

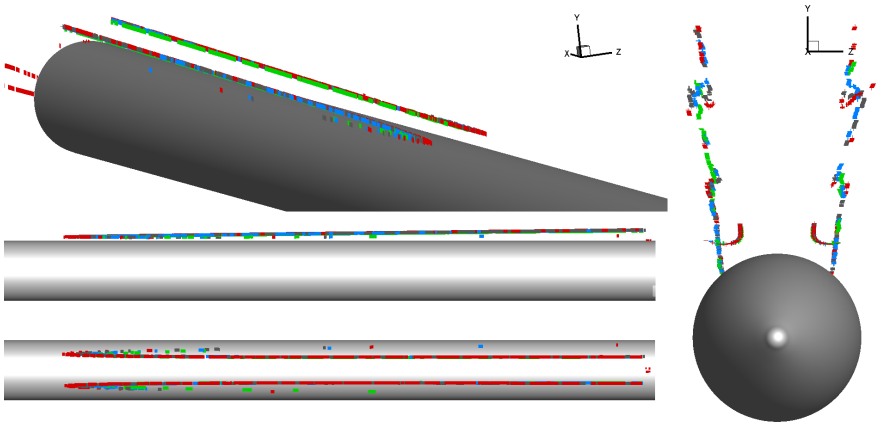

Figure C.13: Vortex trajectories obtained on the fine (green), very fine (blue), extra-fine (red), and super-fine (grey) grids.

The vortex trajectories agreed well between all grids.

C.3.2 High incidence angle calculations

Similar conclusions were drawn from the case at $\sigma = 15$ deg incidence. All coefficients exhibited monotonic behaviour. The change in the pitching moment coefficient between the extra-fine and super-fine grids was again slightly larger than the change between the very fine and extra-fine grids. The surface pressure contours and the vortex trajectories agreed well between the grids.

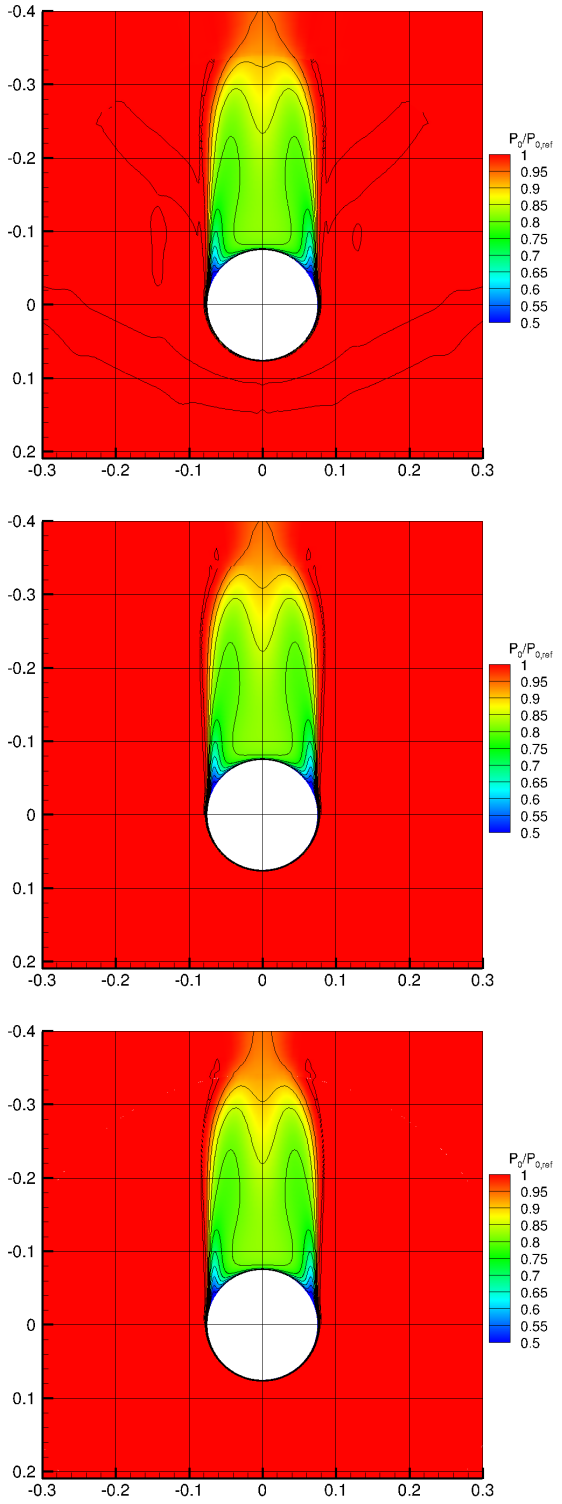

Figure C.14: Stagnation pressure for the $k-\omega$ SST model on the very fine (top), extra-fine (middle), and super-fine (bottom) grids at $x/d_{ref} = 21.5$.

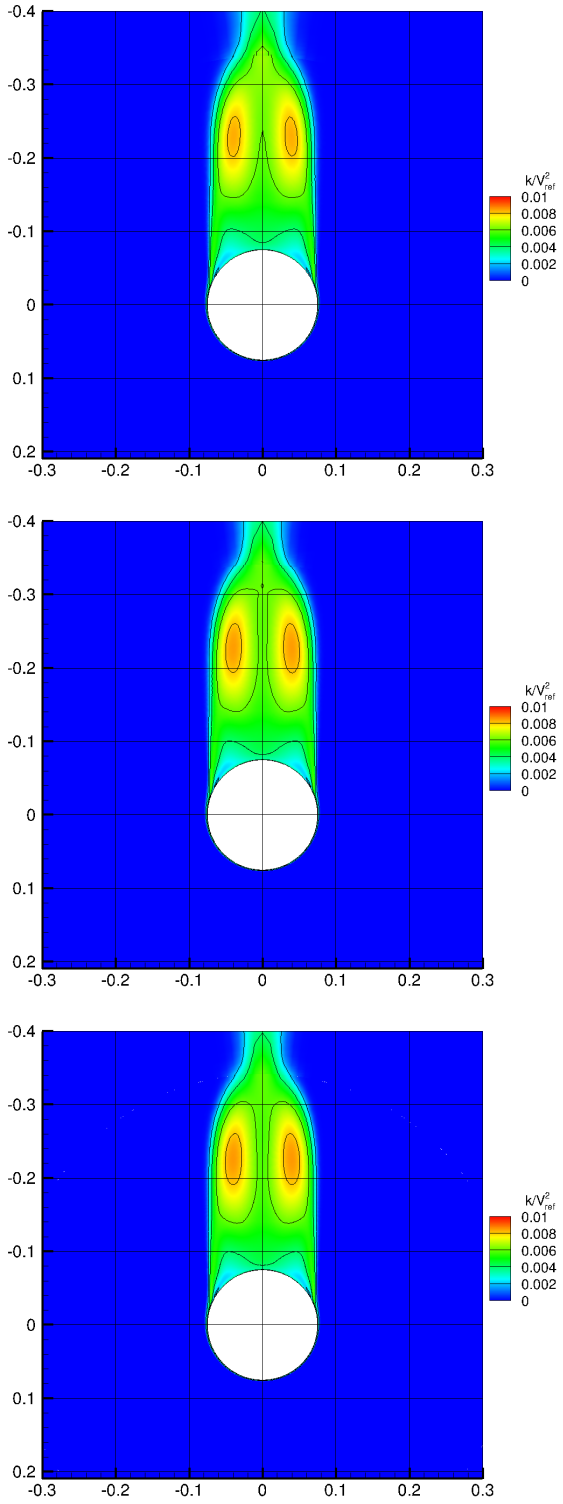

Figure C.15: Turbulent kinetic energy contours for the $k-\omega$ SST model on the very fine (top), extra-fine (middle), and super-fine (bottom) grids at $x/d_{ref} = 21.5$.

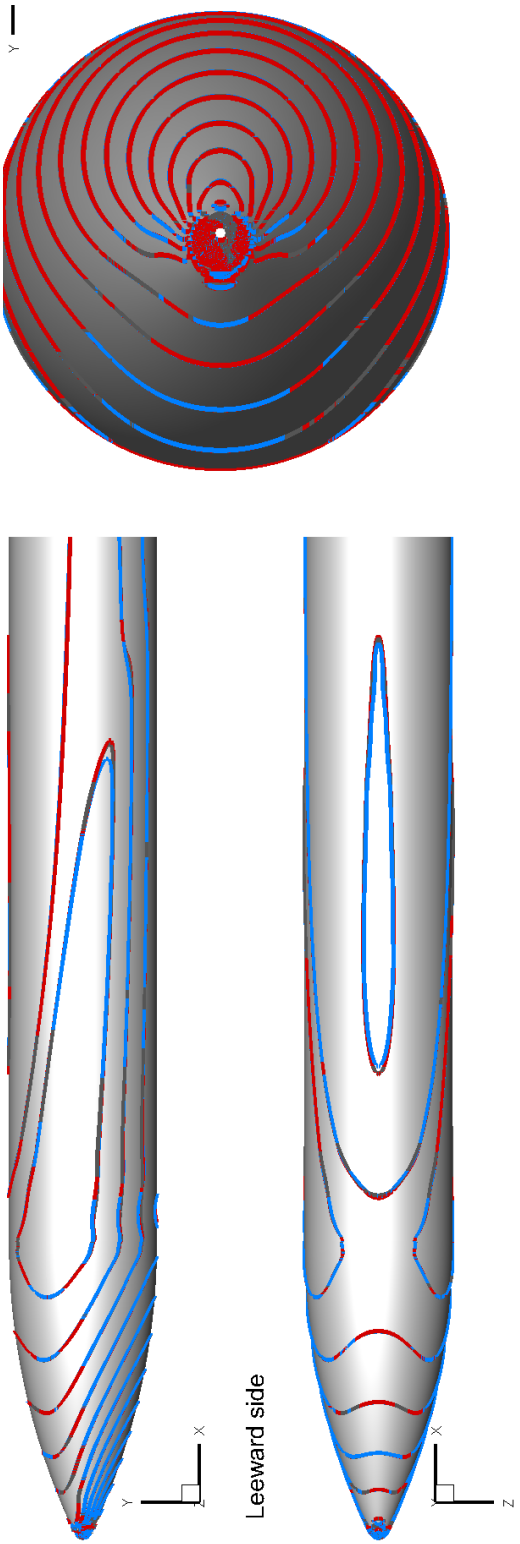

Figure C.16: Surface pressure contours for the $k-\omega$ SST model on the fine (green) very fine (blue), extra-fine (grey), and super-fine (red) grids.

Figures C.14 and C.15 show the stagnation pressure p_0/p_{ref} and the turbulent kinetic energy k/V_{ref}^2 contours at the $x/d_{ref} = 21.5$ streamwise location (base). The vortex trajectory and surface pressure contours comparison is shown in figures C.17 and C.16.

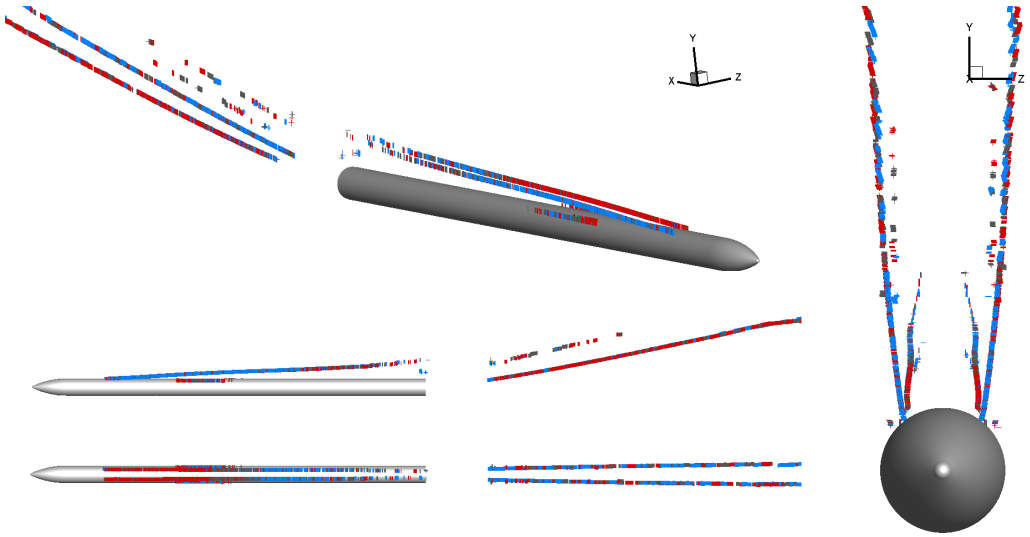

Figure C.17: Vortex trajectories obtained on the fine (green), very fine (blue), extra-fine (red), and super-fine (grey) grids.

C.3.3 Effect of non-linear models

The effect of the $k-\omega$ EARSM and the $k-\omega$ SST QCR V1 models on the loads was investigated. The $k-\omega$ EARSM simulation was restarted from the $k-\omega$ SST simulation and run for additional 70000 iterations. The large number of iterations was necessary for the loads to settle. The largest difference was in the C_X coefficient - approximately 13.4% relative to the $k-\omega$ SST simulation. The differences in C_Z and C_m were approximately 4.6% and 6.3%. Figures C.18 and C.18 show a side by side comparison of the stagnation pressure contours predicted by the $k-\omega$ SST and $k-\omega$ EARSM models. The linear $k-\omega$ SST model predicts higher values for μ_t/μ which reduces unsteadiness in the flow and results in fewer vortical structures. The $k-\omega$ EARSM model, which considers higher-order strain and rotation terms, reduces the μ_t/μ values and results in more pronounced vortical structures with more laminar cores. Unlike the $k-\omega$ SST model, the values of k/V_{ref}^2 at the vortex cores are small. The $k-\omega$ SST QCR V1 was tested only on the extra-fine grid. No significant differences in the loads or in the flow topology were observed when compared to the $k-\omega$ SST . Differences between the two models are expected to occur with the inclusion of wings and/or fins as the right angles between the fins and/or wings and the body give rise to secondary flows which will be accounted for by the $k-\omega$ SST QCR V1 model only.

C.3.4 Unsteady simulations

Unsteady RANS simulations of the body at $\sigma = 15$ degrees were also performed to identify unsteadiness if any. A non-dimensional time step of $\Delta t = 0.01$ was used which corresponded to a dimensional time step of 7.24×10^{-5} s based on L_{ref} and 3.15×10^{-6} s based on d_{ref}. A total of 6 flow travel times were simulated where 1 flow travel time was the time it took the flow to travel the length of the body. Averaging was performed over different intervals, however, no significant differences in the aerodynamic coefficients were observed as long as the first travel time was discarded during the averaging. No significant differences in the aerodynamic coefficients were observed. Table C.4 lists the averaged aerodynamic coefficients.

Table C.4: Unsteady simulations parameters.

C_X	C_Z	C_m	Averaging interval
-0.690	-1.651	7.574	2t-6t
-0.690	-1.651	7.574	3t-6t
-0.690	-1.651	7.574	4t-6t
-0.690	-1.651	7.574	5t-6t
-0.690	-1.652	7.563	RANS

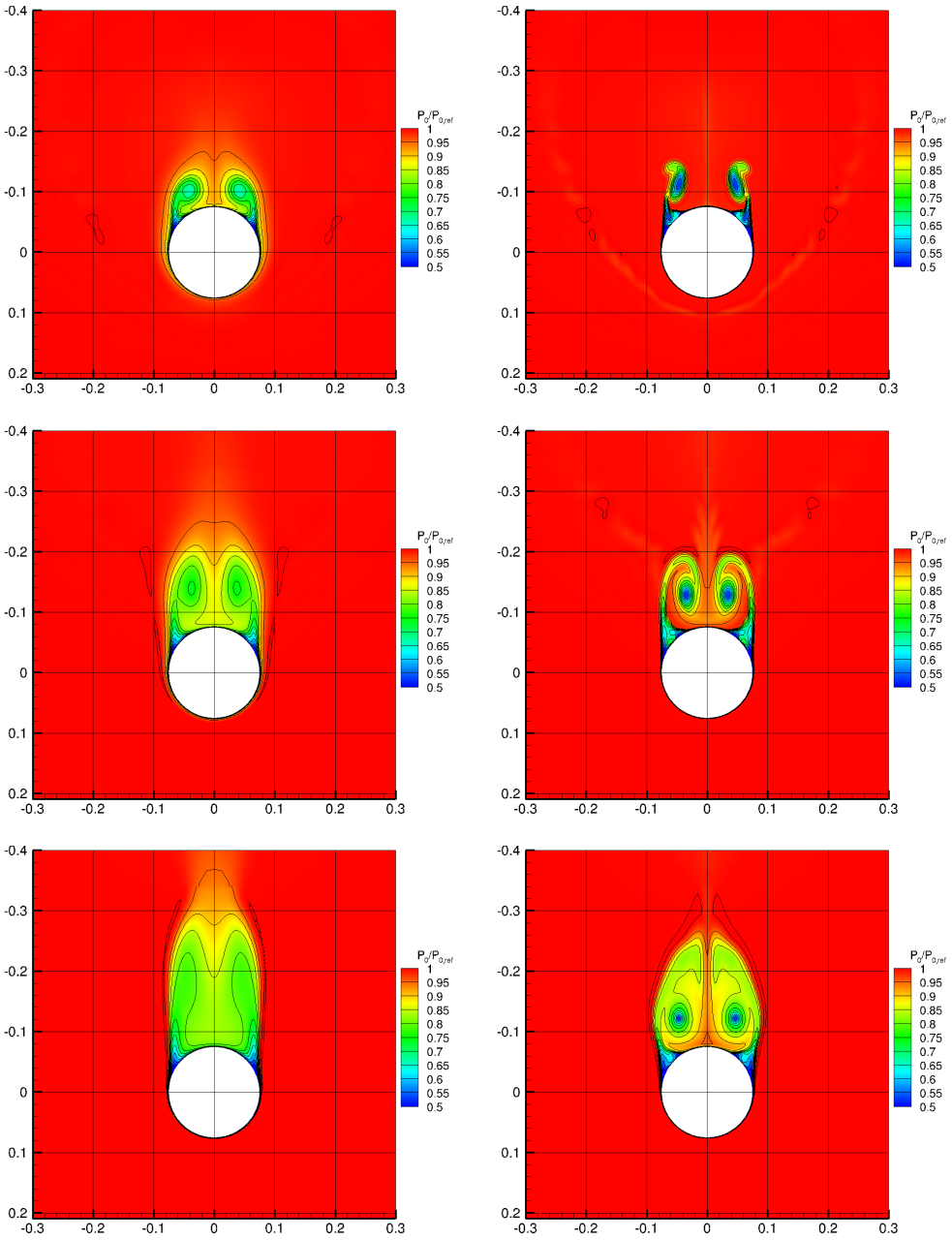

Figure C.18: Stagnation pressure contours for the $k-\omega$ SST model (left) and the $k-\omega$ EARSM model (right) at $x/d_{ref} = 7.5$, $x/d_{ref} = 12.5$, and $x/d_{ref} = 19$.

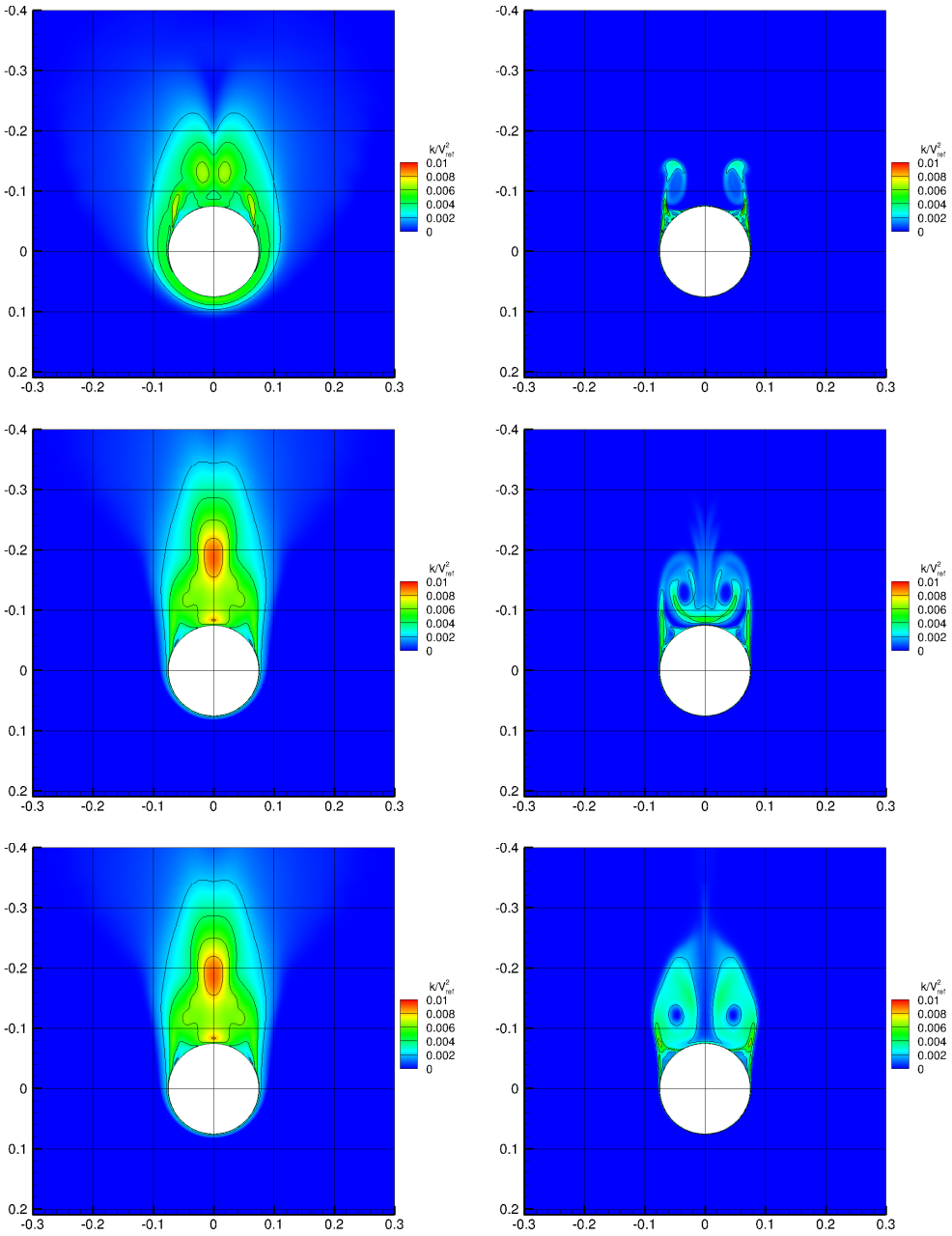

Figure C.19: Turbulent kinetic energy contours for the $k-\omega$ SST model (left) and the $k-\omega$ EARSM model (right) at $x/d_{ref} = 7.5$, $x/d_{ref} = 12.5$, and $x/d_{ref} = 19$.

C.4 Summary of Results

The simulations of the missile (store) body (without any fins or wings) showed that RANS can successfully give grid converged results for a more simplified geometry at small and large incidence angles. There are still uncertainties such as the position at which the nose vortices form, which may be the cause for the larger difference in C_m between the last two grids. The important aerodynamic coefficients for this problem - C_X, C_Z, and C_m showed monotonic behaviour, which was not the case for the full missile at a large incidence angle and non-zero roll angle [134]. There is also uncertainty for the free-stream values of k and ω (not specified for this case). This uncertainty may affect the results but the sensitivity of the solution to the free-stream TKE was not investigated and is believed to be small. Further work will focus on RANS and scale-resolving simulations of the store body with wings. Detailed investigation of the iterative convergence and the integrated loads will be performed component by component to determine whether the lack of convergence for the full store is caused by the complex interaction between the vortices and the fins. This work is carried out as a part of the NATO AVT-316 activity [3].

```
clear all;
close all;
clc;
%  --- VERIFY: Performs verification calculations ---
%
%  Number of data sets read =  3
%
%       Grid Size      Quantity
%
%       1.000000       0.970500
%       2.000000       0.968540
%       4.000000       0.961780
%
%  Order of convergence using first three finest grid
%  and assuming constant grid refinement (Eqn. 5.10.6.1)
%  Order of Convergence, p =  1.78618479
%
%  Richardson Extrapolation: Use above order of convergence
%  and first and second finest grids (Eqn. 5.4.1)
%  Estimate to zero grid value, f_exact =  0.971300304
%
%  Grid Convergence Index on fine grids. Uses p from above.
%  Factor of Safety =  1.25
%
%    Grid      Refinement
```

```
26 %     Step        Ratio, r        GCI(%)
27 %     1  2        2.000000        0.103080
28 %     2  3        2.000000        0.356244
29 %
30 %  Checking for asymptotic range using Eqn. 5.10.5.2.
31 %  A ratio of 1.0 indicates asymptotic range.
32 %
33 %    Grid Range     Ratio
34 %    12 23        0.997980
35 %
36 %  --- End of VERIFY ---
37 h(1)=1;
38 h(2)=2;
39 h(3)=4;
40 %f(1)=0.970300; - this values is for testing and shows that a smaller
41 %difference between f(1) and f(2) will reduce the GCI and improve the
42 %convergence and the observed order of the solution
43 f(1)=0.970500;
44 f(2)=0.968540;
45 f(3)=0.961780;
46 for i=1:(length(h)-1)
47     r(i)=h(i+1)/h(i);
48 end
49 r12=r(1);
50 r23=r(2);
51 p_old=0.0;
52 p=1.0;
53 omega=0.5;
54 while abs(p-p_old) > 1e-6
55     p_old=p;
56     eps23=f(3)-f(2);
57     eps12=f(2)-f(1);
58     beta=((r12^p-1)*eps23)/((r23^p-1)*eps12);
59     p=omega*p+(1-omega)*log(beta)/log(r12);
60 end
61 fprintf('\nOrder of convergence using first three finest grid \nand
       assuming non-constant grid refinement.\n');
62 fprintf('Order of Convergence, p = %0.6f\n',p);
63 f_exact=f(1)+(f(1)-f(2))/(r(1)^p-1.0);
64 fprintf('\nRichardson Extrapolation: Use above order of convergence \nand
       first and second grids\n');
65 fprintf('Estimate to zero grid value, f_exact = %0.6f\n',f_exact);
66 fs=1.25;
67 fprintf('\nGrid Convergence Index on fine grids. Uses p from above.\n');
```

```
68 fprintf('Factor of Safety = %0.2f\n\n',fs);
69 fprintf('Grid \t Refinement\nStep \t Ratio,r \t GCI(%%)\n');
70 for i=1:(length(h)-1)
71     gci(i)=fs*abs(((f(i+1)-f(i))/f(i))/(r(i)^p-1.0));
72     fprintf('%i %i \t %0.4f \t %0.4f \n',i,i+1,r(i),gci(i)*100);
73 end
74 fprintf('\nChecking for asymptotic range\nA ratio of 1.0 indicates
       asymptotic range.\n');
75 fprintf('Grid Range \t Ratio\n\n');
76 for i=1:(length(h)-2)
77     ratio=r(i)^p*gci(i)/gci(i+1);
78     fprintf('%i%i %i%i \t %0.4f\n',i,i+1,i+1,i+2,ratio);
79 end
80 h_extr=[0,h(1)];
81 f_extr=[f_exact,f(1)];
82 figure(1);
83 hold on;
84 plot(h,f,'Color',[0,0,1]);
85 plot(h_extr,f_extr,'Color',[1,0,0]);
86 grid on;
87 xlabel('h');
88 ylabel('f(h)');
```

Appendix D

Fore-body intake geometry drawings

This section shows more detailed drawings of the three fore-body intake geometries investigated in chapter 5. All dimensions are in meters. The only difference between the three geometries is the cross-sectional shape of the intake.

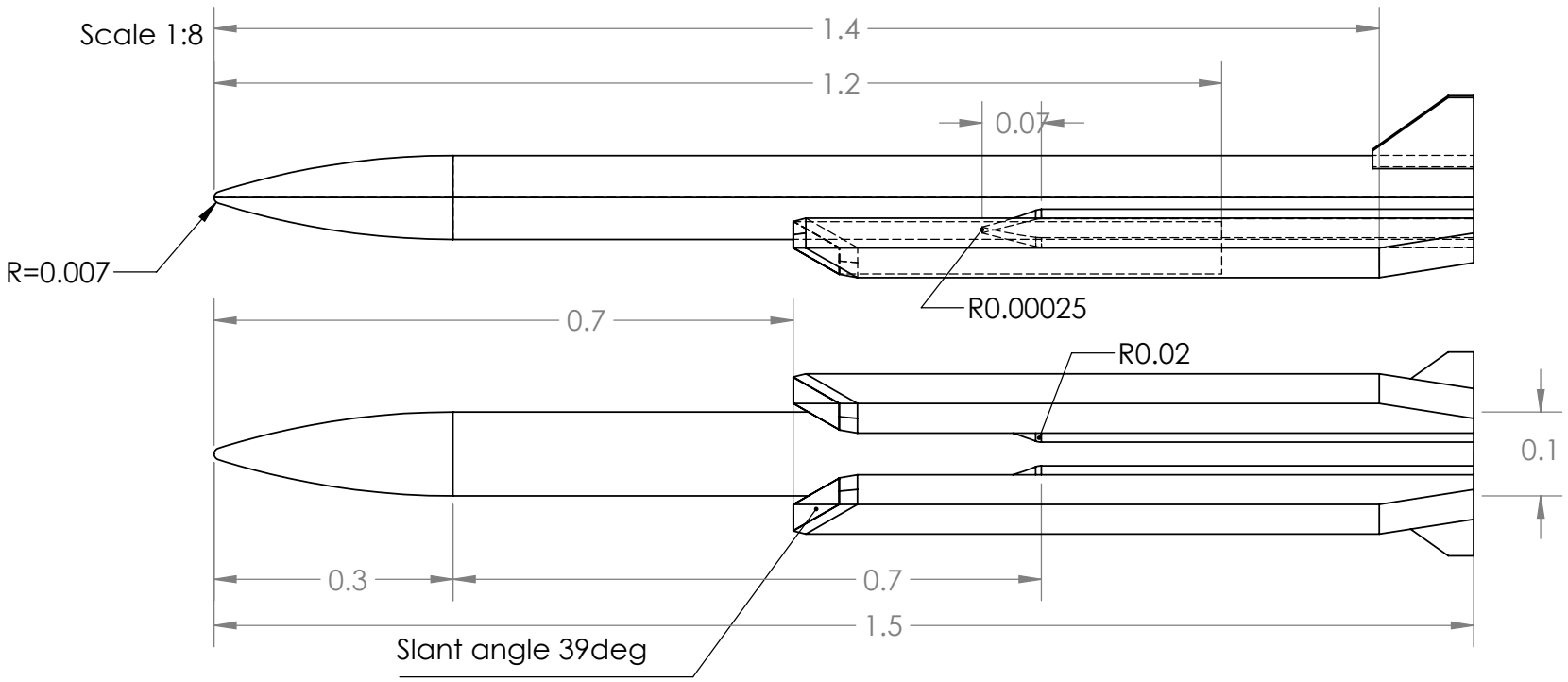

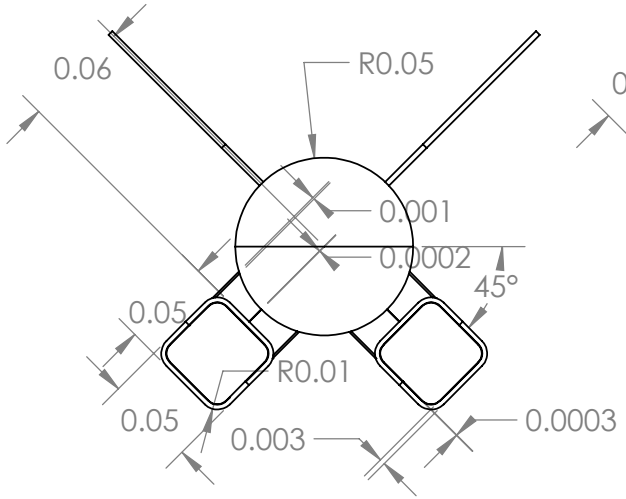

Scale 1:4

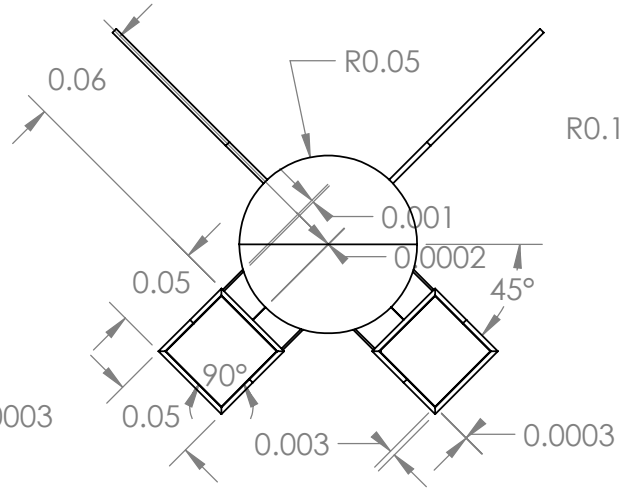

Scale 1:4

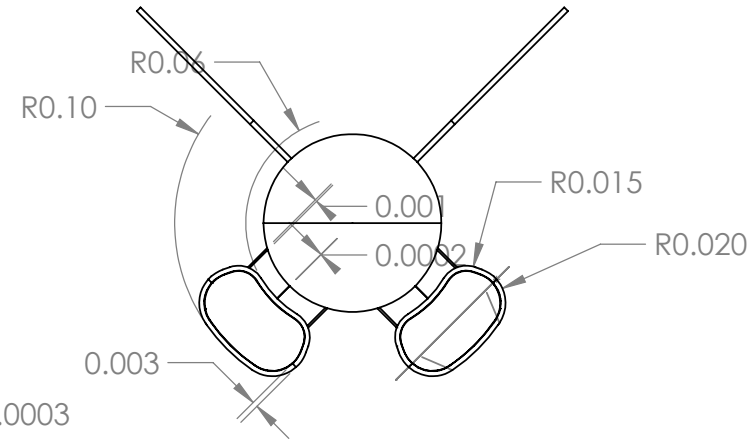

Scale 1:4

Dimensions are in meters.

Bibliography

[1] ANSYS ICEM CFD HEXA. url: https://www.ansys.com/products/fluids.

[2] NASA Langley Research Center. Turbulence Modeling Resource. url: https://turbmodels.larc.nasa.gov.

[3] Vortex Interaction Effects Relevant to Military Air Vehicle Performance. url: https://www.sto.nato.int/lists/test1/activitydetails.aspx?id=16476.

[4] J.D. Anderson. *Modern Compressible Flow: With Historical Perspective*. McGraw-Hill, Second edition, 1990.

[5] T. Arai, H. Sugiyama, and T. Kawase. COMPRESSIBLE TURBULENT BOUNDARY LAYER/MULTIPLE SHOCK WAVE INTERACTION IN A DUCT. In *Space Plane and Hypersonic Systems and Technology Conference*, 1996.

[6] S. Arvidson, S.H. Peng, and L. Davidson. Feasibility of Hybrid RANS-LES Modelling of Shock/Boundary-Layer Interaction in a Duct. In *Progress in Hybrid RANS-LES Modelling, Notes on Numerical Fluid Mechanics and Multidisciplinary Design*, 2012.

[7] C.J. Atkin and L.C. Squire. Study of the interaction of a normal shock wave with a turbulent boundary layer at mach numbers between 1.30 and 1.55. *European Journal of Mechanics - B/Fluids*, 11(1):93–118, 1992.

[8] O. Axelsson. *Iterative Solution Methods*. Cambridge University Press, 1994.

[9] H. Babinsky and J.K. Harvey. *Shock Wave-Boundary-Layer Interactions*. Cambridge University Press, 2011.

[10] B. Baldwin and H. Lomax. THIN-LAYER APPROXIMATION AND ALGEBRAIC MODEL FOR SEPARATED TURBULENT FLOWS. In *16th Aerospace Sciences Meeting*, 1978.

[11] G. Barakos and D. Drikakis. Investigation of Nonlinear Eddy-viscosity Turbulence Models in Shock/Boundary-Layer Interaction. *AIAA Journal*, 38(3):461–469, 2000.

[12] G.N. Barakos, R. Steijl, K. Badcock, and A. Brocklehurst. Development of CFD Capability for Full Helicopter Engineering Analysis. In *Proceedings of the 31st European Rotorcraft Forum*, 2005.

[13] P. Batten, U. Goldberg, and S. Chakravarthy. LNS - AN APPROAHC TOWARDS EMBEDDED LES. In *40th AIAA Aerospace Sciences Meeting & Exhibit*, 2002.

[14] F.S. Billig. Research on Supersonic Combustion. *Journal of Propulsion and Power*, 9(4):499–514, 1993.

[15] E. Blosch, B.F. Carroll, and M.J. Morris. Numerical Simulation of Confined Transonic Normal Shock Wave/Turbulent Boundary-Layer Interactions. *AIAA Journal*, 31(12):2241–2246, 1993.

[16] P.J.K Bruce, D. Burton, N. Titchener, and Babinsky H. Corner effect and separation in transonic channel flows. *Journal of Fluid Mechanics*, 679:247–262, 2011.

[17] P.J.K Bruce and Babinsky H. Unsteady shock wave dynamics. *Journal of Fluid Mechanics*, 603:463–473, 2008.

[18] P.J.K Bruce and Babinsky H. An experimental study of transonic shock/boundary layer interactions subject to downstream pressure perturbations. *Aerospace Science and Technology*, 14(1):134–142, 2010.

[19] P.J.K Bruce, Babinsky H., B. Tartinville, and C. Hirsch. Corner Effect and Asymmetry in Transonic Channel Flows. *AIAA Journal*, 49(11):2382–2392, 2011.

[20] P.J.K Bruce, Babinsky H., B. Tartinville, and C. Hirsch. Experimental and Numerical Study of Oscillating Transonic Shock Waves in Ducts. *AIAA Journal*, 49(8):1710–1720, 2011.

[21] R. Bur, R. Benay, and G.P. Berthouze. Experimental and numerical study if forced shock-wave oscillations in a transonic channel. *Aerospace Science and Technology*, 10(1):265–278, 2006.

[22] D.M.F. Burton and Babinsky H. Corner separation effects for normal shock wave/turbulent boundary layer interactions in rectangular channels. *Journal of Fluid Mechanics*, 707:287–306, 2012.

[23] B.F. Carroll. *Numerical and Experimental Investigation of Multiple Shock Wave/Turbulent Boundary Layer Interactions in a Rectangular Duct*. PhD thesis, University of Illinois at Urbana-Champaign, 1988.

[24] B.F. Carroll and J.C. Dutton. AN LDV INVESTIGATION OF A MULTIPLE NORMAL SHOCK WAVE/TURBULENT BOUNDARY LAYER INTERACTION. In *27th Aerospace Sciences Meeting*, 1989.

[25] B.F. Carroll and J.C. Dutton. Characteristics of Multiple Shock Wave/Turbulent Boundary-Layer Interactions in Rectangular Ducts. *Journal of Propulsion and Power*, 6(2):186–193, 1990.

[26] B.F. Carroll and J.C. Dutton. Multiple Normal Shock Wave/Turbulent Boundary-Layer Interactions. *Journal of Propulsion and Power*, 8(2):441–448, 1992.

[27] B.F. Carroll, P.A. Lopez-Fernandez, and J.C. Dutton. Computations and Experiments for a Multiple Normal Shock/Boundary-Layer Interaction. *Journal of Propulsion and Power*, 9(3):405–411, 1993.

[28] R.M. Chriss, W.R. Hingst, A.J. Strazisar, and T.G. Keith. AN LDA INVESTIGATION OF THREEDIMENSIONAL NORMAL SHOCK WAVE BOUNDARY-LAYER INTERACTION. In *Transonic Symposium: Theory, Application and Experiment*, 1983.

[29] L. Crocco. Sulla trasmissione del calore da una lamina piana a un fluido scorrente ad alta velocita. *L'Aerotecnica*, 12:181–197, 1932.

[30] L. Crocco. ONE-DIMENSIONAL TREATMENT OF STEADY GAS DYNAMICS. In H.W. Emmons, editor, *Fundamentals of gas dynamics*, pages 110–130. Princeton University Press, 2016.

[31] O. Daisuke, T. Handa, and M. Masuda. Three-Dimensional Normal Shock-Wave/Boundary-Layer Interaction in a Diffuser. *Journal of Fluids Engineering*, 135(4), 2013.

[32] S. Deck, N. Renard, R. Laraufie, and P. Sagaut. Zonal detached eddy simulation (ZDES) of a spatially developing flat plate turbulent boundary layer over the reynolds number range $3150 \leq Re_\theta \leq 14000$. *Physics of Fluids*, 26(2):1–32, 2014.

[33] J. Delery. SHOCK WAVE PHENOMENA IN HIGH SPEED FLOWS: STILL A PROBLEM OF MAJOR CONCERN FOR AERODYNAMICISTS! In *E.R.C.O.F.T.A.C. Workshop on Shock/Boundary Layer Interaction*, 1997.

[34] J. Delery and J.P. Dussauge. Some physical aspects of shock wave/boundary layer interactions. *Shock Waves*, 19(1):453–468, 2009.

[35] J.M. Delery. INVESTIGATION OF STRONG SHOCK TURBULENT BOUNDARY LAYER INTERACTION IN 2D TRANSONIC FLOWS WITH EMPHASIS ON TURBULENCE PHENOMENA. In *14th Fluid and Plasma Dynamics Conference*, 1981.

[36] J.M. Delery. Experimental Investigation of Turbulence Properties in Transonic Shock/Boundary-Layer Interactions. *AIAA Journal*, 21(2):180–185, 1983.

[37] J.M. Delery. SHOCK WAVE/TURBULENT BOUNDARY LAYER INTERACTION AND ITS CONTROL. *Progress in Aerospace Sciences*, 22:209–280, 1985.

[38] Burton D.M.F., H. Babinsky, and P.J.K. Bruce. Experimental Investigation into Parameters Governing Corner Interactions for Transonic Shock Wave/Boundary Layer Interactions. In *48th AIAA Aerospace Sciences Meeting Including the New Horizons Forum and Aerospace Exposition*, 2010.

[39] P. Doerffer, C. Hirsch, J.P. Dussauge, H. Babinsky, and Barakos G.N. Unsteady Effects of Shock Wave Induced Separation. In *Notes on Numerical Fluid Mechanics and Multidisciplinary Design*, 2011.

[40] P. Doerffer, O. Szulc, and F. Magagnato. Shock Wave-Boundary Layer Interaction in Forced Shock Oscillations. *Journal of Thermal Science*, 12(1):10–15, 2003.

[41] P. Doerffer, O. Szulc, and F. Magagnato. UNSTEADY SHOCK WAVE - TURBULENT BOUNDARY LAYER INTERACTION IN THE LAVAL NOZZLE. *TASK QUARTERLY*, 9(1):115–132, 2004.

[42] P. Dupont, C. Haddad, J.P. Ardissone, and J.F. Debiéve. Space and time organisation of a shock wave/turbulent boundary layer interaction. *Aerospace Science and Technology*, 9(1):561–572, 2005.

[43] P.A. Durbin. Near-Wall Turbulence Closure Modeling Without âĂIJDamping FunctionsâĂİ. *Theoretical and COmputational Fluid Dynamics*, 3(1):1–13, 1991.

[44] L.M. Edelman and Gamba M. Structure of a Mach 2 Shock Train from Experimental Measurements. In *AIAA SciTech Forum*, 2020.

[45] B. Edney. ANOMALOUS HEAT TRANSFER AND PRESSURE DISTRIBUTIONS ON BLUNT BODIES AT HYPERSONIC SPEEDS IN THE PRESENCE OF AN IMPINGING SHOCK. Technical report, Aeronautical Research Institute Sweden, 1968.

[46] J.R. Edwards, J.-I. Choi, and J.A. Boles. Hybrid LES/RANS Simulation of a Mach 5 Compression-Corner Interaction. In *46th AIAA Aerospace Sciences Meeting and Exhibit*, 2008.

[47] Y. Egorov and F. Menter. Development and Application of SST-SAS Turbulence Model in the DESIDER Project. In *Advances in Hybrid RANS-LES Modelling*, 2008.

[48] R. Fiévet, H. Koo, and V. Raman. Numerical Investigation of Shock-Train Response to Inflow Boundary-Layer Variations. *AIAA Journal*, 55(9):2888–2900, 2017.

[49] R. Fiévet, H. Koo, and V. Raman. Numerical simulation of shock trains in a 3D channel. *AIAA Journal*, 55(9):2888–2900, 2017.

[50] C. Fischer and H. Olivier. Experimental Investigation of the Internal Flow Field of a Scramjet Engine. *AIAA Journal*, 2009.

[51] T. Gawehn, A. Gulham, and N.S. Al-Hasan. Experimental and numerical analysis of the structure of pseudo-shock ststems in laval nozzles with parallel side walls. *Shock Waves*, 20(4):297–306, 2010.

[52] J. Geerts and K.H. Yu. Corner Flow Separation from Shock Train/Turbulent Boundary-Layer Interactions in Rectangular Isolators. In *20th AIAA International Space Planes and Hypersonic Systems and Technologies Conference*, 2015.

[53] J. Geerts and K.H. Yu. Shock Train/Boundary-layer Interaction in Rectangular Isolators. *AIAA Journal*, 54(11):3450–3464, 2016.

[54] J. Geerts and K.H. Yu. Three-Dimensional Nature of Shock Trains in Rectangular Scramjet Isolators. In *54th AIAA Aerospace Sciences Meeting*, 2016.

[55] F.B. Gessner. Experiments on Supersonic Turbulent Flow Development in a Square Duct. *AIAA Journal*, 25(5):690–697, 1978.

[56] M. Giglmaier, J.F. Quaatz, T. Gawehn, A. Gulhan, and N.A. Adams. Numerical and experimental investigations of pseudo-shock systems in a planar nozzle: impact of bypass mass flow due to narrow gaps. *Shock Waves*, 2014.

[57] F. Gnani, F. Zare-Behtash, and K. Kontis. Pseudo-shock waves and their interactions in high-speed intakes. *Progress in Aerospace Sciences*, 82:36–56, 2016.

[58] F. Gnani, F. Zare-Behtash, and K. Kontis. Effect of back-pressure forcing on shock train structures in rectangular channels. *Acta Astronautica*, 145:471–481, 2018.

[59] E.L. Goldsmith and J.M. Seddon. *Practical Intake Aerodynamic Design (AIAA Education Series)*. American Institution of Aeronautics and Astronautics, First edition, 1993.

[60] M.S. Gritskevich, A.V. Garbaruk, J. Schultze, and F.R. Menter. Development of DDES and IDDES formulations for the $k-\omega$ Shear Stress Transport Model. *Flow, Turbulence and Combustion*, 88:431–449, 2012.

[61] Y. Han, G. Ding, Y. He, J. Wu, and J. Le. Assessment of the IDDES method acting as wall-modeled LES in the simulation of spatially developing supersonic flat plate boundary layers. *Engineering Applications of Computational Fluid Mechancis*, 12(1):89–103, 2018.

[62] T. Handa and M. Masuda. Three-Dimensional Normal Shock-Wave/Boundary-Layer Interaction in a Rectangular Duct. *AIAA Journal*, 43(10):2182–2187, 2005.

[63] W.H. Heiser and D.T. Pratt. *Hypersonic Airbreathing Propulsion*. American Institute of Aeronautics and Astronautics, 1994.

[64] A. Hellsten. New Advanced $k-\omega$ Turbulence Model for High-Lift Aerodynamics. *AIAA Journal*, 43(9):1857–1869, 2005.

[65] T. Herges, G. Elliott, C. Dutton, and Y. Lee. Micro-Vortex Generators and Recirculating Flow Control of Normal Shock Stability and Position Sensitivity. In *48th AIAA Aerospace Sciences Meeting Including the New Horizons Forum and Aerospace Exposition*, 2010.

[66] H.A. Holden and H. Babinsky. SHOCK / BOUNDARY LAYER INTERACTION CONTROL USING 3D DEVICES. In *41st Aerospace Sciences Meeting and Exhibit*, 2003.

[67] H.A. Holden and H. Babinsky. Effect of Microvortex Generators on Separated Normal Shock/Boundary Layer Interactions. *Journal of Aircraft*, 44(1):170–174, 2007.

[68] P.G. Huang. Van Driest Transformation and Compressible Wall-Bounded Flows. *AIAA Journal*, 32(10), 1994.

[69] W. Huang, Z-G. Wang, M. Pourkashanian, L. Ma, D.B. Ingham, S-B. Luo, L. Jing, and L. Jun. Numerical investigation on the shock wave transition in a three-dimensional scramjet isolator. *Acta Aeronautica*, 68(1):1669–1675, 2011.

[70] R.L. Hunt, J.F. Driscoll, and M. Gamba. Periodic forcing of a shock train in Mach 2.0 flow. In *55th AIAA Aerospace Sciences Meeting*, 2017.

[71] R.L. Hunt and M. Gamba. On the origin and propagation of perturbations that cause shock train inherent unsteadiness. *Journal of Fluid Mechanics*, 861(1):815–859, 2018.

[72] T. Ikui, K. Matsuo, and M. Nagai. The Mechanism of Pseudo-Shock Waves. *Bulletin of JSME*, 17(108):731–739, 1974.

[73] T. Ikui, K. Matsuo, and K. Sasaguchi. Modified Diffusion Model of Pseudo-Shock Waves Considering Upstream Boundary Layers. *Bulletin JSME*, 24(197):1920–1927, 1981.

[74] N. Jarrin, D. Laurance, S. Benhamadouche, and R. Prosser. A synthetic-eddy-method for generating inflow conditions for large-eddy simulation. *International Journal of Heat and Fluid Flow*, 27(4):585–593, 2006.

[75] M. Jarwowsky, M.A. Woodgate, G. Barakos, and J. Rokicki. TOWARDS CONSISTENT HYBRID OVERSET MESH METHODS FOR ROTORCRAFT CFD. *International Journal for Numerical Methods in Fluids*, 74(8):543âĂŞ576, 2014.

[76] A. Kantrowitz and C. Donaldson. Preliminary Investigation of Supersonic Diffusers. Technical Report NACA-WR-L-713, Langley Memorial Aeronautical Laboratory, 1945.

[77] R. Klomparens, J. Driscoll, and M. Gamba. Unsteadiness characteristics and pressure distribution of an oblique shock train. In *53rd AIAA Aerospace Sciences Meeting, AIAA SciTech Forum 2015*, 2015.

[78] R. Klomparens, J. Driscoll, and M. Gamba. Response of a shock train to downstream back pressure forcing. In *54th AIAA Aerospace Sciences Meeting*, 2016.

[79] J.W. Kooi. Influence of free-stream mach number on transonic shock-wave boundary-layer interaction. Technical Report 78013, National Aerospace Laboratories, 1978.

[80] T.S. Lund, X. Wu, and K.D. Squires. Generation of Turbulent Inflow Data for Spatially-Developing Boundary Layer Simulations. *Journal of Computational Physics*, 140(2):233–258, 1998.

[81] J.J. Mahoney. *Inlets for Supersonic Missiles (AIAA Education Series)*. American Institute of Aeronautics and Astronautics, First edition, 1990.

[82] M. Mani, D.A. Babcock, C.M. Winkler, and P.R. Spalart. Predictions of a Supersonic Turbulent Flow in a Square Duct. In *AIAA Aerospace Sciences Meeting including the New Horizons Forum and Aerospace Exposition*, 2013.

[83] K. Matsuo, Miyazato Y., and H.-D. Kim. Shock train and pseudo-shock phenomena in internal gas flows. *Progress in Aerospace Sciences*, 35:33–100, 1999.

[84] J.D. Mattingly, W.H. Heiser, and D.H. Daley. *Aircraft Engine Design (AIAA Education Series)*. American Institute of Aeronautics and Astronautics, second edition, 2002.

[85] F. Menter. Eddy Viscosity Transport Equations and Their Relation to the $k-\varepsilon$ model. *ASME Journal of Fluid Engineering*, 119:876–884, 1997.

[86] F.R. Menter. Two-Equation Eddy-viscosity Turbulence Models for Engineering Applications. *AIAA Journal*, 32(8):1598–1605, 1993.

[87] F.R. Menter and Y. Egorov. The Scale-Adaptive Simulation Method for Unsteady Turbulent Flow Predictions. Part 1: Theory and Model Description. *Flow, Turbulence and Combustion*, 85(1):113–138, 2010.

[88] F.R. Menter, Y. Egorov, R. Lechner, and D. Cokljat. The Scale-Adaptive Simulation Method for Unsteady Turbulent Flow Predictions. Part 2: Application to Complex Flows. *Flow, Turbulence and Combustion*, 85(1):139–165, 2010.

[89] F.R. Menter, M. Kuntz, and Bender. R. A Scale-Adaptive Simulation Model for Turbulent Flow Predictions. In *Proceedings of the 41th AIAA Aerospace Sciences Meeting and Exhibit*, 2003.

[90] Boussinesq M.J. *Théorie de l'Écoulement Tourbillonant et Tumultueux des Liquides dans des Lits Rectilignes à Grande Section, Tome I-II (Theory of the swirling and turbulent flow of liquids in straight channels of large section, Volume I-II)*. Gaulthier-Villars, First edition, 1989.

[91] R. Morajkar and M. Gamba. Turbulence characteristics of supersonic corner flows in a low aspect ratio rectangular channel. In *54th AIAA Aerospace Sciences Meeting*, 2016.

[92] R.R. Morajkar, J.F. Driscoll, and M. Gamba. Experimental study of supersonic turbulent corner flow evolution in a low aspect ratio rectangular channel. In *53rd AIAA Aerospace Sciences Meeting*, 2015.

[93] B. Morgan, K. Duraisamy, and Lele S.K. Large-Eddy and RANS Simulations of a Normal Shock Train in a Constant-Area Isolator. In *50th AIAA Aerospace Sciences Meeting including the New Horizons Forum and Aerospace Exposition*, 2012.

[94] B. Morgan, J. Larsson, S. Kawai, and Lele S. K. Large-Eddy Simulations of a Normal Shock Train in a Constant-Area Isolator. *AIAA Journal*, 52(3):539–558, 2014.

[95] S.M. Mousavi, R. Kamali, F. Sotoudeh, N. Karimi, and D. Khojasteh. Large eddy simulation of pseudo shock structure in a convergentâĂŞlong divergent duct. *Computers and Mathematics with Applications*, 2019.

[96] A.J. Musker. Explicit Expression for the Smooth Wall Velocity Distribution in a Turbulent Boundary Layer. *AIAA Journal*, 17(6):655–657, 1979.

[97] H. Ogawa and H. Babinsky. Wind-Tunnel Setup for Investigation of Normal Shock Wave/Boundary Layer Interaction Control. *AIAA Journal*, 44(11):2803–2805, 2006.

[98] T. Oka, O. Daisuke, and Y. Miyazato. Study of Shock Trains and Pseudo-Shock Waves in Constant Area Ducts. In *52nd AIAA Aerospace Sciences Meeting*, 2014.

[99] D. Om and M.E. Childs. AN EXPERIMENTAL INVESTIGATION OF MULTIPLE SHOCK WAVE/TURBULENT BOUNDARY LAYER INTERACTIONS IN A CIRCULAR DUCT. In *AIAA 16th Fluid and Plasma Dynamics Conference*, 1983.

[100] S. Osher and S. Chakravarthy. Upwind Schemes and Boundary Conditions with Applications to Euler Equations in General Geometries. *Journal of Computational Physics*, 50(3):447–481, 1983.

[101] S.-H. Peng. Hybrid RANS-LES modeling based on zero- and one-equation models for turbulent flow simulation. In *Proceedings of the 4th Int. Symp. Turb. And Shear Flow Phenomena*, 2005.

[102] S.-H. Peng. Algebraic Hybrid RANS-LES Modelling Applied to Incompressible and Compressible Turbulent Flows. In *Proceedings of the 36th AIAA Fluid Dynamics Conference and Exhibit*, 2006.

[103] S.-H. Peng, L. Davidson, and S. Holmberg. A Modified Low-Reynolds-Number $k-\omega$ Model for Recirculating Flows. *Journal of Fluids Engineering*, 119, 1997.

[104] M. Pizzella, S. Warning, M. Jennerjohn, and M. McQuilling. Numerical Investigation of a Normal Shock Wave Boundary Layer Interaction in a 4.3 Aspect Ratio Test Section. In *54th AIAA Aerospace Sciences Meeting*, 2016.

[105] M. Pizzella, S. Warning, M. Jennerjohn, and M. McQuilling. Shock-Wave/Boundary-Layer Interaction in a Large-Aspect-Ratio Test Section. *AIAA Journal*, 55(9):2919–2928, 2017.

[106] S. B. Pope. *Turbulent Flows*. Cambridge University Press, 2011.

[107] J.F. Quaatz, M. Giglmaier, S. Hickel, and N.A. Adams. Large-eddy simulation of a pseudo-shock system in a Laval nozzle. *International Journal of Heat and Fluid Flow*, 2014.

[108] P. J. Roache. Perspective: A Method for Uniform Reporting of Grid Refinement Studies. *Journal of Fluids Engineering*, 116(3):405–413, 1994.

[109] P. J. Roache. Verification of Codes and Calculations. *AIAA Journal*, 36(5):696–702, 1998.

[110] P. L. Roe. Approximate Riemann Solvers, Parameter Vectors and Difference Schemes. *Journal of Computational Physics*, 43(1):357–372, 1981.

[111] C. Roussel, F. Alizard, and F. Grasso. Turbulence gneration and sensitivity to mean inflow conditions for a supersonic flow in rectangular duct at $M = 1.61$. In *22nd AIAA Computational Fluid Dynamics Conference*, 2015.

[112] S. Roy, K. Subramaniam, and S. Ghosh. Passive Control of Normal-Shock-Wave/Boundary-Layer Interaction using Porous Medium: Computational Study. In *35th AIAA Applied Aerodynamics Conference*, 2017.

[113] K. Sabnis. *Supersonic Corner Flows in Rectangular Channels*. PhD thesis, University of Cambridge, 2020.

[114] M. Sajben, J.F. Donovan, and M.J. Morris. Experimental Investigation of Terminal Shock Sensors for Mixed-Compression Inlets. *Journal of Propulsion and Power*, 8(1):168–174, 1992.

[115] M. Sajben, M. Morris, T. Bogar, and J. Kroutil. Confined Normal-Shock/Turbulent-Boundary-Layer Interaction Followed by an Adverse Pressure Gradient. *AIAA Journal*, 29(12):2115–2123, 1991.

[116] S.R. Sanderson. Gasdynamic wave interaction in two spatial dimensions. *Journal of Fluid Mechanics*, 506(1):187–205, 2004.

[117] J. Seddon. The Flow Produced by Interaction of a Turbulent Boundary Layer with a Normal Shock Wave of Strength Sufficient to Cause Separation. Technical Report 2502, Ministry of Technology ARC RM, 1960.

[118] V.R.P. Sethuraman and H.D. Kim. Characteristics of Shock Train Flow in Divergent Channels. In *Seventh Asian Joint Workshop on Thermophysics and Fluid Science*, 2018.

[119] T.H. Shih, W.W. Liou, A. Shabbir, Z. Yang, and J. Zhu. A NEW $k-\varepsilon$ EDDY VISCOSITY MODEL FOR HIGH REYNOLDS NUMBER TURBULENT FLOWS. *Computers & fluids*, 24(3):227–238, 1995.

[120] Peltier S.J., B.E. Rice, N.J Bisek, C.K. McKenna, and J.W. Hofferth. Structure of Secondary Motion in a Mach 2 Boundary Layer. In *56th AIAA Aerospace Sciences Meeting*, 2018.

[121] J. Smagorinsky. GENERAL CIRCULATION EXPERIMENTS WITH THE PRIMITIVE EQUATIONS. *Monthly Weather Review*, 91(3):99–164, 1963.

[122] P.R. Spalart. Strategies for turbulence modelling and simulations. *International Journal of Heat and Fluid Flow*, 21(2), 2000.

[123] P.R. Spalart and S. R. Allmaras. A one-equation turbulence model for aerodynamic flows. In *30th Aerospace Sciences Meeting and Exhibit*, 1992.

[124] P.R. Spalart and S.R. Allmaras. A one-equation turbulence model for aerodynamic flows. Technical Report 1, Recherche Aerospatiale, 1997.

[125] C. G. Speziale, R. Abid, and Anderson E. C. Critical Evaluation of Two-Equation Model for Near-Wall Turbulence. *AIAA Journal*, 30(2):324–331, 1992.

[126] C.G. Speziale. Turbulence Modelling for Time-Dependent RANS and VLES: A Review. *AIAA Journal*, 36(2), 1998.

[127] R. Steijl, G. N. Barakos, and K. Badcock. A framework for CFD analysis of helicopter rotors in hover and forward flight. *International Journal for Numerical Methods in Fluids*, 51(8):819–847, 2006.

[128] M. Strelets. Detached Eddy Simulation of Massively Separated Flows. In *39th Aerospace sicences meeting and exhibit*, 2001.

[129] H. Sugiyama, R. Minato, K. Mizobata, A. Tojo, and Y. Mueto. Study on Shock Wave and Turbulent Boundary Layer Interactions in a Square Duct at Mach 2 and 4. *Journal of Thermal Science*, 15(1):37–42, 2006.

[130] H. Sugiyama, H. Takeda, J. Zhang, K. Okuda, and H. Yamagishi. Locations and Oscillation Phenomena of Pseudo-Shock Waves in a Straight Rectangular Duct. *JSME International Journal*, 31(1):9–15, 1988.

[131] L. Sun, H. Sugiyama, K. Fukuda, and K. Mizobata. Numerical and Experimental Investigations on the Mach 2 Pseudo-Shock Wave in a Square Duct. *Journal of Visualization*, 6:363–370, 2003.

[132] L. Sun, H. Sugiyama, R. Minato, K. Mizobata, and A. Tojo. Numerical and Experimental Investigations on Mach 2 and 4 Pseudo-Shock Waves in a Square Duct. *Transactions of the Japan Society for Aeronautical and Space Sciences*, 47(156):124–130, 2004.

[133] L.Q. Sun, H. Sugiyama, Mizobata K., T. Hiroshima, and A. Tojo. Numerical and experimental study of the Mach 2 pseudo-shock wave in a supersonic duct. 2005.

[134] N. Taylor, G. McGowan, G. Anderson, C. Schnepf, K. Richter, M. Tormalm, G. Loupy, V. Michel, C. Jeune, S. Shaw, E. DikbaÅ§, G. Barakos, K. Boychev, and J. DeSpirito. The Prediction of Vortex Interactions on a Generic Missile Configuration Using CFD: Current Status of Activity in NATO AVT-316. In *Conference: AVT-307 Symposium onSeparated Flow: Prediction, Measurement and Assessment for Air and Sea Vehicles*, 2019.

[135] N. Titchener, P. Bruce, and Babinsky H. An Experimental Investigation of Corner Bleed Applied to a Normal Shock-Wave/Boundary-Layer Interaction and Diffuser. In *49th AIAA Aerospace Sciences Meeting Including the New Horizons Forum and Aerospace Exposition*, 2011.

[136] N. Titchener and Babinsky H. Shock Wave/Boundary-Layer Interaction Control Using a Combination of Vortex Generators and Bleed. *AIAA Journal*, 51(5):1221–1233, 2013.

[137] N. Titchener and Babinsky H. The Effects of Various Vortex Generator Configurations on a Normal Shock Wave/Boundary Layer Interaction. In *51st AIAA Aerospace Sciences Meeting Including the New Horizons Forum and Aerospace Exposition*, 2013.

[138] N. Titchener and Babinsky H. A review of the use of vortex generators for mitigating shock-induced separation. *Shock Waves*, 25(1):473–494, 2015.

[139] G. D. van Albada, B. van Leer, and W. W. Roberts. A Comparative Study of Computational Methods in Cosmic Gas Dynamics. *Astronomy and Astrophysics*, 108(1):76–84, 1982.

[140] E.R. Van Driest. Turbulent Boundary Layer in Compressible Fluids. *Aeronautical Journal*, 18(3):145–160, 1951.

[141] B. van Leer. Towards the Ultimate Conservative Difference Scheme. V. A Second-Order Sequel to Godunov's Method. *Journal of Computational Physics*, 32(1):101–136, 1979.

[142] Z. Vane, I. Bermejo-Moreno, and S.K. Lele. Simulations of a Normal Shock Train in a Constant Area Duct Using Wall-Modeled LES. In *43rd Fluid Dynamics Conference*, 2013.

[143] H. Versteeg and W. Malalasekera. *An Introduction to Computational Fluid Dynamics: The Finite Volume Method*. Pearson, 2007.

[144] S. Wallin and A.V. Johansson. An explicit algebraic Reynolds stress model for incompressible and compressible turbulent flows. *Journal of Fluid Mechanics*, 403:89–132, 2000.

[145] P.J. Waltrup and Billig F.S. Structure of Shock Waves in Cylindrical Ducts. *AIAA Journal*, 11(10):1404–1408, 1973.

[146] C.P. Wang, K.Y. Zhang, and K.M. Cheng. Pressure Distribution Measurements in Scramjet Isolators under Asymmetric Supersonic Flow. In *44th AIAA Aerospace Science Meeting and Exhibit*, 2006.

[147] A. Weiss, A. Grzona, and H. Olivier. Behaviour of shock trains in a diverging duct. *Experiments in Fluids*, 49(2):355–365, 2010.

[148] A. Weiss and H. Olivier. Behaviour of a shock train under the influence of boundary-layer suction by a normal slot. *Experiments in Fluids*, 52(1):273–287, 2014.

[149] A. Weiss and H. Olivier. Shock boundary layer interaction under the influence of a normal suction slot. *Shock Waves*, 24(1):11–19, 2014.

[150] F.M. White. *Viscous Fluid Flow*. McGraw-Hill, 1974.

[151] D. Wilcox. Reassessment of the Scale-Determining Equation for Advanced Turbulence Models. *AIAA Journal*, 26(11):1299–1310, 1988.

[152] D. Wilcox. Formulation of the $k-\omega$ Turbulence Model Revisited. *AIAA Journal*, 46(11):2823–2838, 2008.

[153] J. Zhang and Morishita E. An Efficient Way of Specifying Profile Inflow Boundary Conditions. *TRANSACTIONS OF THE JAPAN SOCIETY FOR AERONAUTICAL AND SPACE SCIENCES*, 47(156), 2004.